UNIVERSITY OF LEEDS

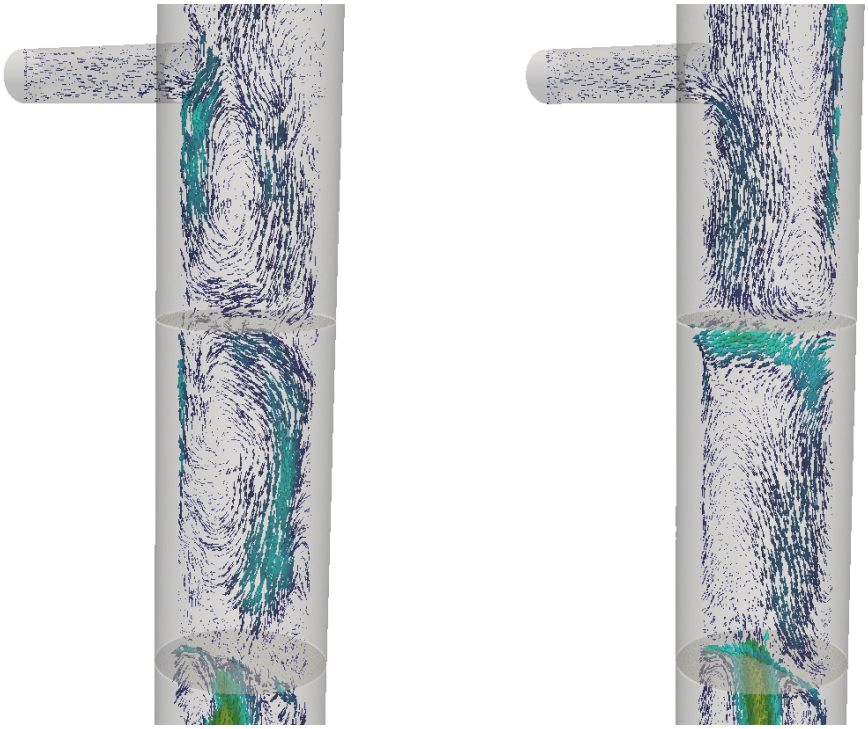

Computational Engineering for Nuclear Solvent Extraction Equipment

Daniel Wesley Theobald

Submitted in accordance with the requirements
for the degree of Doctor of Philosophy

School of Chemical and Process Engineering
UNIVERSITY OF LEEDS
August 2020

PhD Thesis

Computational Engineering for Nuclear Solvent Extraction Processes

Daniel Wesley Theobald

School of Chemical and Process Engineering
Nuclear Research Group
University of Leeds
August 2020

Computational Engineering for Nuclear Solvent Extraction Equipment
Daniel Wesley Theobald

The candidate confirms that the work submitted is his/her own, except where work which has formed part of jointly-authored publications has been included. The contribution of the candidate and the other authors to this work has been explicitly indicated. The candidate confirms that appropriate credit has been given within the thesis where reference has been made to the work of others.

This research is part of the GENIORS project, which has received funding from the Euratom research and training programme 2014-2018 under Grant Agreement No 7555171.

Supervisors: Bruce Hanson, Peter Heggs, Michael Fairweather, University of Leeds.
Examiners: Michael Bluck, Imperial collage London.
Harvey Thompson, University of Leeds.

Cover: Glyph of the ensemble time-averaged velocity fields for (left) the LES simulation and (right) the RANS simulation at maximum flow along the y-plane.

Acknowledgements

I would like to begin by expressing my sincerest gratitude for my hard working supervisors Bruce C. Hanson, Michael Fairweather and Peter J. Heggs for their continuous guidance and patience throughout this research. The experience of working alongside each of you over the years has been life-changing, to say the least.

I would also like to express my appreciation for the UK's EPSRC and the GENIORS research consortium for taking interest in this project and funding this research. Similarly, my gratitude extends to Dr Alan Burns and the EPSRC fluid dynamics CDT for including me within their training programmes and research community. Moreover, I would also like to credit the University of Leeds and its advanced research computing team for providing the maintenance and support for the high performance computing systems that were integral to this research.

A special acknowledgement is necessary for all the researchers who have, in unique ways, had a massive impact on my work. This includes, but is not limited to, Marco, Kostas, Andrea, Lee and all members of the Nuclear Research Group. Your your endless advice, guidance and patience is appreciated.

To Alex, for whom I have passed the torch of pulse column research to. I think you are brave to accept the challenge. However, your unwavering enthusiasm has inspired me to carry on. I wish you all the luck in the world.

On a personal note, being the first in my family to go to university was an achievement unto its own, in their eyes, and I know they have been rooting for me every step of the way.

Without a doubt the past four years have represented some of the most challenging and exciting times in my life. Surely this work would not have been achievable without the unconditional love and support from my closest friends. Namely, from those who have been with me from the start of my undergraduate degree and the new life-long companions I have made along the way.

So to all those acknowledged and to the City of Leeds, which will always hold a special place my heart, i say

Thank You.

Abstract

The ultimate objective of this work is to leverage modern computational tools to provide a unique and contemporary approach to pulse sieve-plate extraction column (PSEC) design and optimisation. Particular attention is given to providing novel analysis on: the functionality of operation, methods of performance analysis, determination of flooding, and development of simulation approaches that faithfully represent PSEC hydrodynamic behaviour.

A detailed assessment is undertaken of the dispersive mixing and turbulence characterisation of an industrially representative PSEC. This is achieved with computational fluid dynamics (CFD) running turbulence resolving large eddy simulation (LES), coupled with the volume of fluid (VOF) multiphase approach. Found was the dependency of PSEC functionality on turbulence production, and not on the viscous plate-induced stresses, generated therein. Consequently, the standard round-hole sieve-plate design is found to perform poorly at producing and distributing the types of flow and turbulence beneficial to droplet size reduction. This milestone discovery marks the first explicit contribution to knowledge of PSEC operation in decades.

Subsequently, a number of typical unsteady Reynolds averaged Navier-Stokes (URANS) turbulence modelling methods were compared against the benchmark LES. The URANS models, highly representative of the available PSEC CFD literature, were not able to produce agreeable solutions in the important hydrodynamic characteristics of the flows. Therefore the standard has been set for turbulence characterisation in PSEC simulation with LES.

The appropriate LES VOF method was carried forward to a campaign of 25 unique case runs that resulted in synergistically rich data set. Novel means of flooding identification was developed and tested. From this a number statistical analysis methodologies were employed to develop tools which successfully resolve the operational envelope and diagnose the likelihood of flooding during operation based on easily measurable variables.

Lastly, a state-of-the-art two-fluid hybrid VOF/Eulerian-Eulerian multiphase CFD model, with population balance, was implemented and interrogated. The model was successful in capturing all scales of the multiphase behaviour to further improve the faithful description of the complete fluid interactions. The population balance produced predictions for the droplet size distributions inline with available examples from literature and therefore provides exciting opportunities for accurate mass transfer predictions in pulse column simulations.

Keywords: Pulse sieve-plate extraction column, OpenFOAM, Droplet, Population Balance, Logistic Regression, CFD, Turbulence, Liquid-liquid, Nuclear, LES.

Contents

List of Figures

List of Tables

Acronyms

ARC	Advanced research computing
CFD	Computational fluid dynamics
E-E	Eulerian-Eulerian
FVM	Finite volume method
GEMMA	Generalised multiphase modelling approach
GPU	Graphics processing unit
HPC	High performance computing
HTU	Height of the transfer unit
LES	Large eddy simulation
LLE	Liquid-liquid exchange
MIBK	Methyl isobutyl ketone
N-S	Navier-Stokes
OPOSPM	One primary one secondary particle method
ORNL	Oak Ridge National Laboratory
PDF	Probability density function
PSEC	Pulsed sieve-plate extraction column
RANS	Reynolds averaged Navier-Stokes
RSM	Reynolds stress model
R&D	Research and development
URANS	Unsteady Reynolds averaged Navier-Stokes
VOF	Volume of fluid

Nomenclature

α	Fraction Function in VOF (-)
$\Delta\rho$	Density difference between both fluids ($\mathrm{kgm^{-3}}$)
ΔP	Pressure drop of the continuous phase (Pa)
ΔP_d	Pressure drop of the dispersed phase (Pa)
Λ_{MI}	Mixing Index (-)
μ_c	Dynamic viscosity of the continuous phase fluid ($\mathrm{Nsm^{-2}}$)
μ_d	Dynamic viscosity of the dispersed phase fluid ($\mathrm{Nsm^{-2}}$)
μ_t	Turbulence eddy viscosity ($\mathrm{m^2s^{-1}}$)
Ω	Vorticity ($\mathrm{s^{-1}}$)
ϕ	Hold-up of the dispersed phase (-)
ρ	Density ($\mathrm{kgm^{-3}}$)
ρ_c	Density of the continuous phase fluid ($\mathrm{kgm^{-3}}$)
ρ_d	Density of the dispersed phase fluid ($\mathrm{kgm^{-3}}$)
σ	Interfacial surface tension (Nm)
τ	Reynolds stresses ($\mathrm{m^2s^{-2}}$)
$\underline{a}$	Effective area ($\mathrm{m^{-2}}$)
ε	Dissipation rate of turbulence kinetic energy ($\mathrm{m^2s^{-3}}$)
A	Pulse amplitude (m)
C_O	Orifice discharge coefficient (-)
D	Column diameter (m)
$d_{[3,2]}$	Sauter Mean Diameter (m)
e	fraction free area of the sieve-plate (-)
f_t	Pulse frequency (Hz)
g	Acceleration due to gravity ($\mathrm{ms^{-2}}$)
h	Sieve-plate spacing (m)
IRQ	Interface resolution quality (-)
IRQ_{crit}	Critical interface resolution quality (-)
k	Turbulence kinetic energy ($\mathrm{m^2s^{-2}}$)
k_{sgs}	Subgrid scale turbulence kinetic energy ($\mathrm{m^2s^{-2}}$)
P	Pressure (Pa)
Re	Reynolds number (-)
S	Rate of strain ($\mathrm{s^{-1}}$)

U	Velocity (ms^{-1})
U_c	Velocity of the continuous phase fluid (ms^{-1})
U_d	Velocity of the dispersed phase fluid (ms^{-1})
U_r	Relative velocity between two phases (ms^{-1})

1

Introduction

1.1 Motivation

As of 2020, there has been monumental shift in both public and governmental perceptions towards environmental conservation and longevity. In the wake of the COVID-19 global pandemic, countries across the planet now stare directly into the abyss of an unprecedented recession, the likes of which have not been seen in modern times. As such, world leaders now scramble frantically to compile economic recovery plans. Many of them seeing this as the perfect opportunity for a 'green recovery' (IEA, 2020).

Nuclear energy continues to provide one of the only feasible means of mass-scale base load power generation whilst meeting net zero CO_2 emissions targets. Consequently, it is understood that nuclear power must play a dominant role if we are to solve the 21st century climate crisis challenge. Figures published through the World Nuclear News put the global nuclear cost estimate, up to 2050, at $8.6 Trillion (2019 USD) based on the United Nations Intergovernmental Panel on Climate change 2018 report (IPCC, 2018; UxC, 2020).

Therefore, presently, there are a number of political and commercial drivers towards sustainable and affordable nuclear technologies. Naturally, particular interest has arisen in the field of advanced solvent extraction processes required to realise sustainable closed-loop next generation nuclear fuel cycles. Challenges lie within the modernisation of waste reprocessing through the development of robust separation flow sheets that rely on the optimisation of particular equipment, pulsed sieve-plate columns (PSECs) (Taylor, 2015). Next-generation fuels, containing higher concentrations of transuranic elements at greater burn-up levels, will require greater flexibility and reliability from processing equipment (Lovasic, 2008). As a result, the development of adaptive and dependable solvent extraction process equipment will be a strong focus of the global nuclear research and development (R&D) sector throughout the coming decades.

To date, the majority of PSEC R&D has involved crude *a posteriori* characterisation of hydrodynamic behaviour. Previous investigations typically follow an empirical philosophy of matching cause-and-effect through limited experimental runs with various alterations to 'independent' variables. Through

successive trial-and-error, various authors have produced a number of correlations linking aspects of column performance to geometric characteristics and operating parameters (Yadav & Patwardhan, 2008). Such relationships can be useful when used alongside pilot plant tests. However, they ultimately fail to describe the fundamental behaviour of PSECs, and do not consider the multivariate coupled nature of the operational parameters. Moreover, designs based off empirical studies tend to result in over-specified systems with poor performance and reliability due to a lack of understanding and large uncertainties (Matar, 2015).

Progression in PSEC research has remained stagnant since the last industry leading studies were conducted throughout the 90s by Kumar & Hartland (1994, 1996, 1999). This is likely due to failing interest in nuclear reprocessing, by far the largest industry market for PSEC units. However, due to a recent resurgence in global reprocessing, a handful of notable studies have been conducted in the interest of improving understanding of PSECs. These investigations have used flow simulation software to more closely analyse hydrodynamic phenomena, mostly in idealised or simplified geometries. The computational fluid dynamics (CFD) models used to represent these systems are questionable in their implementation and are typically promoted as feasibility studies (Din *et al.*, 2010; Khatir *et al.*, 2016; Kolhe *et al.*, 2011; Mehra & Chaturvedi, 2016; Yadav & Patwardhan, 2009). The most modern works in this field exclusively rely on the k-ε turbulence model as closure to Reynolds-averaging finite volume method approaches (Sen *et al.*, 2015, 2016, 2018; Yadav & Patwardhan, 2009; Yi, 2018). The underlying assumption being that time-averaged eddy viscosity-based turbulence modelling is accurate enough to faithfully represent the underlying hydrodynamic phenomena. However, one objective of this work is to challenge this assumption, and to provide insight into the complexities of the physical behaviour of operating PSECs through the use of time-dependent, three-dimensional, turbulent eddy-resolving methods coupled with a number of multiphase modelling methodologies.

1.2 Problem Definition

Currently, operational spent fuel reprocessing technologies have continued to rely on legacy design strategies. Such methods have been developed from empirical analysis of decades old experimental data. As of late, there has been little interest in further development of these technologies. This is despite the necessity for process intensification and optimisation. Advanced flow sheets contain new reprocessing chemistry and diversification of feed material (spent fuel composition). It is therefore evident that there is a need for the development of innovative continuous separation technologies, and to improve the design basis of current ones. With regards to PSECs, experiential approaches have failed to:

- Quantitatively characterise the flow conditions present during operation.
- Definitively outline the conditions/mechanisms that cause flooding.
- Determine the significance of operational variables on PSEC functionality.
- Mechanistically describe droplet formation processes and dispersion (mixing).
- Quantitatively describe the role of turbulence in performance.

With the availability of new computational engineering tools, fluid flow modelling has allowed for some research gaps to be explored. However, most research undertaken in this regard has used arguably low performance modelling techniques. This is either due to lack of computational resources or through ignorance of the range of applicability of such methods.

1.3 Novelty of Research

This project uses high-resolution CFD methods to gain quantitative insight into the hydrodynamics of PSECs, which at present are poorly understood. A selective investigation will be undertaken with the overarching objective of determining the physics of the flow within multiphase counter-current PSECs. This involves the

- use of high performance computing (HPC) facilities and scalable open source CFD codes.
- implementation of eddy-resolving fluid flow modelling techniques and interrogation into the applicability of common turbulence modelling approaches.
- quantisation of performance markers, such as mixing efficiency and levels of dispersion.
- quantitative identification and analysis of flooding in PSECs, particularly during the early onset of flooding for which no examples in the literature exist.
- use of statistical methods of analysis of the relationship between multivariate interacting process variables and column operation and flooding.
- implementation of state-of-the-art multiscale hybrid-style interface tracking and dispersion multiphase modelling methods.

Computational research of this nature on PSECs has seldom been reported. That which exists is limited in depth of analysis or in value to design. This body of work provides significant contributions to PSEC research through the implementation of powerful computational tools, and through the application of methods of analysis never before seen within the context PSEC CFD analysis.

1.4 Goals and Objectives

The focus of the study will involve the use of Large Eddy Simulation (LES) with a high-fidelity mesh resolution of 5.5 M cells. This level of detail is yet to be achieved in PSEC CFD studies, the closest being Khatir *et al.* (2016) with $\sim$ 500,000 cells. This simulation strategy will be implemented using the open source CFD software OpenFOAM®. Their general public licence allows for limitless access and customisation of the source code allowing for tailored solutions to complex flow problems.

In terms of deliverables, the final project goals are outlined as follows:

- Construction of a 3-dimensional CAD model which is representative of industrial PSECs being based off typical industrial design cues/constraints.
- Development of a multiphase LES using the volume of fluid (VOF) method using a mesh with resolution capable of capturing fine levels of flow detail.
- Incorporating and subsequently assessing an appropriate dynamic Sub Grid Scale (SGS) model.
- Evaluation of the applicability of Reynolds-averaged Navier-Stokes (RANS) modelling methodologies for transient multiphase PSECs.
- Discussion of early onset flooding in PSECs and the definition of quantitative means of flooding identification that would form the basis of flooding control systems in PSECs.
- Statistical determination of the effect of interacting operation variables on the performance of the column design presented and the development of analytical methods to do so.
- The delivery of predictive tools to assess the stability of PSEC operation and predict the likelihood of flooding based on physically measurable operational control parameters.
- Assessment of single-fluid, two-fluid and hybrid multiphase liquid-liquid modelling approaches in simulating dispersed counter-current flow in PSECs.
- Suggestions, in each case, for further development of computational tools for high-fidelity PSEC modelling with a mind towards industrialisation.

1.5 Thesis Structure

Chapter 1 Introduction outlining the industrial necessity for the work presented. Included is explicit justification for the novelty of the research undertaken, and goals and objectives of the project.

Chapter 2 Overview of the historical development and functionality of PSECs, and comprehensive review of the literature published on relevant research with a critique and commentary on the work and findings of authors.

Chapter 3 Concise description of the mathematical models used throughout the thesis along with a general overview of their implementation.

Chapter 4 Detailed and explicit analysis of the turbulent behaviour of PSEC counter-current multiphase flow using a LES VOF model. Development and use of performance analysis criteria and validation of hydrodynamic behaviour from qualitative and quantitative analysis of the resulting flow fields. Subsequent cross-examination of the applicability of URANS methods in their capability to faithfully capture the hydrodynamic behaviour of PSECs against the LES benchmark solution.

Chapter 5 Campaign of designed simulations exploring the limits of analysis and applicability of the LES VOF method in uncovering new information on the behaviour of PSEC operation. Reported are conclusive findings from the statistical analysis of multivariate process variables on the performance of PSECs. A true three-dimensional flooding surface is resolved to outline the operational envelope of the PSEC studied. Additionally, predictive tools are developed with potential for applications in process control. The discoveries within this chapter bring to light the value of novel methods of analysis in conjunction with the interrogation of traditional approaches.

Chapter 6 Application of a state-of-the-art hybrid VOF/Eulerian-Eulerian multiphase model with population balance to address the limitations in the VOF method reported on in previous chapters. Predictions in the key flow characteristics are assessed against VOF results in conjunction with a typical Eulerian-Eulerian implementation. Determination of the model to accurately revolve the droplet evolution at the sieve-plates and initial dispersion and break-up of the dispersed phase into the column, as well as to incorporate key dispersed phase flow effects, such as slip velocity and drag modelling to provide improvements in accuracy for the inter-stage hold-up predictions. Droplet size predictions are validated against available information from trusted literature sources.

Chapter 7 Retrospective discussion of the programme of work undertaken in its entirety with a summary of the conclusions ascertained and future work proposals.

1.6 Publications

During the course of this programme of research, a number of peer reviewed publications to either science or engineering journals, or as a result of conference attendance have been produced. In doing so, the research that has been undertaken is fully available to the public. It should be noted as a disclaimer that material from the publications listed have been used in part or in full within the compilation of this thesis. Those marked 'perspective' are publications currently in submission or awaiting submission.

1.6.1 Journal Publications

Theobald, D. W., Hanson, B., Fairweather, M. and Heggs, P. (2020). Implications of hydrodynamics on the design of pulsed sieve-plate extraction columns: A one-fluid multiphase CFD model using the volume of fluid method. *Chemical Engineering Science*. **221**.

Theobald, D. W., Hanson, B., Fairweather, M. and Heggs, P. (perspective, 2021). Discussion on the applicability of unsteady RANS turbulence modelling against highly resolved LES methods in industrial PSEC flows. *Chemical Engineering Science*.

Theobald, D. W., Hanson, B., Fairweather, M. and Heggs, P. (perspective, 2021). Simulation campaign for the statistical analysis of industrial PSEC operation and flooding. *TBD*.

Theobald, D. W., Hanson, B., Fairweather, M. and Heggs, P. (perspective, 2021). Development of a virtual PSEC using multiscale hybrid multiphase modelling and population balance. *Chemical Engineering Journal*.

1.6.2 Papers in Conference Proceedings

Theobald, D. W., Hanson, B., Fairweather, M. and Heggs, P. (2018). Multiphase Large Eddy Simulation of a Pulsed Sieve-Plate Extraction Column. Presented at the Waste Management Symposia. Phoenix, Arizona, US.

2

Literature Review

2.1 Background

This section provides a contextual discussion of solvent extraction processes and their value in industrial engineering applications. Moreover, a brief description of pulsed sieve-plate extraction columns (PSECs), and current understanding of their operation, is given to provide a background for the research topic of the thesis.

2.1.1 Solvent Extraction in the Nuclear Industry

Liquid-liquid extraction (LLE), otherwise known as solvent extraction, was first brought to the forefront of chemical process engineering during the 1930s and heavily industrialised through the petroleum engineering industries as a means for refining products by removing undesirable components (McKetta, 1992). The 1940s saw an increase in the popularity of this process for nuclear industry applications, namely, recovering valuable uranium and plutonium for both power and defence purposes. Since then, many variations in LLE process equipment have been developed in order to achieve safe, reliable and efficient extraction of radionuclides from raw stocks and irradiated nuclear fuels. Additionally, LLE has seen much success in other fields of chemical processing such as hydrometallurgical and pharmaceutical industries (Todd *et al.*, 2000). These technologies continue to be successfully implemented today for nuclear waste reprocessing. However, a significant level of uncertainty lies in the fundamental engineering of such systems resulting in underutilisation and increased operating complexity and cost (Wardle *et al.*, 2006; Yadav & Patwardhan, 2009).

Solvent extraction is founded on the principle of removing constituent chemical components from a liquid solution through the utilisation of an immiscible contacting liquid. Separation will be achieved if a redistribution of components occurs between the original and contacting liquid during mixing. LLE equipment can be categorised into two distinct groups of equipment: single-stage and multi-stage. Single-stage equipment only allows for one extraction stage per piece of equipment; here two liquids are mixed and subsequently separated after extraction has occurred. A counter-current cascade, or bank, of single-stage equipment may be arranged in order to improve the extraction yield. In contrast, multi-stage equipment combines

the necessary extraction stages required into one single piece of apparatus (Treybal, 1968).

Mixer-settlers are an example of single-stage LLE equipment which is traditionally exploited in uranium recovery operations in fuel reprocessing plants or in uranium mining facilities (Edwards & Oliver, 2000; Kishbaugh, 2000). They have the advantage of being able to handle interfacial debris and high volumetric throughputs with good scalability. This allows them to be engineered for a range of applications with particular benefits in mineral refinement where solid debris can be expected. Due to large settling areas, mixer-settlers require a broad floor space, this can be inconvenient when more than one extraction stage is necessary. They generally require long residence times resulting in lengthy start-up procedures in order to achieve steady-state operation. This can be costly and inconvenient not only in terms of time and operability, but can also lead to solvent degradation issues (radiolysis) when used in nuclear environments. Furthermore, they can be difficult to seal which can be a particular safety disadvantage when processing radioactive solutes (Rousseau, 1987).

Alternatively, single-stage centrifugal contactors, adapted for radioactive solutions, have seen recent success in replacing mixer-settlers in various uranium recovery operations; an 18-stage bank was used to replace a 24-stage bank of mixer-settlers at the Savannah River Site (SRS) Plutonium Uranium Redox EXtraction (PUREX) plant. Moreover, they are currently operated in the plutonium purification cycle at La Hague and the Caustic Side Solvent eXtraction (CSSX) process at SRS (Duan *et al.*, 2014). Centrifugal contactor designs sought to amend many of the shortfalls of using mixer-settlers by providing greater flexibility to process alterations, such as changes in solvents, and reducing safety concerns with improved materials handling. Centrifugal contactors also require comparatively less: start-up and shut down time, residence time, space requirements and solvent/aqueous inventories when in operation (Kishbaugh, 2000). Consequently, centrifugal contactors have become the main focus of R&D in nuclear waste management across the world, particularly in advanced solvent extraction processes used in next-generation nuclear fuel cycles (Duan *et al.*, 2014).

For more sensitive operations involving rich solutions of fissile plutonium, geometrically safe pulse columns were designed and incorporated into solvent extraction flow sheets in order to dramatically reduce processing hazards. The pulse column was originally patented in 1935 by Van Dijck (1935) as a novel means of generating liquid-liquid contact for extraction and washing purposes. Subsequently, in 1949 this technology was adopted by the Hanford nuclear production complex for applications in uranium processing due to its enhanced shielding and criticality advantages. The new type of pulsed extraction column offered a two-fold reduction in height in comparison with traditional packed

columns of equal performance. Furthermore, the high surface area to volume ratio of pulsed columns allowed for safer processing of higher plutonium concentrations. As criticality and shielding are of the utmost concern when dealing with the processing of reactor fuels, this technology offered a critical advantage over traditional packed columns of that era (Burkhart & Fahien, 1958; Phillips, 1992). Since its early adoption into the industry, the pulse column has become a vital component of reprocessing facilities such as: Hanford, Idaho National Laboratory, and the UK Thermal Oxide Reprocessing Plant (THORP) (McKetta, 1998). As such, pulse columns will be the main subject of focus for this thesis. Its vital role within current and future nuclear reprocessing strategies ensures that the research presented in this thesis will be of significant interest from industry globally.

2.1.2 Pulse Sieve-plate Extraction Columns: An Overview

Since the conception of the pulse column, a diverse range of design modifications have been made to the original prototype patented by Van Dijck (1935). The design most commonly operated in the nuclear industry is known as a PSEC which can be driven by a mechanical or, more typically in the case of modern columns, a fluid-operated pulsing system (McKetta, 1998). A schematic detailing the geometric layout of a standard fluid-operated PSEC can be seen in Fig. 2.1.

Pulse columns operate on the basic principle of facilitating mass transfer through maximising interfacial contact area during counter-current flow between two mixed fluids, a heavy and light phase. The heavy phase usually consists of a rich aqueous liquor containing the desired components, and an organic phase containing a ligand capable of removing the desired components from the aqueous solvent. The heavy phase enters from the top section of the column and exits from the bottom. Conversely, the light phase will enter from the bottom and flow from an outlet at the top. Settling sections are located at the top and bottom of the column for the organic and aqueous phases respectively (Burkhart & Fahien, 1958). As shown from Fig. 2.1, the outlets are positioned as to not remove feed material unintentionally, for example, the organic raffinate outlet it placed within the organic settling region, but above the aqueous inlet.

In this case, pressurised air is used as the driving mechanism to actuate pulsation in the pulse leg depicted in Fig. 2.1. The pulse leg is connected in-line to the organicf feed and compressed air is fed into the top of the pulse leg in a cyclic fashion. Air feed, and therefore pulsation frequency, is controlled via the actuation of a dual valve system. An air reservoir is placed upstream from the valve system in order to dampen pressure fluctuations in the air feed (Weech & Knight, 1967).

In order for this system to achieve a controlled pulsation, the system relies on the exchange of momentum between the column and pulse leg. The hydrostatic head differential between the column and pulse leg drives fluid exchange. At the start of

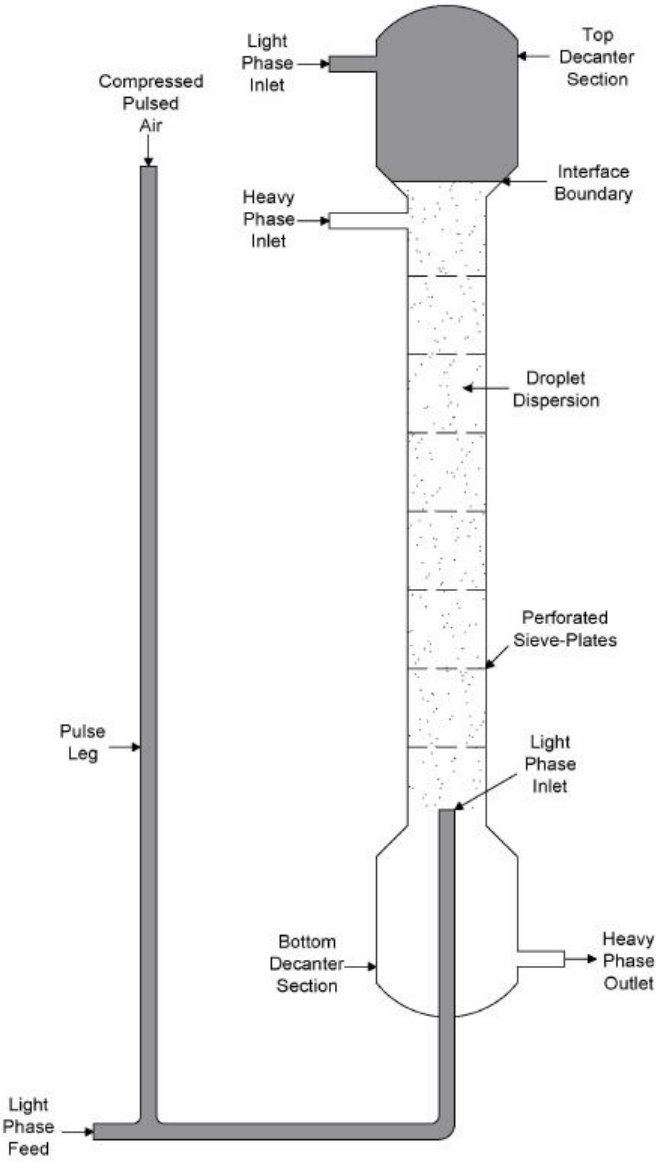

Figure 2.1: Design of a PSEC system with air pulser.

a pulse cycle, compressed air is introduced which depresses the pulse leg liquid level. This causes an increase in liquid level in the PSEC resulting in a positive stroke. In turn, this column level increase causes liquid to flow back into the pulse leg and return to an equilibrium position resulting in the negative, return, stroke. A dual valve system is typically used introduce compressed air into the system and to vent the compressed air during the return stroke (Weech & Knight. B. E., 1977).

The fluid mixture can be arranged in one of two ways, a dispersion of aqueous droplets falling through a continuous solvent layer or a dispersion of solvent droplets rising though a continuous aqueous layer (Nash & Lumetta, 2011). The determination of which fluid is the continuous phase is governed by a number of considerations designed to maximise interfacial contact area. Factors include: plate wetting ability, interfacial tension, fluid viscosity, and flow rates. In order to achieve finer droplet dispersion, the fluid with the greater affinity for the plate

(superior wettability) will be chosen as the continuous phase. However, this design consideration maybe irrelevant if the interfacial tension is low as dispersion will be sufficient in either direction. Volumetric flow rates will then be the controlling factor effecting column performance. If the throughput of the dispersed phase is low, mass transfer will be hindered due to limited interfacial contact area. The continuous phase viscosity can largely effect the settling rates, and therefore throughput, of the dispersed phase and is consequently taken into consideration when determining the phase arrangement. Phase arrangement is usually quoted as a solvent-to-raffinate flow ratio (or solvent flow ratio) wherein a ratio < 1 typically indicates a raffinate continuous phase (Cohen & Beyer, 1952; Rousseau, 1987).

Similarly, such factors used to determine the phase arrangement can also explicitly effect the level of the principle bulk interface (Cohen & Beyer, 1952). Control of the position of this level is essential for stable column operation and, consequently, mass transfer. For an aqueous continuous phase this interface is located at the top settler and for an organic continuous phase at the bottom settler. Interface level control is achieved via manipulation of the fluid outlet flow rates. For example, for a system with a bottom principle interface the interface level would be controlled through alterations in the rate of aqueous phase removal from the bottom settler (Nash & Lumetta, 2011).

In order to generate dispersion, and therefore maximise contact area, mechanical energy is applied to the system via the pulsation mechanism (pulser). A periodic pulsation creates the necessary shear forces required to provide sufficient agitation of the fluids upon interaction with the internal perforated plates (Jaradat *et al.*, 2011). The pulsation frequency and amplitude are two fundamental operating variables used to control the extraction process during operation, and are manipulated via the pulse leg mechanism, mentioned previously. Frequency and amplitude can affect the column throughput and extraction efficiency as well as the 'flow regime' of the column. Pulsed columns can extract effectively in 3 primary modes of operation: mixer settler, dispersion and emulsion flow regimes. Additionally, poor column control can lead to unstable flow and, ultimately, flooding either by an excessive, or insufficient level of pulsation. Figure 2.2 illustrates the difference in the flow patterns that can be expected from different modes of operation. Some research focuses on correlating frequency and/or amplitude with flow regimes and/or flooding limits and this work will be discussed in greater detail in Section 2.2 (Yadav & Patwardhan, 2008).

The final major design component of the pulse column are the internal plates used to separate extraction stages and produce dispersion through shear on contact with the fluids. Perforated plate designs, referred to as sieve plates, are commonly used in nuclear applications for high performance extraction in reprocessing (Jiao *et al.*, 2013). Disc and doughnut (baffle) type plated pulse

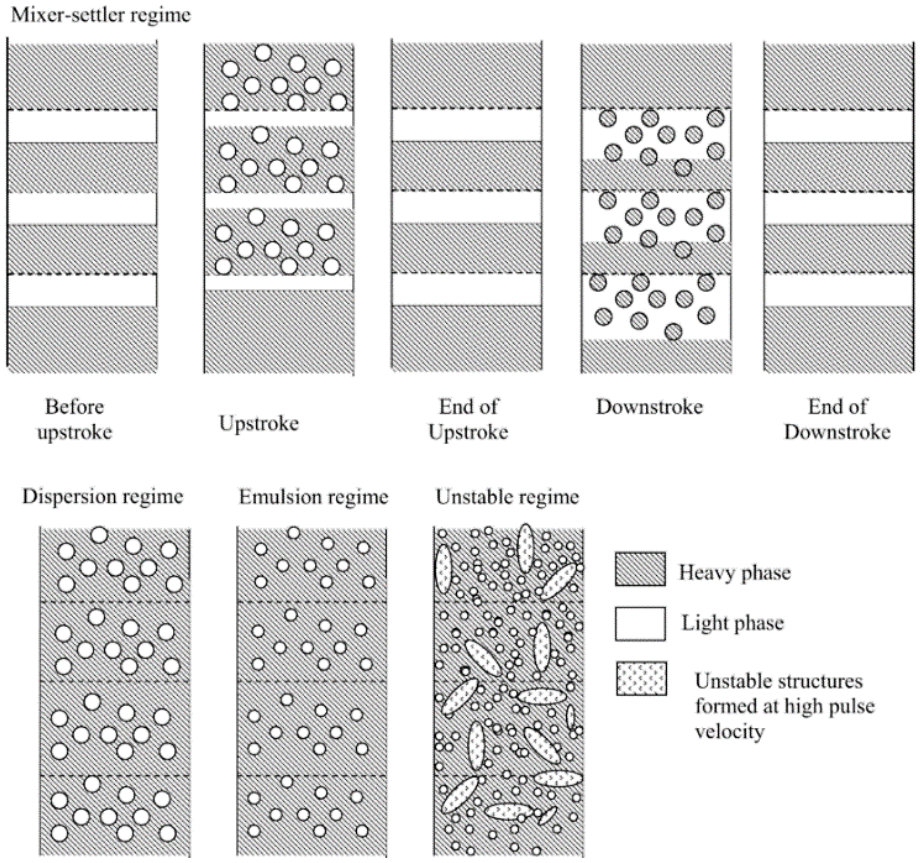

Figure 2.2: Expected flow regimes in PSECs (Yadav & Patwardhan, 2008).

columns have seen some increase in popularity for replacing mixer-settlers in base metal extraction of uranium and other commodity metals such as zinc and copper (Misra *et al.*, 2002). This is presumably due to their ability to handle higher throughputs and some solids content. However, as reprocessing is the main focal application of this study only PSEC will be discussed.

Sieve plates, horizontal cylindrical sections of material with perforated holes spaced evenly apart, allow fluid to flow in both directions during operation and produce the necessary stage separation along the column in order to achieve high efficiency extraction (Burns & Johnson, 1953). The holes are to be designed so that no ordinary flow occurs across the plate without agitation due to surface tension forces at the interface between the two immiscible fluids (Treybal, 1968). Certain design factors of sieve plates can affect the behaviour of pulse columns. These include: plate spacing, plate-hole diameter, hole distribution (pitch), and fractional free area. A number of authors have attempted to correlate these design features with column performance and this is will be discussed further in Section 2.2 (Bril & Costa, 1964). Additionally, the plate material can affect column performance; some designs incorporate dual-material plates in order to improve wetability of the heavy phase on the top side and vice versa. The intention is to enhance droplet coalescence after agitation and prior to passing though the holes, thus improving mixing (Burns & Johnson, 1953). Furthermore,

more advanced plate designs including nozzle-hole plates and flow redistributors have been investigated and incorporated into industrial design to improve mixing performance (Bril & Costa, 1964; McKetta, 1992).

2.1.3 Incentives towards a Modelling and Simulation Approach

The primary focus of this project is to develop a more complete understanding of pulse sieve plate extraction columns. More specifically, to produce modelled equations to describe and predict the physical phenomena of droplet evolution, hold-up and mass transfer a priori. The complexity and diversity of pulse column designs present certain unique challenge, viz. the many geometric, material and operating variables which influence hydrodynamics (Yadav & Patwardhan, 2009). Previous efforts correlate column performance aspects a posteriori. The most notable of which are works from authors such as: Smoot *et al.* (1959) Thornton (1957), Kumar & Hartland (1983, 1986, 1994, 1996, 1999), Tribess & Brunello (1998), Sreenivasulu *et al.* (1997), and Venkatanarasaiah & Varma (1998). Each author has chosen to take an empirical approach, relying on a limited set of experimental runs in order to examine relationships between the hydrodynamics and column variables. Each study has generally focused around a singular type of system with little variation in the geometries or materials used. As such, the resulting correlations are prone to limitations and often require supplementary pilot plant tests before they can be confidently used for industrial design applications (Yadav & Patwardhan, 2009). Furthermore, the lack of understanding and reliability inevitably results in significant over-design; this typically involves exaggerated safety-margins to compensate for the increased risk from uncertainty (Matar, 2015).

By moving away from empiricism, reliable predictive tools can be formulated which will reduce design complexity, thus reducing overhead cost and commissioning times for the end-user (Matar, 2015). However, in order to achieve this, an enhanced level of detail is required that cannot be reasonably achieved through conventional laboratory experimentation. The industry has seen a large shift towards simulation methods since the turn of century, particularly in industrial nuclear R&D and in PSEC research. Computer aided engineering tools, such as CFD, can offer profound insight into flow characteristics and other transport phenomena, such as heat and mass transfer. When done correctly, numerical simulation produces data to a high degree of accuracy and will incorporate a fundamental understanding of the basic physical mechanisms governing fluid dynamics. Naturally, this will lead to a deeper understanding of the physical parameters that effect, or are affected by, fluid flow (Sagaut, 2010).

CFD can provide a number of other distinctive advantages over conventional

experimental research. Lead times and R&D costs can be substantially reduced as pilot plant trials become less relevant, studies can be performed on larger scales when controlled experiments are impractical or even impossible to achieve, and systems can be studied beyond their safe operating limits (Versteeg & Malalasekera, 2007). The latter point is of particular importance for this investigation which would otherwise involve the use of hazardous solvents and radioactive species. Consequently, CFD has been incorporated, or used primarily, in a number of new PSEC studies. Notably, in works from Yadav & Patwardhan (2009) Din *et al.* (2010), Kolhe *et al.* (2011), Khatir *et al.* (2016), and Mehra & Chaturvedi (2016). These studies have taken advantage of the benefits of computational modelling in order to characterise either mass transfer efficiencies, axial dispersion effects, droplet evolution and/or hold-up. Although this research has revitalised interest and progression in PSECs, it could be argued that the modelling approaches used are rudimentary and/or outdated or require additional work. Yadav & Patwardhan (2009), Kolhe *et al.* (2011), and Din *et al.* (2010) each model turbulence via the k-ε model, used to close the RANS equations. Khatir *et al.* (2016), and Mehra & Chaturvedi (2016) have made efforts to move towards a superior simulation method using LES. However, Mehra & Chaturvedi (2016) do not mention the inclusion of turbulence. Additionally, Khatir *et al.* (2016) has only considered single-phase flow in a LES study. The papers discussed here, along with others, will be reviewed in depth in Section 2.3.

To conclude, much of the legacy work involved in PSEC characterisation has involved the development, and subsequent use of, unreliable empirical correlations. The development of more robust and accurate fundamental models will provide greater benefit for the end-user. In order to achieve this, a high level of detail and accuracy is required that can only be realisable through advanced CFD simulation techniques.

2.2 Pulse Column Parameters

This section covers the numerous design considerations of PSECs. Available literature concerned with the determination of these parameters, either through empirical correlations or fundamental modelling, will be considered for review. Namely, flooding limits, regime transitions, droplet size, hold-up, and mass transfer. Additionally, the different pulsing methods used by historical pulse column designs will be reviewed and the most appropriate will be selected with justification and used as a basis for the geometry design and setting of the boundary conditions.

2.2.1 Pulsing Techniques

2.2.1.1 Early Systems from the 1930s - 1960s

The original van Dijck pulse column design called for moving plates as the main agitation method to initiate contact between the two immiscible fluids therein. The plates were connected via a reciprocating chain mechanism connected to a motor. As mentioned by Van Dijck (1935), this chain mechanism could be replaced by other means of initiating plate movement such as a central shaft or similar. There are obvious issues associated with a moving plate design, especially when considered for use in chemical processes in a nuclear environment. Firstly, this design incorporates a large amount of moving parts which, in nuclear applications, is not considered good design practise, part failures can be difficult, dangerous and costly to repair or replace due to safety limitations concerning radiation dose and contamination. It should be noted that in this instance, the internal components are more perceptive to failure as they are submerged in corrosive liquid environments and experience wear and physical stress during prolonged operation. Corrosion of internal components can also lead to inefficiencies and contamination during reactive operations leading to undesirable product purity. Lastly, issues with stage-wise leakage is inherent in such a system with moving plates; this can lead to inefficiencies in fluid dispersion leading to lower yields than expected (Van Dijck, 1935).

In order for this equipment to be successfully adopted into the nuclear industry operative reliability was of paramount importance. Switching from a moving plate to oscillating feed (stationary plate) design expedited the advancement of this technology through use in nuclear solvent extraction operations. Van Dijck's seemingly less complicated stationary plate design utilises an oscillating moving fluid feed in order to cause agitation, and therefore dispersion, of the immiscible fluids. Specifically, his original design called for fixed plates with the use of a reciprocating piston pump in the bottom feed line in order cause an oscillating flow due to the piston movement. It was mentioned that this pump could be

replaced by other positive-displacement pumps. Aside from the mentioned modifications the working theory of the column remains mostly the same. Moving the fluid, however, has the advantage of distributing the agitation energy across the entire fluid volume whilst maintaining the continuity of the counter current action (Feick & Anderson, 1952; Van Dijck, 1935). However, the mechanical differences in the operating design of the stationary plate lead to improved reliability through the use of fewer moving parts and, therefore, a reduced likelihood of equipment failure and improved serviceability.

Early preliminary pulsed column experiments were conducted at both Oak Ridge National Laboratory and Hanford site by Ellison (1951) and Burns *et al.* (1949), respectively, using similar equipment. Ellison (1951) conducted pulse column trials using a fixed bellows pump feeding a 1/2" (12.7 mm) I.D. column. The pump is driven mechanically via a motor attachment allowing for 60 pumps per min (1 Hz pulse frequency) which a push-pull effect allowing for oscillating flow. Additionally, this system could be modified in order to alter the pulse amplitude between 1/16" (1.59 mm) and 14/16" (22.3 mm). His investigation showed that increasing the pulse frequency from 0.5 Hz to 1 Hz increased performance and increasing the pulse amplitude lead to a trend of increasing extraction efficacy to a maxima with falling extractability thereafter. This is in direct disagreement with that found by Burns *et al.* (1949) wherein a straight line negative correlation was found for uranium extraction vs. pulse amplitude. Their explanation for this negative correlation is that as amplitude increases, droplet size increases leading to less efficient mass transfer conditions; this explanation fits for that seen by Burns *et al.* (1949). However, to justify the turning point of his correlation, Ellison explains that at a critical amplitude the flow becomes dramatically more turbulent leading to droplet separation and therefore increase mass transfer Ellison (1951) .

Later, during the mid to late 1950s, Oak Ridge National Laboratory also began to study the effect of pulsation on the operating characteristics of pulsed columns for a variety of columns sizes and arrangements. This study emphasised less on extraction efficiencies and more the hydrodynamic flow properties of the pumping systems. In each case a piston type displacement pump was used as the pulser mechanism coupled to an in-line check valve used as energy rectifier in order to prevent back-flow on negative strokes. A selection of check valves were first considered for this system: floating disk (non-spring-loaded), centre-guided disk (spring-loaded), and swing check (spring-loaded). Certain design criteria such as cracking pressure and valve closure time determined the choice for this system which, in this case, called for spring loaded centre-guided disk. All things considered, this is a basic pulse pumping system which resulted in complications during operating mostly due to fluid leakages and air ingress into the system (Irvine, 1957). However, this study

found that the sizing and design of a pulse column can largely affect the pumping characteristics of the feed line. This leads to the conclusion that the scale up of a typical pulse column system, particularly with this pumping mechanism, can be difficult in part due to the diverging pumping characteristics with changes in column size.

In response to the work conducted by Feick & Anderson (1952), on pulsed packed columns, a deeper study was conducted by Han Li (1952) at the Georgia Institute of Technology with the aim of characterising the effect of pulsation on column performance. This study was founded from the lack of correlations presented by Feick & Anderson (1952). Amongst others, the chief variables considered were pulse frequency and pule amplitude on extraction efficiencies and HTU values. The experimental apparatus devised for this study included a working sieve-plate pulsed column experimental rig designed accurately measure the sought after correlations. In order to provide pulsed flow, a proportioning pump was fitted with a speed reducer to the feed line of the column. A mercury seal was used to prevent recirculation effects occurring between the feed and column fluids. This study first identified two operational regions of dispersion patterns. The operational regions were differentiated by the turbulence present in the flow and so were identified according to Re value ranges. A 'streamline' range, Re<1000, produces less dispersion and poor column performance. Within this region large cell like structures, large droplet sizes, appear which move vertically within an interrupted laminar manner. At Re>1800 a fine dispersion appears within a 'turbulent' region with a drastic increase in column performance and extraction efficiencies. A unique trend found within this study found that mass transfer rates were independent of pulsation frequency or pulse amplitude but was found directly dependent on the product of the two variables (Han Li, 1952).

Similarly, Pinzow (1957) also attempted to expand on the work by Feick & Anderson (1952) by investigating the effect of altering pulse frequency on the performance of a pulsed packed column. His pulsation mechanism used a non-conventional pulsation mechanism wherein a bellows pump was coupled to the base of the heavy liquid settling region directly and was driven via a motorised cam mechanism, see Fig. 2.3. His investigation also found that an increase in the pulse frequency has direct positive correlation on the effectiveness of mass transfer and causes a decrease in the HTU value of packed columns. This investigation disagrees with the work from Han Li (1952), he states only changing the pulse frequency, independently, has very little effect on pulse column performance when pulse amplitude is not considered.

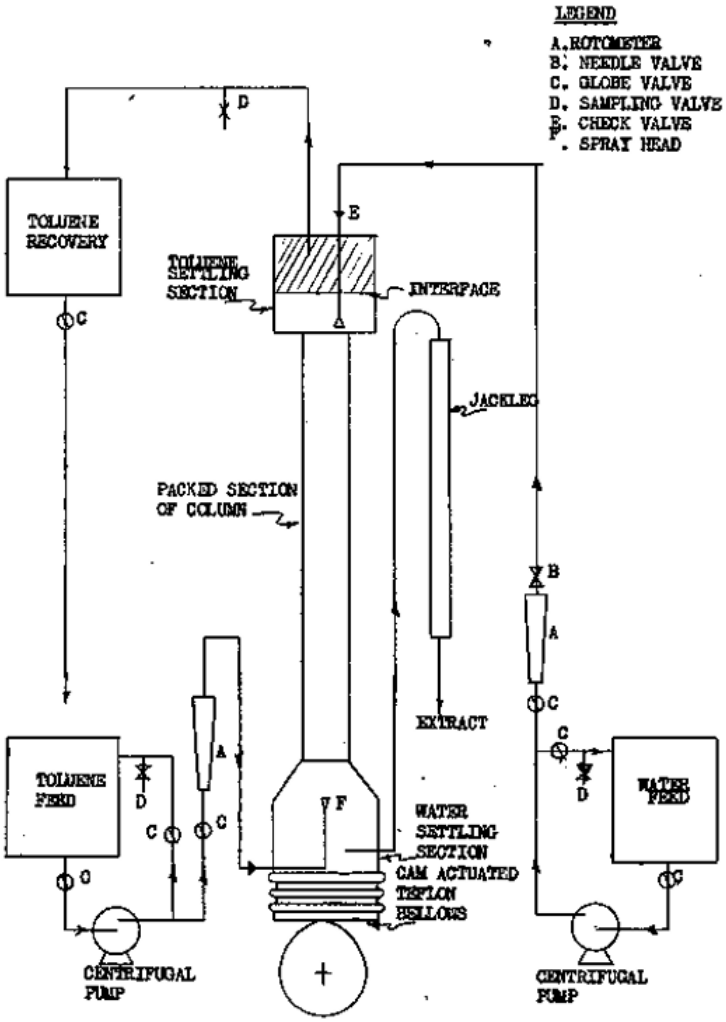

Figure 2.3: Base driven pulse mechanism for packed column (Pinzow, 1957).

2.2.1.2 Advanced Systems from the 1960's – Present

Idaho Chemical Processing Plant (ICPP) had, for many years, attempted to evaluate pulsation systems that would fulfil the basic requirements necessary for use within nuclear environments for the processing of irradiated nuclear fuels. By the 1960's, previous efforts had produced less than acceptable mechanically-driven pulsers resulting in poor reliability, serviceability, and operating performance. In response to this, the US Atomic Energy Commission sought to develop a fully re-designed type of fluid-operated pulser for use at ICPP and, subsequently, West Valley processing plant (Weech & Knight, 1967; Weech *et al.*, 1961). This new mechanism would meet the requirements of a system:

- That is simple and reliable.
- Consists of no moving components present within active (shielded) areas.
- Operates within frequencies of $40 - 100$ cycles per minute ($0.67 - 1.67$ Hz).
- Produces column amplitudes of $0.25 - 1$" ($6.35 - 25.4$ mm).

The fluid-operated direct column air pulser assembly was designed and

mathematically evaluated in 1959 and consequently constructed and tested at ICPP thereafter. At first glance, initial concerns were raised regarding the stability and pulsation frequency and amplitude ranges of the system. Mathematical assessments concluded that these concerns were unsubstantiated and later operational trials verified the reliability and operability of the system in full scale operation Weech *et al.* (1961). This type of fluid operated pulse system has been mentioned in detail in Section 2.1.2.

2.2.2 Operating Regime Transition Correlations

As mentioned previously in Section 2.1.2, PSECs can effectively operate within three main characteristic modes of operation determined primarily by pulse velocity:

- Mixer-settler regime: separation of light and heavy phases, during quiescent portion of the pulse cycle, leads to poor mass transfer and high hold-up. Separation is discrete and appears as layers between plates. An increase in pulse velocity cause the production of large droplets with low residence time, thus, decreasing hold-up.
- Dispersion regime: when hold-up reaches a minimum with increasing pulse velocity, the dispersion regime begins, wherein; non-coalescing droplets form a dispersion with a broad droplet size distribution. Hold-up begins to increase with a further increase in pulse velocity.
- Emulsion regime: hold-up increases rapidly, droplets continue to breakup into a fine micro-dispersion forming an emulsion stabilised by the increased shear and inertial forces. Droplet become entrained within dominant flow paths and become entrained in continuous phase flow during reverse strokes.

Increasing the pulse velocity beyond the emulsion regime leads to unstable operation and then flooding due to excessive pulsation. Unstable operation is defined at the point at which local phase inversion occurs due to very high hold-up and further breakage of droplets. Flooding occurs when the rise velocity of the dispersion droplets is less than that of the superficial continuous phase velocity. Similarly, flooding can occur at very low pulse velocities when the energy supplied to the system is not great enough to overcome the interfacial tension of fluids settling in the mixer-settler regime. This level of flooding is known as flooding due to insufficient pulsation (Yadav & Patwardhan, 2008).

A number of correlations were constructed that allow for discrete separation of the different operating regimes based on a number of column variables. These calculated boundaries can used in conjunction with flooding curve correlations to define full operating limits in each regime; flooding is result of an imbalance between capacity limits (throughput) and pulse velocity and so can occur within any regime. Table 2.1 provides a list the most useful regime transition correlations taken from investigators. For a correlation to be useful it must define transition pulse velocity

(Af_t) explicitly as a function of column variables, and independent of throughputs or superficial phase velocities. This will become apparent when used in conjunction with the format of flooding curve relationships.

Miyauchi & Oya (1965) formulated this correlation based off their own experimental set-up of water-MIBK PSEC systems, although different column sizes were investigated limitations are likely to occur due to lack of diversity. Each of the other four investigators used information gathered from a wide range of independent experiments and so are likely to be much more accurate and robust (Yadav & Patwardhan, 2008). It should be noted that authors, some of which are listed in Table 2.1, have also defined regime transitions via energy dissipation, see Table 2.3.

Table 2.1: Regime transition correlations for PSECs.

Author(s)	Transition Correlation	Transition Limits	
Miyauchi & Oya (1965)*[a]	$Af_t = 0.0021(\beta h)^{\frac{1}{3}}\left(\frac{\mu_d^2}{\sigma\Delta\rho}\right)^{-0.25}$	$Af < Af_t$ Dispersion Regime $Af > Af_t$ Emulsion Regime	(2.1)
Boyadzhiev & Spassov (1982)	$Af_t = 0.5\left(\frac{0.96e^2}{\rho_c}\right)^{\frac{1}{3}}$	$Af < Af_t$ Dispersion Regime $Af > Af_t$ Emulsion Regime	(2.2)
Kumar & Hartland (1983)*[a]	$Af_t = \left[0.05\beta h\left(\frac{\rho_c}{\Delta\rho^{0.75}\sigma^{0.25}g^{1.25}}\right)^{-1}\right]^{\frac{1}{3}}$	$Af < Af_t$ Dispersion Regime $Af > Af_t$ Emulsion Regime	(2.3)
Kumar & Hartland (1994)	$Af_t = 9.96\times10^{-3}\left(\frac{\sigma\Delta\rho^{0.25}e}{\mu_d^{0.75}}\right)^{0.33}$	$Af < Af_t$ Mixer-Settler Regime $Af > Af_t$ Dispersion Regime	(2.4)
Tung & Luecke (1986)	$Af_t = \left(\frac{0.062e^2}{\rho_c}\right)^{\frac{1}{3}}$	$Af < Af_t$ Dispersion Regime $Af > Af_t$ Emulsion Regime	(2.5)

[a] Here: $\beta = \dfrac{e^2}{(1-e)(1-e^2)}$

2.2.3 Flooding Correlations

2.2.3.1 Defining Flooding in PSECs

From a review of the literature, it is clear that the phenomena of flooding in PSECs is widely misunderstood and that a characteristic definition is usually avoided or ill posed. The challenge in understanding flooding lies in the identification of the phenomena during operation. As with all modes of PSEC operation, the transition between the different characteristic modes appears to be gradual and non-discrete. A few notable researchers, Mcallister *et al.* (1967) and Berger & Walter (1985), have made efforts to discuss flooding and they suggested a definition based on the rate of change of hold-up during fixed operation. This has, however, been ignored in later investigations wherein the presence of phase carry-over is accepted instead (Mehra & Chaturvedi, 2016). It could be argued that phase carry-over is only (sometimes) a symptom of flooding, particularity when flooding is severe, but the two descriptions are not synonymous. It is therefore mandatory that a fixed and agreed definition of flooding is accepted allowing for comparative studies and explicit design procedures.

In order to confidently understand and define flooding in PSECs, it can be useful to examine the ways in which flooding is defined in other multi-stage counter-current two-phase columns. In bubble-cap and sieve tray distillation columns, flooding is explicitly defined in terms of fluid dynamics on and around plates. Here, increased throughput of either the gas or liquid causes entrainment and/or flow disruption of either phase due to a sharp rise in the pressure drop of the column. Note that the flooding in these columns is discussed in terms of the pressure complications as a function of the throughput, a large difference in pressure between the plates causes the undesirable behaviour. Similarly, for gas-liquid packed columns, the flooding is characterised by liquid-phase entrainment and defined by the change in the slope of the pressure drop curve, rather than through visible effect. Interestingly, packed columns present the same issue as with PSECs where the onset of flooding is gradual and non-discrete, hence for the need for an analytical definition via pressure drop (Treybal, 1968).

All well as PSECs, other alternative liquid-liquid extraction columns (ECs) exist for liquid-liquid mass transfer operations; notable ones include disc and doughnut pulsed EC, mixer-settler EC, Hanson mixer-settler EC, pulsed packed EC and Wirz EC. Operators of these columns characterise flooding as an undesirable internal phenomenon of excessive hold-up of the dispersed phase, localised phase inversion and/or isolated accumulation of the dispersed at individual points in the column. This leads to a a gradual but clear drop in mass extraction efficiency within the column with the formation of dead-zones and disruption of counter-current flow. Furthermore, Phase inversion can take place near to flooding point simultaneously across all stages. It is clear here then that hold-up is primary marker for undesirable

flooding behaviour in these columns, and can be measured indirect measurement via differential column pressure (Asadollahzadeh *et al.*, 2011; Rincón-Rubio *et al.*, 1993; Takahashi & Nii, 1999; Torab-Mostaedi *et al.*, 2009, 2011).

In regards to PSECs specifically, both Mcallister *et al.* (1967) and Berger & Walter (1985) agree with the sentiment that a rigid definition of, or procedure for identifying, flooding is necessary. Mcallister *et al.* (1967) discuss flooding investigations prior to his own work. In short, he reports that hold-up is the primary factor that can be quantitatively used to indicate flooding. This is based on similar operational characteristics observed amongst previous PSEC researchers during, and up to the point of, flooding. Berger & Walter (1985) describes this as "accumulations of dispersed phase that appear at individual points in the column and these block the counter-current flow, and sometimes a phase reversal can also be observed". This statement agrees with the flooding characteristics described for other liquid-liquid ECs mentioned previously. Mcallister *et al.* (1967) also suggest defining flooding as when the hold-up of the column deviates over time, despite fixed and stable operational conditions. This method was used by the Oak Ridge National Laboratory during their study of PSECs in the early 60s. Hold-up was measured every 30 and 60 minutes, when the measurements disagreed flooding was assumed. Despite some ignorance from some investigators, this parameter has been used in a number of subsequent PSEC flooding investigations typically via indirect pressure measurement of hold-up Amani *et al.* (2016); Berger & Walter (1985); Tribess & Brunello (1998).

As part of the aims of objectives of this thesis, Chapter 5 will consider the above descriptions in an assessment of simulations of a flooded PSEC. The fine flow detail captured by the CFD flow resolving methods will allow for a ridged analytical definition of flooding and quantitative means of it's identification. Particularly, during the early onset of flooding for which no discussions are available in the literature for this area of PSEC operation.

2.2.3.2 Previous Work on Flooding in PSECs

Along with transition limits, a number of investigators have attempted to define flooding limits using correlations capable of either predicting an entire flooding curve such such Smoot *et al.* (1959); Thornton (1957), example shown in Fig. 2.4, or by predicting a maximum possible throughput at which flooding occurs for a given solvent flow ratio. Practically, the former would be used during operations in order to control a columns under flooding limits. The latter would more conventionally be used in a preliminary design to determine maximum throughput thresholds. Such design-intended calculations are available from authors (Berger & Walter, 1985) and Tribess & Brunello (1998).

The main correlations that will be to be discussed are summarised in Table 2.2,

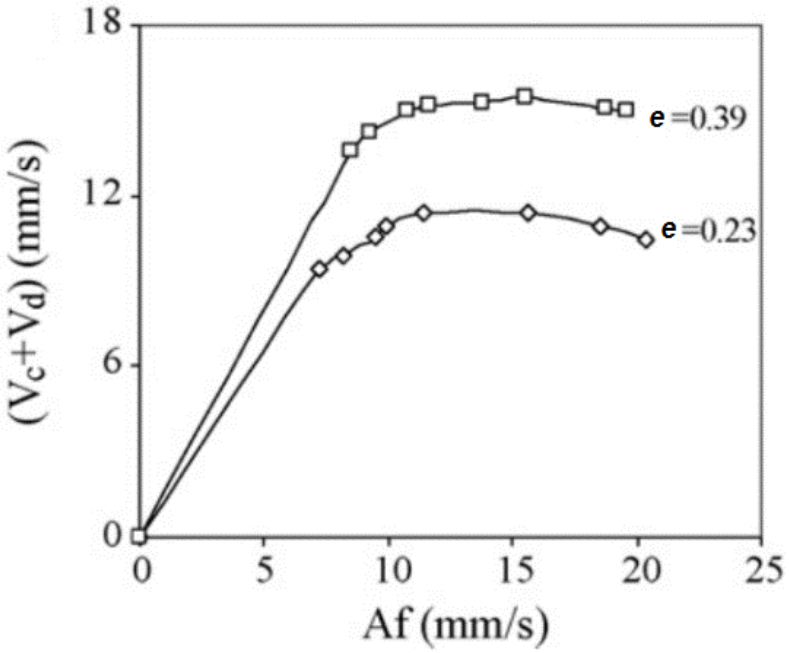

Figure 2.4: Flooding curve given by experiments from Lorenz *et al.* (1990).

which can be used alongside regime transition correlations seen in Table 2.1 to determine theoretically stable operating conditions. Thornton (1957) first thought of aspects of PSEC flooding by considering them analogous to spray columns. They formed a correlation, Eq. (2.6a), based on column parameters, material properties and energy dissipation (ε) which is split into K, Eq. (2.6b), and Af components, this allows it to be used to plot $(U_c + U_d)$ vs. Af. Other models of energy dissipation are available by Hafez & Baird (1978), Eq. (2.16b), and Miyauchi & Oya (1965), Eq. (2.16c). Smoot *et al.* (1959) provide an arguably simpler correlation also taking into account energy dissipation in the same way. This correlation was formulated using data from a number of different investigators and so should prove more robust. However, he didn't include information on the operating regimes form which the different data sets were taken from and so could perform less accurately. According to Mcallister *et al.* (1967), both correlations, although different, produce similar flooding curves. Lastly, Mcallister *et al.* (1967) also produce a correlation for flooding based on data from previous investigators. The number of physical and physiochemical parameters included is extensive and is derived through regression analysis making this correlation extremely complex by comparison (Berger and Walter, 1985). Equation (2.8a) is an modified version from Berger & Walter (1985) as the original is believed to contain printing errors and was unusable. Although comprehensive, this correlation is cumbersome and difficult to use, requiring iterative numerical methods to solve.

Correlations from Kagan *et al.* (1965) allow for the prediction of a flooding curve. However, the correlations do not include terms for variations in physiochemical properties and so severely limit their applicability and accuracy

(Yadav & Patwardhan, 2008). Correlations from Berger & Walter (1985) and Tribess & Brunello (1998) are used the calculate the maximum throughput at flooding for a column based on the solvent flow ratio chosen. The latter, from Tribess & Brunello (1998), is a adjusted correlation of the former, by Berger & Walter (1985), to account for mass transfer (solute loading, C_t) and geometric parameters of the column. The structure of these correlations suggests the primary factors that determine flooding are the throughput and solvent flow ratios. Furthermore, these factors are affected most significantly by surface tension (σ) and the fractional free area of the plate (e), the additional factors in Eq. (2.11a) have exponents close to zero providing little contribution to the resulting expression. Yadav & Patwardhan (2008) recommend that for design and scale-up the equation from Tribess & Brunello (1998) is used due to the additional factors considered within the correlation. However, in the paper from Tribess & Brunello (1998) the original correlation from Berger & Walter (1985), used the basis for a newly proposed correlation, is copied across incorrectly as negative coefficients are mistaken for positive ones. As a result, the correlation offered by Tribess & Brunello (1998) shows good agreement but from a limited range of experimental data as clearly a simple curve-fitting procedure was used to define the flooding relationship. Additionally, the diversity of column designs used to correlate this relationship is limited. The studies considered used data from columns of small diameters between $25 - 80$ mm.

Table 2.2: Flooding Correlations for PSECs.

Author(s)	Flooding Correlation	
Thornton (1957)[a]	$(U_c+U_d)_f = 0.6\frac{h^{0.24}d^{0.9}\Delta\rho^{0.79}g^{1.01}\mu_d^{0.3}}{\sigma^{0.17}\mu^{0.26}K^{0.24}\rho_c^{0.66}}[(1-2\phi_f)(1-\phi_f)^2+\phi_f^2(1-\phi_f)](Af)^{-0.72}$	(2.6a)
	$K = \left(\frac{\pi^2}{2C_0^2}\right)\left(\frac{1-e^2}{e^2}\right)$	(2.6b)
	$\phi_f = \frac{\sqrt{R^2+8R}-3R}{4(1-R)}$	(2.6c)
	$R = \left(\frac{U_d}{U_c}\right)_f$	(2.6d)
Smoot *et al.* (1959)	$(U_c+U_d)_f = 0.527\frac{\sigma^{0.144}\Delta\rho^{0.63}\mu_c^{0.489}h^{0.207}d^{0.458}g^{0.81}}{\rho_c^{0.775}\mu_d^{0.2}K^{0.207}}\left(\frac{U_d}{U_c}\right)^{0.014}(Af)^{-0.621}$	(2.7)
Mcallister *et al.* (1967)[a]	$(U_c+U_d)_f = (\Delta_c-\Delta_d)exp\Big[-3.741+0.2568ln(X)-0.07194(lnX)^2+0.006191(lnX)^3$ $-1.034lnY-0.09096(lnY)^2-0.0008898(lnY)^3$ $+0.1424ln\left(\frac{U_c}{U_d}\right)-0.1807ln\left(\frac{A}{h}\right)+0.07198ln\left(\frac{X}{Y}\right)\Big]$ $X = \frac{\delta\rho de^2 g}{\rho_c\pi_M^2} \qquad Y = \frac{\mu_c\pi_v}{e\sigma}$	(2.8a)
	$\Delta_c = 5Af\left[\sqrt{1-\lambda^2}-\lambda\left(\frac{\pi}{2}-arcsin\lambda\right)\right]$	(2.8b)
	$\Delta_c = 5Af\left[\sqrt{1-\lambda^2}+\lambda\left(\frac{\pi}{2}+arcsin\lambda\right)\right]$	(2.8c)
	$\pi_v = \frac{1}{2}(\pi_D+\pi_C)$	(2.8d)
	$\pi_M^2 = \frac{1}{2}(\pi_D^2+\pi_C^2)$	(2.8e)
	$\pi_D = 5\pi Af\left[\frac{\sqrt{1-\lambda^2}}{\frac{\pi}{2}-arcsin\lambda}-\lambda\right]$	(2.8f)
	$\pi_C = 5\pi Af\left[\frac{\sqrt{1-\lambda^2}}{\frac{\pi}{2}+arcsin\lambda}+\lambda\right]$	(2.8g)
	$\lambda = \frac{U_c f - U_d f}{5\pi Af}$	(2.8h)
Kagan *et al.* (1965)	$\frac{U_d}{gD} = 2.5\times10^{-2}\left(\frac{U_d}{U_c}\right)^{1.1}\left(\frac{A}{D}\right)^{1}\left(\frac{f^2D}{g}\right)^{0.81}\left(\frac{h}{D}\right)^{0.5}$	(2.9a)
	$\frac{V_{df}}{gD} = 3\times10^{-9}\left(\frac{U_d}{U_c}\right)^{1.1}\left(\frac{A}{D}\right)^{-1.75}\left(\frac{f^2D}{g}\right)^{-1.3}\left(\frac{h}{D}\right)^{0.5}$	(2.9b)
Berger & Walter (1985)[b]	$(V_{cf}+V_{df})_m = (24.528+2.537\sigma-0.0548\sigma^2)(1-1.455e+3.247e^2)$ $\times\left[1+0.1778ln\frac{U_c}{U_d}+0.0437\left(ln\frac{U_c}{U_d}\right)^2\right]$	(2.10a)
	$f_m = 29.45+6.679\sigma-0.1082\sigma^2-(2.067+0.426\sigma)\left(ln\frac{U_d}{U_c}\right)$	(2.10b)
Tribess & Brunello (1998)[b]	$(V_{cf}+V_{df})_m = (24.528+2.537\sigma+0.0548\sigma^2)(1+1.455e+3.247e^2)$ $\times\left[1+0.1778ln\frac{U_c}{U_d}+0.0437\left(ln\frac{U_c}{U_d}\right)^2\right](0.2115D^{0.2}h^{0.18})\left(1+\frac{U_c}{U_d}\frac{h}{d}C_t\right)^{0.09}$	(2.11a)
	$f_m = (29.45+6.679\sigma-0.1082\sigma^2)\left[1-\frac{U_d}{U_c}-0.001\sigma ln\left(\frac{U_d}{U_c}\right)\right](2.46A^{-1}D^{0.2}h^{-0.01})\left(1+\frac{U_c}{U_d}\frac{h}{d}C_t\right)^{0.07}$	(2.11b)

[a] Revised corellation taken from Berger & Walter (1985).
[b] σ measured in mNm, f_m measured in $strokes/min$.

2.2.4 Prediction of Droplet Size

Many of the hydrodynamic and mass transfer properties of LLE units are inherently dependent on the droplet size of the dispersed phase during operation. The relative velocity and, therefore, throughput of a pulsed column is directly affected by the droplet size. Likewise, mass transfer efficiency is largely consequential of the interfacial area between the dispersed phase droplets and the continuous phase (Pietzsch & Pilhofer, 1984). Accordingly, droplet size plays an influential role in determining the stage-wise dispersed phase hold-up and residence time (Kumar & Hartland, 1996).

Many authors have attempted to correlate Sauter mean diameter ($d_{[3,2]}$) as a function of the columns operating variables and/or physical dimensions (Yadav & Patwardhan, 2008). This method of characterising droplet distributions is commonly employed in this type of study, however, many other options are available that can effectively characterise a droplet distribution such as arithmetic, geometric and harmonic means, as well sophisticated fractal-scaling theory. However, the physical implications of using $d_{[3,2]}$ are predominately the reason for its popularity in droplet size studies, particularly in characterising LLE units, as well as for solid particles and gas bubble systems (Kowalczuk & Drzymala, 2016).

The Sauter mean diameter is generally described as a surface volume mean, wherein, the averages of the particulate matter are taken from the volume-to-surface area ratios. Kowalczuk & Drzymala (2016) demonstrate, through mathematical derivation, a poly and mono-dispersion can be classified as equienergetic if both have the same volume and surface area. Under these circumstances, the total surface energy - the product of the droplet surface tension and surface area - of the all the poly dispersed droplets will be equal to that of the mono dispersed droplets. This is particularly relevant for LLE systems, in that it links the surface area of the dispersed phase to its volume and therefore mass transfer rates. $d_{[3,2]}$ is mathematically defined as the ratio of the third and second moment of the probability density function:

$$d_{[3,2]} = \frac{\int_{d_{min}}^{d_{max}} d_p^3 p(d) \mathrm{d}d}{\int_{d_{min}}^{d_{max}} d_p^2 p(d) \mathrm{d}d} \tag{2.12}$$

where d_{min} and d_{max} represent the minimum and maximum values for droplet diameter respectively. For systems with size distributions of discrete entities, the equation simplifies to:

$$d_{[3,2]} = \frac{\sum_{i=1}^{n} n_i d_i^3}{\sum_{i=1}^{n} n_i d_i^2} \tag{2.13}$$

where n_i and d_i are the number and diameter of the droplets within a particular size fraction, respectively (Pacek *et al.*, 1998).

2.2.4.1 Droplet Size Models

Droplet size can either be modelled by developing a fundamental understanding of the hydrodynamic mechanisms at play, or can be calculated using empirical correlations developed from observing relationships from experimental analysis between various parameters. This subsection discusses the current theoretical models developed so far that attempt to determine droplet size in PSECs based on first principles.

Under non-turbulent conditions, or at low levels of agitation, the ratio of buoyant to interfacial forces principally govern the breakup of droplets, therefore, a limiting value for droplet size can be determined from Equation Eq. (2.14).

$$d_{max} = C_1 \left(\frac{\sigma}{\Delta \rho g} \right)^{0.5} \tag{2.14}$$

Here, σ is the interfacial tension, characterised by the properties of the liquid system, ρ is the density of the droplet, and g is gravitational acceleration constant (9.81 ms^{-2}). C_1 is a characteristic constant determined by the columns geometry, for pulsed columns Logsdail & Slater (1983) suggest a value of 0.92. Turbulence can cause breakup when the forces exerted on the droplet by the motion of the continuous phase exceed the cohesive forces of interfacial tension and dispersed phase viscosity (Kumar & Hartland, 1996). Furthermore, shear forces acting on droplets of similar diameter to the sieve-plate holes will cause significant breakup also (Yadav & Patwardhan, 2008). As this model does not account for either scenario it can be considered rudimentary and invalid in most cases.

An advancement of Eq. (2.14) was developed by (Hinze, 1955) and Shinnar & Church (1960), Eq. (2.15a), which includes a term derived from Kolmogoroff's theory of isotropic turbulence (Kolmogoroff, 1941a,b). The additional term ε represents the power dissipated per unit mass of fluid (Wkg^{-1}) and is used to more accurately calculate the maximum stable droplet size attainable under turbulent conditions.

$$d_{max} = C_2 \left(\frac{\sigma}{\rho_c} \right)^{0.6} \varepsilon^{-0.4} \tag{2.15a}$$

Although Eq. (2.15a) is limited to calculating the maximum droplet size, it is assumed that $d_{[3,2]} = 0.5\ d_{max}$ and thus C_3 is half of C_2 in Eq. (2.15b), this gives (Baird, 1979):

$$d_{[3,2]} = C_3 \left(\frac{\sigma}{\rho_c} \right)^{0.6} \varepsilon^{-0.4} \tag{2.15b}$$

The first authors to investigate PSEC power requirements, Jealous & Johnson (1955), treated the total power requirements a series of categories of: static head, inertia of liquid, and friction loss. Thornton (1957) produced a model for calculating ε for sinusoidal pulse wave systems, as a function of Af through evaluation of the

integral mean velocity and integral mean square velocity. The equation provides an average power dissipation per unit mass of fluid due to transient nature of the PSEC. The potential and inertial energies cancel out over a complete cycle giving Eq. (2.16a).

$$\varepsilon = N_p \frac{\pi^2(1-e^2)}{2e^2 C_O^2 h}(Af)^3 \tag{2.16a}$$

A modification to this equation by Hafez & Baird (1978) considered using integral mean cubed velocity as an alternative to improve the accuracy of the model to give:

$$\varepsilon = N_p \frac{\pi^2(1-e^2)}{1.5e^2 C_O^2 h}(Af)^3 \tag{2.16b}$$

in both cases the pressure recovery after the plate is neglected. Miyauchi & Oya (1965) considered pressure recovery and presented the equation:

$$\varepsilon = N_p \frac{5\pi^2(1-e)(1-e^2)}{6\sqrt{2}e^2 C_O^2 h}(Af)^3 \tag{2.16c}$$

these equations show that ε is not dependent on plate-hole diameter and that combining Eqs. (2.16a) and (2.16b) into Eq. (2.15b) shows that $d_{[3,2]}$ is proportional to $Af/h^{1/3}$. Miyauchi & Oya (1965) model, Eq. (2.16c), is considered the most accurate means of calculating energy dissipation per unit mass of fluid given its considerations. However, in all cases, the term $(Af)^3$ tends to over embellish the effect of pulse velocity on droplet size and, thus, over estimates at moderate levels of pulsation. This is most apparent during operation in the mixer-settler regime, which shows correlations based from Kolmogoroff's theory of isotropic turbulence cannot be applied across all operating regimes Yadav & Patwardhan (2008).

A force balance approach formulated by Pietzsch & Pilhofer (1984) considers modelling the evolution of droplets via the sieve-plate orifices as jets. Their method considered the buoyant, inertial and drag forces acting upon a given spherical drop as it enters a low velocity region to that of a high one (i.e. to the main compartment from a jetting region) causing the break-up of droplets. A final balancing force, interfacial tension, determines the stability of the droplet and is responsible for determining a stable droplet size (d_p) when combined with the other three destructive forces. Each force is determined by the following relationships:

$$\text{Buoyancy force: } F_A = (\pi/6)\Delta\rho g d_p^3 \tag{2.17a}$$

$$\text{Inertial force: } F_W = (\pi/6) b \rho_d d_p^3 \tag{2.17b}$$

$$\text{Drag force: } F_D = C_o(\rho_c/2)U_{hvr}^2(\pi/4)d_p^2 \tag{2.17c}$$

$$\text{Interfacial tension force: } F_I = \pi\sigma d_p \tag{2.17d}$$

combination of all four balanced forces results in the following quadratic equation, Eq. (2.18a), which can be solved to find a stable droplet size, Eq. (2.18b).

$$\left(\frac{\Delta\rho g + b\rho_d}{6\sigma}\right)d_p^2 + \left(\frac{C_o U_{hvr}^2 \rho_c}{8\sigma}\right)d_p - 1 = 0 \tag{2.18a}$$

$$d_p = \sqrt{\frac{6\sigma}{\Delta\rho g + b\rho_d} + \frac{9}{64}\left(\frac{C_w U_{hvr}^2 \rho_c}{\Delta\rho g + b\rho_d}\right)^2} - \frac{3}{8}\frac{C_o U_{hvr}^2 \rho_c}{\Delta\rho g + b\rho_d} \tag{2.18b}$$

For this calculation process, Pietzsch & Pilhofer (1984) report 'very good agreement' with predicted droplet sizes and published measurements from other authors. Although derived methodically from a balance of forces, this model requires knowledge of the droplet velocity (U_p), droplet velocity in the high velocity region (U_{hvr}), the deceleration (b), and the drag coefficient (C_o). The droplet velocity is found through a summation of the total orifice velocity, derived from U_hvr, and the terminal velocity of a single particle. Pietzsch & Pilhofer (1984) explain that the latter component, as well as the drag coefficient, requires an understanding of the single particle Reynolds number, Archimedes number, and the 'fluid number' ($K'F$). While calculable, such an intimate understanding of a system, especially from a design point of view, is impractical and likely unnecessary. As part of an extended study, Yadav & Patwardhan (2008) made an attempt to test this model against experimental data taken from various studies. Correlations were taken from Hu & Kintner (1955) in order to calculate single droplet terminal velocity, the same calculation procedure was mentioned by Pietzsch & Pilhofer (1984) which is briefly discussed above. Findings from Yadav & Patwardhan (2008) conclude that the model is unusable on the grounds that negative values for terminal velocity were calculated when using the experimental data they collated. Furthermore, this conclusion is supported by similar findings by Kumar & Hartland (1986) which reported a 27.9 % error when used with their collated data. With all things considered, this method can be described as cumbersome, inaccurate and complex, requiring a long iterative modelling process which first demands an assumed droplet diameter in order to determine its terminal velocity.

An alternative concept by Pietzsch & Blass (1987) used a less complex energy balance model to predict maximum stable droplet size. This mathematical-physical model is based on the energy equilibrium that exists between the energy of the drops in the orifice region and the droplet's surface energy. The difference between the maximum kinetic energy of the droplet as it flows through the sieve tray ($E_{k\,max}$), and in the minimum kinetic energy of the droplet in the flow region outside of the tray ($E_{k\,min}$) is calculated. The difference (ΔE_k) is assumed to be transferred to its surroundings via the droplet surface. The cohesion energy (E_σ) of the droplets result in droplet stability, if the energy omitted to the surface is less than that of

the cohesive energy then then the droplet does not breakup. The energy balance and resulting droplet size equation are as follows:

$$E_k = \frac{1}{2}U^2\rho_d\left(\frac{\pi}{6}\right)d_p^3 \tag{2.19a}$$

$$\Delta E_k = E_{k\,max} - E_k\,min = \frac{1}{12}\rho_d\pi d_p^3(U_1^2 - U_2^2) \tag{2.19b}$$

$$E_\sigma = d_p^2\pi\sigma - \frac{2}{3}d_p^2\pi\sigma = \frac{1}{3}d_p^2\pi\sigma \tag{2.19c}$$

$$d_p = \frac{4\sigma}{\rho_d(U_1^2 - U_2^2)} \tag{2.19d}$$

where U_1 is the velocity of the drops in the sieve tray region and U_2 is the velocity of the drops in the region away from the sieve tray. As is apparent from Eq. (2.19d), the maximum stable droplet size is largely dependent on the material properties of the system as well as the squares of the velocity difference. As this model only gives an estimation for maximum droplet size, it is less applicable for determining/designing true-to-life systems and will likely result in misrepresentation when used for mass transfer modelling. A further criticism is that this model places a large emphasis on the effect of interfacial tension (σ) and does not consider other system variables such as: fluid viscosities, plate spacing, and plate-hole diameter.

2.2.4.2 Droplet Size Correlations

This subsection summarises various correlations developed from an empirical approach to determine droplet size in PSECs. Such correlations are based on the analysis of experimental results from one or more studies. Although a number of correlations for PSEC droplet size calculations have been developed, only the most notable/useful ones will be discussed within this section. These correlations have already been reviewed, studied and/or tested in other investigations.

Observations made by Jones (1962) for early experimentation with water-MIBK PSEC systems suggested that droplet size is a function of the pulse velocity, a product of the amplitude and frequency, Af. More uniform droplets were produced at high pulse velocities, and that the majority of droplet breakup was observed during transit of the fluids through the first two or three sieve-plates. Additionally, the flow rates of either phase seemed to have little-to-no effect on droplet size and that larger droplets were observed when the plate-hole diameter increased. Further investigations for water-MIKB PSECs by Miyauchi & Oya (1965) found that for a given pulse velocity, droplet size increased with an increase in plate spacing due to an increased likelihood of coalescence and a reduction in the rate of applied shear forces. From their data they were able to produce an empirical correlation for droplet size, pulse velocity and plate spacing Eq. (2.20) based on the relationship mentioned previously for $Af/h^{1/3}$.

$$d_{[3,2]} = 2.03 \times 10^{-5} \left(\frac{Af}{h^{1/3}} \right)^{-1.2}; \text{ for } \frac{Af}{h^{1/3}} > 5.57 \times 10^{-2} \text{ m}^{2/3}\text{s}^{-1} \tag{2.20}$$

This correlation was derived for the system at a low fixed dispersed phase, MIBK, velocity ($Vd = 0.43$ mms^{-1}) and was said to diverge when $Af/h^{1/3}$ rose above 5.57×10^{-2} m$^{2/3}$s^{-1} with the Af exponent changing from -1.2 to -0.6. This severely limits the flexibility and applicability of the equation at higher dispersed phase and pulse velocities.

An independent study by Míšek (1964) found that their system could be represented by an empirical correlation, Eq. (2.21), to calculate droplet size. Kumar & Hartland (1996) found the correlation to perform poorly when calculating droplet size using data collated for emulsion region operation, giving a fitting error of 31.8%. Additionally, Yadav & Patwardhan (2008) also reported over-prediction for droplet size when using the Míšek (1964) correlation in there study of comparing four key correlations.

$$d_{[3,2]} = 0.439 \sigma^{0.6} \rho_c^{-0.6} e^{0.3} d^{0.4} (\pi Af + U_c)^{-1.2} \tag{2.21}$$

Additionally, three other main correlations have been tested by Yadav & Patwardhan (2008): two from Kumar & Hartland (1994, 1996) and one from Sreenivasulu *et al.* (1997). Firstly, Kumar & Hartland (1994) proposed the following correlation, Eq. (2.22), for droplet size prediction based on their own findings, it includes the effect and direction of mass transfer.

$$\begin{aligned} d_{[3,2]} = & C \left(\frac{\sigma}{\Delta \rho g} \right)^{0.5} e^{0.74} \left(\frac{h}{h_*} \right)^{0.1} exp \left(-3 \frac{Af \Delta \rho^{0.25}}{g^{0.25} \sigma^{0.25}} \right) \\ & + exp \left(-28.56 \frac{Af \Delta \rho^{0.25}}{g^{0.25} \sigma^{0.25}} \right) \end{aligned} \tag{2.22}$$

Here $h_* = 0.05$ m, $C = 1.51$ when mass transfer is not present, $C = 1.36$ for $c \rightarrow d$, and $C = 2.01$ for $d \rightarrow c$. In an effort to improve accuracy and reliability, Kumar & Hartland (1996) extended their study to include a larger set of collated experimental data allowing for a more robust and reliable correlation,

$$d_{[3,2]} = \frac{C e^{0.32} h}{0.645 \sigma^{-0.5} \Delta \rho^{0.66} g^{0.14} h^{1.15}} \tag{2.23}$$

here $C = 1$ for no mass transfer, $C = 0.92 for c \rightarrow d$, and $C = 1.67$ for $d \rightarrow c$. Both of the correlations by Kumar & Hartland (1994, 1996) imply droplet size is not affected by the plate-hole diameter. However, as Yadav & Patwardhan (2008) point out, plate hole diameter was found to directly effect droplet size in a series of experimental studied conducted by Jones (1962), Boyadzhiev & Spassov (1982) Míšek (1964),

and Sreenivasulu *et al.* (1997). It was postulated by Yadav & Patwardhan (2008) that this could be due to little variation in the data used when formulating both correlations. Regardless, their independent investigation found that the both of correlations from Kumar & Hartland (1994, 1996) tended to overpredict droplet size, possibly by devaluing the effects of plate spacing and overstating the dependency of interfacial tension. In any case, it can be concluded that both correlations appear to be rather complex and lacking necessary variables leading to limited flexibility and performance.

The last major correlation of interest was presented by Sreenivasulu *et al.* (1997). They measure droplet sizes produced in a 0.043 m diameter water-kerosene pulse column system operating across a range of low-to-medium pulse velocities. With this, they were able to access droplet size evolution within mixer-settler and dispersion operating regimes, something not confidently reported on previously. They noted that a dramatic change in the distribution profile occurs with an increase in pulse velocity, wherein a multimodal distribution shifts towards unimodal profile. This is likely an effect of the increasing turbulence levels they observed with higher pulse velocities. Greater levels of turbulence would cause more violent droplet collisions with the column internals and increase the shear forces affecting transit droplets through the sieve-plates. Furthermore, no influence on the droplet size was reported regarding either the continuous or dispersed phase velocities. The main column variables that they observed to influence droplet size were: plate-hole diameter, fractional free area, and plate spacing leading to Eq. (2.24).

$$d_{[3,2]} = C\left(\frac{\sigma}{\rho_c}\right)^{0.4}(Af)^{-0.8}e^{0.48}d^{0.26}h^{0.34} \tag{2.24}$$

Here C = 0.08 for no mass transfer, and $C = 0.1$ for $d \rightarrow c$. This formulation provides a more complete and reasonable list of variables between the expected column parameters and droplet size in comparison to competing correlations.

Yadav & Patwardhan (2008) claim 'satisfactory' prediction of droplet size when using the Sreenivasulu *et al.* (1997) correlation and state the performance of this correlation to be greater than all others examined in their study. In their investigation, they found that this correlation provided a more reasonable dependence of interfacial tension on droplet size compared to correlations from Kumar & Hartland (1994, 1996) and Míšek (1964) which tend to over embellish this effect leading to over predictions for droplet size. Furthermore, Sreenivasulu *et al.* (1997) rightly consider the effect of plate-hole diameter on droplet size, a factor that was neglected in the correlations from Kumar & Hartland (1994, 1996). However, one issue that is apparent is that no constant was provided for mass transfer from the continuous to the dispersed phase ($c \rightarrow d$). This implies that their investigation still requires further work in order to fully satisfy requirements for droplet size prediction within design applications for continuous to dispersed

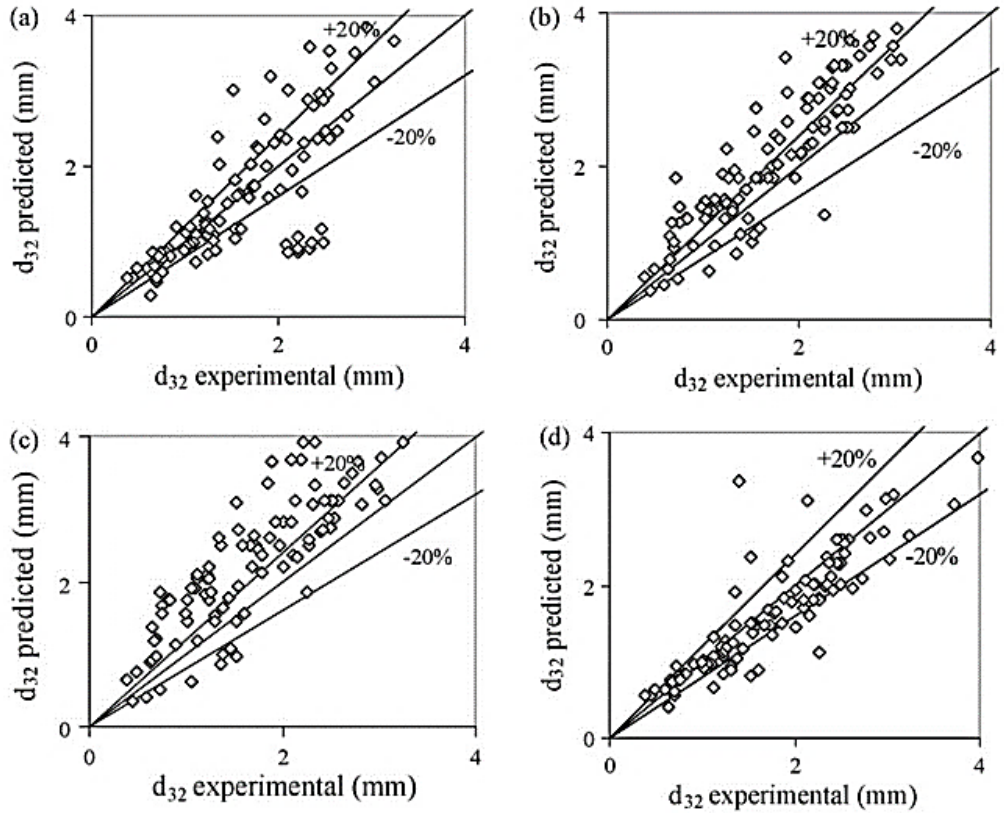

Figure 2.5: Comparison of four main correlations to predict droplet size in PSEC's taken from Yadav and Patwardhan (2008): (a) Míšek (1964), (b) Kumar & Hartland (1994), (c) Kumar & Hartland (1996) and (d) Sreenivasulu *et al.* (1997).

phase mass transfer operations. Additionally, it should be noted that this correlation, although comparatively effective, is still lacking accurate predictability.

Fig. 2.5 shows the results of the investigation Yadav & Patwardhan (2008), wherein the predicted droplet size from the four main correlations were plotted against the experimentally measured droplet sizes. Both correlations from Kumar & Hartland (1994, 1996), as mentioned, tend to overpredict droplet size largely outside of a ± 20% error margin. Míšek (1964) shows more effective predictability at low droplet sizes. Sreenivasulu *et al.* (1997) shows the greatest predictability across a wide range of droplet sizes, as stated by Yadav & Patwardhan (2008). However, it can be seen that the correlation tends to underpredict droplet size past a 20% error margin and so cannot be considered reliable due to its lack of consistency regarding accuracy. None of the available correlations presented are able to consistently reproduce accurate predictions of droplet size, this suggests that this method of system characterisation is flawed. A modelling approach, aimed towards to understanding the fundamental behaviour of PSEC's, would be better suited to this aspect of engineering due to complexity and variety of variables involved. The modelling approaches presented here are clearly ineffective. Therefore, a proportion of this study will be devoted to looking at various droplet size modelling approaches.

2.2.5 Prediction of Hold-up

Dispersed phase volume fraction, otherwise known as hold-up (ϕ), is an important design factor for LLE equipment. Knowledge of hold-up will allow for the calculation of resident time distributions and mass transfer rates, and is fundamental to understanding the operating characteristics of PSECs (Sehmel & Babb, 1963). This is apparent when discussing operating regimes, wherein, the regime transition can be quantified via hold-up as well as droplet size, see Section 2.2.2.

There are two approaches to calculating hold-up. Firstly, one could calculate the characteristic velocity ($\overline{U}_0$) or slip velocity (U_s) then use the hold-up and velocity relationship, Eq. (2.25), (Gayler *et al.*, 1953). Secondly, hold-up could be calculated directly using correlations not defined by droplet size, slip velocity or characteristic velocity. Instead, the correlations are defined as functions of basic column parameters such as superficial dispersed phase velocity, pulse velocity, material properties and column geometry. This is advantageous by way of allowing for direct solution methods but, as with all correlations, are likely inaccurate and ridged.

2.2.5.1 Hold-up via Slip/Characteristic Velocity

Eq. (2.25) was introduced by Gayler *et al.* (1953) as a means of calculating hold-up from superficial phase velocities and the characteristic velocity. The characteristic velocity is simply defined as the mean relative velocity of droplets extrapolated to zero flow rates (and hold-up), or more simply, the terminal velocity of a single drop in the equipment concerned. This model was found satisfactory for columns of different types, including pulsed columns (Gayler *et al.*, 1953; Thornton, 1957). However, this equation cannot be solved for ϕ linearly, and requires non-linear solution methods such as root-finding algorithms/iterative techniques.

$$U_s = \overline{U}_0(1-\phi) = \frac{U_d}{\phi} + \frac{U_c}{1-\phi} \tag{2.25}$$

The characteristic (terminal) velocity of a droplet through a continuous fluid can be calculated via Stokes' law (Chhabra, 1993).

$$F_g = 6\pi\mu_c r\overline{U}_0 \tag{2.26a}$$

Stokes' law defines the drag force experienced by a particle moving through a fluid. When this force is equal to the driving, or buoyant, forces due to gravity (F_g) movement occurs. F_g can be found by:

$$F_g = mg = \overline{U}_0(\rho_d - \rho_d)g = \frac{4}{3}\pi r^3 v \tag{2.26b}$$

Combining Eq. (2.26) and Eq. (2.26b) allows one to calculate the rising velocity of a single droplet:

$$\overline{U}_0 = \frac{2r^2(\rho_d - \rho_d)g}{9\mu_C} \tag{2.26c}$$

Stokes' law and Eq. (2.26c) both work under the assumptions that the droplet behaves as a rigid sphere and the continuous phase viscosity remains constant throughout the column - i.e., it exhibits Newtonian behaviour (Schramm, 2005). Modification to this law can be made for non-Newtonian fluids, though this is likely not of concern in this investigation (Chhabra, 1993). Eq. (2.26c) is a force balance model and so fundamentally describes the relationship between the terminal velocity of a particle driven by a density differential. However, knowledge of the droplet radius (r) is required a priori. As part of this investigation, droplet size models will be developed that can be used in conjunction with Eq. (2.26c) and Eq. (2.26b) to allow for calculation of hold-up. Similarly, droplet size models and correlations in Section 2.2.4 can also be investigated.

Authors have also provided correlations for calculating U_s and $\overline{U}_0$ without the need for droplet size information. Thornton (1957) provides an equation for characteristic velocity, this is an alternative arrangement of Eq. (2.6a), used for calculating flooding curves:

$$\frac{\overline{U}_0\mu_c}{\sigma} = 0.6\left(\frac{\varepsilon\mu_c^5}{\rho_c\sigma^4}\right)^{-0.24}\left(\frac{d\rho_c\sigma}{\mu_c^2}\right)^{1.01}\left(\frac{\Delta\rho}{\rho_c}\right)^{1.8}\left(\frac{\mu_d}{\mu_c}\right)^{0.3} \tag{2.27}$$

Little literature is readily available on the effectiveness of this correlation and should be considered for further evaluation in this study.

Kumar & Hartland (1994) developed a correlation for U_s based on column geometry and operating conditions:

$$U_s = K_1 exp[K_2|Af - (Af)_m|]\Delta\rho^{0.29}\rho_d^{0.67}\mu_d^{-0.66}e^{0.44}h^{0.43} \tag{2.28}$$

where $K_1 = 6.14 \times 10^{-6}$ for no solute transfer, $K_1 = 5.04 \times 10^{-6}$ for $c \rightarrow d$, and $K_1 = 6.43 \times 10^{-6}$ for $d \rightarrow c$. $K_2 = -36.91$ for no solute transfer, $K_2 = -30.79$ for $c \rightarrow d$, and $K_2 = -31.81$ for $d \rightarrow c$. Similarly, Venkatanarasaiah & Varma (1998) also provide a correlation for Vs based on their water-kerosene system using n-butyric acid and benzoic acid as solutes:

$$U_s = K_1 exp[K_2|Af - (Af)_m|]\Delta\rho^{0.22}\mu_d^{-0.38}e^{0.32}h^{0.31}d^{0.22} \tag{2.29}$$

where $K_1 = 1.35 \times 10^{-2}$ for no solute transfer, $K_1 = 1.65 \times 10^{-2}$ for $c \rightarrow d$, and $K_1 = 1.55 \times 10^{-2}$ for $d \rightarrow c$. $K_2 = -33.3$ for no solute transfer, $K_2 = -29.6$ for $c \rightarrow d$, and $K_2 = -29.6$ for $d \rightarrow c$. All three of these authors are also discussed in the next section, further review will be given there.

2.2.5.2 Direct Hold-up Correlations

The correlations discussed within this section are listed in Table 2.3. Each correlation for hold-up is calculated independently of droplet size. Miyauchi & Oya (1965) provide two hold-up correlations produced from data taken from their water-MIBK system and six other published investigations, Eq. (2.30a). Each correlation corresponds to a particular operating regime, either dispersion or emulsion. Mass transfer effects are not considered. It was found that there appeared to be a non-linear relationship between ψ and U_d . Also the effect of U_c on ψ was negligible and, therefore, was not included.

Kumar & Hartland (1983) considered each operating regime discretely to produce three independent equations, Eq. (2.30a)-Eq. (2.30c). To produce these correlations, data was taken from numerous investigators. As with Miyauchi & Oya (1965), these equations do not include the effects of mass transfer. In both cases, each set of correlations are defined by a regime boundary, between dispersed and emulsion, which is quantified by ε with the units m^2s^{-2} or a variant ψ which has the units $m^{11/12}s^{-1}$, see Eq. (2.31e) and eq:Venk1 respectively. Kumar & Hartland (1983) noted Miyauchi & Oya (1965) unconventional use of the quantity ψ: "In view of the peculiar units it is not clear why the authors chose to modify ε in this way".

Tung and Luecke (1986) produce a single equation that allows for the calculation of hold-up for a system absent from mass transfer, or for when mass transfer occurs in either direction. Changing the constant C for the appropriate value will accommodate for this. The major disadvantage of this simple, easy-to-use correlation is that it is most likely inaccurate and inflexible. Data used to from this relationship was taken solely from emulsion regime experiments and so must satisfy the criteria of $\rho_c(Af)^3/2e^2 > 0.06$ before it can be applied.

Prior to the formulation of Eq. (2.28), Kumar & Hartland (1988) formulated a direct equation for hold-up, Eq. (2.33a), from data taken from a number of other authors. Both of these equations can be applied across all operating regimes, for systems absent of mass transfer and for those with mass transfer in either direction. Similarly to Tung & Luecke (1986), the addition of terms K_1 and K_2 accommodate for different mass transfer configurations. Investigative reviews by Yadav & Patwardhan (2008) found that Eq. (2.33a) tended to largely overpredict values for hold-up when calculated directly. Eq. (2.28), when used with Eq. (2.25), fared much better in accurately predicting hold-up from U_s. The results of their comparative investigation concerning both of the methods from Kumar & Hartland (1988, 1996) are displayed graphically in Fig. 2.6. There is indeed a more consistent performance in using the U_s calculation route across hold-ups from $30 - 80\%$, however, there is less contrast in performance at hold-ups $> 30\%$. Additionally, at hold ups from roughly $15 - 25\%$, there is a tendency for each method to both over and under predict hold-up. Between this region, there is very

little accuracy with values shifting towards both error boundaries (±20%). This is problematic as it appears to be a popular region of operation based on the collection of results collected by Yadav & Patwardhan (2008) from other researchers.

In contrast, Venkatanarasaiah & Varma (1998) found some additional dependent terms which effect hold-up that had been disregarded or downplayed in other correlations. Plate-hole diameter, fractional free area and plate spacing each showed a profound influence on hold-up, and a measurable effect on hold-up from U_d was observed also. As a result, they produced Eq. (2.34a), presumably as a rectification of Eq. (2.33a) from Kumar & Hartland (1994). Likewise, Venkatanarasaiah & Varma (1998) also produced an additional correlation for the U_s calculation route, Eq. (2.29). Again, all regimes and mass transfer configurations can be explored through these correlations via different K_1 and K_2 values. Yadav & Patwardhan (2008) found the method from Venkatanarasaiah & Varma (1998), Eq. (2.34a), to be more effective at accurately predicting hold-up. Fig. 2.6 shows that at hold-ups between $30 - 80\%$, accuracy is improved greatly with calculation of U_s and subsequently hold-up. Below 30% there is less of a performance improvement.

Table 2.3: Hold-Up Correlations for PSECs.

Author(s)	Hold-Up Correlation	Comment	
Miyauchi & Oya (1965)	$\phi = 4.93^2 \psi^{0.84} U_d^{2/3}$	Dispersion Regime: $\psi < 0.0031$	(2.30a)
	$\phi = 3.42 \times 10^6 \psi^{0.24} U_d^{2/3}$	Emulsion Regime: $\psi > 0.0031$	(2.30b)
	$\psi = \frac{Af}{(\beta h)^{1/3}} \left(\frac{\mu_d}{\sigma \Delta \rho} \right)^{1/4}$		(2.30c)
Kumar & Hartland (1983)	$\phi = 3.91^{-3} \left(\frac{A^2 \rho_c g}{\sigma} \right)^{-0.26} \left(\frac{f^4 \sigma}{\rho_c g^3} \right)^{-0.19} \left(\frac{U_d^4 \rho_c}{g \sigma} \right)^{0.19} \left(1 + \frac{U_d}{U_c} \right)^{0.19} \left(\frac{\Delta \rho}{\rho_c} \right)^{-0.81} \left(\frac{\mu_d^4 g}{\rho_c \sigma^3} \right)^{-0.13}$	Mixer-settler regime	(2.31a)
	$\phi = 6.91 \left[\frac{(Af)^3 \rho_c^{1/4}}{\beta h \sigma^{1/4} g^{5/4}} \right]^{0.31} \left(\frac{U_d^4 \rho_c}{g \sigma} \right)^{0.3} \left(1 + \frac{U_d}{U_c} \right)^{0.14} \left(\frac{\Delta \rho}{\rho_c} \right)^{-0.79} \left(\frac{\mu_d^4 g}{\rho_c \sigma^3} \right)^{-0.01}$	Dispersion regime: $\varepsilon < 0.05$	(2.31c)
	$\phi = 3.73 \times 10^{-3} \left[\frac{(Af)^3 \rho_c^{1/4}}{\beta h \sigma^{1/4} g^{5/4}} \right]^{0.31} \left(\frac{U_d^4 \rho_c}{g \sigma} \right)^{0.31} \left(1 + \frac{U_d}{U_c} \right)^{0.45} \left(\frac{\Delta \rho}{\rho_c} \right)^{-2.2} \left(\frac{\mu_d^4 g}{\rho_c \sigma^3} \right)^{-0.29}$	Emulsion regime: $\varepsilon \geq 0.05$	(2.31d)
	$\varepsilon = \frac{Af}{\beta h \Delta \rho^{3/4} \sigma^{1/4} g^{5/4}}$		(2.31e)
Tung & Luecke (1986)	$\phi = C \left[\frac{Af}{(\beta h)^{1/3}} \right]^{1.9} \left(\frac{\mu_d^2}{\sigma \Delta \rho} \right)^{0.36} U_d^{1.1}$ for $\frac{\rho_c (Af)^2}{2e^2} > 0.06$	No solute: $C = 3.98 \times 10^5$ Solute: $C = 2.52 \times 10^5$	(2.32)
Kumar & Hartland (1988)	$\phi = K_1 exp[K_2 \lvert Af - (Af)_m \rvert] U_d^{0.86} (U_c + U_d)^{0.28} \Delta \rho^{-3} \rho_d^{-0.93} \mu_d^{0.77} e^{-0.56} h^{-0.56}$	No solute: $K_1 = 2.10 \times 10^6 K_2 = 44.53$ $c \rightarrow d$: $K_1 = 2.14 \times 10^6$ $K_2 = 44.53$ $d \rightarrow c$: $K_1 = 1.10 \times 10^6$ $K_2 = 50.56$	(2.33a)
	$(Af)_m = 9.96^{-3} \left(\frac{\sigma \Delta \rho^{1/4} e}{\mu_d^{3/4}} \right)^{0.33}$		(2.33b)
Venkatanarasaiah & Varma (1998)	$\phi = K_1 exp[K_2 \lvert Af - (af)_m \rvert] U_d^{1.02} U_c^{0.02} \Delta \rho^{-0.23} \mu_d^{0.52} e^{-0.4} h^{-0.4}$	No solute: $K_1 = 116.5 K_2 = 39.35$ $c \rightarrow d$: $K_1 = 54.6 K_2 = 42.56$ $d \rightarrow c$: $K_1 = 92.0 K_2 = 42.56$	(2.34a)

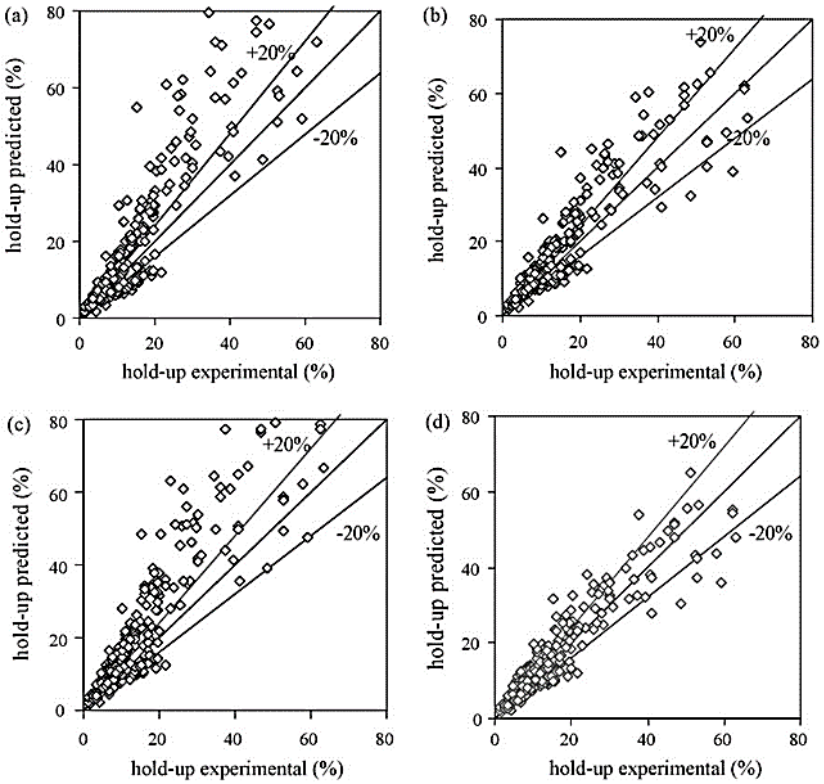

Figure 2.6: Comparison of four main correlations to predict hold-up in PSEC's taken from Yadav and Patwardhan (2008): (a) Kumar & Hartland (1988), (b) Kumar & Hartland (1994),(c)Venkatanarasaiah & Varma (1998) [direct], (d) Venkatanarasaiah & Varma (1998) [U_s]

2.2.6 Prediction of Mass Transfer Efficiencies

This section will outline the main methods used to characterise mass transfer efficiencies in PSECs by various authors for completeness. Although this thesis does not include mass transfer investigations, ultimately, the ambition of work is this field is to move towards models capable of predicting the rate of transfer of solutes in PSECs. The rate of this process will large determine the size of the unit; a useful tool for the design communities if established. Mass transfer is primarily characterised through an overall mass transfer coefficient (K_{oc}). Considering mass transfer phenomena from the perspective of the continuous phase, the overall mass transfer coefficient is simply defined as follows:

$$\dot{n}_A = K_{oc}(C_{Ac} - C^*_{Ac}) \tag{2.35}$$

where $\dot{n}_A$ is the molar flow rate of solute A from the dispersed phase into the continuous phase, and the term $(C_{Ac} - C^*_{Ac})$ being the driving force for mass transfer, i.e. the difference between the bulk continuous phase solute concentration and interface solute concentration respectively. It should be understood that mass transfer coefficients are a convenient means of representing behaviours that are not

fully understood, by incorporating the effects of both convective and diffusive mass transfer phenomena. The unique behaviour of turbulence ensures that the relative contributions of convective and diffusive effects differ depending on the situation (Treybal, 1968). As such, it has been challenging for researchers to build theory in order to predict accurate values for K_oc. Some have opted towards building upon established mathematical models that predict fractional extraction E which lead to K_oc, or by simply formulating empirical correlations from their own findings. Both approaches will be covered and critiqued within this section.

A conventional, and well established model for explaining mass transfer phenomena is given by the resistance in series model. This model is based on Whitman two-film theory. The assumptions of the theory explain that mass transfer occurs across an interface, wherein, the rate of mass transfer is controlled by the rates of diffusion through each phase on either side of the interface, and no resistance is offered during diffusion across the interface boundary. The resistance in series model mathematically describes this simply by considering mass transfer rates as dependent on an overall resistance ($1/K_oc$) which can be broken down as the sum of local resistances to mass transfer on either side of the interface:

$$\frac{1}{K_{oc}} = \frac{1}{k_c} + \frac{1}{mk_d};\ m = \frac{C_d}{C_c} \tag{2.36}$$

where k_c is the local mass transfer coefficient at the continuous phase interface boundary and k_d is the local mass transfer coefficient at the dispersed phase interface boundary. The distribution constant m describes the ratio of the concentrations of the solute in each phase. In practical terms, it approximates the ratio of the solubility of the solvent in each phase and, thus, corrects the mass transfer resistances accordingly (Pratt, 1991; Welty *et al.*, 2007).

Kumar & Hartland (1999) proposed the use of the resistance in series model and considered the development of correlations that would enable one to calculate the Sherwood number (Sh) of the dispersed or continuous phase fluids. Subsequently, one could calculate the local dispersion coefficients using Eq. (2.37).

$$k_i = Sh_i\mathcal{D}_i/d_{[3,2]} \tag{2.37}$$

The Sherwood number is defined as the ratio of convective to diffusive mass transfer. Eq. (2.37) is a re-arrangement of the Sherwood equation wherein the characteristic length is assumed to be the droplet sauter mean diameter (Treybal, 1968). Eq. (2.37) and Eq. (2.48a), see Table 2.4, show the correlations used to predict Sh for the continuous and dispersed phase respectively, each were formulated using data published from other authors. They were developed on the bases of considering mass transfer in circulating and oscillating droplets, including effects of power input into the extraction column and dispersed phase hold-up.

However, Kumar & Hartland (1999) acknowledge that the predicted values for overall mass transfer coefficient deviated by an average of 24.5 % from experimental points.

The correlations outlined by Kumar & Hartland (1999) were later explored by Gameiro *et al.* (2010) to define a method for determining K_{oc} for a PSEC involved in a copper extraction process. $\mathcal{D}$ was, in this case, estimated via methods outlined by Wilke & Chang (1955). Other, more relevant models are available that allow the estimation of $\mathcal{D}$ which will be discussed later. Ultimately, they discovered that the resistance in series model, coupled with the Kumar & Hartland (1999) equations, tended to over predict those experimental results. It should be noted that mass transfer efficiencies where not taken directly but were modelled computationally based on concentration profiles from their experimental data and through the *axial dispersion model*:

$$\mathbb{D}_c \frac{d^2 C_c}{dz^2} - \frac{Q_c}{s}\frac{dC_c}{d_z} - \underline{a} K_{oc}(C_c - C_c^*) = 0 \tag{2.38a}$$

$$\mathbb{D}_d \frac{d^2 C_d}{dz^2} - \frac{Q_d}{s}\frac{dC_d}{d_z} - \underline{a} K_{oc}(C_c - C_c^*) = 0 \tag{2.38b}$$

They found this model to be very good at computationally predicting K_{oc}. However, to be solved one requires a values for $\mathbb{D}_c$ and $\mathbb{D}_d$ known as the continuous and dispersed phase axial dispersion coefficients respectively, used to evaluate the deviation from ideal plug flow for the system in question. Again, these values have been estimated using correlations, namely those from Ingham *et al.* (1995) and Miyauchi & Oya (1965) respectively. Other correlations for $\mathbb{D}$ are available and are examined in depth by Kumar & Hartland (1989). Therefore it is hard to say exactly where the error resides within this investigation; both sides of the investigation are prone to misanalysis through the use of correlation.

Bahmanyar *et al.* (1990) tested a number of correlation aimed at predicting the mass transfer based on the calculated theoretical height of the transfer unit (HTU_t) which is defined as:

$$HTU_t = \frac{Q_d t_c 4}{\pi D^2 \phi} \tag{2.39}$$

where Q_d is the dispersed phase flow rate and t_c is the contact time. Here correlations were used to determine t_c, the theoretical height was then compared the actual height as a measure of accuracy for each method. He mentioned that the best predictions were from those using a variation of the Newman (1931) equation originally designed to determine mass transfer inside of droplets:

$$\frac{C_{d0} - C_d}{C_{d0} - C_d^*} = 1 - \frac{6}{\pi^2}\left[\sum n = 1 \frac{1}{n_i^2} exp\left(-\frac{4 n_i^2 \pi^2 R \mathcal{D}_d t_c}{d_{pi}^2}\right)\right] \tag{2.40}$$

Here C_{d0} is the initial concentration of the solute in the dispersed phase, and n_i and

d_{pi} are the number and diameter of a droplets belonging to a particular size group, respectively. R is known as the modifying diffusivity coefficient used in conjunction with $\mathcal{D}$ to account for internal circulations. Here data for D_d has been provided and the aim is to use correlations to estimate R in order accurately predict HTU. In order to do this, he chose correlations from Johnson & Hamielec (1960) and Lochiel & Calderbank (1964), Eq. (2.41) Eq. (2.42a) respectively.

$$R = 1 + \frac{U_s d}{2048\left(1 + \frac{\ddot{E}_{0c}}{6}\right)\mathcal{D}_d} \tag{2.41}$$

$$R = 1 + \frac{U_s d}{2048\left(1 + \frac{\ddot{E}_{0c}}{6}\right)\mathcal{D}_d}\left\{1 - \left[\frac{2 + \frac{\ddot{E}_{0c}}{2}}{1 + \left(\frac{\mu_d \rho_d}{\mu_c \rho_c}\right)^{0.5}}\right]\frac{1.45}{Re^{0.5}}\right\} \tag{2.42a}$$

$$\ddot{E}_{0c} = \frac{g d_p^2 \Delta\rho}{\gamma} \tag{2.42b}$$

They found these correlations to be relatively accurate when used to determine HTU via the Newman equation; he did offer his own correlation however this is likely to be descriptive of the PSECs used in his investigation. What has been proved here is the effectiveness of the Newman, and associated equations, for predicating HTU for a PSEC that was built and tested over 40 years after the newest of these equations were formulated.

Tung & Luecke (1986) used older correlations, including a simplification of the Newman Equation, to predict local mass transfer coefficients. Four correlations where chosen to calculate either k_c or k_d depending on the level of turbulence in the system. These correlations are presented in Table 2.4. A transition droplet size is defined; above the transition size turbulent mass transfer can be assumed and an appropriate correlation can then be used to account for this. A full guide on how to determine the transition droplet size is given by Tung & Luecke (1986). The complication of this method is that it relies on additional correlations for predicting hold-up and axial mixing. They describe their model as more of a design tool than one capable of predictable accuracy in its current form (Tung & Luecke, 1986). Similarly, Luo *et al.* (1998) provides correlations a correlation for calculation of the overall mass transfer coefficient but, again, relies on other correlations for prediction of hold-up. Additionally, constants are required in order to solve said equations, provided in Table 2.4 for PSECs, specifically C. It is, however, unknown if these constants apply to all PSECs or just the systems used in their investigation, therefore, accuracy and applicability is questionable.

Thornton (1957) used the developed concept of characteristic velocity (U_0), see Eq. (2.25), to formulate a correlation for the overall mass transfer equation.

Eq. (2.43) shows how all the considered column and operating variables may affect mass transfer. In order to solve this equation one must define the missing constant terms, b and n, which can only accurately be done through experimentation. Smoot *et al.* (1959) considered data from 285 investigators in order to provide exponents and constants for an equation developed from Thornton (1957). However, the correlation provided, Eq. (2.44), only applies to the emulsion regime for PSECs with steel plates, with mass transfer $d \rightarrow c$, and where the continuous phase is water. This limits the applicability of this correlation and is said to only be accurate when the major resistance to mass transfer is in the dispersed phase, said correlation has not been corrected for axial mixing also, i.e. $(1/k_d) \gg (1/k_c)$ (Yadav & Patwardhan, 2008). Alternatively, Smoot & Babb (1962) attempted to correlate an overall mass transfer coefficient for their water-MIBK system, Eq. (2.45). Here corrections have been made for axial mixing. However, no terms are included for the effects of interfacial tension and fractional free area and the operating conditions used have not been mentioned. Also, this correlation has been formulated where mass transfer was from $d \rightarrow c$.

Lastly, He *et al.* (2004) considered mass transfer in a PSEC designed for the removal of caprolactum from waste water. Their equation are presented in Table 2.4 They found that their correlation, for $\mathcal{D} = 0.6$, was particularly sensitive to changes in columns diameter, and so have provided other correlations for different column widths. Clearly, this study was of a superficial nature, likely for their individual design purposes. There is some speculation as to the ability of these correlations to extend to nuclear PSEC design given difference in the materials used; no terms are given for material properties. Additionally, the consistency of the exponents on the different correlations is suspect and questionable (Yadav & Patwardhan, 2008).

To conclude, many alternative methods to defining mass transfer efficiencies have been presented. Some are extensions of mass transfer models and theories, whereas some are simply just correlations formulated from individual experiments or large collections of data from other authors. One thing they all have in common is their reliance on empiricism. The axial dispersion model, Eq. (2.38a) and Eq. (2.38b), could be used to accurately predict mass transfer given representative values for axial dispersion coefficients are available for the specific system of study. However, this is not a simple method and requires computational efforts in order to model stage-wise concentration changes. All of the correlations presented in Table 2.4 were studied and tested by Yadav & Patwardhan (2008) against large sets of data from various authors. They concluded that none of them were capable of accurately and consistently predicting mass transfer, primarily for the same reasons mentioned before. Mass transfer will continue to a difficult subject in PSEC research until phenomena such as hold-up and droplet size evolution can be understood (Yadav & Patwardhan, 2008).

Table 2.4: Correlations for predicting mass transfer in PSECs.

Author(s)	Mass Transfer Correlation	Comment	
Thornton (1957)	$K_{oc}\underline{a} = U_c\left[b\left(\frac{\mu_c^2}{g\rho_c^2}\right)^{0.33}\left(\frac{\mu_C g}{U_0^3(1-\sigma)^3\rho_c}\right)^{\frac{2n}{3}}\left(\frac{U_d}{U_c}\right)^{0.5}\left(\frac{U_c^3\rho_c}{g\mu_c\sigma^3}^{0.33}\right]^{-1}$	$n = 0.5$ $c \rightarrow d$ $n = 0.25$ $d \rightarrow c$ b is system specific and should be detemrined experimentlly	(2.43)
Smoot *et al.* (1959)	$K_{oc}\underline{a} = 0.2\left[\left(\frac{U_0 d\rho_d}{\mu_d}\right)^{-0.424}\left(\frac{\Delta\rho}{\rho_D}\right)^{1.04}\left(\frac{\mu_d}{\rho_d\mathcal{D}_d}^{0.865}\left(\frac{\sigma}{\mu_c U_c}\right)^{0.096}\left(\frac{U_d}{U_c}\right)^{-0.636}\left(\frac{D}{h}\right)^{0.317}\left(\frac{\mu_c}{\mu_d}\right)^{4.57}\right]^{-1}$	Applicable for $d \rightarrow c$ and water cont. phase with stainless steek plates: $U_0 = Afe$	(2.44)
Smoot & Babb (1962)	$K_{oc}\underline{a} = 504U_c\left[h\left(Af\frac{d_0\rho_d}{\mu_d}\right)^{-0.4}\left(\frac{U_C}{Af}\right)^{0.43}\left(\frac{U_c}{U_d}\right)^{0.56}\left(\frac{d_0}{h}\right)^{0.62}\right]^{-1}$	Operating conditions not mentioned	(2.45)
Tung & Luecke (1986)	$k_d = \frac{2\pi^2}{3}\left(\frac{\mathcal{D}_d}{d_{[3,2]}}\right)$	Bellow transition droplet size	(2.46a)
	$k_c = 0.582\left(\frac{\mathcal{D}_c}{d_{[3,2]}}\right)Re^{0.5}Sc^{1/3}$		(2.46b)
	$k_d = 0.00375\frac{U_s}{1+\mu_d/\mu_c}$	Above transition droplet size, considered turbulence effects	(2.46c)
	$k_c = [50 + 0.0085ReSc^{0.7}]\left(\frac{\mathcal{D}_c}{d_{[3,2]}}\right)$		(2.46d)

Table 2.4 Cont: Correlations for predicting mass transfer in PSECs.

Author(s)	Mass Transfer Correlation	Comment	
He *et al.* (2004)	$K_o c\underline{a} = 5.1705 U_c^{0.6685} U_d^{0.204} (Af)^{0.5536}$	When $D = 0.6$ m	(2.47*a*)
	$K_o c\underline{a} = 1.4296 U_c^{0.6685} U_d^{0.204} (Af)^{0.5536}$	When $D = 0.05$ m	(2.47*b*)
	$K_o c\underline{a} = 1.8125 U_c^{0.6685} U_d^{0.204} (Af)^{0.5536}$	When $D = 0.1$ m	(2.47*c*)
Kumar & Hartland (1999)	$\frac{Sh_c/(1-\phi) - Sh_{c,rigid}}{Sh_{c,\infty} - Sh_c/(1-\phi)} = 5.26 \times 10^{-2} Re^{\frac{1}{3}+6.59\times10^{-2}Re^{\frac{1}{4}}} Sc_c^{1/3} \left(\frac{U_s \mu_c}{\sigma}\right)^{1/3} \times \frac{1}{1+(\mu_d/\mu_c)^{1.1}} \left[1 + C_1 \left\{\frac{\psi}{g}\left(\frac{\rho_C}{g\sigma}\right)^{1/4}\right\}^{n_1}\right]$	$C_1 = C_2 = 4.33$ $n_1 = n_2 = 1/3$	(2.48*a*)
	$Sh_{c,\infty} = 50 + \frac{2}{\sqrt{\pi}} (Pe_c)^{0.5}$		(2.48*b*)
	$Sh_{c,rigid} = 2.43 + 0.775 Re^{1/2} Sc_c^{1/3} + 0.0103 ReSc_c^{1/3}$		(2.48*c*)
	$Sh_d = 17.7 + \frac{3.19^{-3} (ReSc_d^{1/3})^{1.7}}{1 + 1.43 \times 10^{-2} (ReSc_d^{1/3})^{0.7}} \left(\frac{\rho_d}{\rho_c}\right)^{2/3} \frac{1}{1+(\mu_d/\mu_c)^{2/3}} \left[1 + C_1 \left\{\frac{\psi}{g}\left(\frac{\rho_C}{g\sigma}\right)^{1/4}\right\}^{n_1}\right]$		(2.48*d*)
Luo *et al.* (1998)	$K_{oc}\underline{a} = \left[K \frac{1}{\phi(1-\phi)^n}\right]^{-1}; \qquad n = 0.67 + 0.028 \left(\frac{\mu_c}{\mu_d}\right)^{0.26} \left(\frac{\rho_c^2 \sigma^3}{\mu_c^4 \Delta\rho g}\right)^{0.17}$	$K = K_1/C$	(2.49*a*)
	$K_1 = \frac{(3\mu_d + 2\mu_c)}{(3\mu_d + 3\mu_c)} \left(\frac{4}{225} \frac{\Delta\rho^2 g^2}{\rho_c \mu_c}\right)^{-1/3} \frac{m(1+\mu_d/\mu_c)}{6 \times 0.00375}$	$C = 0.52;\ K = 25.86$	(2.49*b*)

2.3 CFD studies Relating to PSEC Research

The purpose of this investigation is to introduce a greater insight into the hydrodynamic characteristics of sieve-plate pulsed extraction columns. This is achieved through the utilisation of advanced computational simulation of fluid flow, turbulent behaviour and multiphase modelling through LES and RANS/Unsteady RANS CFD techniques.

Presently, there is little research available regarding, specifically, CFD focused PSEC research. However, due to the continuing reductions in affordable computational power and a resurgence in reprocessing technologies in other areas of the world, namely India, a few notable CFD studies have been conducted.

The review process of this section will primarily focus on previous works and current developments in CFD research relating to PSECs, the modelling methodologies used and their applicability/capability. The information gathered here allows one to gain a full appreciation for the progression of work within this field and will highlight the knowledge gap this research aims to bridge.

2.3.1 2-Dimensional RANS Simulations

Din *et al.* (2010) attempted to model a water-kerosene PSEC system using a RANS approach closed with the standard $k - \varepsilon$ turbulence model in FLUENT 6.3. Their main focus was to produce a multiphase PSEC model of low computational requirement that would simulate flows from a experimental rig with reasonable accuracy. The system modelled is 0.05 m in diameter, 38-plate PSEC with plates of 25 % fractional free area and 2×10^{-3} diameter holes. The 2-dimensional axisymmetric PSEC model uses a porous media model to mimic the porosity of plates instead of modelling them explicitly and only includes 4 plates. An Eulerian-Eulerian multiphase model was used with kerosene as the continuous phase. The multiphase model requires that a droplet size must be specified beforehand. Interestingly, without justification, a constant droplet size of 5×10^{-3} m is used. The geometry was meshed with 33,578 unstructured quadrilateral elements with refinement towards the plates. Coefficients for the porous media model were taken from residence time distribution (RTD) data taken from the experimental rig using a 99mTc radio-tracer. They use a second order upwind discretisation scheme for momentum, turbulent kinetic energy and turbulent kinetic energy dissipation rate, and first order upwind for void fraction. The SIMPLE algorithm was used for the coupled velocity-pressure equations. They do not mention convergence tolerances, likely set to default values of 10^{-3}, but mention a 100 iterations were performed for each time step of 0.01 s (Ansys, 2009). Simulation hold-up results were compared to experimental RTD data used to assess hold-up within their physical rig. Their results claimed to be accurate

within 72.17 % of experimental values measured.

Similarly, Yi *et al.* (2020), modelled a 2-dimensional TBP/kerosene-water multiphase PSEC using Eulerian-Eulerian multiphase modelling with a RANS realisable k-ε turbulence closure. It is a 6-plate model with a plate spacing of 0.05 m, each plate containing five 3×10^{-3} m 'holes' giving a fractional free area of 23 % for a 72.5×10^{-3} m diameter column. Simulations were performed in FLUENT 14 using unsteady SIMPLE with convergence tolerance of 10^{-4}. Hold-up and axial dispersion were studied. The defined droplet size is said to have been set according to experimental results reported previously by Yi *et al.* (2017). This is troubling as the exact droplet size used is not explicitly mentioned and the previous work from Yi *et al.* (2017) provides a range of droplet sizes resulting from a range of experiments. The authors claim the the CFD model could not predict the trend in hold-up at low pulse velocities or in situations of high hold-up. This is expected as the typical Eulerian-Eulerian model, without population balance, fails to predict the coupled effect of droplet size distribution and hold-up as function of changing operational conditions. The Authors also claim their model is capable of predicting the trends in axial dispersion as a function of operational parameters, yet their results clearly show lower predictions from that of their experiments.

An alternative and novel reduced order multiphase approach, which includes mass transfer of acetone, has been suggested and trailed by Alzyod *et al.* (2018). Here a 1-dimensional CFD multi-sectional grid population balance solver (PPBLab) is used to estimate coalescence and breakage kernels. Next, a one-primary-one-secondary particle method (OPOSPM) population balance model (PBM), written into FLUENT 18.1 as a user defined function, is solved conserving the zeroth and third moments of the droplet size distribution and mass transfer equations. This user defined PBM is coupled with an 2-dimensional Eulerian-Eulerian multiphase model running alongside a RANS K-ε turbulence model. The system is modelled is said to be a toluene/acetone/water system 2.95 m tall, be 0.08 m in diameter, have a plate hole diameter of $2 \times^1 0{-}3$ m with a plate fractional free area of 20 %. The flow rates specified are 40 and 48 Lh^{-1} for the dispersed and continuous phase with a pulse velocity of 0.02 ms^{-1}. The computational domain represents a simplified symmetric column with 2 holes (4 including symmetry boundary condition) per plate. The grid resolution is not specified and it is unlikely that a grid independence has been achieved due to visibility low resolution and lack of grid refinement. This can drastically affect the solution of RANS based fluid modelling approaches if not taken into consideration (Versteeg & Malalasekera, 2007). Validation of this model is said to be achieved via comparison against experimental data from Garthe (2006). Only three points are compared for mean mass droplet size and five points for solute concentration in the light phase. Alzyod *et al.* (2018) states good agreement is observed here. However, one could argue that not enough data is present to conclude

validation and that because no quantitative fitting parameter (i.e. coefficient of determination) is given against both sets of data that there is no justification to this claim. Additionally, the information extracted from the turbulence model is validated against a correlation taken from Milot *et al.* (1990) which was formulated for disc and doughnut columns, an argument against this can be made also with regards to applicability.

2.3.2 3-Dimensional RANS Simulations

Kolhe *et al.* (2011) studied single phase (water) flow through PSECs in order to review the accuracy of computational methods of determining axial dispersion coefficients, which as mentioned in Section 2.2.6, can be useful during design when considering mass transfer. The investigation considers how dispersion changes with pulse velocity using a RTD tracer data from rig experiments and CFD simulations. However, their experimental rig consisted of a 20-plate PSEC, whereas the model contained only 4 plates. All other parameters were kept the same except for the number of stages and column height. Final results from each case were normalised and RTD curves where compared on that basis. Their 3-dimensional CFD geometry consisted of a 4-plate 0.07962 m column meshed into 876,741 tetrahedral elements with mesh refinement towards the plates. A RANS k-ε turbulence model was used along with a second order upwind scheme and SIMPLE algorithm in FLUENT 6.2. The simulation was initialised with a full column of water and convergence tolerances were kept at the default 10^{-3} with a timestep of 0.01 s. The simulation was successful at reproducing experimental RTD curves, however, this was only assessed qualitatively. It would have been useful to see a comparison via curve fitting error or by way of other numerical means. In any case, visual observation shows that the CFD simulation results fail to reproduce the profile of the RTD curves. It is clear from the language and representation of the results that the CFD simulation claimed feasibility in estimating axial dispersion rather than being able to accurately simulate PSEC hydrodynamics.

Yadav and Patwardhan (2009) studied the hydrodynamics of PSECs with downcomer plate accessories. They attempted to model the hold-up and dispersed phase accumulation layers under the plates, the model was then extended to study regime transition. They opted for an Eulerian-Eulerian multiphase RANS based k-ε turbulence model approach using FLUENT 6.2. Their water-toluene system consisted of a 0.05 m diameter 3-plate column meshed to 450,000 unstructured tetrahedral elements with progressive refinement towards to the plates. A second order upwind discretisation scheme along with the SIMPLE algorithm was used to solve the velocity-pressure coupled equations. Maximum pulse velocities of 0.016-0.050 mms^{-1} and flow rates of 15 Lh^{-1} were specified and the column was initialised under steady state (zero pulse velocity) with only continuous phase

water ($\phi = 0$) present. Convergence criteria was kept at 10^{-3} for residual tolerances. For validation, they used correlations taken from literature including Eqs. (2.4), (2.25) and (2.28), a review of these correlations has been given previously. They claimed their simulations fell within the agreed limits given by regime transitions limits from Kumar & Hartland (1988) and within ±10 % of that predicted by correlations from Laddah & Degaleesan (1976). The range of this investigation is lacking, only mixer-setter operation was simulated and largely only hold-up investigated. A constant droplet size was specified using an outdated correlation from Vedaiyan (1969) intentionally formulated for spray columns. Previously, the two investigators published "Design Aspects of Pulsed Sieve Plate Columns" outlining all of the available droplet size equations formulated of PSECs available from literature, which raises the question - why one would choose to use a correlation for spray columns instead?

2.3.3 3-Dimensional LES

Mehra & Chaturvedi (2016) considered modelling a PSEC without comparable experimental data. They used a multiphase Volume Of Fluid (VOF) approach using OpenFOAM®. They modelled a 3-plate 3-dimensional 0.06 m diameter PSEC with a plate fractional free area of 23 %. Settling zones were used within this geometry. They chose 3 plates on the assumption that hold-up changes negligibly after the third plate. A continuous phase of organic TBP (30 %)–dodecane was used along with a water dispersed phase. The descriptive equations were solved using the PISO algorithm ran via the OpenFOAM® interFoam solver. The system was initialised with segregated continuous and dispersed phases and allowed to run for 120 s to achieve steady state counter-current flow. Their experimental procedure entailed running their 3-plate PSEC model at different pulse velocities and throughputs into order to produce a flooding curve and regime transition data. Flooding was reported when outlets streams became contaminated with carry-over from the other phase and regime transitions where determined visually. It has not been discussed whether VOF was ran with LES or if turbulence was even included at all. Additionally, there is little mention of discretisation schemes or convergence criteria. Ultimately, they explain that their investigation was primarily an exercise in demonstrating the feasibility of using open source CFD software and VOF to model PSEC regime transitions, without the aid of experimental data, in-light of more detailed future experimentation.

Lastly, Khatir *et al.* (2016) looked into a detailed analysis of RANS vs. LES PSEC simulation. A 0.15 m diameter 2-plate PSEC without settling zones was chosen for the geometry. Simulation was performed on half of the PSEC, planar-symmetric geometry, in order to reduce computational requirements. A

mesh of 520,000 unstructured tetrahedral elements was used with refinement closer to the plates. The k-ε turbulence closure model was used for the RANS simulations and one equation eddy viscosity SGS model was used for LES. The PIMPLE algorithm, a mixture of PISO and SIMPLE, was to solve the LES filtered Navier-Stokes equations through OpenFOAM®. A comparison was made on the ability of each modelling approach to accurately simulate turbulence and axial dispersion when compared against correlations taken from literature. It was found that the LES simulations produced more realistic results when compared to literature. Axial dispersion was compared using Ingham *et al.* (1995) equations and turbulence dissipation rate was compared against correlations from (Kumar & Hartland, 1996). Additionally, pressure profiles taken along the y-symmetric plane were compared in order to highlight differences between the solutions given by both modelling approaches. It was found that pressure differed greatly, the LES pressure prediction was $10 - 33$ % greater than that of RANS predictions. However, it is suspect that the pressure should differ so much given both simulations were performed under the same boundary conditions and mesh. Furthermore, the equation used to evaluate turbulence dissipation rate was originally formulated for Karr reciprocating-plate columns as well as PSECs, there are more established correlations available such as those mentioned in Section 2.2.4.1. However, the result of this work demonstrates the effectiveness of LES to accurately simulate hydrodynamics in PSECs.

2.3.4 Summary

To conclude, a number of published works on simulation of PSECs using CFD techniques have been reviewed and critiqued. Very little progression has been made within this field of research as of late. Studies, by Alzyod *et al.* (2018); Din *et al.* (2010); Kolhe *et al.* (2011); Yadav & Patwardhan (2009); Yi *et al.* (2020), all choose to use RANS k-ε style formulations to determine hydrodynamics in each of their respective systems. In taking this approach it is not known if all key aspects of the flow behaviour is faithfully captured. Typically, k-ε RANS closures are used for quick low-cost industrial studies were resolution of turbulence and accuracy is of less importance. However, it is widely understood that this closure is inadequate at capturing systems exhibiting low Reynolds numbers, swirling flows, impinging flows, transitional flows, and systems containing large pressure gradients (Versteeg & Malalasekera, 2007). All of these characteristics are likely to be displayed in multiphase PSEC flow. Furthermore, Khatir *et al.* (2016) has demonstrated the ineffectiveness of RANS approaches at accurately predicting turbulence effects within PSECs when compared against LES simulations.

As for multiphase modelling options, most of the research reviewed opt to use two-fluid Eulerian-Eulerian techniques either modelled with fixed droplet sizes,

with questionable justifications, or using reduced population balance methods. There is small body of work coming out of Bhabha Atomic Research Centre in India, Mehra & Chaturvedi (2016), considering the use of VOF multiphase simulation. However, their research is still in its infancy is not likely to progress substantially within the time frame of this investigation. Regardless, the benefits of proposed investigation are apparent in that it will spearhead progression in fundamental PSEC research through interrogation of available turbulence simulation methods and through exploration of various multiphase approaches.

3

Computational Method and Governing Equations

3.1 Fluid Flow Simulation Methodology

Described here are the derived system of equations which describe the transport of viscous fluids in motion. Namely, the Navier-Stokes equations and the methods used to approximate their solution.

3.1.1 The Navier-Stokes Equations

The general purpose model for fluid flow and heat transfer is a mathematical expression derived from fundamental laws of physics. Namely, *conservation of mass, Newton's second law of motion*, and *the first law of thermodynamics*. Conservation of mass states that, for any isolated closed system, the mass present within the system must remain constant over time. Newton's second law states that, the rate of change of momentum of a fluid particle is directly proportional to the force applied on the fluid particle, and takes effect in the direction of the applied force. Lastly, the first law of thermodynamics states that for a thermodynamic process in a closed system, any change in energy is equal to the difference between the heat accumulated by the system and the work done by it.

Fluids are regarded as a continuum and are analysed in terms of their macroscopic properties - velocity, pressure, density and temperature - which are functions of space and time. At these scales, molecular structure and motion can be disregarded as the macroscopic properties are considered averages on a large enough scale (>1 μm). For FVM codes the meshing process involves dividing the flow geometry into a number of discrete volume sub-domains (cells). Accountancy of the changes of mass, momentum and energy of each cell-volume, due to fluid flow or internal sources, forms the basis of the fluid flow equations. The rate of increase of mass in a fluid cell must equal the net rate of flow into fluid cell and so the mass conservation of a fluid for each cell-volume can be expressed as:

$$\frac{\partial \rho}{\partial t} + \frac{\partial (\rho U_i)}{\partial x_i} = 0 \tag{3.1}$$

Here, the first left hand term describes the rate of change of density (ρ), and the second hand term describes the convective term – the net flow of mass out of the cell boundaries (cell faces) - of the fluid velocity vector (U_i). Together both terms describe the unsteady, three dimensional mass conservation principle or *the continuity equation*. Eq. (3.1) is used in conjunction with the conservative form of the three dimensional Navier-Stokes equations which is derived as:

$$\rho\frac{\partial U_i}{\partial t} + \rho\frac{\partial U_i U_j}{\partial x_i} = -\frac{\partial P}{\partial x_i} + \frac{\partial}{\partial x_i}(2\mu S_{ij}) + \frac{\partial}{\partial x_i}\left(\lambda\frac{\partial U_j}{\partial x_j}\right) + F_i \tag{3.2a}$$

where the rate of strain tensor is given by

$$S_{ij} = \frac{1}{2}\left(\frac{\partial U_i}{\partial x_j} + \frac{\partial U_j}{\partial x_i}\right) \tag{3.2b}$$

P is pressure, μ is the fluid viscosity, and F_i describes the effects of body forces (momentum source terms). Together Eq. (3.1) and Eq. (3.2a) form the foundation of all FVM CFD codes used to predict fluid flow. Additionally, assuming viscous Newtonian behaviour, a transport equation for energy (E) can also be derived as:

$$\frac{\partial E}{\partial t} + \rho\frac{\partial E U_i}{\partial x_i} = -P\frac{\partial U_i}{\partial x_i} + \lambda\frac{\partial U_i}{\partial x_i}\frac{\partial U_j}{\partial x_j} + 2\mu S_{ij}S_{ij} + \frac{\partial}{\partial x_i}\left(\mathrm{k}\frac{\partial T}{\partial x_i}\right) \tag{3.3}$$

where (k) is the thermal conductivity of the fluid. In the above equations the second coefficient of viscosity, λ, is related to the bulk viscosity and produces a viscous effect associated with volume change. For compressible flows it is often approximated as $\lambda = -2/3\mu$, and is neglected for incompressible flows under the conditions of the mass continuity equation (Schlichting & Gersten, 2016). A full derivation of the N-S equations are outlined in Chapter 2 of "An introduction to Computational Fluid dynamics: The Finite Volume Method" (Versteeg & Malalasekera, 2007, pp. 10−40).

3.1.2 Solution methods to the Navier-Stokes Equations

The preliminary study in this programme of research, Chapter 4, involves investigating various methods of simulating fluid flow within multiphase counter-current PSECs. This can be a tricky endeavour due to the complex nature of the flow structures and the turbulent nature of the system. Expected to be observed are both low and high Reynolds numbers, swirling flows, impinging flows and transitional flows that are time-dependent. It is therefore necessary to investigate the appropriateness and feasibility of common computational fluid modelling methodologies to faithfully represent the underlying physics before conducting evaluative studies on PSECs for optimisation (Chapter 5).

By far the simplest method of flow simulation is through the direct high-fidelity solution of the N-S equations. Theoretically, all laminar, transitional and turbulent

flows can be simulated this way. As a result, the whole spectrum of turbulence scales can be resolved without the need of modelling efforts. This method is referred to as Direct Numerical simulation (DNS). However, DNS requires a large amount of computation power and has limitations on the maximum Reynolds number that can be considered for a DNS case. Coleman & Sandberg (2010) deduce (through derivation) that an increase in the Reynolds number by factor of 2 would increase the computation requirements for CPU time and memory by a rough factor of 11. Additionally, DNS requires a domain that is large enough to capture large eddy features with a mesh resolution fine enough to resolve the dissipation scales. In the context internal industrial flows, DNS has only been performed on simplified systems and for pipe and duct flows due to the high computational cost (Kim *et al.*, 2019). With these points in mind, it is likely not feasible, even with access to HPC, to be able to solve the N-S equations directly and that lower order models and approximative mathematical methods are required for this particular study.

3.1.2.1 Large Eddy Simulation and Subgrid Scale Modelling

The large eddy simulation approach works on the basis of reducing the degrees of freedom of the flow problem through scale-separation of the flow domain. This is the removal of small-scale information that would otherwise be computationally expensive to resolve (energy scale filtering). Larger scales representative of the grid size can be calculated directly by solving the Navier-Stokes equations. More precisely, the velocity fluctuations (turbulence) are calculated explicitly within the resolved scale field, defined by a cut-off length. Subsequently, the subgrid scales are modelled implicitly through additional subgrid scale (SGS) models. Typically, and especially for dynamic SGS models, the cut-off length is defined via mathematical filtering operations (Sagaut, 2010). A general definition for filtering is given by (Leonard, 1975):

$$\overline{U}(x,t) = \int G(r,x)U(x-r,t)dr \tag{3.4}$$

where the normalization condition is met when integrating over the entire flow domain and specified filter function G:

$$\int G(r,x)dr = 1 \tag{3.5}$$

and the velocity field is decomposed to the filtered velocity $\overline{U}$ and residual field u':

$$U(x,t) = \overline{U}(x,t) + u'(x,t) \tag{3.6}$$

The filtered mass and momentum equations in conservative form are then given by:

$$\frac{\partial \overline{U}_i}{\partial x_i} = 0 \tag{3.7}$$

$$\frac{\partial \overline{U}_j}{\partial t} + \frac{\partial \overline{U_i U_j}}{\partial x_i} = \nu \frac{\partial^2 \overline{U}_j}{\partial x_i \partial x_i} - \frac{1}{\rho}\frac{\partial \overline{P}}{\partial x_j} \tag{3.8}$$

The SGS modelling occurs through a decomposition of the advection term ($\overline{U_i U_j}$) and closure of the the residual stress tensor (τ_{ij}^R):

$$\tau_{ij}^R = \overline{U_i U_j} - \overline{U_i}\,\overline{U_j} \tag{3.9}$$

with the residual kinetic energy (k_r) defined as:

$$k_r = \frac{1}{2}\tau_{ii}^R = \frac{1}{2}\overline{U_i U_j} - \frac{1}{2}\overline{U_i}\,\overline{U_j} \tag{3.10}$$

The role of any SGS model is to provide approximations for τ_{ij}^R through modelling of the energy cascade from the resolved (filtered) scales of the flow down to the residual subgrid scales.

Provided the numerical mesh has been refined adequately, the approximated contributions from the SGS model should not dramatically impact the accuracy of the LES solution. However, given that a well-defined LES can have up to 20% of the energy spectrum modelled (80% resolved) it is still useful to consider the appropriateness of the SGS model available (Pope, 2000). In this case the LES was coupled with either the Smagorinksy (1963) algebraic SGS model or, more preferably, the dynamic Lagrangian SGS model from Meneveau *et al.* (1996).

The Smagorinksy (1963) SGS model uses a quadratic formulation to approximate the residual sub-grid scale turbulence kinetic energy k_r from the resolved rate of strain tensor S_{ij}:

$$\nu_{t,r} = C_s \Delta \sqrt{k_r} \tag{3.11a}$$

$$k_r = \left(\frac{-b + \sqrt{b^2 + 4ac}}{2a}\right)^2 \tag{3.11b}$$

$$ak^2 + bk^2 + c = 0 \tag{3.11c}$$

$$a = C_\epsilon / \Delta \tag{3.11d}$$

$$b = \frac{2}{3}\delta_{ij} S_{ii} \tag{3.11e}$$

$$c = 2C_k \Delta \left[\left(S_{ij} - \frac{1}{3}\delta_{ij} S_{ii}\right) S_{ji}\right] \tag{3.11f}$$

$$S_{ij} = \frac{1}{2}\left(\frac{\partial U_i}{\partial x_j} + \frac{\partial U_j}{\partial x_i}\right) \tag{3.11g}$$

$$C_s^2 = C_k \sqrt{C_k / C_\epsilon} \tag{3.11h}$$

where coefficients $C_\epsilon = 1.048$ and $C_k = 0.094$.

In the dynamic Lagrangian model, temporal averaging approach is applied over fluid path-lines in order to calculate SGS model coefficients based on information

from the larger unfiltered energy scales. This SGS model, therefore, incorporates considerations for the turbulence history of the case, in contrast to older and less accurate spatial averaging schemes that disregard such information. Although originally validated for systems with homogeneous directions it is readily applicable for unsteady flows with complex geometries, ideal for this study Meneveau *et al.* (1996).

The dynamic Lagrangian SGS system of equations start with a decomposition of the residual stresses through double-filtering operations using *Germano's identity* (Germano, 1992):

$$T_{ij} = \widehat{\overline{U_i}\overline{U}_j} - \widehat{\overline{U}}_i\widehat{\overline{U}}_j = \widehat{\tau}_{ij}^R + L_{ij} \tag{3.12}$$

where the Leonard stresses (known as the 'resolved stresses') are:

$$L_{ij} = \widehat{\overline{U}_i\overline{U}_j} - \widehat{\overline{U}}_i\widehat{\overline{U}}_j = T_{ij} - \widehat{\tau}_{ij}^R \tag{3.13}$$

In the above equations the $\overline{()}$ represents single-filtering at length scale Δ and $\widehat{()}$ indicates double-filtering at length scale 2Δ. The LES simulations conducted in this research all used the length scale defined by the cell volume (V_C) as:

$$\Delta = C(V_C)^{\frac{1}{3}} \tag{3.14}$$

where the model coefficient C is taken as 1 (OpenCFD Ltd, 2016).

The framework of the Smagorinksy (1963) model is used to approximate the residual stresses from the Smagorinsky constant (c_s) and resolved rate-of-strain tensors ($\overline{S}_{ij}$ and $\widehat{\overline{S}}_{ij}$) using the model equations:

$$\tau_{ij}^R = -2c_s^2\Delta^2|\overline{S}|\overline{S}_{ij} \tag{3.15}$$

$$T_{ij} = -2c_s^2(2\Delta)^2|\widehat{\overline{S}}|\widehat{\overline{S}}_{ij} \tag{3.16}$$

together with a model equation for the scaled composite rate-of-strain tensor:

$$M_{ij} = 2\Delta^2\left[\widehat{|\overline{S}|\overline{S}}_{ij} - 4|\widehat{\overline{S}}|\widehat{\overline{S}}_{ij}\right] \tag{3.17}$$

For the model to dynamically consider turbulence evolution over time, C_s is evaluated at each time-step using:

$$C_s^2(x,t) = \frac{\mathscr{F}_{LM}}{\mathscr{F}_{MM}} \tag{3.18}$$

using the transport equations:

$$\frac{\partial\mathscr{F}_{LM}}{\partial t} + \frac{\partial}{\partial x_j}\overline{U}_j\mathscr{F}_{LM} = \frac{1}{\mathrm{T}}(L_{ij}M_{ij} - \mathscr{F}_{LM}) \tag{3.19}$$

$$\frac{\partial \mathscr{F}_{MM}}{\partial t} + \frac{\partial}{\partial x_j}\overline{U}_j \mathscr{F}_{LM} = \frac{1}{\mathrm{T}}(M_{ij}M_{ij} - \mathscr{F}_{MM}) \tag{3.20}$$

In this case, the relaxation time scale T, that is the memory length of the Lagrangian averaging, is taken as:

$$\mathrm{T} = \theta\Delta[\mathscr{F}_{LM}\mathscr{F}_{MM}]^{\frac{1}{8}} \tag{3.21}$$

with θ representing a dimensionless coefficient used for fine-tuning the model and time length of the Lagrangian averaging process (Meneveau *et al.*, 1996). Typically $\theta = 1.5$, however for more complex industrial flows it is more appropriate to use $\theta = 3$, with the time scale increased to better capture historic turbulence effects of changing geometric properties of the flow along the fluid flow path-lines (Verma & Mahesh, 2012).

It should be stressed that LES uses numerical techniques in order to optimise the direct solution of the Navier-Stokes equations, as opposed to estimation of the flow problem through spatial or temporal averaging, as with Reynolds-averaged Navier-Stokes (RANS) techniques Section 3.1.2.2. Consequently, the solution is as fine as the continuum model, but now optimised. LES is, therefore, regarded as one of most accurate methods available for fluid flow modelling and provides a suitable balance of performance to computation burden with respect to today's available technology. Moreover, it is said to be most suited for transient cases, although some argument stands for the justified use of unsteady RANS approaches, particularly for flows with external time-varying driving forces. Consequently, LES provides obvious advantages for research of a fundamental nature.

3.1.2.2 Unsteady Reynolds Averaged Navier-Stokes Equations

Unsteady Reynolds averaged Navier-Stokes (URANS) equations uses statistical averaging by decomposing the fluctuating flow properties to provide an approximate solution to the flow problem. The velocity (U) is decomposed into two realisable components of the fluctuating velocity, U', and the statistically average velocity, $\langle U \rangle$. This is represented in the following equation:

$$U(x,t) = \langle U(x,t) \rangle + U'(x,t) \tag{3.22}$$

and the conservative URANS momentum equation for incompressible Newtonian fluids is given by:

$$\frac{\partial \langle U_i \rangle}{\partial x_i} = 0; \frac{\partial U_i'}{\partial x_i} = 0 \tag{3.23a}$$

$$\rho\frac{\langle U_i \rangle}{\partial t} + \frac{\partial}{\partial x_j}(\rho\langle U_i \rangle\langle U_j \rangle) = -\frac{\langle P \rangle}{\partial x_i} + \frac{\partial}{\partial x_j}\left[\mu\left(\frac{\partial \langle U_i \rangle}{\partial x_j} + \frac{\partial \langle U_j \rangle}{\partial x_i}\right) + \tau_{ij}\right] \tag{3.23b}$$

Additional unknown variables, Reynolds stresses, are introduced into the momentum equations which are a result of the averaging processes (Sagaut, 2010). This is known as the closure problem, additional turbulence models are then required in order to close the URANS equations and account for fluctuations present from the influence of turbulence. Classical RANS/URANS models achieve this through an extension of the Boussinesq approximation which presumes the Reynolds stress tensor τ_{ij} could be linked to the mean rates of deformation as follows (Versteeg & Malalasekera, 2007):

$$\tau_{ij} = -\rho\langle U_i' U_j' \rangle \tag{3.24}$$

This method is very effective at modelling flow when coupled with appropriate turbulence models. However, it should be understood that there is a severe lack of the description of the physical mechanisms involved due to the statistical nature of the simulations and does not provide a possibility of isolating rare events. It is by far the most common means of flow simulation in industry, thanks to its vastly reduced computation requirements and the lack of need for complex detail in industrial applications, but may not be considered appropriate for studies of a fundamental nature (Sagaut, 2010).

3.1.2.3 Turbulence Closure Models

As described previously, the Reynolds averaging process leads to the addition of Reynolds Stress terms in time-averaged Navier-Stokes momentum equations requiring closure. As part of the development of a PSEC CFD model two common turbulence closures will be investigated and compared against LES solutions. Namely, the k-ε model from Launder & Spalding (1974), and the Reynolds stress transport model using the pressure-strain correlation from Speziale *et al.* (1991) often referred to as the SSG RSM closure in reference to the authors.

The k-ε eddy viscosity turbulence model has been well documented in literature and is used extensively in industry through commercial CFD codes such as ANSYS Fluent. It is dependent on the extension of the Boussinesq approximation and therefore assumes isotropic turbulence in modelling the eddy viscosity term (μ_t). It is comparatively quick to solve, compared to LES and DNS, at the cost of fundamental detail and therefore accuracy, but given its low computation requirements it is ideal for initial studies (Ansys, 2009; Versteeg & Malalasekera, 2007). Moreover, it is the most commonly used fluid modelling method for PSECs, see Section 2.3, and so can provide a benchmark case to compare against higher order closures and eddy resolving methods (LES).

The transport equations for turbulence kinetic energy (k) and turbulence

dissipation rate (ε) and calculation of the eddy viscosity (μ_t) are as follows:

$$\frac{\partial(\rho k)}{\partial t} + \frac{\partial(\rho k U_j)}{\partial x_j} = \frac{\partial}{\partial x_j}\left[\frac{\mu_t}{\sigma_k}\frac{\partial k}{\partial x_j}\right] + 2\mu_t S_{ij} S_{ij} - \rho\varepsilon \tag{3.25a}$$

$$\frac{\partial(\rho \varepsilon)}{\partial t} + \frac{\partial(\rho \varepsilon U_j)}{\partial x_j} = \frac{\partial}{\partial x_j}\left[\frac{\mu_t}{\sigma_\varepsilon}\frac{\partial \varepsilon}{\partial x_j}\right] + C_{\varepsilon 1}\frac{\varepsilon}{k} 2\mu_t S_{ij} S_{ij} - C_{\varepsilon 2}\rho\frac{\varepsilon^2}{k} \tag{3.25b}$$

$$\mu_t = \rho C_\mu \frac{k^2}{\epsilon} \tag{3.25c}$$

where $C_\mu = 0.09$, $\sigma_k = 1.00$, $\sigma_\varepsilon = 1.3$, $C_{\varepsilon 1} = 1.44$ and $C_{\varepsilon 2} = 1.92$. The modelled eddy viscoity term (μ_t) is then used to model the Reynolds stresses:

$$\tau_{ij} = \mu_t\left(\frac{\partial\langle U_i\rangle}{\partial x_j} + \frac{\partial\langle U_j\rangle}{\partial x_i}\right) - \frac{2}{3}\mu_t\frac{\partial\langle U_k\rangle}{\partial x_k}\delta_{ij} - \frac{2}{3}\rho k \delta ij \tag{3.25d}$$

In contrast, the SSG RSM closure, from Speziale *et al.* (1991), attempts to solve transport equations for each of the 6 terms in the symmetric Reynolds stress tensor (τ_{ij}), Eq. (3.26a). It is known as a second-moment closure model which addresses many of the inherent drawbacks of the k-ε model. In particular, in flows exhibiting complex strain fields or significant body forces the solution of individual Reynolds stress components includes directional information of the turbulent stresses. Although greater detail can be produced, the model is typically avoided in industrial applications as it is computational more expensive, prone to convergence issues, and extremely sensitive to boundary and initial conditions, sometimes requiring an initial approximation from a k-ε solution. The transport of Reynold stresses for incompressible flows in non-rotating reference frames can be characterised by the equation:

$$\frac{\partial \tau_{ij}}{\partial t} + \langle U_k\rangle\frac{\partial \tau_{ij}}{\partial x_k} = D_{ij} + P_{ij} + \Pi_{ij} - \varepsilon_{ij} \tag{3.26a}$$

here, only the is the known stress production term (P_{ij}) is known and all other terms require modelling. A generalised gradient diffusion model for D_{ij} is given by Daly & Harlow (1970). From Speziale *et al.* (1991), a quadratic relation is used for the pressure-strain correlation (Π_{ij}) in terms of the anisotropy tensor (a_{ij}) rate of strain tensor (S_{ij}) and vorticity tensor (Ω_{ij}).

$$\begin{aligned}\Pi_{ij} = &-(C_1\varepsilon + C_1^* P_{ii})a_{ij} + C_2\varepsilon(a_{ik}a_{kj} - \frac{1}{3}a_{mn}a_{mn}\delta_{ij}) + (C_3 - C_3^*(a_{ij}a_{ij})^{\frac{1}{2}})kS_{ij} \\ &+ C_4 k(a_{ik}S_{jk} + a_{jk}S_{ik} - \frac{2}{3}a_{mn}S_{mn}\delta_{ij}) + C_5 k(a_{ik}\Omega_{jk} + a_{jk}\Omega_{ik})\end{aligned} \tag{3.26b}$$

Here $C_1 = 0.3.4$, $C_1^* = 1.8$, $C_2 = 4.2$, $C_3 = 0.8$, $C_3^* = 1.3$, $C_4 = 1.25$, $C_5 = 0.4$ and

the anisotropy tensor is given by:

$$a_{ij} = \frac{\tau_{ij}}{k} - \frac{2\delta_{ij}}{3} \tag{3.26c}$$

The dissipation term is modelled though the isotropic tensor ($\varepsilon_{ij} = \frac{2}{3}\varepsilon\delta_{ij}$) using a separate transport equation for the dissipation rate:

$$\frac{\partial(\rho\varepsilon)}{\partial t} + \frac{\partial(\rho U_k \varepsilon)}{\partial x_k} = \frac{d}{dx_k}\left[\left(\frac{k}{\varepsilon}\tau_{kl}\right)\frac{\partial\varepsilon}{\partial x_l}\right] - C_{\varepsilon 1}\rho\tau_{ik}\frac{\partial U_i}{\partial x_k}\frac{\varepsilon}{k} - C_{\varepsilon 2}\rho\frac{\varepsilon^2}{k} \tag{3.26d}$$

where $C_{\varepsilon 1} = 1.44$ and $C_{\varepsilon 2} = 1.92$. More information on the implementation of each closure model can be found in the publicly available source code (The OpenFOAM Foundation, 2017).

3.2 Modelling of Liquid-Liquid Multiphase Flow

A number of multiphase modelling techniques are explored within this research programme. One goal being to determine a multiphase modelling approach that can appropriately capture the underlying physics necessary to model PSEC operation. Initially, the one-fluid volume of fluid (VOF) method is used and interrogated through Chapter 4 and Chapter 5. Subsequently, the more complex two-fluid Eulerian-Eulerian (E-E) approach is explored along with a reportedly novel generalised hybrid VOF/E-E method, both of which are analysed in Chapter 6. The following subsections outline the theory of each technique along with how each method is implemented.

3.2.1 The One Fluid Volume of Fluid Approach

The VOF implementation used was developed by Weller (2008) for OpenFOAM®'s 'interFoam' solver. Here, the motions of both incompressible immiscible fluids, i.e. the organic phase and aqueous phase liquids, are solved using a single set of momentum equations, see Section 3.1.2. Surface tension (σ) is incorporated via an additional source term (F_s) added to the momentum equations using the continuum surface force model from Brackbill *et al.* (1992)

$$F_s = \sigma\kappa\frac{\partial\alpha}{\partial x_i} \tag{3.27}$$

computed from the curvature (κ) using

$$\kappa = -\frac{\partial n^f}{\partial x_j} = -\frac{\partial}{\partial x_j}\left(\frac{\partial\alpha/\partial x_j}{|\partial\alpha/\partial x_j|}\right) \tag{3.28}$$

n^f is the face centred interface normal vector.

The position of each fluid is tracked via the scalar field α representing the localised volume fraction. The aqueous phase liquid is represented when $\alpha = 1$ and the organic phase liquid is represented when $\alpha = 0$. Any intermediate value represents an immiscible mixture of the two fluids, particularly in regions of low mesh refinement. The time-dependent distribution of α is given by the modified continuity equation:

$$\frac{\partial\alpha}{\partial t} + \frac{\partial}{\partial x_j}U_i\alpha + \frac{\partial}{\partial x_i}U_i^r\alpha(1-\alpha) = 0 \tag{3.29}$$

Here, any spatial variation in the fluids physical property, Φ, can be modelled and tracked through α using the weighting method:

$$\Phi = \alpha\Phi_{aq} + (1-\alpha)\Phi_{org} \tag{3.30}$$

In order to dampen numerical diffusion, the last term on the left-hand side of Eq. (3.29) is added to limit smearing of the interface via the relative artificial compression velocity U^r. The magnitude of numerical compression can be controlled via the user input variable C_α:

$$U_i^r = n_i^f min\left[C_\alpha \frac{|\phi_f|}{|s^f|}, max\left(\frac{|\phi_f|}{|s^f|}\right)\right] \tag{3.31}$$

ϕ_f is the volumetric flux evaluated at the cell face surface and S^f is the cell face area vector. A more detailed breakdown of the specifics of the interFoam code is given by Deshpande *et al.* (2012). Typically $C_\alpha = 1$ is set as the default value when modelling free surface problems. However, for droplet dynamics it is more realistic to increase the level of compression to $C_\alpha = 4$, as shown by Tretola *et al.* (2017). Therefore, this modification was adopted.

3.2.2 The Two Fluid Eulerian-Eulerian Approach

The two-fluid E-E multiphase model implemented in OpenFOAM®'s 'twoPhaseEulerFoam' solver is the result of work by Rusche (2002). In the case of an E-E framework, both the organic (dispersed) and aqueous (continuous) phase fluids are considered as interpenetrating continua wherein interface interactions are modelled (coupled) through an additional inter-phase momentum transfer source term. Included as standard are heat transfer predictions through solution of an energy transport equation. In this study only isothermal systems are considered and so all energy transport terms have been removed within the source code, this does not effect solution of any other governing equations mentioned.

The incompressible continuity and momentum equations for each phase φ are given by:

$$\frac{\partial \alpha_\varphi}{\partial t} + \frac{\partial}{\partial x_i} U_{i,\varphi} \alpha_\varphi = 0 \tag{3.32a}$$

$$\frac{\partial \alpha_\varphi U_{i,\varphi}}{\partial t} + \frac{\partial}{\partial x_j} \alpha_\varphi U_{i,\varphi} U_{j,\varphi} = -\frac{\alpha_\varphi}{\rho_\varphi} \frac{\partial P}{\partial x_i} + \alpha_\varphi g_i + \frac{M_\varphi}{\rho_\varphi} \tag{3.32b}$$

where α_φ is the phase local void fraction and M_φ is the inter-phase momentum transfer term. M_φ can be predicted by accounting for forces acting on a dispersed phase droplet, the major force contributions include drag (F_d), lift (F_l) and virtual mass (F_{vm}):

$$\frac{MV}{\alpha} = F_d + F_l + F_{vm} \tag{3.33}$$

here conservation laws must be met which ensure the total sum of momentum exchange between both fluids is zero, $\sum M_\varphi = 0$.

The drag, lift and virtual mass models used to approximate forces acting on a

droplet are listed below respectively:

$$F_d = \frac{1}{2}\rho_b C_d A|U_r|U_r \tag{3.34}$$

$$F_l = C_l \rho_b V U_r \times (\nabla \times U_b) \tag{3.35}$$

$$F_{vm} = C_{vm}\rho_b V\left(\frac{\partial U_b}{\partial t} - \frac{\partial U_a}{\partial t}\right) \tag{3.36}$$

where U_r is the relative velocity between both phases $(U_a - U_b)$. The expressions exchange both ways to allow for the modelling of flows containing high void fraction and for the prediction of phase inversion, where the continous phase becomes the dispersed phase and *vice versa*. Subscript 'a' represents the property of fluid in question and subscript 'b' represents the other fluid property. When all inter-phase models are in use, the full expression for the momentum exchange then becomes:

$$\begin{aligned} M_a = {} & \alpha_a\alpha_b\left(f_a\frac{C_{da}\rho_b}{d_a} + f_b\frac{C_{db}\rho_a}{d_b}\right)\frac{3}{4}|U_r|U_r \\ & + \alpha_a\alpha_b f_a(C_{la}\rho_a U_r \times (\nabla \times U_a)) + \alpha_a\alpha_b f_a(C_{lb}\rho_b U_r \times (\nabla \times U_b)) \\ & + \alpha_a\alpha_b(f_a C_{vma}\rho_b + f_b C_{vmb}\rho_a)\left(\frac{\partial U_b}{\partial t} - \frac{\partial U_a}{\partial t}\right) \end{aligned} \tag{3.37}$$

where d_a is the droplet diameter and is usually stated as prerequisite or can be modelled. However, in this case the droplet size is fixed and is assumed to maintain spheriosidy. Further information on the exact implementation of the OpenFOAM® two-fluid method is detailed by Rusche (2002).

The drag coefficient (C_d) modelled in Eq. (3.34) is predicted using an empirical relationship based on the particle Reynolds number for ridged spherical particles $(Re_p = [\rho_b|U_r|d_a]/\mu_b)$ as presented by Schiller & Naumann (1933).

$$C_d = \frac{24}{Re_p}(1 + 0.15Re^{0.687}) \tag{3.38}$$

The virtual mass coefficient (C_{vm}) is set as a constant value of 0.5 in these studies, a typical value for flows of this nature (Marschall, 2011).

In previous PSEC E-E studies, the necessity of the contribution of the lift force and virtual mass forces have been dismissed. Yadav & Patwardhan (2009) state the reason for this is due their negligible contritions compared to the drag force. Part of the development of the E-E PSEC model will include looking at the impact of including contributions from the lift and virtual mass forces, in this case the the lift coefficient (C_l) is model using the empirical relationship given by Legendre &

Magnaudet (1998):

$$C_l = \sqrt{C_{l,lowRe}^2 + C_{l,highRe}^2} \tag{3.39a}$$

$$C_{l,lowRe} = \frac{6}{\pi^2\sqrt{ReSr}} \tag{3.39b}$$

$$C_{l,highRe} = \frac{1}{2}\left(\frac{Re+16}{Re+29}\right) \tag{3.39c}$$

$$Sr = \frac{\sqrt{d_a}}{Re\nu_b}|l\nabla U_b| \tag{3.39d}$$

where a blended coefficient is calculated from two analytical solutions for high and low Reynolds numbers, (Sr) is the dimensionless shear rate.

3.2.3 The Generalised Multiphase Modelling Approach: GEMMA

The generalised multiphase modelling approach (GEMMA) is a novel hybrid E-E/VOF multiphase model implementation developed and reported by De Santis *et al.* (2020). A brief summary of the necessity for the development of this method is introduced in Section 6.1. GEMMA builds on the n-phase momentum transport equations, Eqs. (3.32a) and (3.32b) of the E-E framework, described in Section 3.2.2, but also attempts to incorporate resolution of large-interface (mesh-resolved) regions with similar treatments to that of VOF, described in Section 3.2.1. Namely, for the resolved surface tension forces (VOF), and scaling of the interfacial momentum transfer terms (E-E) such as drag, lift and virtual mass for variability in the flow regimes present locally. To achieve this, a switching variable (C_α) is introduced used to apply VOF style interface compression which is determined by the locally evaluated the flow regime. Moreover, De Santis *et al.* (2020) have also identified the necessity for variable droplet size modelling, in E-E modelling, and have therefore included a reduced population balance model based on the one primary one secondary particle method (OPOSPM) described by Drumm *et al.* (2010).

3.2.3.1 Interface Model Switch

As mentioned, the GEMMA model uses two distinct methods of modelling the momentum transfer over the dispersed phase fluid and continuous phase fluid interface. Specifically, a large-interface VOF style model is used in regions of identified acceptable mesh resolution. Where the interface morphology and, therefore, the interfacial forces can not be resolved, the modelling defaults to E-E style dispersed-interface models to approximate the forces acting on the dispersed phase droplets and the surrounding continuous phase fluid. In each case a switching logic is employed to define the state of a scalar binary marker field. In

this implementation, the marker used is the C_α variable. In the standard VOF model, C_α is used to scale the amount of interface compression. As only large interfaces are attempted to be resolved, with interface compression applied, a value of $C_\alpha = 1$ is used. This is instead of $C_\alpha = 4$ which is used with the VOF method to attempt to improve the accuracy of flow surrounding small droplets which, in this case, are modelled by other means (in dispersed-interface mode). When the switch is activated in large-interface mode $C_\alpha = 1$. When the switch is deactivated in dispersed-interface mode $C_\alpha = 0$. A flow chart of how the switching algorithm is structured is given in Fig. 3.1. It is noted that in the latest development version of GEMMA that a C_α value is still assigned if the cells do not meet any of the three criteria (De Santis *et al.*, 2020). This is not the case here. In the version used the cells passively retain the value from the previous time-step or from initialisation. The criterion for deactivation/activation of the large-interface mode is explained in sequence below.

The first criterion used to locally deactivate large-interface mode is given by the interface resolution quality (IRQ) index, originally proposed by Hecht (2015). The IRQ index is calculated from the locally calculated interface curvature:

$$IRQ = \frac{2}{\Delta\kappa} \tag{3.40}$$

where Δ is the cell length scale and is given the same way as in Eq. (3.14) and κ is approximated using the CSF model which evaluates the local volume fraction field (α) in Eq. (3.28). As explained by (De Santis *et al.*, 2020), when a spherical interface is assessed it results in $\kappa = 1/r$. So, for large spherical interfaces the IRQ increases, suggesting better mesh-resolution of the interface. For 'flat' interfaces, the $IRQ \longrightarrow \infty$. This concept, therefore, requires the assignment of a minimum critical threshold (IRQ_{crit}) value that defines the point at which the switch is deactivated locally.

Additionally, minimum and maximum thresholds are assigned for the dispersed phased volume fraction, $\alpha_{d,min}$ and $\alpha_{d,max}$ respectively. This ensures that the switch is deactivated in regions where pure phases are present in abundance . Consequently, this also ensures that large-interface modelling is only active when in the proximity of resolvable interfaces.

Lastly, for dispersed-interface mode the switch can be activated into large-interface mode via the local droplet size. Specifically, When the population balance is actively calculating the local droplet size, the droplet interface can be resolved with the user defined condition:

$$d_{[3,2]} \geqslant \Gamma\Delta \tag{3.41}$$

where the calculated dispersed phase droplet diameter is larger than the local mesh

size (Δ) by a factor of Γ. This is a final criterion to ensure that the droplet interface is resolvable before large-interface modelling is activated.

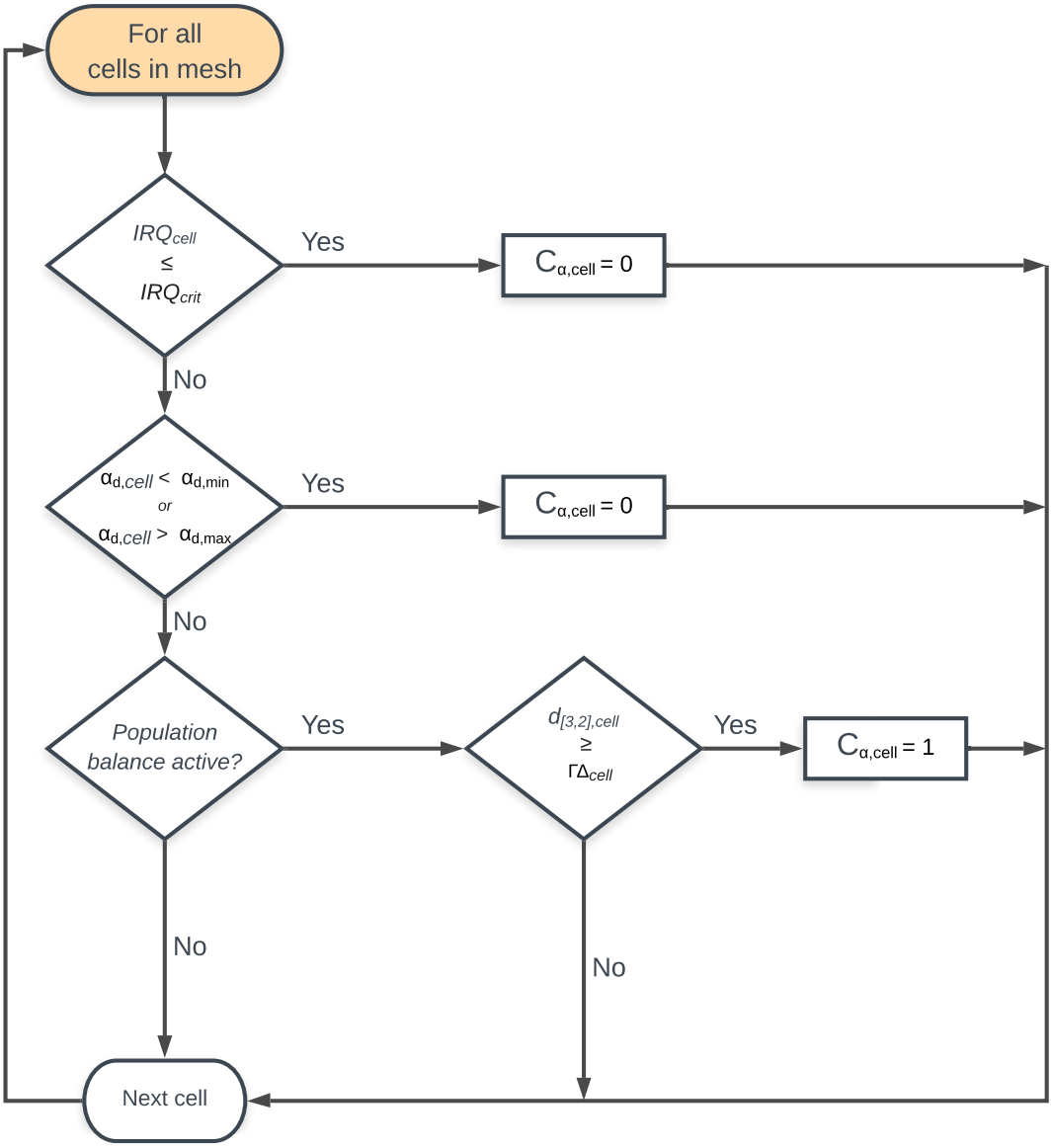

Figure 3.1: A flowchart to represent the switching algorithm used to locally determine the state of the switching variable C_α on a per-cell basis.

3.2.3.2 Large-Interface Modelling

The large-interface modelling is achieved by incorporating the interface compression method, Eq. (3.31), and CSF model for surface tension, Eq. (3.27), into the E-E continuity equation, Eq. (3.32a), and momentum transport equation, Eq. (3.32b), respectively. With interface compression, the continuity equation becomes:

$$\frac{\partial \alpha_\varphi}{\partial t} + \frac{\partial}{\partial x_i} U_i \alpha_\varphi + \frac{\partial}{\partial x_i} U_i^r \alpha_\varphi (1 - \alpha_\varphi) = 0 \tag{3.42}$$

note that Eq. (3.42) now takes a form identical to that of the VOF volume fraction advection equation, Eq. (3.29).

As mentioned, the CSF model is used to include the surface tension force F_{st} which is included in the momentum equation source terms M_φ see in Eq. (3.32b). However, De Santis *et al.* (2020) have chosen to use a density corrected CFS model to ensure that the surface tension force is only dependent on the density gradient and not on the density itself. This is introduced to improve stability for systems with large density differences between phases. The surface tension force is therefore calculated in GEMMA as:

$$F_s = \sigma \kappa \frac{\partial \alpha}{\partial x_i} \frac{2\rho_{local}}{\Delta \rho} \tag{3.43}$$

where ρ_{local} is the local mixture density and $\Delta\rho$ is the density difference between the phases.

3.2.3.3 Dispersed-Interface Modelling

As with the standard E-E dispersed-interface modelling, the drag (F_d), lift (F_l) and virtual mass (F_{vm}) forces, that contribute to interface momentum transfer, are individually accounted for, see Section 3.2.2. In regions where the interfacial forces can be resolved, where $C_\alpha = 1$, only the drag force should be included. Moreover, a blending function is used to scale F_l and F_{vm} to correct for variability in flow regimes and allow for phase inversion.

For a generic force F between phases i and j:

$$F = (1 - C_\alpha) f_i F_{disp,ij} + (1 - C_\alpha) f_i F_{disp,ji} \tag{3.44}$$

where the subscripts $disp, ij$ and $disp, ji$ refer to phase i being dispersed in the phase j and vice versa f_i is the blending function:

$$f_i = max\left[0, min\left(1, \frac{(\alpha_j - alpha_{j,min})}{(\alpha_{j,max} - \alpha_{j,min})}\right)\right] \tag{3.45}$$

For the drag force, F_d must still be included for large-interface modelling, albeit with a more appropriate closure. It should be noted that in the VOF method described in Section 3.2.1, drag forces are neglected by nature of the single-fluid formulation.

A segregated flow closure is used for the large-interface drag force $F_{d,LI}$ (Marschall, 2011):

$$F_{d,LI} = \frac{\alpha_i \alpha_j \rho_i \rho_j}{\alpha_i \rho_j + \alpha_j \rho_i} |U_r| U_r \tag{3.46}$$

this is blended with the dispersed-interface drag force(s), $F_{d,ij}$ $F_{d,ji}$, Eq. (3.34), using:

$$F_d = (1 - (1 - C_\alpha) f_i - (1 - C_\alpha) f_j) F_{d,LI} + (1 - C_\alpha) f_i F_{d,ij} + (1 - C_\alpha) f_j F_{d,ji} \tag{3.47}$$

3.2.3.4 OPOSPM Reduced Population Balance Modelling

The OPOSPM method by Drumm *et al.* (2010) considers modelling the droplet distribution by only a single moment. This allows for simpler computation, and implementation, reducing the population balance down to the the number density (N_d) and the total volume, thus only requiring one additional transport equation:

$$\frac{\partial \rho_d N_d}{\partial t} + \frac{\partial}{\partial x_i} \rho_d U_d d_{[3,0]} N_d = \rho_d S \tag{3.48}$$

here S is the droplet size-dependent breakage and coalescence rates:

$$S = [n_d(d_{[3,0]}) - 1] \mathbf{g} d_{[3,0]} N_d - \frac{1}{2} \mathbf{a}(d_{[3,0]}, d_{[3,0]}) N_d^2 \tag{3.49}$$

where n_d is the mean number of daughter particles due to breakage ($\mathbf{g}$) and coalescence ($\mathbf{a}$). The breakage kernel accounts for the daughter droplet distribution implicitly and is reflected by the n_d term, and collisions of equal-sized droplet are considered by the coalescence kernel. Following the work from Wardle & Shonibare (2015), the breakage and coalescence kernels used are from Martínez-Bazán *et al.* (1999) and Prince & Blanch (1990) respectively.

The breakage rate $\mathbf{g}$ is is given by the breakage kernel in the form:

$$\mathbf{g} = K_g \frac{\sqrt{\beta_g (\varepsilon_c d_{[3,0]})^{2/3} - 12\sigma/(\rho_c d_{[3,0]})}}{d_{[3,0]}} \tag{3.50}$$

where the constant $\beta_g = 8.2$ and $K_g = 0.25$. In this implementation the developers, Wardle & Shonibare (2015) and subsequently De Santis *et al.* (2020), have chosen to consider the coalescence of droplets of a single size, therefore the coalescence kernel, derived form Prince & Blanch (1990), becomes:

$$h = \frac{\pi}{2\sqrt{2}} d_{[3,0]}^2 (2 d_{[3,0]}^{2/3})^{1/2} \varepsilon_c^{1/3} \tag{3.51a}$$

$$\lambda_{ij} = exp(-\frac{d_{[3,0]}^{5/6} \rho_c \varepsilon_c^{1/3} ln(h_i/h_j)}{4\sigma}) \tag{3.51b}$$

$$\mathbf{a} = h \lambda_{ij} \tag{3.51c}$$

Here, h is the collision rate of the two droplets, of size $d_{[3,0]}$, and λ_{ij} is the coalescence

efficiency of the collisions, the product of these terms returns the actual coalescence rate **a**.

For the solution to be consistent with the population balance, the the number density transport equation, Eq. (3.48), should be coupled with the CFD solution. Here, the volume weighted mean droplet size $d_{[3,0]}$ is fed back into dispersed-interface modelling which corrects the solution of momentum equation. Drumm *et al.* (2010) explains that this description of the droplet size takes advantage of that fact that only information for the third and zeroth moment of the size distribution is required. Normally, in much more expensive and complex population balances, the second moment would also be calculated to give the droplet surface area. In the context of solvent extraction research, it is more appropriate to analyse a system based on the surface-volume weighted mean (Sauter mean) diameter $d_{[3,2]}$, see Section 2.2.4. Therefore, the droplet size is evaluated as

$$d_{[3,2]} = 0.76\left(\frac{6\alpha_d}{\pi N_d}\right)^{1/3} \tag{3.52}$$

and it is this description of the droplet size that is coupled with the CFD De Santis *et al.* (2020). The conversion coefficient (0.76) is taken from the method presented by Wardle (2013). It was evaluated from comparing the distributions of droplet sizes out of a number of centrifugal contactor experiments. They are said to have similar distributions to that in other high dispersion solvent-extraction systems, such as PSECs.

Moreover, it is clear that the population balance is largely driven by the turbulence kinetic energy dissipation rate of the continuous phase fluid (ε_c). This is calculated using the the continuous phase fluid LES solution and time-averaged flow statics. The system of equations used to calculate ε are explained in detail in Section 4.2.4.

3.3 Choice of Code

A number of open source and commercial CFD codes are currently available. This section describes the code chosen for use in this research and the reasons for this decision.

3.3.1 OpenFOAM®

The open source software OpenFOAM® was chosen as the appropriate CFD code for this investigation. General public licenced codes provide a number of user focused incentives which are not available from any of the commercial CFD codes on the market. Namely, the accessibility to modify and redistribute any part of the software under a guarantee of continued free use within the terms of the licence agreement. The C++ based solvers and utilities allow for limitless customisation and offer a familiar syntax for those with low-level coding experience. This allows for bespoke solutions to complex flow problems, as well as accessibility to calculation methodologies via the original source code for troubleshooting purposes. Moreover, OpenFOAM® has shown suitable speed performance in large cases were extensive parallelisation is required due the computational requirement of the flow problem (Wardle *et al.*, 2006).

OpenFOAM® offers a full suite of pre-processing and post-processing utilities that allow for mesh generation, mesh conversion, data visualisation, and data manipulation. A wide variety of RANS turbulence closures, LES SGS models and filters, and solvers are available that are fully customisable and accessible through the source code. The solvers are capable of handling complex single phase or multiphase incompressible or compressible flow problems, running through either dedicated SIMPLE and PISO algorithms or through a mixture of both (PIMPLE). Each have fully optimisable numerical schemes and solutions methods through the interface system. The optimisable numerical algorithms and variety in LES SGS models are particularly advantageous to this research project and is ultimately the reason for selecting this software package.

OpenFOAM operates through the Linux command-line interface via a case dedicated file structure. The minimum requirements for an operable case directory is shown in Fig. 3.2. The system directory contains information relating to the solution procedure: fvSchemes holds the necessary discretisation schemes used in solution method chosen; fvSolution retains information on algorithm control such as tolerances and under-relaxation factors; and the controlDict contains the run-control settings such as stop/start times, data output controls and Courant number control as well as any additional settings required. The constant directory contains the case mesh information with in the polyMesh file directory, the physical properties of the materials used under the file transportProperites, and

the turbulent model is selected under turbulenceProperties. Lastly, the time directories hold written time-step information for the scalar, vector or tensor solutions or initial boundary conditions under the start time folder 0 unless otherwise specified in the controlDict startTime control. Additional information relating to the OpenFOAM software suite is available from the user guide and programmers guide (OpenCFD Ltd, 2016).

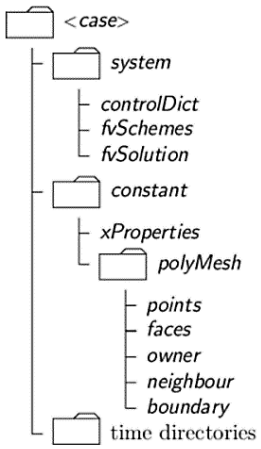

Figure 3.2: File structure for a generic CFD case run through OpenFOAM.

3.3.2 The PIMPLE Algorithm

The PIMPLE algorithm is used to provide a stable solution framework to all multiphase models investigated within this programme of research. An iterative solution to a chosen system of equations can be achieved through sequential processes, and looping over sections of these processes to provide stability and accuracy. Namely, a mixture of inner-loop pressure correction steps and outer-looping over the entire solution procedure, before solving for turbulence and SGS transport equations, provides a stable time-step convergent solution. PIMPLE, therefore, is used for transient fluid problems, where the SIMPLE algorithm is not appropriate, and provides a more robust framework over PISO methods particularly in instances were the maximum Courant number (Co) may consistently be above 1. Moreover, outer-looping provides options for under-relaxation techniques, however, this can lead to impairment of the time-accuracy of the solution and so is avoided.

The system of equations solved by each multiphase solver used in this research is unique. However, operating under the PIMPLE algorithm, the multiphase solvers share commonality in their workflow structure. A generalised diagrammatic representation of the PIMPLE workflow is provided in Fig. 3.3.

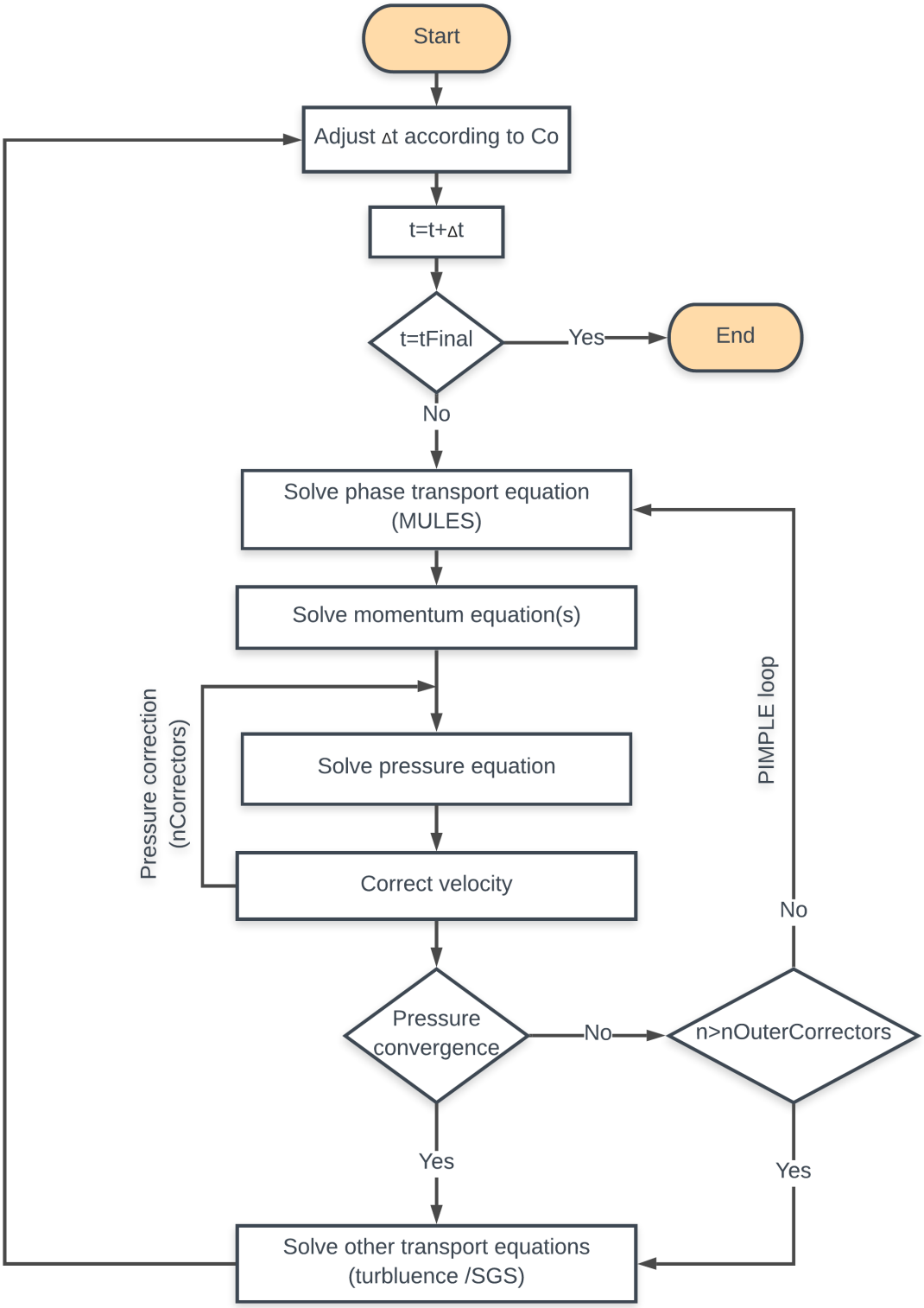

Figure 3.3: A flowchart representing a generalisation of the PIMPLE algorithm used in all multiphase solvers in this programme of research.

3.4 Computational Domain and Geometry

To best replicate industrial PSEC unit operations found in the nuclear reprocessing industry, the geometry used in this investigation was designed using generic sizing constraints taken from Logsdail & Slater (1991) in '*The Handbook of Solvent Extraction*' which provides a range of dimensions for previously operational PSECs. The dimensions of this column are listed in Table 3.1. Due to the complexities and varying length scales inherent to this geometry, a tetrahedral mesher was chosen to produce an unstructured three-dimensional purely tetrahedral mesh of 5.5 M nodes with refinement towards the plates and column walls, seen in Fig. 3.4. The open source computer-aided design software SALOME (version 8.3.0) was used to produce the three-dimensional geometry seen in Fig. 3.4 which was subsequently meshed using the CD-adapco® STAR-CCM+® environment (version 10.06.010) and converted across for use with OpenFOAM®.

Table 3.1: Characteristic dimensions of PSEC geometry.

Parameter	**Dimension**
Column Diameter, D (m)	0.150
Column Height (m)	1.604
Decanter Heights (m)	0.300
Decanter Diameters (m)	0.250
Inlet / Outlet Diameters (m)	0.050
Number of Plates	2
Number of Holes per Plate	283
Hole Diameter, d (m)	4.46×10^{-3}
Fractional Free Area, e	0.25
Plate Thickness (m)	0.002
Plate Spacing, h (m)	0.300
Bottom Inlet Height from Base (m)	0.350

The mesh in the near plate region was resolved in order to discreetly capture droplet formation, droplet-fluid interactions and fluid transfer behaviour across the plate throughout pulsing. In order to reduce the computational burden, the mesh in the bulk flow region was resolved to a level high enough to accurately resolve enough of the turbulence energy spectrum and implicitly track the fluid motions of the dispersed phase fluid. More specifically, the volume of the largest tetrahedral cell (V_C) in the mesh (2.016×10^{-7} m^3) corresponds to an insphere radius of 2.44 mm comparable to the radius of the sieve-plate holes:

$$R = \frac{l}{\sqrt{24}} = \frac{\sqrt[3]{V_C 6\sqrt{2}}}{\sqrt{24}} \tag{3.53}$$

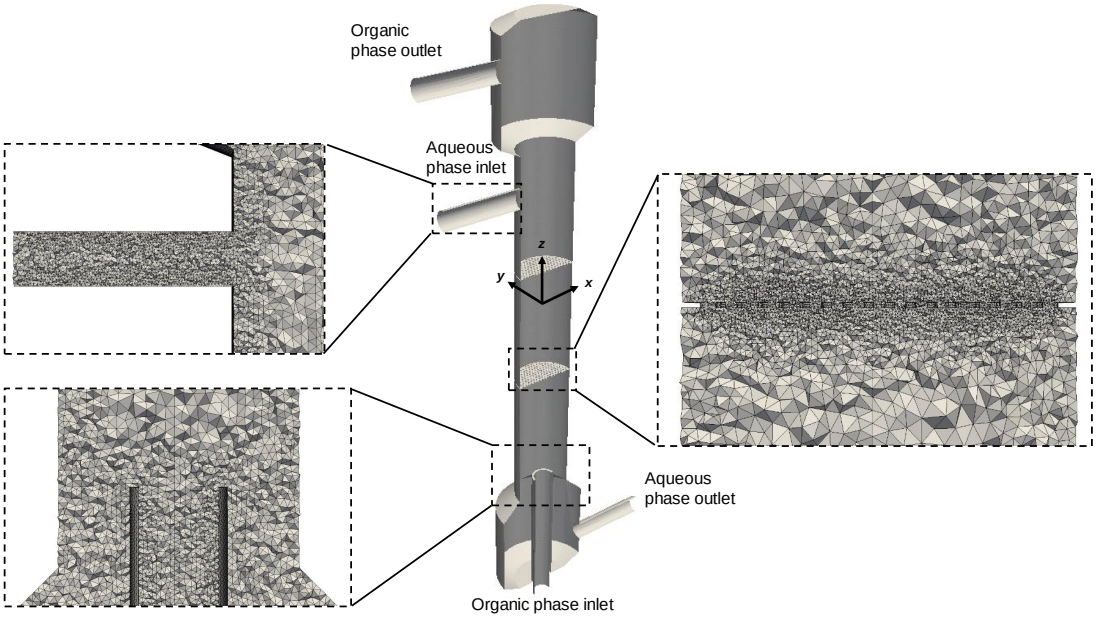

Figure 3.4: Geometry and mesh, with axis orientation, of PSEC used in CFD simulations.

A two-plate geometry was chosen on the basis that the inter-compartmental hydrodynamics remain largely unchanged past the second plate. Similar reasoning has been used for justification of 2 - 4 plate models by previous investigators (Khatir *et al.*, 2016; Kolhe *et al.*, 2011). A large plate spacing of 300 mm was chosen in order to observe the inter-compartmental flow characteristics. A reasonable decanter height and diameter was chosen to provide enough fluid volume to dissipate agitative effects and allow for settling in these regions. The light phase inlet represents an ANSI schedule 80 pipe with a thickness of 5.54 mm.

The quality and suitability of the mesh was assessed using OpenFOAM®'s checkMesh tool. In order for the solvers to run stably, there are limits on: the boundary openness, cell openness, aspect ratio, face area limits, cell volume limits, cell face orientation, mesh orthogonality and skewness. The output of the code is shown below and reports that the mesh is fit for purpose. The reported mesh non-orthogonality is high and so requires the use of corrected gradient schemes OpenCFD Ltd (2016).

```
Checking geometry...
    Overall domain bounding box (-0.325 -0.124978 0) (0.325 0.124976 1.604)
    Mesh has 3 geometric (non-empty/wedge) directions (1 1 1)
    Mesh has 3 solution (non-empty) directions (1 1 1)
    Boundary openness (5.54765e-16 1.94054e-16 -1.45013e-16) OK.
    Max cell openness = 4.26371e-16 OK.
    Max aspect ratio = 10.482 OK.
    Minimum face area = 3.71046e-09. Maximum face area = 7.79745e-05.  Face area magnitudes OK.
    Min volume = 3.0005e-13. Max volume = 2.01634e-07.  Total volume = 0.0449717.
Cell volumes OK.
    Mesh non-orthogonality Max: 63.096 average: 15.8806
    Non-orthogonality check OK.
    Face pyramids OK.
    Max skewness = 1.28595 OK.
    Coupled point location match (average 0) OK.
Mesh OK
```

3.5 Fluid System

The fluid system studied in this body of research involves the use of commonly used chemicals from PUREX and other nuclear solvent extraction processes. Namely a tributyl phosphate (TBP)/dodecane mixture at 30/70 vol % and nitric acid acting as the light (organic) and heavy (aqueous) phase fluids respectively.

The density of the organic phase mixture was calculated based on a weighted average of the two fluids by the chosen vol %. The kinematic viscosity of the organic phase mixture was calculated using:

$$\nu^{1/3} = x_a \nu_a^{1/3} + x_b \nu_b^{1/3} \tag{3.54}$$

where x is the mass fraction of the fluid component (Gambill, 1959). The fluid properties of chemicals used, and the properties of the constituent components used to estimate properties of the mixture, are listed in table Table 3.2, are in close agreement with that measured and more recently reported by Yi *et al.* (2020) (Green & Perry, 2008).

Table 3.2: List of fluid properties for chemicals used in studies.

Chemical	**Property**		
	Density ($\mathrm{kgm^{-3}}$)	**Kinematic Visocity** ($\mathrm{m^2s^{-1}}$)	**Surface Tension** (mNm)
TBP	973	3.62×10^{-6}	0.00983
Dodecane	750	1.82×10^{-6}	
TBP/Dodecane 30/70 vol %	806	2.35×10^{-6}	
HNO3	1110	1.02×10^{-6}	

4

Numerical Investigation of Modelling the Hydrodynamics of a Multiphase PSEC

4.1 Introduction

A resurgence in pulsed column research has been made apparent over the past decade through new investigations into their hydrodynamics using computational fluid dynamics. However, these studies are mainly rudimentary, typically employing Reynolds-averaged Navier-Stokes methods using k-ε turbulence modelling to close the descriptive equations (Din *et al.*, 2010; Kolhe *et al.*, 2011; Sen *et al.*, 2015, 2016, 2018; Yadav & Patwardhan, 2009).

Some preliminary advancements in PSEC fluid flow modelling made by Khatir *et al.* (2016) compared the suitability of LES over unsteady Reynolds-averaged Navier-Stokes (URANS) calculations to capture the complex turbulence and flow behaviour within simplified PSEC-like geometries. The results showed promise for the suitability of LES to perform well in capturing time-dependent information and resolve the complex turbulence properties over URANS methods. However, the analysis performed was limited within the context of a small journal article. Furthermore, the geometry and operational conditions employed likely do not faithfully represent the full complexity of an industrial PSEC system and, by extension, may not fully capture the complete physical behaviour therein.

The work presented within this chapter aims to expand substantially upon the limited PSEC fluid modelling efforts described in the current literature. This will be achieved by (i) producing a high resolution LES of an industrially representative PSEC geometry with appropriate boundary conditions, and (ii) comparing those results against URANS simulations closed using typical turbulence model approaches.

i Firstly, through the use of a time-dependent, three-dimensional, turbulent eddy-resolving method, the important time-varying, energy-containing turbulence structures within PSECs can be predicted allowing a detailed analysis of their mode of operation. This is achieved using LES coupled with

dynamic sub-grid scale (SGS) modelling that can provide accurate and reliable predictions of complex flows and allow for characterisation of the dispersive mixing mechanisms.

ii Secondly, the suitability of different fluid flow modelling approaches are analysed for their ability to capture the necessary level of physical detail in the operation of PSECs. Comparisons are made between the LES predictions obtained from (i) and compared directly against URANS k-ε and SSG RSM closures (Launder & Spalding, 1974; Speziale *et al.*, 1991).

All the simulations within this chapter use the VOF method to approximate the interactions within an operational multiphase PSEC, see Section 3.2.1. Here, multiphase interface interactions are modelled with appropriate heavy and light phase fluidic properties (listed in Table 3.2) capturing surface tension, density and viscous effects. In Chapter 6, alternative multiphase models will be compared and analysed. This investigation only focuses on examining the fluid behaviour with regards to turbulence and macroscopic flow properties captured from the various Navier-Stokes solution methods compared.

4.2 Large Eddy Simulation Using the One-Fluid Volume of Fluid Approach

4.2.1 Choice of Operational Parameters

To achieve a stable operation under the column flooding limit (maximum throughput), the inlet flow velocities, and pulse velocity (Af), described in Section 4.2.2, were calculated using Eq. (2.7), from Smoot *et al.* (1959), and Eq. (2.10a), from Berger & Walter (1985), here C_o is the orifice discharge coefficient taken as 0.6, a solvent-flow-ratio of 1 was chosen and C_t is the mass fraction of the solute in the aqueous feed. Since no mass transfer is included in this study C_t is taken to be 0.

$$(V_c + V_d)_f = 0.527 \frac{\sigma^{0.144} \Delta\rho^{0.63} \mu_c^{0.489} h^{0.207} d^{0.458} g^{0.81}}{\rho_c^{0.775} \mu_d^{0.2} Q^{0.207}} \times \left(\frac{V_d}{V_c}\right)^{0.014} (Af)^{-0.621} \tag{2.7}$$

$$Q = \frac{\pi^2}{2C_o^2} \frac{1 - e^2}{e^2}$$

$$\begin{aligned}(U_c + U_d)_m = {} & (24.528 + 2.537\sigma + 0.0548\sigma^2) \\ & \times (1 + 1.455e + 3.247e^2) \\ & \times \left[1 + 0.1778 ln\frac{U_c}{U_d} + 0.0437\left(ln\frac{U_c}{U_d}\right)^2\right] \\ & \times (0.2115 D^{0.2} h^{0.18}) \left(1 + \frac{U_c}{U_d}\frac{h}{d} C_t\right)^{0.09}\end{aligned} \tag{2.10a}$$

The column was characterised to be operating under a dispersed regime (between mixer-settler and emulsion regimes) using Eqs. (2.3) and (2.5) from Kumar & Hartland (1983) and Tung & Luecke (1986) respectively.

$$Af_t = \left[0.05\beta h \left(\frac{\rho_c}{\Delta\rho^{0.75}\sigma^{0.25} g^{1.25}}\right)^{-1}\right]^{\frac{1}{3}}$$
$$\beta = \frac{e^2}{(1-e)(1-e^2)} \tag{2.3}$$

$Af < Af_t$ Dispersion Regime

In this operational regime, the column produces stable mixing conditions forming clear dispersed organic phase droplets rising via gravity driven flow. More details of PSEC operating regimes and flooding is avilable in the paper '*Design aspects of*

pulsed sieve plate columns' by Yadav & Patwardhan (2009).

4.2.2 Boundary/Initial Conditions and Initialisation for LES

A summary of the boundary conditions used are listed in Table 4.1. Conditions for the volume fraction, pressure, velocity and SGS model fields ($\mathscr{F}_{LM}, \mathscr{F}_{MM}, \nu_t$) were specified at the inlet, outlet and wall boundary patches as well as for the internal (initialised) field.

Inlet values for α were set according to the phase relevant at each boundary patch with a zero gradient condition (from cell centres to boundary faces) applied at the walls. The internal field for α was initialise to include a volume of organic fluid in the decanter zone at the top of the column, creating a droplet disengagement interface between the two fluids characteristic of PSECs. This was achieved by assigning any cell above a given reference height, in this case 1.3 m, $\alpha = 0$ and any cell below as $\alpha = 1$.

Table 4.1: Summary of boundary conditions used in LES simulation.

	α	P_{local} (Pa)	U (ms^{-1})	$\mathscr{F}_{LM}$ (m^4s^{-4})	$\mathscr{F}_{MM}$ (m^4s^{-4})	ν_t (ms^{-2})
Heavy Phase Inlet	Fixed value 1	Fixed gradient corrected for velocity boundary	Fixed value (0 0 0.015)	Fixed gradient 0	Fixed gradient 0	Fixed gradient 0
Light Phase Inlet	Fixed value 0	Fixed gradient corrected for velocity boundary	Time-varying sinesoidal $A = 0.0125$ $f = 1$ $U_{offset} = 0.015$	Fixed gradient 0	Fixed gradient 0	Fixed gradient 0
Heavy Phase Outlet	Outflow: Fixed gradient 0 Return flow: Fixed Value 1	0 Customised condition Eq. (4.2)	Outflow: Fixed normal gradient 0 Return flow: Calculated from flux	Fixed gradient 0	Fixed gradient 0	Fixed gradient 0
Light Phase Outlet	Outflow: Fixed gradient 0 Return flow: Fixed Value 0	0 Customised condition Eq. (4.2)	Outflow: Fixed normal gradient 0 Return flow: Calculated from flux	Fixed gradient 0	Fixed gradient 0	Fixed gradient 0
Wall	Fixed gradient 0	Fixed gradient 0	No slip	Fixed gradient 0	Fixed gradient 0	Fixed gradient 0
Initialised Internal Field	Non-uniform value	Uniform value 0	Uniform value (0 0 0)	Uniform value 1×10^{-3}	Uniform value 1×10^{-3}	Uniform value 0

The OpenFOAM® interFoam solver solves the momentum equation using a modified pressure field 'p_rgh', the static pressure excluding the hydrostatic contribution (calculated from the local cell density):

$$\text{p\_rgh} = P_{static} - \rho_{cell} g(h - h_{ref}) \tag{4.1}$$

This causes complications at the pressure boundary patches when modelling closed systems in instances where the density of the fluid varies significantly with height. In this case without modification, the pressure at the bottom (aqueous) outlet is overestimated as the hydrostatic head at that point is calculated based on the local heavier density and doesn't account for the lighter fluid in the disengagement section.

In order to rectify this imbalance a custom condition was used:

$$P_{local} = P_0 - \rho_{cell}(1 - |U|^2) + \rho_{cell} g(h - h_{ref}) \tag{4.2}$$

This allows one to correctly assign considerations for the hydrostatic head contribution at each outlet via P_0 estimated through the expression:

$$P_0 = \rho_c g z_f - h_{ref} \tag{4.3}$$

where z_f is the z-direction cell-face-centre height and ρ_c is the density of the continuous phase in that region, namely nitric acid at the bottom outlet and TBP/dodecane at the top outlet. In both cases a reference height h_{ref} is used to discreetly set where there is a sharp change in density, i.e. at the disengagement interface.

A fixed velocity of 0.015 ms^{-1} was assigned for the aqueous phase inlet. In order to simulate pulsed dispersed flow, the organic phase inlet was prescribed a time-varying sinusoidal boundary condition, available within the standard OpenFOAM® libraries, characterised as:

$$U = Afsin(2\pi ft) + U_{offset} \tag{4.4}$$

where the amplitude of the pulsation is controlled via A, the frequency of pulsation set by f and the mean velocity (average throughput) set by U_{offset}. Together, both conditions provide a solvent-flow-ratio of 1 and a total volumetric throughput of 0.106 $\mathrm{m}^3\mathrm{h}^{-1}$. The velocity at the outlets were given a mixed condition type. During normal outflow a zero gradient condition applies, whilst during events of return flow the incoming velocity is obtained from the flux in the patch-face normal component of the internal-cell value.

For the SGS transport equations, a value for the internal field must be set in order initialise the solution. However, these values are immediately overwritten and so are of little consequence to the final solution provided stable initial values are given.

4.2.3 Solution Method

A transient Euler time-derivative scheme was used along with a multi-dimensional cell limited least-squares gradient scheme for all equations solved. Additionally, the velocity and volume fraction transport equations were solved using second-order divergence schemes. The SGS model transport equations were solved using a bounded first-order upwind divergence scheme, this of particular necessity for this SGS model as unbounded scalars can quickly lead to divergence through negative values (Stoll & Porté-Agel, 2006).

Convergence for the transient case was reached when the final residual fell below 1×10^{-6} for each transport equation at each time step. The transient PIMPLE algorithm was used, see Section 3.3.2, solving within 2 outer-loop iterations at each time step. Within each outer-loop, 3 inner-loop iterations are preformed. Here, the pressure equation is solved and repeated an additional 2 times via 'corrector loops'. Repetition of the pressure equation reduces the influence of non-orthogonal mesh areas. No under-relaxation is used in order to maintain transient accuracy.

Using the semi-implicit MULES (Multi-dimensional limiter with explicit solution) algorithm for discretisation of the volume fraction field, a fixed maximum Courant number was applied using an adjustable time-stepping option. The average Courant number oscillated between 0.006 and 0.012. An additional four inner-loop sub-cycling steps, through MULES, was implemented to improve stability and accuracy of the solution of the volume fraction transport term. Final solutions were taken when time step convergence was observed, and the volume fractions and outlet velocities showed cyclic steady-state behaviour.

The simulation was parallelised and ran across 192 processors (∼28,600 cells per processor) using the University of Leeds' ARC3 HPC facilities (University of Leeds, 2019). The time step was in the order of 0.0003 s once fully developed cyclic stead-state flow had been achieved. On average, a wall-clock time of 1.32 hrs produced 1 s of simulated transient flow.

4.2.4 Post-Processing Operations and Analysis Methods

In order to extract more information from the simulations than is generated directly by the solver, additional mathematical operations were performed in post-processing. To highlight persistent characteristics of the fluctuating flow field, results across 200 pulse cycles were ensemble time-averaged, denoted by $\langle\cdot\rangle$, into four sets of results at $\frac{1}{2}\pi$, π, $\frac{3}{2}\pi$ and 2π during the sinusoidal pulse cycle. From this, the mean velocity and pressure fields were calculated. Additionally, one can extract information on the turbulence kinetic energy from the velocity fluctuations, $U_i' = U_i - \langle U_i \rangle$, and residual sub grid contribution,

$$k_t = \frac{1}{2}\langle \overline{U_i' U_i'} \rangle + \frac{2}{3}\langle k_r \rangle \tag{4.5}$$

as well as, consequently, the 'turbulence resolution':

$$M = \frac{k_r}{\frac{1}{2}\langle \overline{U_i' U_i'} \rangle + k_r} \tag{4.6}$$

and the resolved field turbulence dissipation rate from the fluctuating rate-of-strain tensor and residual sub grid contribution:

$$\varepsilon = 2\nu\langle\overline{S'_{ij}S'_{ij}}\rangle + \langle\varepsilon_r\rangle \tag{4.7}$$

where the rate-of-strain tensor is defined as:

$$S_{ij} = \frac{1}{2}\left(\frac{\partial U_i}{\partial x_j} + \frac{\partial U_j}{\partial x_i}\right) \tag{3.11g}$$

with

$$\varepsilon_r = \frac{C_\mu k_r^2}{\nu_t} \tag{4.8}$$

and the constant C_μ is taken to be 0.09 (Pope, 2000, 2004; Tennekes & Lumley, 1972). The total production of turbulence kinetic energy was calculated using Eq. (4.9). Both the mechanical production and buoyant flux terms were considered. Neglecting to include contribution from the buoyant flux term can result in a negative production of turbulence kinetic energy, an observed phenomena in multiphase flows (Gayen & Sarkar, 2011)

$$\begin{aligned}\text{Production of } k_t = & \begin{matrix}\text{Mechanical}\\ \text{production}\end{matrix} + \text{Buoyant flux} \\ = & -\langle U_i U_j\rangle\frac{\partial\langle U\rangle}{\partial x_j} + \delta_{i3}\frac{g_i}{\rho_c}\langle\rho' U'_i\rangle\end{aligned} \tag{4.9}$$

In order to determine the dispersive mixing capability, the 'mixing index' λ_{MI} field can be calculated from the magnitudes of the rate-of-strain tensor (shear-strain-rate), $|S|$, and vorticity tensor, $|\Omega|$. In this case, both were calculated from the filtered velocity field:

$$\overline{\lambda_{MI}} = \frac{|\overline{S}|}{|\overline{S}| + |\overline{\Omega}|} \tag{4.10}$$

where,

$$\Omega_{ij} = \frac{1}{2}\left(\frac{\partial U_i}{\partial x_j} - \frac{\partial U_j}{\partial x_i}\right) \tag{4.11}$$

The mixing index is a scalar variable used to quantify the ratio of rotational and irrotational flow components and is commonly used in industrial colloidal applications in assessing mixing effectiveness (Cullen, 2009). A value of 0 represents pure rotational flow, 0.5 represents simple shear flow, and value of 1 represents pure elongational flow. When irrotational flow is dominant, droplets

experience a type of deformation which stretches (elongates) them inducing breakage and dispersion. Other modes of flow (rotational and shear) do not contribute as efficiently to dispersive mixing, instead inducing bulk or local rotation of the suspended droplets (Rauwendaal, 1999). Using this criteria, one can evaluate the dispersive mixing efficiency of the system *a priori* based purely on the velocity field. The mixing index field calculated from Eq. (4.10) was ultimately ensemble time-averaged for analysis.

Alternatively, other turbulence characteristics have been used to explain droplet breakup mechanisms in the formation of emulsions in turbulent flows. As described by Vankova *et al.* (2007), classical studies of emulsification theorise two modes of emulsification defined by the turbulent length scales and droplet sizes. When the size of the smallest turbulent eddies in the continuous phase are smaller than the droplets, deformation results under the action of pressure fluctuations and is known as the "turbulent inertial regime". When the smallest eddies are larger than the droplets viscous stresses inside and between the eddies result in deformation under the "turbulent viscous regime". Through comparison of the turbulent (Reynolds) stresses, Eq. (4.12), viscous stresses, Eq. (4.13) and eddy length scales, defined by the *Kolmogorov length scale* Eq. (4.14), the primary mode of mixing can be identified and used to describe mechanistically the functionality of PSEC mixing:

$$\tau_{ij}^{t} = \rho\langle U_i' U_j' \rangle \tag{4.12}$$

$$\tau_{ij}^{v} = 2\mu S_{ij} \tag{4.13}$$

$$\lambda_0 = (\nu_c^3/\varepsilon)^{1/4} \tag{4.14}$$

4.2.5 Results and Discussion

Follows are the results from the LES used to predict the transient flow within an operational PSEC. Presented are details of the instantaneous flow field, suitability of the mesh for the flow investigated (via the $y+$ and turbulence resolution), discussions of the two-phase flow interactions predicted by the VOF model and flow field properties (pressure, turbulence kinetic energy and dissipation rate). Moreover, a method for assessing the mixing performance is presented via mixing index criterion, and the stresses arising from the flow are also investigated in order to demine the primary mode of mixing through either turbulent or viscous stresses.

4.2.5.1 Flow Detail and Mesh Suitability

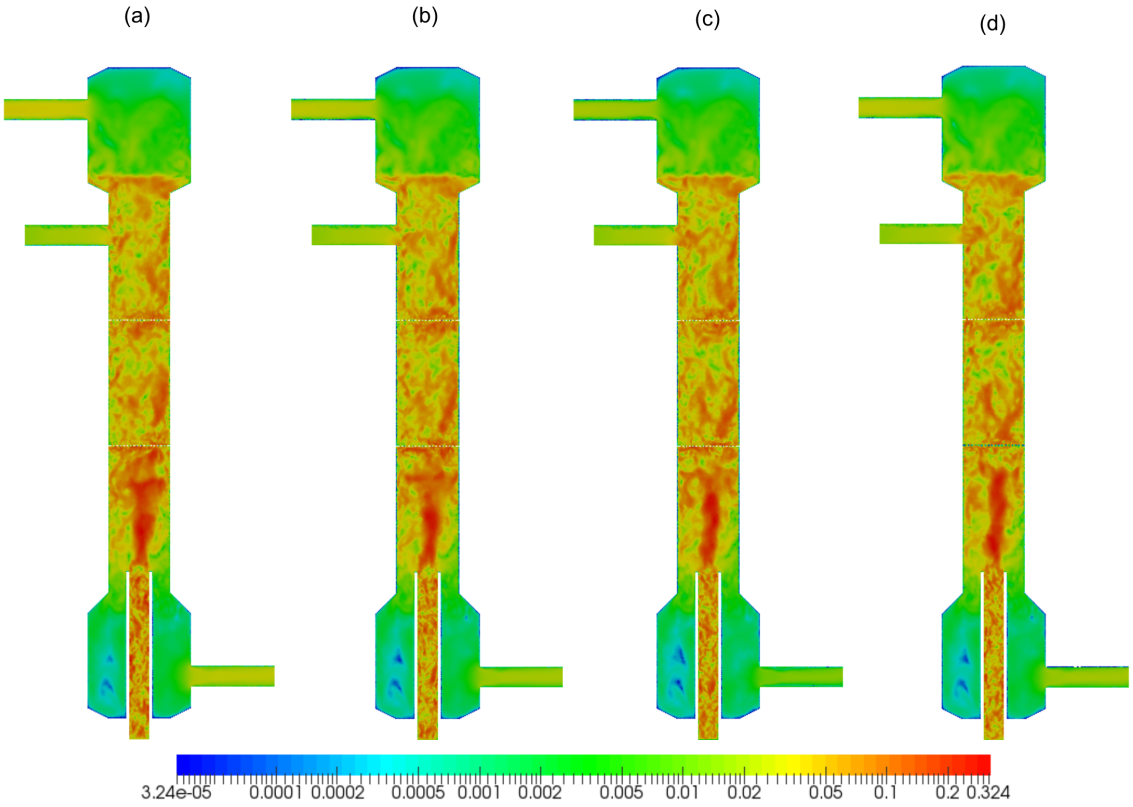

Figure 4.1: Magnitude of the instantaneous velocity field at (a) $\frac{1}{2}\pi$, (b) π, (c) $\frac{3}{2}\pi$ and (d) 2π. Velocities in ms^{-1}.

Profiles of the magnitude of the instantaneous velocity fields are presented in Fig. 4.1. Shown here are two-dimensional slices across the y-normal plane ($x = 0$ m) at the end of the simulation at the four chosen characteristic points in the sinusoidal pulse cycle, the colour plot is presented on a logarithmic scale. From Fig. 4.1 it can seen that the LES was successful in capturing certain time-dependent features of the velocity field at various length scales throughout the flow domain. Notable characteristics in the flow include the large scale jet emerging from the organic

phase inlet, the turbulent features in the organic inlet pipe and in those emerging before and after each sieve plate. In each decanter zone, a sharp reduction in the flow velocity can be seen with development of the flow in the boundary regions. The flow entering the column from the aqueous phase inlet is mostly laminar/transitional in nature, with no sharp gradients in the velocity. The turbulent features observed in the organic inlet are a consequence of the multiphase interface interactions between the two fluids in that region, discussed further in Section 4.2.5.2.

One criterion of the mesh suitability was to check the $y+$ (dimensionless wall distance) values to ensure an appropriate mesh density in the near-plate region to capture the turbulence generated. Ideally, for a LES a $y+ < 1$ should be achieved meaning turbulence is resolved down to the viscous sublayer. In some areas it is acceptable to exceed this value up to $y+ = 12$, where the linear viscous sublayer and log law region relationships intercept, understanding some accuracy maybe sacrificed.

Examination of the $y+$ values on the surface of each plate and column walls, seen in Fig. 4.2 and Fig. 4.3 respectively, reveals the density of the mesh to be, on balance, appropriate to resolve wall effects of turbulence in areas of particular interest. The $y+$ values around the plate surfaces show the flow behaviour captured in this area to be within the viscous sublayer with the majority of the flow with $y+ \leqslant 1$ with only some small areas reaching values $y+ \leqslant 10$. As for the column walls, where resolving the turbulent wall effects is less consequential to the study, $y+ \leqslant 10$ is observed across the vast majority of the surfaces with only a very small regions exceeding this value further.

In addition to examining the mesh resolution based on $y+$, the quality and accuracy of the LES was assessed using the resolution of the turbulence within the system. This was based on how much of the turbulence kinetic energy was explicitly resolved, from the velocity fluctuations, and what contributions were made from the SGS model. Fig. 4.4 shows a colour plot of the cell values of the turbulence resolution calculated using Eq. (4.6). The LES was found to resolve turbulence throughout the domain, with some individual cells under-resolved in the bulk flow region. However, a volumetric average showed only 2.6% of the turbulence energy spectrum is represented by the SGS model in this system, with the remaining resolved explicitly from the filtered LES, well above the recommended 80% resolution criteria (Pope, 2000, 2004). It was observed that close to the column wall boundaries and near the aqueous phase inlet k_r was likely overestimated. Large k_r contributions in the wall region are a consequence of the model which does not correctly consider scaling towards the wall; i.e. k_t should tend to zero at the wall. This was less of an issue in the plate region where the velocities, and therefore k_r, was explicitly resolved to the surface due to a high local mesh density. With regards to the aqueous phase inlet, the flow in this region

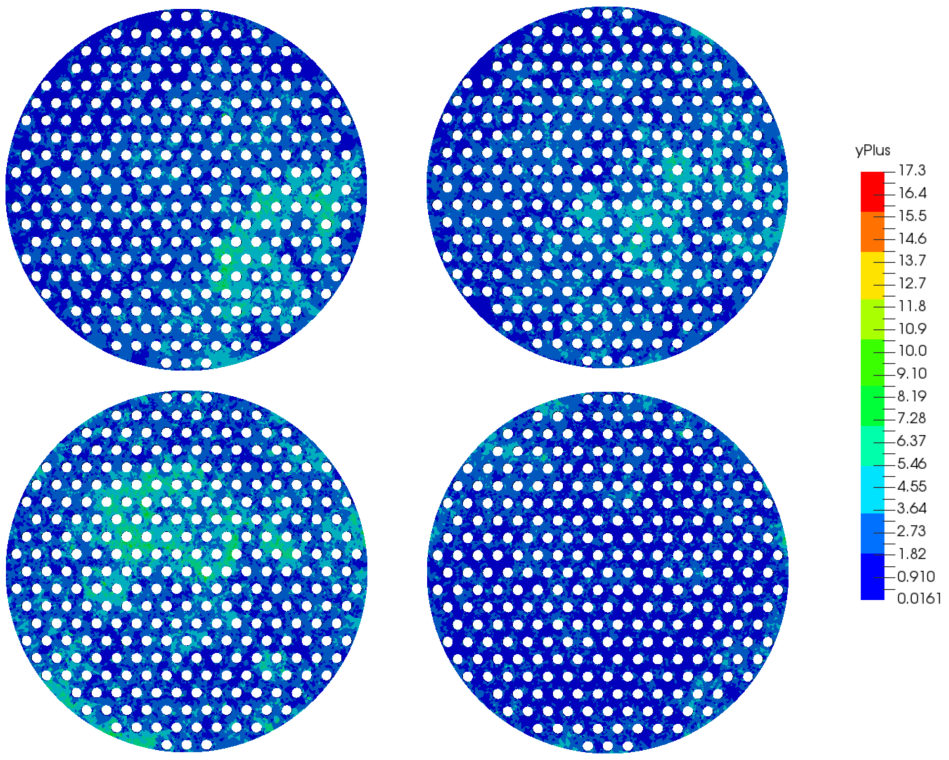

Figure 4.2: $y+$ values across (a) topside of bottom plate, (b) topside of top plate, (c) underside of bottom plate, and (d) underside of top plate.

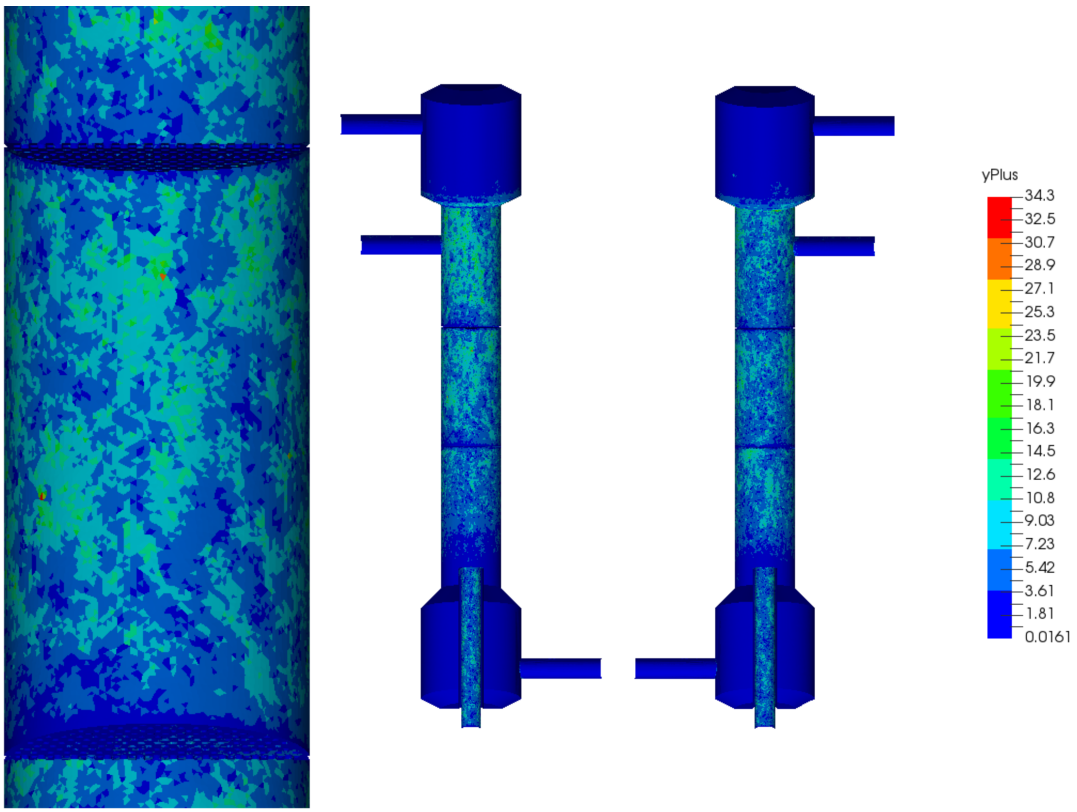

Figure 4.3: $y+$ values across the column walls with enhanced view in high velocity regions.

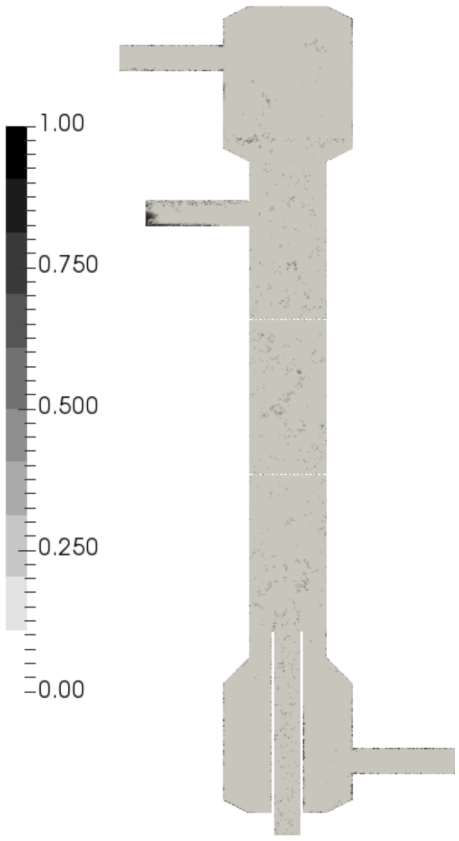

Figure 4.4: Plot of the LES turbulence resolution at $\frac{1}{2}\pi$.

is laminar/transitional due to low inlet velocity boundary condition. Consequently, k_r is likely to be over-contributing in this area also implying that the sub grid model employed may be less applicable at low Reynolds numbers. This could be avoided by increasing the grid resolution in these areas, however, it is of little consequence to the accuracy of the solution in the areas of interest.

4.2.5.2 Representation of the Multiphase System

The time-dependent volume fraction of each fluid was tracked throughout the flow domain using the VOF method, a snap-shot of which has been provided in Fig. 4.5 at π. At the organic phase inlet the boundary condition was set to feed pure organic liquid ($\alpha = 0$). Here, the organic phase quickly coalesces into droplets through entrained aqueous liquid in the feed pipe, likely by way of surface tension and local turbulence effects. A small amount of organic liquid is also seen to entrain in the aqueous phase inlet pipe which reached an equilibrium amount after some time. This feature did not significantly influence development of the flow in the incoming aqueous phase feed.

The primary interface, between the aqueous and organic phases at the top disengagement section, was seen to deviate and equilibrate +40 mm from its initial position. During typical operation, the level of this interface is managed to avoid carry-over during unstable operation. With severe flooding it is reported that hold-up tends to continuously deviate from equilibrium and the disengagement interface rises until carry-over eventually occurs (Mcallister *et al.*, 1967).

The total hold-up of the system, which includes fluid in both the decanter regions, was found to equilibrate at 30.6 vol%, thus indicating stable (non-flooding) behaviour. Droplets were observed to form throughout the domain with little organic phase hold-up behind/under each plate, indicative of dispersion regime operation predicted by empirical correlations outlined in Section 4.2.1. The stage-wise equilibrium hold-up, from plate to plate at $z = 0.702 - 1$ m, was found to be low at 5.1 vol% despite running the column at a solvent-flow-ratio of 1. Industrial columns have run to hold-up values of 30 vol% before phase inversion occurs (Logsdail & Slater, 1991). The sinusoidal pulse caused the stage-wise hold-up to oscillate but by a small amount of $\approx \pm 0.1\%$. The extent of the stage-wise hold-up is important as it primarily dictates the extent of mass-transfer in the system, along with the hold-up distribution and interfacial surface area contact with the aqueous phase via the droplet-size distribution. Older laboratory experiments describe PSEC's running upto solvent-flow-ratios of 7 in order to achieve higher solvent loading (Lade *et al.*, 2013). Solvent loading limitations highlight an obvious area for improvement in traditional PSEC designs and should be the focus of further research and development regarding process intensification of these units.

In regards to the numerical description and motion of the dispersed phase, a distinguishable level of numerical diffusion of α was observed in the bulk flow region despite the use of suggested numerical compression schemes and high mesh resolution. This is a consequence of the VOF method. Nevertheless, the general motion of droplet swarms between the plates were distinguishable in the bulk continuous phase flow and mechanisms of droplet formation can be seen above and

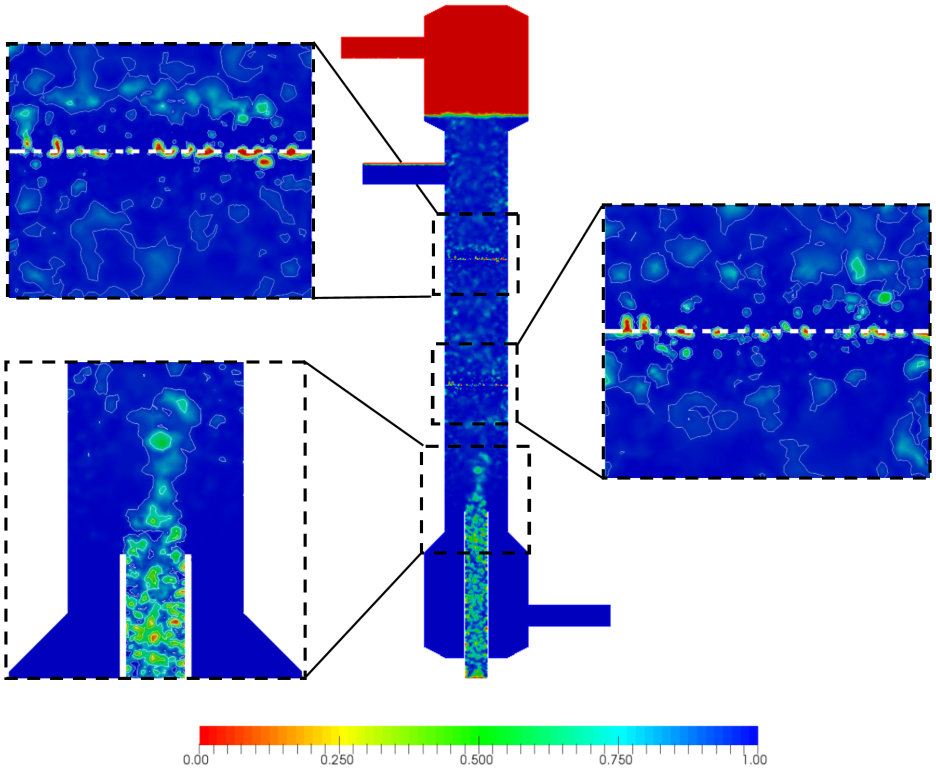

Figure 4.5: Plot of the instantaneous volume fraction field, α, at π. Contour lines have been plotted for reference at α values of 0.25, 0.5, 0.75 and 0.95.

across the plates. As for the near plate regions, droplets were observed to percolate through the plates continuously, detaching from the plate once enough fluid coalesced near a plate-hole to break surface tension and drive flow across. The VOF model used does not account for contact angle which may affect the wetting behaviour observed here. Further investigations into the extent of the applicability of VOF to model a verity of PSEC operational conditions is explored within Chapter 6.

4.2.5.3 Evaluation of Hydrodynamic Predictions

Hydrodynamic behaviour was evaluated primarily from observation and predictions of the system's ensemble-averaged flow characteristics in terms of values of velocity, pressure, mixing index number, turbulence kinetic energy and turbulence kinetic energy dissipation rate. In doing so, persistent features of the flow can be evaluated.

Fig. 4.6 was generated by taking discrete values of the averaged velocity field across the column (x-axis at $y = 0$) at heights corresponding to the centre of the bottom plate ($z = 0.701$ m), the centre of the middle compartment ($z = 0.850$ m), and the centre of the top plate ($z = 1.001$ m) at each time considered. Continuous plots of the mean velocity components can be seen for predictions taken across the centre of the middle compartment. Discontinuous predictions across the plates are a result of the geometry, in that each curve is a prediction across a single hole with adjacent curves corresponding to adjacent holes. Due to the formation of large

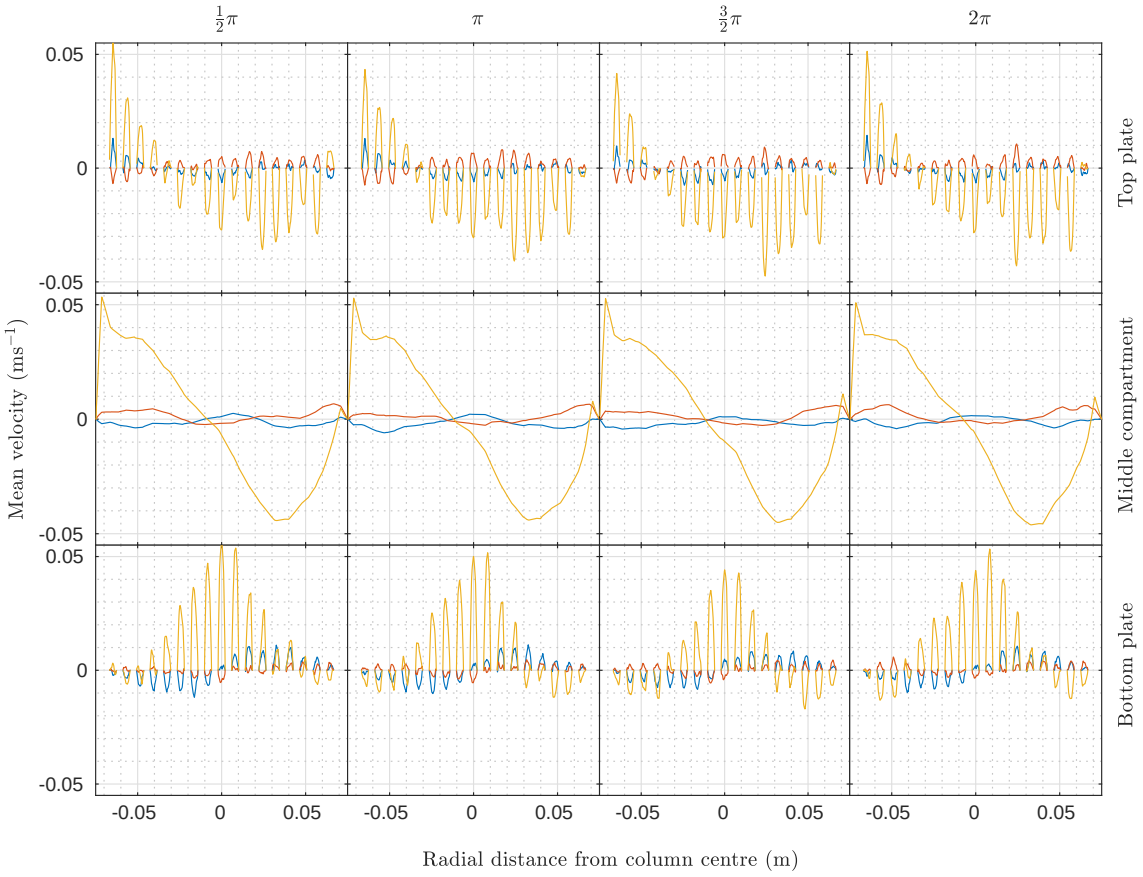

Figure 4.6: Ensemble averaged mean velocity components plotted along the x-axis ($y = 0$ m) at $z = 0.701$ m (centre bottom plate), $z = 0.850$ m (middle of the compartment), $z = 1.001$ m (centre of top plate) at $\frac{1}{2}\pi$, π, $\frac{3}{2}\pi$ and 2π; $\langle U_x \rangle$ (—), $\langle U_y \rangle$ (—), $\langle U_z \rangle$ (—).

rotational structures between the plates, driven by gravitational effects, most of the momentum in the system is expressed largely in the z-direction with small rotational elements in the x and y directions. The flow in the centre of the compartment is seen to remain mostly invariant with regards to time with only small deviations in the flow structure. Conversely, the flow across each plate shows an observable evolution across the pulse cycle. At the maximum pulse amplitude (at $1/2\pi$) momentum in the positive (upward) z-direction is at its greatest and negative z-direction momentum is small, with the opposite observed at the minimum amplitude ($3/2\pi$). One might expect the flow to be comparable when the pulse cycle is at its median amplitude states, at π and 2π. However, a slight preference in the positive z-direction is observed at 2π compared with that at π. Nevertheless, the variations observed across the plate, with respect to time, are relatively small despite the fact that the pulse velocity is comparable to the mean feed velocity.

With respect to the spatial distribution of momentum across the bottom plate, a persistent positive peak in the z-direction is observed in the flow with small negative peaks towards the edge of the plate (where $x > \pm 0.05$ m). This is indicative of the large pulsing jet from the organic phase inlet impinging on the bottom plate. At

this point, the organic phase is distributed across the plate and the surrounding continuous phase flow (under the plate) separates into two large vortices either side of the jet. This also indicates that during this mode of operation (dispersed regime) there is an uneven transfer of fluids across the plate, with the continuous phase more likely transferring across, in the downward direction, at the outer edges of the plate.

The continuous phase flow in the centre of the middle compartment was observed to be dominated by a large rotational structure, in the y-normal plane, encompassing the entire volume of the compartment. This is represented in Fig. 4.6 by the distribution of the mean velocity across the column, with a clear upward momentum for $x < 0$ m and downward momentum for $x > 0$ m. Without quantitative historical (Lagrangian) tracking of the droplets unavailable in the VOF model is it unclear how such structures affect the path and residence time distribution of the droplets in the column. However, the droplets were observed to more likely transit across the compartment where $x < 0$ m. Such behaviour will hinder the extraction efficiency during mass transfer operations due to the creation of artificial concentrations of the solvent droplets on one side of the column. Moreover, the continuous phase fluid is likely to stagnate within the rotational structure increasing residence time which would effect the equilibrium concentration of the solute within the column.

The rotational structure observed in the middle compartment clearly influences the flow across the top plate, resulting in a similar distribution of the z-direction momentum. This is likely a consequence of the resulting path of the droplets before reaching the plate. Assuming this behaviour persists in a PSEC with more stages, this could have serious implications for the efficiency of the system in terms of solute-solvent contact, discussed previously, and flow resistance across the plate. Systems which exhibit flow resistance across the plates could be more sensitive to flooding having a lower maximum throughput capacity, in which case it would be advisable to introduce downcomers and other plate features in order to control the distribution of the dispersed phase and improve transfer paths of each fluid across the plates. The hydrodyamics of such design features in PSECs have been briefly explored by Yadav & Patwardhan (2009).

The ensemble-averaged pressure ($P_{static} - \rho gh$), turbulence kinetic energy , turbulence kinetic energy dissipation rate, and mixing index were calculated along the z-axis at x= 0 m, x= -0.05 m, and x= 0.05 m, all at y= 0 m with the results presented in Fig. 4.7, Fig. 4.8, and Fig. 4.9 respectively. In each case, plots of the flow properties highlight notable characteristic behaviour at the plates and proportionally little variation with respect to time, with the exception being the turbulence kinetic energy dissipation rate at the plates.

Fig. 4.7 shows that the organic phase enters the column at high pressure, with respect the rest of the column. The velocity of the fluid and buoyancy effects in

the confined pipe region lead to a relatively high velocity and, therefore, a high dynamic pressure contribution which is quickly damped on exit of the inlet pipe (at $z = 0.4$ m). Even after averaging, there is still a significant level of spatial fluctuation in the pressure gradient within the organic inlet pipe, this feature also being observable in plots of the turbulence properties. This suggests that the flow in this region is particularly dynamic and turbulent despite having an assigned low Reynolds number velocity condition at the boundary. Variations in the local density from droplet formation and buoyancy effects are likely driving the creation of turbulence in this region. This observation is of particular importance for those implementing URANS models wherein the turbulent conditions must be assigned at the boundary. One may assume rather laminar conditions, but the observations here suggest this is clearly not the case.

Between the organic phase inlet and the first plate (0.4 m $< z <$ 0.7 m) the pressure quickly normalises, as mentioned before, to a stable operating dynamic pressure $\approx$ 120 Pa. This pressure is roughly maintained throughout the column, although large pressure spikes observed across each plate. More specifically, there is a pressure spike, drop, and recovery across each plate. This is a consequence of *Bernoulli's principle* and conservation of mass across the sieve-plate, which is expected behaviour in a choked flow (Yadav & Patwardhan, 2009). Comparing pressure results between the centre of the column, Fig. 4.7, and close to the walls, Fig. 4.8 and Fig. 4.9,the pressure between the plates is comparable (little variation with radial distance), although the pressure spike across the sieve-plates is greater towards the walls than in the centre of the column. Similar patterns are also apparent in the turbulence kinetic energy dissipation rate. The uneven distribution of pressure and turbulence kinetic energy dissipation rate across each plate is likely a consequence of the uneven velocity distribution, seen in Fig. 4.6.

The turbulence kinetic energy of the system at $x = 0$ m is seen to increase towards the bottom plate then quickly drop off as the pulsing jet of organic fluid passes through the plate. The organic phase below the bottom plate accelerates, as a result of buoyancy, with this and impingement on the plate resulting in a gain in turbulence kinetic energy. This is then quickly dampened at the first plate suggesting that the overall distribution of the organic fluid is inefficient with regards to desired mass transfer performance. Subsequently, the level of turbulence kinetic energy remains approximately constant throughout the rest of the column, and roughly constant with regards to radial distance, although with a slight increase and then drop and recovery through the top plate. The level of turbulence kinetic energy dissipation rate is also shown to be approximately equal throughout the bulk flow regions of the column with some notable spikes through the plates. Again, comparing Fig. 4.7 to Fig. 4.8 and Fig. 4.9 it is evident that more dissipation occurs towards the walls of the column than in the centre line.

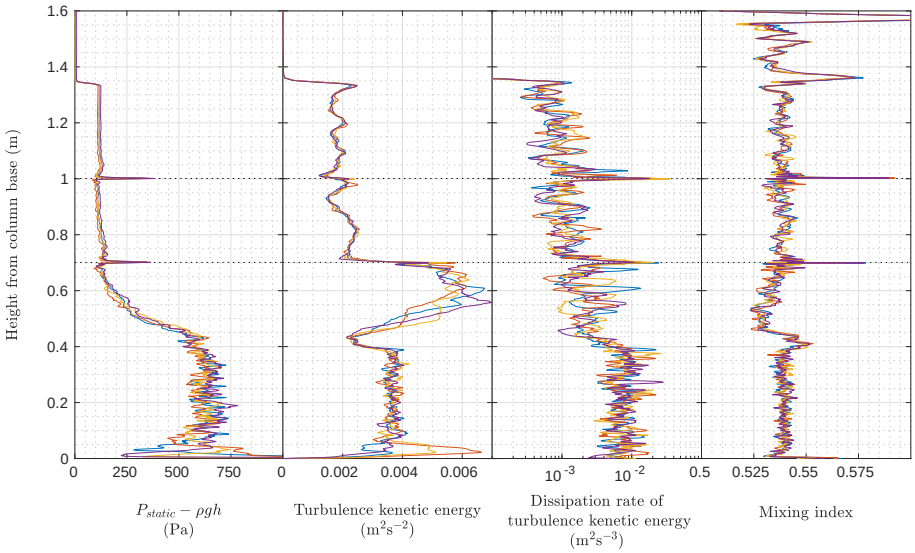

Figure 4.7: Field properties plotted along the height of the column at $x = 0$ m, $y = 0$ m; $\frac{1}{2}\pi$ (—), π (—), $\frac{3}{2}\pi$ (—), 2π (—).

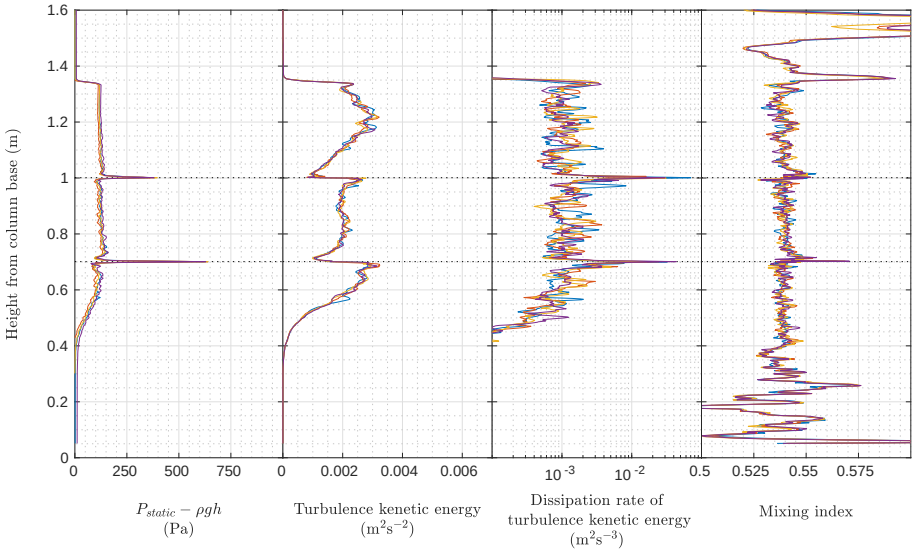

Figure 4.8: Field properties plotted along the height of the column at $x = -0.05$ m, $y = 0$ m; $\frac{1}{2}\pi$ (—), π (—), $\frac{3}{2}\pi$ (—), 2π (—).

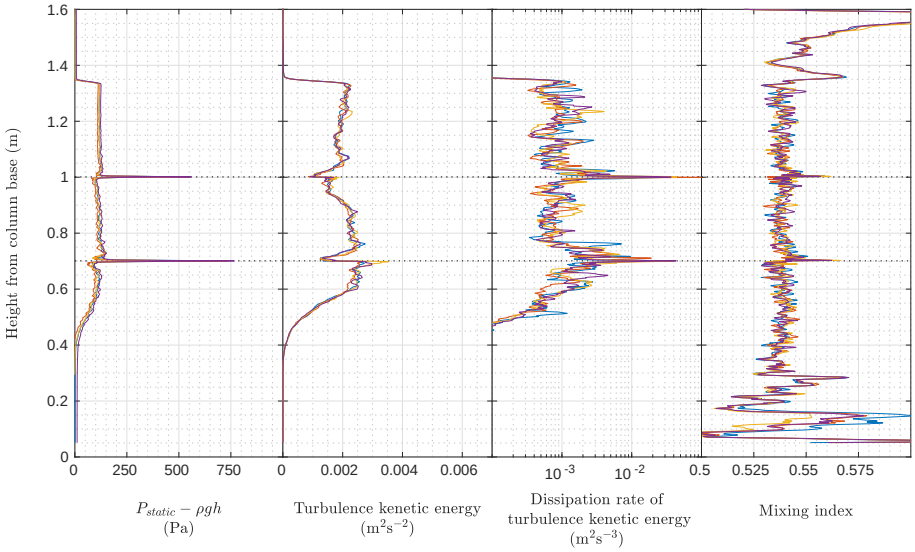

Figure 4.9: Field properties plotted along the height of the column at $x = 0.05$ m, $y = 0$ m; $\frac{1}{2}\pi$ (—), π (—), $\frac{3}{2}\pi$ (—), 2π (—).

The quality of dispersive mixing in the system was determined using the mixing index value which quantitatively assesses the types of flow inherent within the system. Fig. 4.7, Fig. 4.8 and Fig. 4.9 all indicate the system is principally characterised as a simple shear flow with all values of the index between $0.5 - 0.6$. An average value of 0.54 is consistent along the height of the working section of the column ($0.4 \text{ m} < z < 1.3 \text{ m}$) with some slight improvement across the plates. Macroscopically, this means that the system is poor at producing the types of flow that are thought to contribute to the breakup of droplets as discussed in Section 4.2.4. This also suggests that in order to improve the performance of these columns more consideration should be given to the plate design and manipulation of the resulting flow structure to promote elongational flow.

Additionally, the turbulence characteristics were further assessed in relation to their impact on mixing. Namely, in terms of the comparative contributions of the turbulent to viscous stresses, the turbulence length scales, turbulence kinetic energy and budget terms in the production and dissipation of turbulence kinetic energy.

Classical discussion of PSECs, in particular in Yadav & Patwardhan (2008), mention 'shear forces' as directly responsible for the determination of droplet size/hold-up and, by extension, the column operational regime. Moreover, shear forces are said to result from the sieve-plate geometry and spacing. It is unclear whether the authors are describing viscous, turbulent or the total shear in the system, stresses, often used as a synonym to describe shear indirectly, or the individual shear components of the stress tensor or some other mathematical description relating to shear. In this study, the magnitude of the viscous and turbulent stress tensors were calculated and compared, the aim being to understand mechanistically how PSECs accomplish mixing. Fig. 4.10 compares the turbulent stresses, arising from fluctuations in fluid momentum, and viscous stresses, resulting from a fluids resistance to physical deformation.

Firstly, the turbulent stresses within the system are three orders of magnitude greater than the viscous stresses. Consequently, these results illustrate that turbulence has the greatest influence on PSEC operation. Secondly, although the viscous stresses are influenced by the sieve-plates, increasing by an order of magnitude in the near-plate region, the dominant turbulent stresses show no direct relationship with the plate (i.e. no increase near the plate). The turbulent stresses do show a slight increase and drop before and after the sieve-plate however, a result of the turbulence kinetic energy changes in these regions observed in Fig. 4.7, Fig. 4.8 and Fig. 4.9. Thirdly, the size of the smallest eddies were calculated to be 1.68×10^{-4} m, an order of magnitude smaller than the droplets observed evolving from the sieve-plate, as can be seen in Fig. 4.5. The eddie size was calculated using Eq. (4.14) with an estimated a dissipation rate of 0.0013 m^2s^{-3} taken from averaging dissipation rates given in Fig. 4.7 between both plates

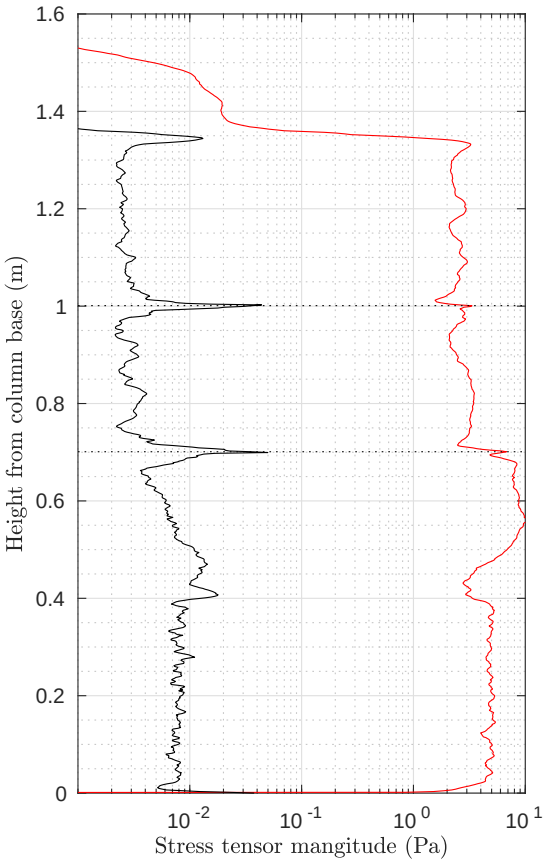

Figure 4.10: Magnitudes of the viscous (—) and turbulent stress (—) plotted along the height of the column at 2π.

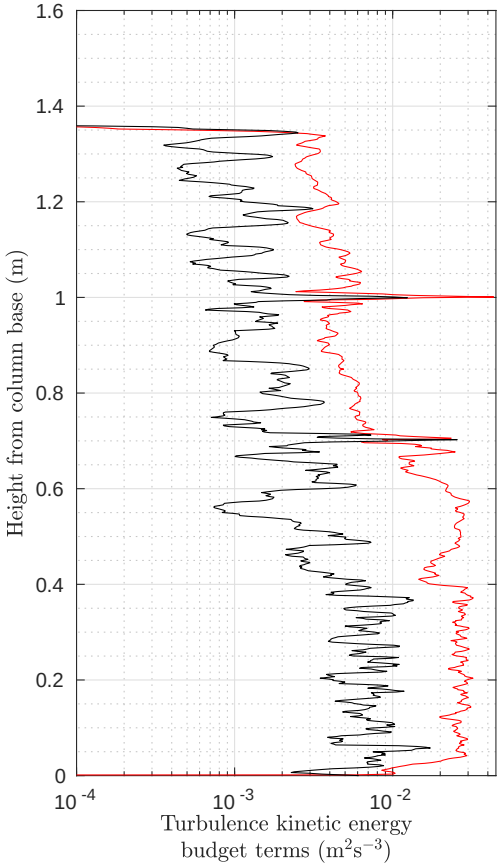

Figure 4.11: Disspation rate (—) and total production (—) of turbulence kinetic energy plotted along the height of the column at 2π.

(0.702 m $< z <$ 1.002 m). Eddies within the plate sieve-holes, where the dissipation rate spikes, will be even smaller. As mentioned in Section 4.2.4, the Kolmogorov length scale can be used to determine if mixing occurs due to turbulence or viscous influences (Vankova *et al.*, 2007). Here, the length scale indicates that mixing is performed under a turbulent inertial regime further justifying the hypothesis that the turbulent stresses are predominately responsible for mixing in PSECs.

In contrast to the previous points, a number of studies have shown sieve-plate geometry and spacing to directly influence PSEC operating behaviour (Yadav & Patwardhan, 2008). Rather than this being explained through viscous (shear) effects in the near-plate region, the evidence presented here suggests that sieve-plate design may instead have a direct relationship with the production, dissipation and resulting kinetic energy within the system, and therefore with the operation of PSECs. Fig. 4.11 compares the total production, see Eq. (4.9), and dissipation of turbulence kinetic energy along the height of the column. In both plots there are clear increases through the sieve-plates indicating that the plates do influence the turbulence in these regions. However, both terms are relatively balanced which would explain why no significant increase was observed in the

turbulent stresses near the plates. Moreover, the difference between the production and dissipation terms in the bulk flow drops after the first plate resulting in less turbulence kinetic energy throughout the rest of the system. Consequently, the turbulence potential available for mixing thereafter is dampened due to the design of the first plate. Eq. (4.14) describes the minimum size of the turbulence length scale, and therefore mixing performance, to be inversely proportional to the dissipation rate. Therefore, improvement to sieve-plates capacity to produce turbulence kinetic energy would, in-turn, facilitate increases in the dissipation rate in the bulk flow and likely improve mixing throughout the system.

4.2.6 Conclusions

Presented here are the conclusions from a numerical investigation concerning the hydrodynamic characteristics of a PSEC representative of those found in nuclear reprocessing industries. Evidence was presented to show the column operating in a pseudo steady-state dispersed regime, via available design correlations, and analysis and assessment of the predictions from the LES coupled VOF CFD model are as follows:

1. During dispersed regime operation the macroscopic fluid flow properties were found to show time-invariance despite a prescribed sinusoidal pulsing condition at the organic phase inlet boundary.
2. For dispersed regime PSECs, turbulence was found to be the biggest contributing hydrodynamic factor to dispersive mixing determined through direct comparison of viscous and turbulent stresses.
3. The PSEC sieve-plate design used in this study, based on traditional designs, was found to be ineffective for the distribution and facilitation of turbulence for mixing which directly influences the size and stability of dispersed phase immiscible droplets.
4. Analysis of the decomposed turbulence kinetic energy budget suggests improvements to the plate design could be made to preserve the dissipation rate throughout the column, via greater turbulence production at the plates, resulting in smaller droplets in the bulk flow region improving mass transfer.
5. Assessment of the mixing index criteria also highlights that classic square-edge round-hole sieve-plate designs are poor at generating the types of (elongational) flow that contribute to the breakup of droplets in turbulent flow, therefore reducing the efficiency of turbulent mixing.
6. The stage-wise organic phase hold-up for the PSEC design considered was found to be low, at 5.1 vol%, when operating at a solvent-flow-ratio of 1.
7. Although stable non-flooding operation was achieved in the simulation, the resulting flow structures showed observable restriction in the near-plate regions and non-homogeneous distribution of droplets between the plates.
8. The LES was successful in producing time-dependent information of the hydrodynamics to a high resolution capturing the majority of the turbulence energy spectrum.

This study highlights the importance of time-dependent three-dimensional flow modelling in understanding the intricacies of PSEC operation. Further studies are required to compare the presented results against previously explored Reynolds-averaged predictive approaches and two-fluid multiphase flow models. Quantified validation of the LES-based PSEC model against experimental data is also necessary, although at the present time there is a paucity of data that could be used in this regard.

4.3 Suitability of Unsteady Reynolds-Averaged Navier-Stokes Methods Against Large Eddy Simulation Data

4.3.1 Boundary/Initial Conditions and Initialisation for URANS Simulations

The boundary conditions for both URANS simulations are listed in Table 4.3 and Table 4.4 for the k-ε and SSG RSM runs respectively. In both cases, the boundary conditions for velocity (U), pressure (P_{local}) and volume fraction (α) were specified exactly as with the LES in order to provide a direct operational comparison. Furthermore, the fluidic properties of the two fluids were kept the same across all simulations, see Section 4.2.1 for details. For calculation of turbulence, each closure uses a specific system of equations, see Section 3.1.2.3, each requiring boundary and initial conditions which may also include additional wall modelling functions. The values for such quantities may have been more accurately obtained out of the former LES model described in Section 4.2 but common methods of approximating turbulence boundary conditions were taken in order to best replicate standard practice. Consequential deviations in the URANS predictions only serves to highlight the deficiencies in using turbulence closure modelling.

4.3.1.1 k-ε Closure

The simulation, when using the k-ε closure, was initialised in the same way as with the LES. Here, all boundary conditions were specified with the disengagement interface for the organic phase set at the appropriate height (1.3 m) via the initialised α internal field, as with the LES. With regards to the turbulence fields, turbulence kinetic energy (k) and turbulence dissipation rate (ε), values for boundary conditions were approximated using the commonly applied relationships:

$$I = 0.16(Re_{D_h})^{-1/8} \tag{4.15a}$$

$$k = \frac{3}{2}(U_{ave}I)^2 \tag{4.15b}$$

$$l = 0.07D_h \tag{4.15c}$$

$$\varepsilon = C_\mu^{3/4}\frac{k^{3/2}}{l} \tag{4.15d}$$

Here, the I is the turbulence intensity, U_{ave} being the mean flow velocity, l is the turbulence length scale based on the size restriction of turbulent eddies within pipe flow, 0.07 being an empirical scaling factor (Ansys, 2009). A list of values for each of these three quantities, used to calculate the k and ε values listed in Table 4.3, are

listed in Section 4.3.1.1. The U_{ave} value chosen for the pulsing light-phase inlet was based on the mean flow rate over a given cycle.

Table 4.2: List of turbulence parameters used to calculate k and ε.

	D_h (m)	Re_{D_h}	I	l (m)	U_{ave} (ms^{-2})
Heavy Phase Inlet	0.05	737	0.0700	3.5×10^{-3}	0.015
Light Phase Inlet	0.05	319	0.0778	3.5×10^{-3}	0.015

Table 4.3: Summary of boundary conditions used in RANS simulation with k-ε closure.

	α	P_{local} (Pa)	U (ms^{-1})	ε (m^2s^{-3})	k (m^2s^{-2})
Heavy Phase Inlet	Fixed value 1	Fixed gradient corrected for velocity boundary	Fixed value (0 0 0.015)	Fixed value 1.002×10^{-7}	Fixed value 1.658×10^{-6}
Light Phase Inlet	Fixed value 0	Fixed gradient corrected for velocity boundary	Time-varying sinesoidal $A = 0.0125$ $f = 1$ $U_{offset} = 0.015$	Fixed value 1.399×10^{-7}	Fixed value 2.042×10^{-6}
Heavy Phase Outlet	Outflow: Fixed gradient 0 Return flow: Fixed Value 1	0 Customised condition Eq. (4.2)	Outflow: Fixed normal gradient 0 Return flow: Calculated from flux	Outflow: Fixed gradient Return flow: Fixed value 1.002×10^{-7}	Outflow: Fixed gradient Return flow: Fixed value 1.658×10^{-6}
Light Phase Outlet	Outflow: Fixed gradient 0 Return flow: Fixed Value 0	0 Customised condition Eq. (4.2)	Outflow: Fixed normal gradient 0 Return flow: Calculated from flux	Outflow: Fixed gradient Return flow: Fixed value 1.399×10^{-7}	Outflow: Fixed gradient Return flow: Fixed value 2.042×10^{-6}
Wall	Fixed gradient 0	Fixed gradient 0	No slip	Low Re wall function	Low Re wall fucntion
Initialised Internal Field	Non-uniform value	Uniform value 0	Uniform value (0 0 0)	Uniform value 0	Uniform value 0

Wall functions impose conditions for turbulence properties which result in velocity profiles which adhere to *the law of the wall* proposed by von Karman (1930). For both k and ε, wall functions were used to constrain values on boundaries acting as walls, this would include the column wall and sieve-plates surfaces. Both functions work for low and high Reynolds number systems. In each case, the function implemented is dependent on the dimensionless wall cell centre location, y^+, and using the calculated laminar/turbulent (linear/log) law intercept value, y^+_{lam}, which approximates to 11.6 assuming $\kappa = 0.41$ and $E = 9.8$ for smooth walls. y^+ is evaluated using the following identities:

$$y^+ = \frac{y \times u_\tau}{\nu};\ u^+ = u/u_\tau;\ u_\tau = C_\mu^{1/4}\sqrt{k} \tag{4.16}$$

where y is wall-cell-centre the distance to the wall, u^+ is the dimensionless velocity attained from the wall parallel velocity u, and u_τ is the friction velocity, and k is the turbulence kinetic energy approximated from the turbulence model.

In the case of turbulence kinetic energy, the dimensionless cell face values, k^+, are first calculated:

when $y^+ > y^+_{lam}$ as

$$k^+ = \frac{C_\kappa}{\kappa} log(y^+) + B_\kappa \tag{4.17a}$$

or when $y^+ < y^+_{lam}$ as

$$k^+ = \frac{2400}{C^2_{\varepsilon 2}} C_f \tag{4.17b}$$

where

$$C_f = \frac{1}{(y^+ C)^2} + \frac{2y^+}{C^3} - \frac{1}{C^2} \tag{4.17c}$$

the value is then transformed using u_{tau} evaluated using Eq. (4.16)

$$k = k^+ u^2_\tau \tag{4.17d}$$

For turbulence kinetic energy dissipation rate, ε, the wall cell center value is the sum of the weighted face values. The weighting value, W, corresponds to the number of wall cell faces where the boundary condition is applied, k uses the corresponding cell-centre value:

when $y^+ > y^+_{lam}$ the cell-centre value is

$$\varepsilon = \frac{1}{W} \sum_{f=i}^{W} \frac{C^{3/4}_\mu k^{3/2}}{\kappa y_i} \tag{4.18a}$$

when $y^+ < y^+_{lam}$ the cell-centre value is

$$\varepsilon = \frac{1}{W} \sum_{f=i}^{W} \frac{2k\nu_i}{y^2_i} \tag{4.18b}$$

Here $C_\kappa = -0.416, B_\kappa = 8.366, C = 11$. More information on how wall functions are implimented within OpenFOAM can be accessed directly from the source code OpenFOAM (2011).

4.3.1.2 SSG Reynolds Stress Model Closure

The Initialisation process for the SSG RSM closure originally followed that of the $k - \varepsilon$ model, in that the simulation was to be 'started from scratch' using the same conditions, or those derived from, the initial conditions of the $k - \varepsilon$ closure.

A number of unsuccessful starts that the SSG RSM closure was too unstable to initialise. Subsequently, a number of common practices were utilised to reduce the computational burden and facilitate convergence. These include:

- The use of first-order divergence and gradient schemes.
- Initialisation of RSM SSG closure from $k-\varepsilon$ closure second order-solution.
- Light phase inlet boundary turbulence properties approximated from plane-averaged downstream solutions from $k-\varepsilon$.

The boundary conditions for the Reynolds stress tensor terms were approximated using the solution to the $k-\varepsilon$ closure and the Boussinesq eddy viscosity assumption:

$$\langle U_i' U_j' \rangle = \frac{2}{3} k \delta_{ij} - \nu_t \left(\frac{\partial U_i}{\partial x_j} + \frac{\partial U_j}{\partial x_i} - \frac{2}{3} \frac{\partial U_k}{\partial x_k} \delta_{ij} \right) \tag{4.19a}$$

where for incompressible flows:

$$\frac{\partial U_k}{\partial x_k} = 0 \tag{4.19b}$$

Table 4.4: Summary of boundary conditions used in RANS simulation with SSG RSM closure.

	α	P_{local} (Pa)	U (ms^{-1})	ε (m^2s^{-3})	R_{ij} (m^2s^{-2})
Heavy Phase Inlet	Fixed value 1	Fixed gradient corrected for velocity boundary	Fixed value (0 0 0.015)	Fixed value 1.002×10^{-7}	Fixed non-uniform value Calcualted from Eq. (4.19a) $k = 4.5 \times 10^{-4} m^2 s^{-2}$
Light Phase Inlet	Fixed value 0	Fixed gradient corrected for velocity boundary	Time-varying sinesoidal $A = 0.0125$ $f = 1$ $U_{offset} = 0.015$	Fixed value 2.632×10^{-2}	Fixed non-uniform value Calcualted from Eq. (4.19a) $k = 4.5 \times 10^{-4} m^2 s^{-2}$
Heavy Phase Outlet	Outflow: Fixed gradient 0 Return flow: Fixed Value 1	0 Customised condition Eq. (4.2)	Outflow: Fixed normal gradient 0 Return flow: Calculated from flux	Outflow: Fixed gradient Return flow: Fixed value 5.322×10^{-6}	Outflow: Fixed gradient Return flow: Fixed value (0 0 0 0 0 0)
Light Phase Outlet	Outflow: Fixed gradient 0 Return flow: Fixed Value 0	0 Customised condition Eq. (4.2)	Outflow: Fixed normal gradient 0 Return flow: Calculated from flux	Outflow: Fixed gradient Return flow: Fixed value 4.965×10^{-6}	Outflow: Fixed gradient Return flow: Fixed value (0 0 0 0 0 0)
Wall	Fixed gradient 0	Fixed gradient 0	No slip	Low Re wall function	Fixed value (0 0 0 0 0 0)
Initialised Internal Field	Non-uniform value	Uniform value 0	Uniform value (0 0 0)	Uniform value 0	Non-uniorm field Calucated from Eq. (4.19a)

4.3.2 Solution Method

4.3.2.1 k-ε Closure

A transient Euler time-derivative scheme was used along with a multi-dimensional cell limited least-squares gradient scheme for all equations solved, as for the LES.

With regards to divergence terms, the velocity transport equations were solved using a blended second-order (linear) and first-order (upwind) vector limited scheme. A single limiter, towards upwind, is calculated for all the vector components based

on the direction of the most rapidly changing gradient. Similarly, a limited van leer scheme is used for the volume fraction equations, as well as limited linear schemes for ε and k.

Laplacian terms are solved with a linear interpolation scheme. Surface normal gradient terms are solved using limited corrected term, a limiter coefficient of 0.333 is used to improve stability in areas of mesh non-orthogonality.

Convergence for the transient case was reached when the final residual fell below 1×10^{-6} for the velocity and pressure equations, and 1×10^{-7} for the k and ϵ transport equations at each time step. The transient PIMPLE algorithm was used, see Section 3.3.2, solving within 2 outer-loop iterations at each time step. Within each outer-loop, 4 inner-loop iterations are preformed. Here, the pressure equation is solved and repeated an additional 2 times via 'corrector loops'. Repetition of the pressure equation reduces the influence of non-orthogonal mesh areas. No under-relaxation is used in order to maintaining transient accuracy.

Using the semi-implicit MULES (Multi-dimensional limiter with explicit solution) algorithm for discretisation of the volume fraction field, a fixed maximum Courant number was applied using an adjustable time-stepping option. The average Courant number oscillated between 0.0015 and 0.002. An additional four inner-loop sub-cycling steps, through MULES, was implemented to improve stability and accuracy of the solution of the volume fraction transport term. Final solutions were taken when time step convergence was observed, and the volume fractions and outlet velocities showed cyclic steady-state behaviour.

The simulation was parallelised and ran across 720 processors ($\sim$7,640 cells per processor) using the University of Leeds' ARC2 HPC facilities (University of Leeds, 2019). The time step was in the order of 7.5×10^{-5} s once fully developed cyclic steady-state flow had been achieved. On average, a wall-clock time of 7.71 hrs produced 1 s of simulated transient flow.

4.3.2.2 SSG Reynolds Stress Model Closure

A transient Euler time-derivative scheme was used along with a multi-dimensional cell limited least-squares gradient scheme for all equations solved except for the epsilon and Reynolds stress tensor equations. In which case, the face limited linear scheme is used to improve stability.

With regards to divergence terms, the velocity transport equations were solved using a blended second-order (linear) and first-order (upwind) limited scheme. Limiters, towards upwind, are calculated for all the vector components individually in areas of rapidly change gradient. Similarly, a limited van leer scheme is used for the volume fraction equations, as well as upwind schemes for ε and Reynolds stress tensor due issues with stability.

Laplacian terms are solved with a point linear interpolation scheme. Surface

normal gradient terms are solved using a limited corrected term, a limiter coefficient of 0.333 is used to improve stability in areas of mesh non-orthogonality.

Convergence for the transient case was reached when the final residual fell below 1×10^{-6} for the velocity and pressure equations, 1×10^{-7} for the ϵ equation and 1×10^{-9} for Reynolds stress tensor equations at each time step. The transient PIMPLE algorithm was used, see Section 3.3.2, solving within 2 outer-loop iterations at each time step. Within each outer-loop, 4 inner-loop iterations are preformed. Here, the pressure equation is solved and repeated an additional 2 times via 'corrector loops'. Repetition of the pressure equation reduces the influence of non-orthogonal mesh areas. No under-relaxation is used in order to maintaining transient accuracy.

Using the semi-implicit MULES (Multi-dimensional limiter with explicit solution) algorithm for discretisation of the volume fraction field, a fixed maximum Courant number was applied using an adjustable time-stepping option. The average Courant number oscillated between 7×10^{-4} and 8×10^{-4}. An additional four inner-loop sub-cycling steps, through MULES, was implemented to improve stability and accuracy of the solution of the volume fraction transport term. Final solutions were taken when time step convergence was observed, and the volume fractions and outlet velocities showed cyclic steady-state behaviour.

The simulation was parallelised and ran across 720 processors ($\sim$7,640 cells per processor) using the University of Leeds' ARC2 HPC facilities (University of Leeds, 2019). The time step was in the order of 3×10^{-5} s once fully developed cyclic stead-state flow had been achieved. On average, a wall-clock time of 17.88 hrs produced 1 s of simulated transient flow.

4.3.3 Results and Discussion

This section provides the results and discussion of a comparison of the two URANS turbulence model closures against the LES solution for accuracy and suitability. The instantaneous velocity and volume fraction fields are compared qualitatively, and field properties of velocity pressure, turbulence kinetic energy, dissipation rate and mixing index are compared quantitatively.

4.3.3.1 Comparison of Transient Flow Fields

The instantaneous velocity fields for all three cases are given in Fig. 4.12. The velocity magnitude is compared in conjunction with the z-directional component of the velocity field. All results have been discretised using colour contour plots of 20 levels. Initially, it is clear that the fidelity of the LES far exceeds that of either URANS solution. It appears that both URANS methods were able to provide an order-of-magnitude prediction of the velocity magnitude fields in the areas of interest. However, on inspection of the z-component velocity field, there are some major contradictions in the flow compared to the LES. Moreover, there are disagreements between the flow structures across all three solutions.

At the dispersed phase inlet to the bulk flow, the LES shows the flow rising directly to the bottom plate. The k-ε shows clear stratification in the flow between the rising inlet flow and the surrounding continuous phase bulk fluid. The SSG RSM predicts heavy rotation in this area also. Both solutions provide an approximate representation of the flow within the centre compartment. However, the direction of counter-current flow is reversed in both URANS solutions compared to the LES. These observations are distinct when comparing the z-component velocity contours. The velocity magnitude field of the LES shows the pure continuous phase fluid entering the bulk flow in the compartment by arcing across the column producing a persistent rotational flow. Neither URANS methods capture this feature.

In general, the SSG RSM was able to capture greater velocity gradients and provide a higher resolution in the flow, particularly with the z-competent velocity fields, more inline with LES. The SSG RSM could also capture certain dead-zones (top decanter), and the velocity profile in both outlet pipes. These findings could prove consequential when considering CFD for engineering design applications such as placement of control instrumentation.

The instantaneous volume fraction field for all three cases are presented in Fig. 4.13. Snap shots of the dispersed phase inlet, bottom and top sieve-plate are shown. The amount of dispersion inside the dispersed phase inlet is comparable between the LES and SSG RSM solution. However, the behaviour of the dispersion before the bottom plate is more comparable between the LES and k-ε predictions. At the bottom plate, the LES and SSG RSM solutions show little accumulation. conversely, the k-ε shows accumulation of the dispersed phase in the

region where the flow impinges on the plate. The behaviour here clearly influenced by the velocity field, see Fig. 4.12.

Between the plates, the LES shows a much greater dispersion and hold-up than either URANS method. The predicted hold-up in this region for the LES, URANS k-ε and SSG RSM closures are 5.1 %, 4.21 %, and 3.57 % respectively. At the top plate, the LES again shows little accumulation whereas both URANS solutions show some accumulation and regions of mixer-settler behaviour are observed in the SSG RSM model.The global hold-up for the LES, URANS k-ε and SSG RSM closures are 30.6 %, 31.0 %, and 31.3 % respectively.

In summary, the behaviour between all three solutions are distinct and contradictory. This is largely in part to the differences in the solutions of the velocity fields. The URANS methods show less dispersion in the field overall. A more diffuse/less resolved velocity solution would result in underestimation of mixing and advection of the volume fraction field. Also, despite a lower prediction of stage-wise hold-up, the global hold-up of was over-predicted by URANS.

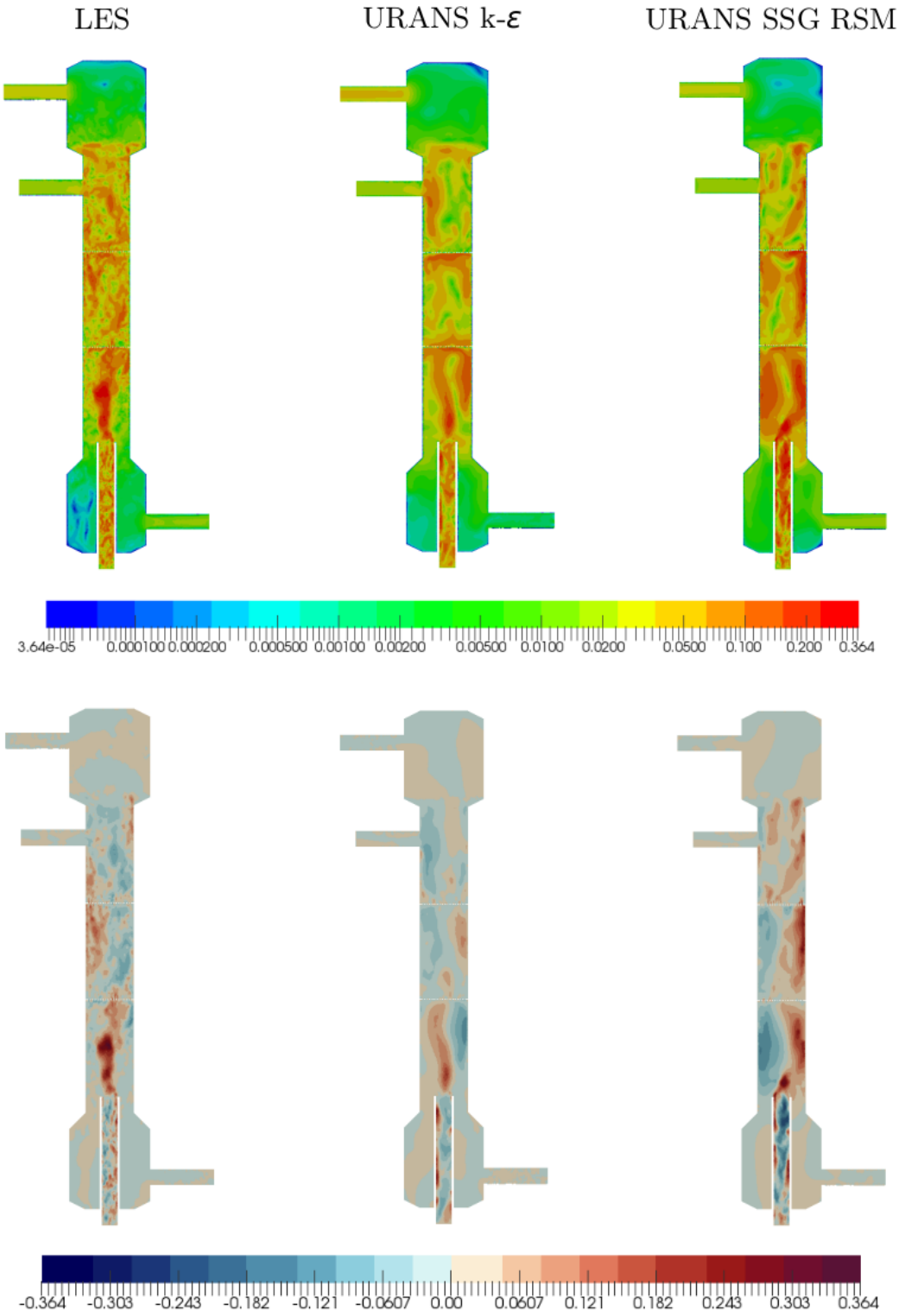

Figure 4.12: Magnitude of the instantaneous velocity field (top) and instantaneous z-component velocity (bottom) for the LES, URANS k-ε and URANS SSG RSM at 2π. Velocities in ms^{-1}.

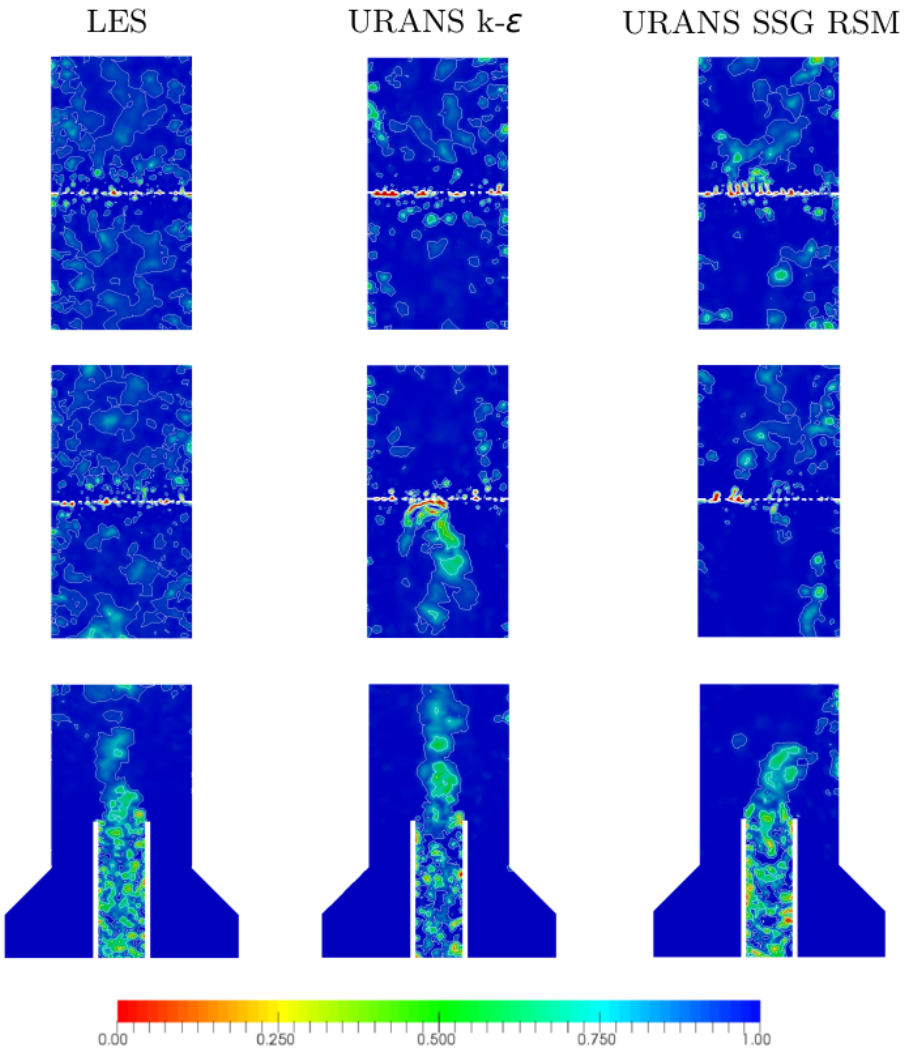

Figure 4.13: Plot of the instantaneous volume fraction field, α, for the LES (right), URANS k-ε (centre) and URANS SSG RSM (left) at 2π. Contour lines have been plotted for reference at α values of 0.25, 0.5, 0.75 and 0.95.

4.3.3.2 Comparison of Ensemble Average Field Properties

The ensemble averaged field properties of velocity, pressure ($P_{static}-\rho gh$), turbulence kinetic energy, turbulence kinetic energy dissipation rate and mixing index from the URANS models, using k-ε and SSG RSM closures, are compared directly against the LES predictions. In each case, the results were ensemble-averaged until converged data resulted. For the LES the data from 200 pulse cycles was used. For both URANS predictions significantly less time-dependent data was averaged, due to the already averaged nature of the simulations, requiring only 10 pulse cycles to achieved converged data.

Fig. 4.14 contains line plots of the ensemble averaged velocities taken across the column (x-axis at $y = 0$) at heights corresponding to the centre of the bottom plate ($z = 0.701$ m), the centre of the middle compartment ($z = 0.850$ m), and the centre of the top plate ($z = 1.001$ m) separately for each velocity component. Only data averaged at peak pulsation ($t = 1/2\pi$) was compared as little difference is observed in the flow velocities, for a column operating under these conditions, as mentioned in the analysis of the LES predictions of Fig. 4.6 in Section 4.2.5.3.

In general, both the URANS closures fail to predict the mean velocity components U_x, U_y and U_z. This is less clear in the U_x and U_y as flow is weak in these directions due to the dominant gravitationally driven counter-current flow. However, the results for U_z from both the URANS closures show a clear divergence from that predicted by the LES.

Firstly, at the bottom plate, the URANS k$-\varepsilon$ model result shows a segregated flow across the plate between the pathway of both phases. The URANS SSG RSM result shows closer characteristic behaviour to the LES, however, the magnitudes of the flow streams through the sieve-holes differ and are lower in the axis (centre) of the plate and higher in the radial (outer) direction. Secondly, in centre compartment, both URANS models show contradictory flow behaviour. The k-ε turbulence model shows a fully segregated flow between the pathways of each phase and the SGS RSM develops the expected rotational behaviour, dominant in the bulk of the continuous phase, but in the reverse rotational direction to that of the LES prediction. Thirdly, neither URANS closures accurately replicate the profiles of the LES but the SGS RSM once more provides a closure prediction in terms of flow direction across the top plate.

Initially from comparing only the predictions of the mean velocities, it is clear that neither closure can accurately replicate the predictions of the LES. Overall, however, the SGS RSM closure provides a close approximation of the LES data showing the development of similar flow structures/pathways and congruent flow behaviour overall but with disagreement in the magnitudes of the predicted velocities. On the other hand, the k-ε closure struggles to provide flow predictions that in anyway agree, characteristically, with what is predicted with LES.

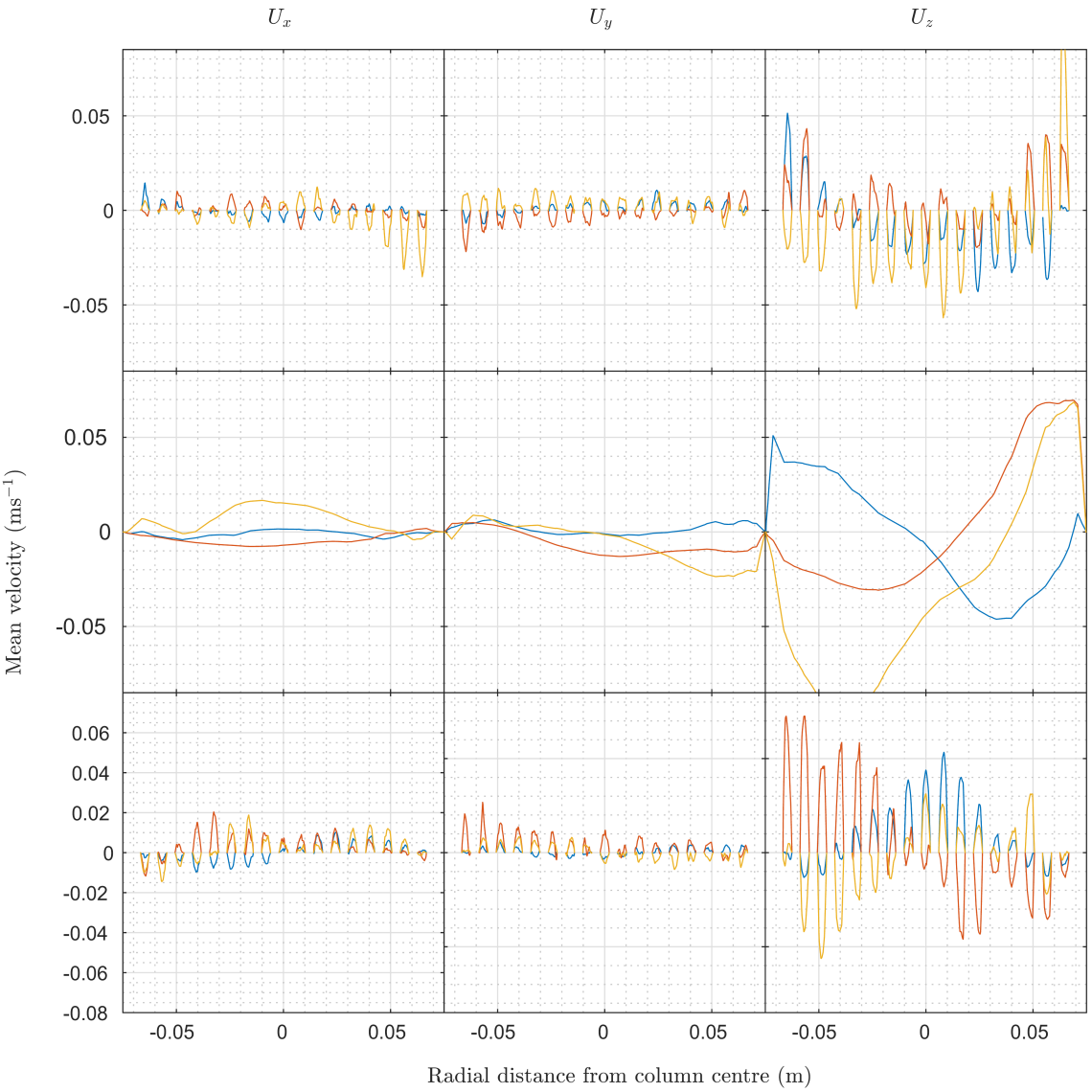

Figure 4.14: Mean velocity components plotted along the x-axis ($y = 0$ m) at $z = 0.701$ m (centre bottom plate), $z = 0.850$ m (middle of the compartment), $z = 1.001$ m (centre of top plate) at $\frac{1}{2}\pi$. LES (—), URANS $k - \varepsilon$ (—), URANS SSG RSM (—).

Naturally this conclusion is expected due to the many inherent deficiencies of the k$-\varepsilon$ model, e.g., not being able to handle rotational, impinging and buoyancy driven flows which are all predominant characteristics of PSEC hydrodynamics observed from the LES, see Section 4.2.5. RSM models are known to numerically incorporate terms that can better handle such flow phenomena. However, inconsistencies can still arise because the SSG RSM model can still be subject to issues of correctly identifying turbulence boundary conditions and, as with this case, relying on the solution of the k-ε model as an initial condition which can lead to divergence in the final solution (Versteeg & Malalasekera, 2007).

Figs. 4.15, 4.16 and 4.17 are axial centreline plots of pressure ($P_{static} - \rho gh$), turbulence kinetic energy, turbulence kinetic energy dissipation rate and mixing index parameter for the LES, URANS k-ε and URANS SSG RSM predictions

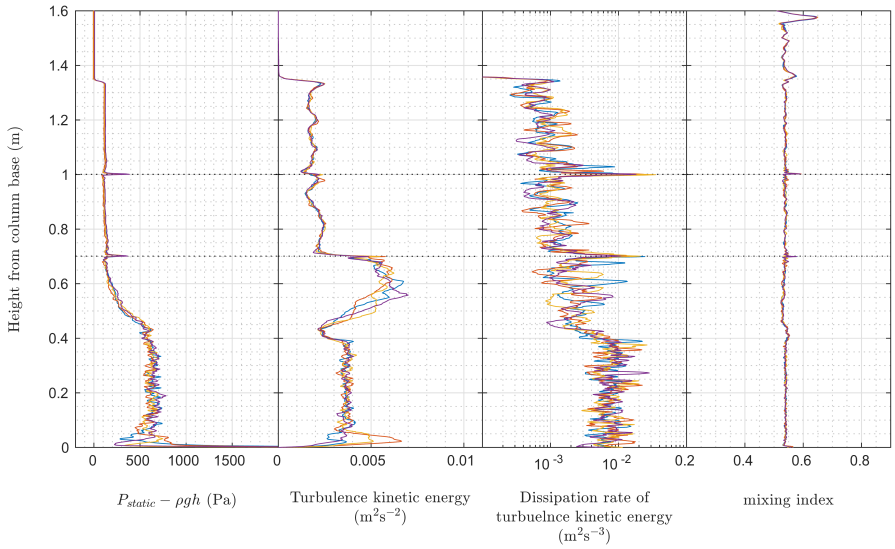

Figure 4.15: LES field properties plotted along the height of the column at $x = 0$ m, $y = 0$ m; $\frac{1}{2}\pi$ (—), π (—), $\frac{3}{2}\pi$ (—), 2π (—).

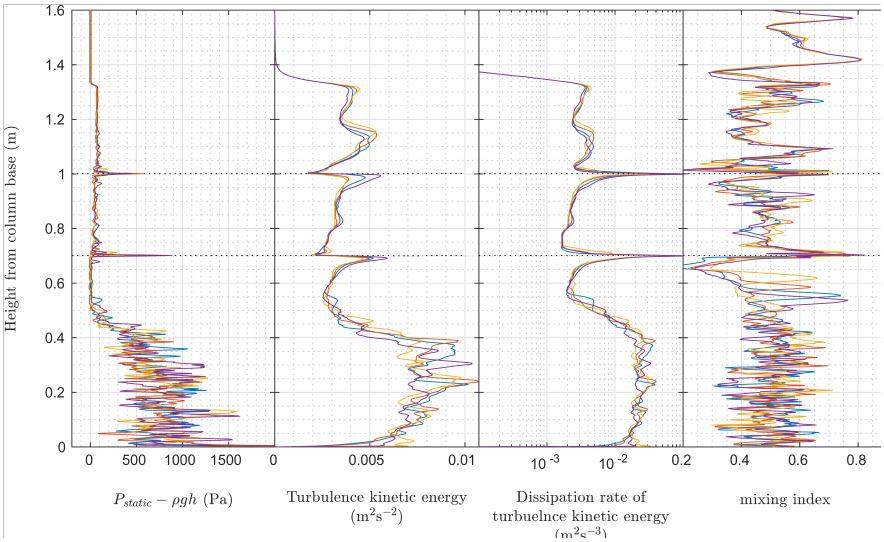

Figure 4.16: $k - \varepsilon$ field properties plotted along the height of the column at $x = 0$ m, $y = 0$ m; $\frac{1}{2}\pi$ (—), π (—), $\frac{3}{2}\pi$ (—), 2π (—).

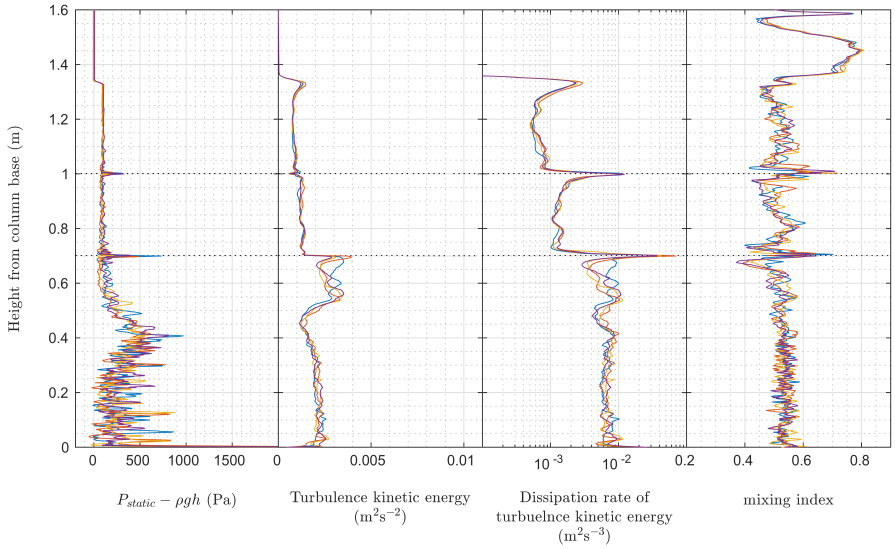

Figure 4.17: SSG RSM field properties plotted along the height of the column at $x = 0$ m, $y = 0$ m; $\frac{1}{2}\pi$ (—), π (—), $\frac{3}{2}\pi$ (—), 2π (—).

respectively. A quantitative summary of the observations taken for each field inspected is available in Tables 4.5 and 4.6. A qualitative description of the observations follows.

The pressure profiles given by the URANS models predict the characteristic features of the LES results to varying degrees of accuracy. The average pressure within the bottom inlet was overpredicted by k-ε and under predicted by SSG RSM, both URANS closures failed to reproduce the trend of profile towards the $z = 0.4$ where the organic fluid enters the bulk flow. In the bulk flow regions the the SSG RSM closure showed greater success in replicating the predicted pressures from the LES, whereas the k-ε failed to do so predicting an unphysical negative pressure across the PSEC height. At the plates, both models tended to overpredict the pressure spike feature.

In general the turbulence kinetic energy was overpredicted by k-ε and underpredicted by the SSG RSM. By extension, both URANS models would be unable to accurately predict the magnitudes of the turbulence stress tensors which would lead to a poor assessment of mixing as identified in Section 4.2. The trends within the profile were more successfully replicated by the SSG RSM with regards the qualitative observations along the height of the PSEC.

For the dissipation of turbulence kinetic energy, k-ε made predictions almost an order of magnitude over that from the LES. Again the SSG RSM provided values more closely matching the LES. However, in both cases there is a clear difference in the resolution of the turbulence. This is apparent from the larger fluctuations in the converged ensemble-averaged results of the LES compared to that from the URANS closures. This can have implications to the use of URANS methods with common population balance models used to predict mean droplet size distributions based on turbulence dissipation rate Alzyod *et al.* (2018).

The mixing index profile of the LES shows a consistent mean value across the PSEC with slight increases near the plates. The k-ε is unable to provide a consistent value and large fluctuations are observed. As a result, the ability for the k-ε closure to predict PSEC mixing is questionable and is due to poor approximations of irrotational and rational flow components. The SSG RSM closure suffers less in this regard, it can provide a consistent mean prediction for the mixing index parameter that is similar to the LES results, but is still overpredicted. This is due to the more sophisticated turbulence transport equations of the closure and ability of the RSM to handle complex turbulent structures.

Table 4.5: Summary of observations of pressure and turbulence kinetic energy for Figs. 4.15, 4.16 and 4.17

Observation	LES	URANS k-ε	URANS SSG RSM
	Pressure ($P_{static} - \rho gh$)		
Dispersed phase inlet pipe ($z = 0 - 0.4$ m)	Small local fluctuations. Average of 625 Pa. Stabilises immediately. Exit pressure of 600 Pa.	Large local fluctuations. Average of 830 Pa. Decreases with height. Exit pressure of 500 Pa.	Large local fluctuations. Average of 190 Pa. Increase with height. Exit pressure of 500 Pa.
Bottom compartment ($z = 0.4 - 0.7$ m)	Steady decrease in pressure with height to 125 Pa.	Sudden decease down to 0 Pa.	Steady decrease down to 90 - 120 Pa.
Bottom plate	Drop, spike and recovery. Peak of 372 Pa.	Spike and recovery (no drop). Peak of 884 Pa.	Spike and recovery (no drop). Peak of 730 Pa.
Centre compartment ($z = 0.7 - 1$ m)	Drop from 125 to 90 Pa.	Increase from 42 to 50 Pa.	Stable profile at 80 - 90Pa.
Top plate	Drop, spike and recovery. Peak of 385 Pa.	Spike and recovery (no drop). Peak of 570 Pa.	Spike and recovery (no drop). Peak of 320 Pa.
Upper compartment ($z = 1 - 1.3$ m)	Steady pressure at 116 Pa.	Fluctuations up to 1.15m. Steady at 70 Pa.	Stable profile at 80 - 90 Pa.
Disengagement section ($z = 1.3 - 1.6$ m)	Drop to 0 Pa across primary interface.	Drop to 0 Pa across primary interface.	Drop to 0 Pa across primary interface.
	Turbulence kinetic energy		
Dispersed phase inlet pipe ($z = 0 - 0.4$ m)	Small local fluctuations. Average of 0.00375 m^2s^{-2}.	Large local fluctuations. Increase with height from 0.005 - 0.011 m^2s^{-2}.	Small local fluctuations Decrease with height frim 0.0021 - 0.0015 m^2s^{-2}.
Bottom compartment ($z = 0.4 - 0.7$ m)	Sudden drop to 0.002 m^2s^{-2} then increase to 0.007 m^2s^{-2} towards bottom plate.	Slow drop to 0.00326 m^2s^{-2} then increase to 0.0059 m^2s^{-2} towards bottom plate.	Small drop to 0.0011 m^2s^{-2} then increase to 0.004 m^2s^{-2} towards bottom plate. Fluctuations near to plate.
Bottom plate	Drop to 0.002 m^2s^{-2}.	Drop to 0.002 m^2s^{-2}.	Drop to 0.0012 m^2s^{-2}.
Centre compartment ($z = 0.7 - 1$ m)	Slow drop to 0.0015 m^2s^{-2} then increase to 0.0021 m^2s^{-2} towards top plate.	Steady increase to 0.0034-0.0055 m^2s^{-2} towards top plate.	Stable at 0.0012 m^2s^{-2} with small fluctuations near the top plate.
Top plate	Drop to 0.0014 m^2s^{-2}.	Drop to 0.0018 m^2s^{-2}.	Small drop to 0.0005 m^2s^{-2} and recovery.
Upper compartment ($z = 1 - 1.3$ m)	Recovery to 0.002 m^2s^{-2}.	Recovery and peak at 0.0053 m^2s^{-2}.	Stable at 0.009 m^2s^{-2}.
Disengagement section ($z = 1.3 - 1.6$ m)	Drop to 0 m^2s^{-2} across primary interface. Peak before interface to 0.0024 m^2s^{-2}.	Drop to 0 m^2s^{-2} across primary interface. No substantial peak before interface.	Drop to 0 m^2s^{-2} across primary interface. Peak before interface to 0.0014 m^2s^{-2}.

Table 4.6: Summary of observations of turbulence dissipation rate and mixing index for Figs. 4.15, 4.16 and 4.17

Observation	LES	URANS k-ε	URANS SSG RSM
Dissipation of turbulence kinetic energy			
Dispersed phase inlet pipe ($z = 0 - 0.4$ m)	Large local fluctuations spanning an order of magnitude. Average value of 0.005 m^2s^{-3} increasing to 0.009 m^2s^{-3}.	Small local fluctuations. Initial increase of average from 0.017 0.025 m^2s^{-3}.	Small local fluctuations. Average value of 0.007 m^2s^{-3}.
Bottom compartment ($z = 0.4 - 0.7$ m)	Drop to 0.002 m^2s^{-3}.	Drop to 0.0019 m^2s^{-3}. Smooth exponential increase towards bottom plate.	Initial drop to 0.004 m^2s^{-3}. Recovery to 0.011 m^2s^{-3}. Second drop to 0.003 m^2s^{-3}. Smooth exponential increase towards bottom plate.
Bottom plate	Spike of 0.025 m^2s^{-3}.	Peak of 0.2 m^2s^{-3}.	Peak of 0.07 m^2s^{-3}.
Centre compartment ($z = 0.7 - 1$ m)	Steady decrease from 0.0013 - 0.0009 m^2s^{-3}.	Fast exponential decrease away from bottom plate to 0.0017 m^2s^{-3}. Smooth exponential increase towards top plate.	Fast xponential decrease away from plate to 0.001 m^2s^{-3}. Slow exponential increase towards top plate.
Top plate	Spike of 0.035 m^2s^{-3}.	Peak of 0.2 m^2s^{-3}.	Peak of 0.011 m^2s^{-3}.
Upper compartment ($z = 1 - 1.3$ m)	Steady decrease from 0.001 - 0.0005 m^2s^{-3}.	Fast exponential decrease to 0.0025 m^2s^{-3}.	Smooth exponential decrease to 0.0007 m^2s^{-3}. Decrease to 0.00052 m^2s^{-3}.
Disengagement section ($z = 1.3 - 1.6$ m)	Drop to 0 m^2s^{-3} across primary interface. Peak before interface to 0.0013 m^2s^{-3}.	Drop to 0 m^2s^{-3} across primary interface. Peak before interface of 0.0044 m^2s^{-3}.	Drop to 0 m^2s^{-3} across primary interface. Parabolic spike before interface to 0.003 m^2s^{-3}.
Mixing index			
Dispersed phase inlet pipe ($z = 0 - 0.4$ m)	Minor local fluctuations. Average value of 0.51.	Very large fluctuations. Average value of 0.59 increasing to 0.54.	Small local fluctuations. Average value of 0.51.
Bottom compartment ($z = 0.4 - 0.7$ m)	Small drop to 0.49 and recovery towards bottom plate to 0.51.	Drop to <0.2 before bottom plate.	Drop to 0.38 before bottom plate.
Bottom plate	Spike of 0.55.	Spike of 0.825.	Spike of 0.67
Centre compartment ($z = 0.7 - 1$ m)	Average value of 0.51.	Average value of 0.48 and drop to 0.28 before top plate. Large fluctuations	Fluctuations from 0.4 - 0.57. Drop to 0.48 before top plate/
Top plate	Spike of 0.59.	Spike of 0.7.	Spike of 0.68.
Upper compartment ($z = 1 - 1.3$ m)	Average value of 0.51.	Large fluctuations between 0.34 - 0.69.	Fluctuations between 0.41-0.51
Disengagement section ($z = 1.3 - 1.6$ m)	Spike before interface of 0.54.	Drop and spike over interface 0.3 - 0.8.	Drop to 0.45 and increase to 0.78 after interface.

4.3.4 Conclusions

The suitability of common URANS fluid flow modelling techniques were evaluated against a benchmark LES prediction from Section 4.2. Here, both the k-ε and SSG RSM turbulence closure models were investigated. In each case, the boundary conditions were kept consistent across all three methods resulting in comparison of pseudo steady-state dispersion regime operation of a representative industrial PSEC geometry. Achievable URANS solutions were presented employing second order and/or blended first/second order discretisation schemes. In each case the VOF method was used to model multiphase effects. The conclusions from the analysis and comparison of the URANS methods against the LES predictions are as follows:

1. The URANS methods show less dispersion overall when comparing the volume fraction fields. The predicted stage-wise hold-up for the LES, URANS k-ε and SSG RSM closures are 5.1 %, 4.21 %, and 3.57 %, and global hold-up predictions are 30.6 %, 31.0 %, and 31.3 % respectively. Despite a lower prediction of stage-wise hold-up, the global hold-up of was overpredicted by URANS.
2. Both URANS methods were able to provide an order-of-magnitude prediction of the instantaneous velocity magnitude fields in the areas of interest but the fidelity of the LES far exceeded that of either URANS solution.
3. With regards to the mean velocity fields, the SGS RSM closure provided a close approximation of the LES data in terms of flow structures and velocity magnitudes. The k-ε closure struggled to provide flow predictions that in anyway agreed, characteristically,with the LES.
4. The pressure profiles given by the URANS models predict the characteristic features of the LES results to varying degrees of accuracy. At the plates, both models tended to overpredict the pressure spike feature.
5. In general the turbulence kinetic energy was overpredicted by k-ε and underpredicted by the SSG RSM.
6. For the dissipation of turbulence kinetic energy, k-ε made predictions almost an order of magnitude over that from the LES, the SSG RSM provided values more closely matching the LES.
7. The ability for the k-ε closure to predict PSEC mixing is questionable as evident from the inability to provide a consistent mixing index prediction. The SSG RSM, however, provided a consistent mean prediction for the mixing index parameter that is similar to the LES results, but is still overpredicted.

5

Designed Simulation Campaign: Sensitivity Study of PSEC Using VOF & LES

5.1 Introduction

Historically, PSEC research has focused on the development of 'design equations' formulated from pilot plant experiments. The chemical systems studied are typically general purpose combinations of solvents and solutes. Trial methods are used to establish the relationship of 'independent' process variables with column performance using *'one variable at a time'* experimental design. Given the age of the research, these studies are often lacking in their reported sampling range and accuracy of measurementation due to the limitations in the technology available. Curve fitting or dimensional analysis techniques are used to develop empirical equations to predict regime transition boundaries, flooding limits, hold-up, droplet size and mass transfer coefficients. They tend to be system specific and limited in their applicability. This is problematic in that such equations, although still useful, do not provide any insight into the relationships and interactions of all the variables (degrees of freedom) inherent in PSECs. Some authors have attempted to mitigate any bias by incorporating large data sets from other investigators in order to make their formulations universal. This approach suffers from misinterpretation of results and inconsistencies in the experimental methods. None have been able to explicitly define the importance of each process variable on the functionality of PSECs. An exhaustive list of available PSEC design equations are reviewed in Section 2.2.

The aim of this work is not to provide a universal model or correlation to describe PSEC behaviour. This work provides a novel contribution by showcasing a framework of analytical methods that provide depth and breadth in the investigation of PSEC operation. Reported here is a designed CFD simulation campaign utilising highly detailed turbulence resolving methods, established in Section 4.2, using LES with the VOF method allowing for a high level of precision and detail of the simulated PSEC hydrodynamic behaviour. Means of designed

variation in operational parameters between simulations and incorporation of statistics into the analysis are used. The level of analyses preformed here is comprehensive and is unparalleled with respect to reported and published PSEC literature.

The objective of this this chapter is two-fold:

i to investigate the appropriateness of the VOF multiphase method for prediction of global properties, such as inter-stage hold-up and modes of operation, see Section 2.2.2, in an extreme range operational conditions.

ii to investigate the relationship of certain predictor variables and response variables, in large part, to determine a feasible means of predicting and/or identifying flooding in physical PSECs in an industrial setting.

5.2 Designing the Matrix of Simulations

As mentioned, the LES VOF simulation developed in Section 4.2 is used as the basis for the simulation campaign. Numerical settings and boundary conditions are kept the same except for the velocity boundary conditions which are altered in each case as per the simulation matrix. The matrix of simulations was generated through a three-level Box-Behnken *'design of experiments'* (DOE) methodology.

The process variables analysed are:

- Pulse velocity (Af).
- Total column throughput ($U_d + U_c$).
- Solvent-flow-ratio (U_d/U_c).

Note that, for this investigation pulse amplitude (A) and pulse frequency (f) can be individually set. This level of variation was exploited to provide a greater range of variability with respect to the possible modifications of velocity boundary condition. For later analysis, these variables were recombined into the control variable (Af)

The effected operational conditions analysed are:

- Probability of flooding ($Probability_{Flooding}$).
- Mean Average working pressure between the two sieve-plates ($P - \rho g h_{Mean}$)
- Maximum pressure peak across each plate ($P - \rho g h_{BP,Max}, P - \rho g h_{TP,Max}$).
- Pressure drop across the column w.r.t. each phase ($\Delta P_d, \Delta P_c$).
- Stage-wise and plate-wise hold-up during stable operation (ϕ).

5.2.1 Box-Behnken Design

The simulation matrix was produced using the Box-Behnken design (BBD) method (Box & Behnken, 1960). For the study of four or less variables, BBD requires fewer treatment combinations than alternative central composite design methods. Other full/fractional factorial design methods are available, however, BBD provides an efficient balance of model accuracy to number of simulations. As such, BBD has been used in a number engineering applications for novel design optimisation of extraction/separations processes in complex systems (Singh Brar, 2018; Stamenković *et al.*, 2018).

In BBD, three levels (+1, 0 and -1) are assigned for each of the four control variables. The levels chosen for U_d/U_c spread from 0.25 to 4, a typical range for most reprocessing separation chemistries. Levels for A, f, and $U_d + U_c$ were chosen to produce a wide distribution across the experiential region. In this case, the operational area over a flooding curve marked out in Fig. 5.1. The flooding curve was calculated using Eq. (2.7) from Smoot *et al.* (1959):

$$(U_c + U_d)_f = 0.527 \frac{\sigma^{0.144} \Delta\rho^{0.63} \mu_c^{0.489} h^{0.207} d^{0.458} g^{0.81}}{\rho_c^{0.775} \mu_d^{0.2} Q^{0.207}} \times \left(\frac{U_d}{U_c}\right)^{0.014} (Af)^{-0.621} \tag{2.7}$$

$$Q = \frac{\pi^2}{2C_o^2} \frac{1 - e^2}{e^2}$$

along with notable transition boundaries calculated using the correlations given in Table 2.1. As the CFD simulations are deterministic in nature, no repeat experiments were necessary. The full matrix of simulations is given in Table 5.1, this outlines the treatment combinations and their corresponding boundary conditions.

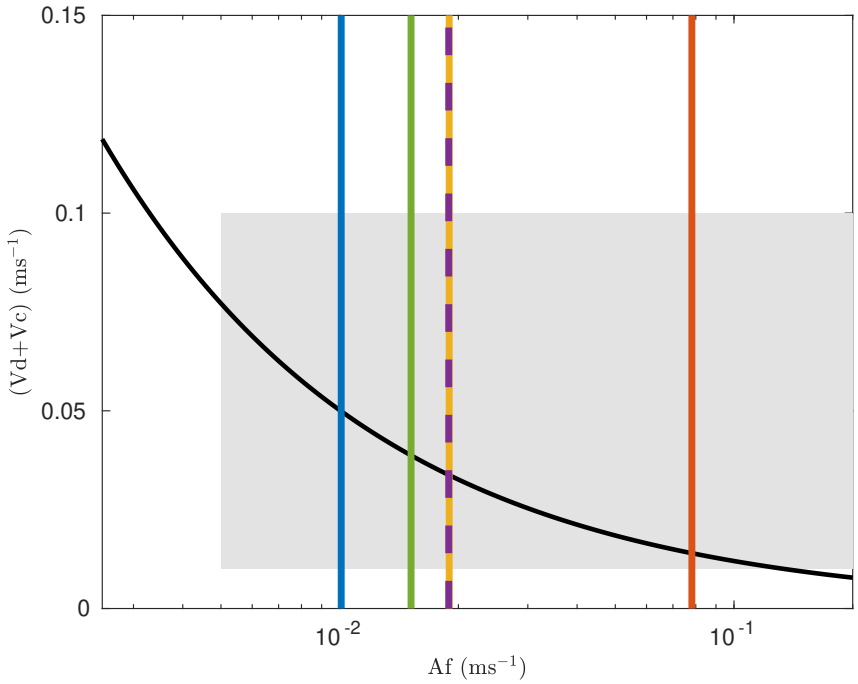

Figure 5.1: Calculated PSEC flooding curve from Smoot *et al.* (1959) (—) with the chosen experimental region marked out in gray. Mixer-settler to dispersion regime transition boundary from Kumar & Hartland (1994) (—), dispersion to emulsion regime transition boundary from Kumar & Hartland (1983)(—), dispersion to emulsion regime transition boundary from Miyauchi & Oya (1965) (—), dispersion to emulsion regime transition boundary from Boyadzhiev & Spassov (1982) (—), dispersion to emulsion regime transition boundary Tung & Luecke (1986) (—).

Table 2.1 : Regime transition correlations for PSECs.

Author(s)	Transition Correlation	Transition Limits	
Miyauchi & Oya (1965)*[a]	$Af_t = 0.0021(\beta h)^{\frac{1}{3}}\left(\frac{\mu_d^2}{\sigma\Delta\rho}\right)^{-0.25}$	$Af < Af_t$ Dispersion Regime $Af > Af_t$ Emulsion Regime	(2.1)
Boyadzhiev & Spassov (1982)	$Af_t = 0.5\left(\frac{0.96e^2}{\rho_c}\right)^{\frac{1}{3}}$	$Af < Af_t$ Dispersion Regime $Af > Af_t$ Emulsion Regime	(2.2)
Kumar & Hartland (1983)*[a]	$Af_t = \left[0.05\beta h\left(\frac{\rho_c}{\Delta\rho^{0.75}\sigma^{0.25}g^{1.25}}\right)^{-1}\right]^{\frac{1}{3}}$	$Af < Af_t$ Dispersion Regime $Af > Af_t$ Emulsion Regime	(2.3)
Kumar & Hartland (1994)	$Af_t = 9.96\times10^{-3}\left(\frac{\sigma\Delta\rho^{0.25}e}{\mu_d^{0.75}}\right)^{0.33}$	$Af < Af_t$ Mixer-Settler Regime $Af > Af_t$ Dispersion Regime	(2.4)
Tung & Luecke (1986)	$Af_t = \left(\frac{0.062e^2}{\rho_c}\right)^{\frac{1}{3}}$	$Af < Af_t$ Dispersion Regime $Af > Af_t$ Emulsion Regime	(2.5)

[a] Here: $\beta = \frac{e^2}{(1-e)(1-e^2)}$

Table 5.1: Matrix of Simulations from BBD Method

	Control Variable Level				**Assigned Variable Velocity Boundary Condition**						
Run	A	f	$(U_d + U_c)$	(U_d/U_c)	A	f	Af	U_d	U_c	$(U_d + U_c)$	(U_d/U_c)
No.	(m)	(s^{-1})	(ms^{-1})	-	(m)	(s^{-1})	(ms^{-1})	(ms^{-1})	(ms^{-1})	(ms^{-1})	-
1	-1	-1	0	0	0.01	0.5	0.005	0.0374	0.0176	0.055	2.125
2	-1	1	0	0	0.01	2	0.02	0.0374	0.0176	0.055	2.125
3	1	-1	0	0	0.1	0.5	0.05	0.0374	0.0176	0.055	2.125
4	1	1	0	0	0.1	2	0.2	0.0374	0.0176	0.055	2.125
5	0	0	-1	-1	0.055	1.25	0.06875	0.002	0.008	0.01	0.25
6	0	0	-1	1	0.055	1.25	0.06875	0.008	0.002	0.01	4
7	0	0	1	-1	0.055	1.25	0.06875	0.02	0.08	0.1	0.25
8	0	0	1	1	0.055	1.25	0.06875	0.08	0.02	0.1	4
9	-1	0	0	-1	0.01	1.25	0.0125	0.011	0.044	0.055	0.2500
10	-1	0	0	1	0.01	1.25	0.0125	0.044	0.011	0.055	4
11	1	0	0	-1	0.1	1.25	0.125	0.011	0.044	0.055	0.2500
12	1	0	0	1	0.1	1.25	0.125	0.044	0.011	0.055	4
13	0	-1	-1	0	0.055	0.5	0.0275	0.0068	0.0032	0.01	2.125
14	0	-1	1	0	0.055	0.5	0.0275	0.068	0.032	0.1	2.125
15	0	1	-1	0	0.055	2	0.11	0.0068	0.0032	0.01	2.125
16	0	1	1	0	0.055	2	0.11	0.068	0.032	0.1	2.125
17	-1	0	-1	0	0.01	1.25	0.0125	0.0068	0.0032	0.01	2.125
18	-1	0	1	0	0.01	1.25	0.0125	0.068	0.032	0.1	2.125
19	1	0	-1	0	0.1	1.25	0.125	0.0068	0.0032	0.01	2.125
20	1	0	1	0	0.1	1.25	0.125	0.068	0.032	0.1	2.125
21	0	-1	0	-1	0.055	0.5	0.0275	0.011	0.044	0.055	0.25
22	0	-1	0	1	0.055	0.5	0.0275	0.044	0.011	0.055	4
23	0	1	0	-1	0.055	2	0.11	0.011	0.044	0.055	0.25
24	0	1	0	1	0.055	2	0.11	0.044	0.011	0.055	4
25	0	0	0	0	0.055	1.25	0.06875	0.0374	0.0176	0.055	2.125

5.3 Post-Processing

5.3.1 Identification of Flooding

Flooding was identified using the method described by Mcallister *et al.* (1967) used in flooding experiments performed at Oak Ridge National Laboratory. In their studies, hold-up was measured after 30 and 60 minutes of operation. If the measurements disagreed then flooding was identified.

In this scenario, it is not feasible to run each of the 25 proposed simulations, or even a single simulation of this nature, for an hour. However, with CFD one can track hold-up as a continuous function over time at high levels of precision. Therefore in context of this study, the global average hold-up was monitored and recorded throughout the progress of the simulation.

Each simulation required around 200 s of run time in order to show clear identification of the state of operation. For stable operation, producing a negative flooding response, the hold-up converges and oscillates about a stable value. For cases identified as producing a positive flooding response, the hold-up diverges (decreases) continuously over time. Examples of identification of non-flooded and a flooded cases are given in Fig. 5.2.

Atleast 100 s ($\sim 3 \times 10^6$ iterations) are first required for the system to adjust to new conditions. After this time, the characteristic behaviour and identifiable trends in hold-up emerge. Moreover, characteristic oscillations were observed due to the pulsating boundary conditions. Larger oscillations were observed as a result of small local accumulations of the dispersed phase fluid. This is expected due to the transient nature of the flow and in flooded cases these fluctuations are more dramatic and indicate instability.

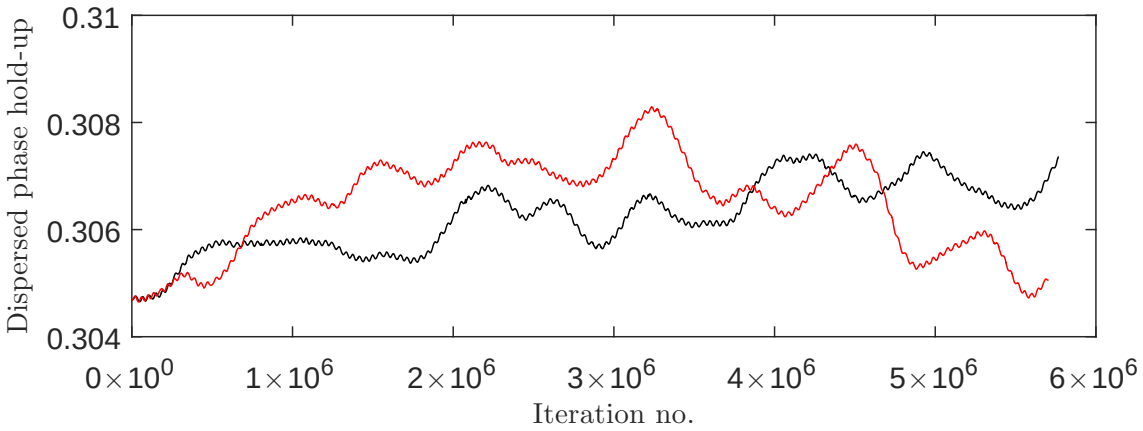

Figure 5.2: Development of the global average of hold-up over time (iterations). Example of negative flooding response (—) (Run 20) and a positive flooding response (—) (Run 22).

5.3.2 Pressure Field Analysis

The analysis of each run includes extracting a number of pressure ($P - \rho gh$) field characteristics evaluated in the context of flooding as well in identifying trends between stable runs. Such characteristics include the:

- pressure drop across each phase stream.
- average working pressure between the sieve-plates.
- maximum pressure peaks across each plate.

This was achieved using bespoke post-processing code written for OpenFOAM®.

The pressure drop for each phase stream was calculating by taking the difference between the area averaged pressure of the inlet and outlet boundaries for each respective phase. The area averaged pressure for each boundary surface, $\langle P - \rho gh \rangle_{BS}$, was calculated using the magnitude of the cell face area vector, $|s_f|$, and the cell face pressure:

$$\langle P - \rho gh \rangle_{BS} = \frac{\sum_{f=i}^{n} (P - \rho gh)_i |S_f|_i}{\sum_{f=i}^{n} |S_f|_i} \tag{5.1}$$

where n is the number of boundary cell faces. Similarly, the average pressure of the cells between the two sieve-plates, $\langle P - \rho gh \rangle_{CC}$, was calculated by:

$$\langle P - \rho gh \rangle_{CC} = \frac{\sum_{c=i}^{m} (P - \rho gh)_i V_i}{\sum_{c=i}^{n} V_i} \tag{5.2}$$

where m is the number of cells between each plate (0.702 m $< Z <$ 1000 m) and V is the cell volume.

The maximum pressure peaks across each plate were obtained by taking the maximum value between spacial coordinate limits. The limits define a ±5 mm range (in height) from the centre point of each plate. For the bottom plate the limits are 0.695 m $< z <$ 0.705 m. For the top plate the limits are 0.905 m $< z <$ 1.005 m. Here, z is the cell centroid z-coordinate position.

5.3.3 Dispersed Phase Hold-up Analysis

The dispersed phase inter-stage hold-up (ϕ) was calculated by taking the volume-weighted average of the dispersed phase volume fraction field (α_d) between each plate:

$$\phi = \frac{\sum_{c=i}^{m} V_i \alpha_{d,i}}{\sum_{c=i}^{m} V_i} \tag{5.3}$$

this equates to the mean value of the α_d field sampled, volume-weighted to account for difference in cell (sample) sizes. With this, the variance (σ^2) and standard deviation (SD) of ϕ can be determined in order to quantify the distribution of the cell values of α_d:

$$\sigma^2 = \frac{\sum_{c=i}^{m} V_i (\alpha_{d,i} - \phi)^2}{\sum_{c=i}^{m} V_i} \tag{5.4}$$

$$SD = \sqrt{\frac{\sum_{c=i}^{m} V_i (\alpha_{d,i} - \phi)^2}{\sum_{c=i}^{m} V_i}} \tag{5.5}$$

where (m) is the number of cells between each plate (0.702 m $< z <$ 1.000 m) and V is the cell volume. The standard deviation can then be normalised using the definition of the *coefficient of variation* (C_V) via:

$$C_V = \frac{SD}{\phi} \tag{5.6}$$

Lastly, the dispersed phase plate-wise hold-up was calculated using using the same method above but for cells in the range of 0.700 m $< z <$ 0.702 m and 1.000 m $< z <$ 1.002 m.

5.4 Analysis Methods

A number of analytical methods were employed in order to clean, transform and model the data extracted from the CFD simulations. This allows for rich visualisation of trends and relationships hidden in the data. PSECs are highly complex systems consisting of many degrees of freedom in their operation. The relationships between possible control and response variables could potentially be non-linear and interacting in their nature. It is therefore important that a diverse range of analysis methods be leveraged in order to examine the complex numerical relationships.

Moreover, certain under-represented methods have been researched and applied in the context of this study in order to showcase a new possibility of performance analysis over classic *'one variable at a time'* dimensional analysis techniques which are heavily represented in previous PSEC research and engineering R&D in general.

5.4.1 Response Surface Methodology

Observations between the relationships of the three controlled variables (Af, U_d+U_c, U_d/U_c) and a fourth response variable were visualised via four-dimensional grid interpolation methods.

The analysis procedure is to outlined as:

1. First, a three-dimensional grid was generated with a single control variable plotted on the x, y, and z axis within the respective operational limits investigated.
2. Next, each run can be position within the grid, as a point, with respect to their operational configuration. This also outlines the operational range explored.
3. Relationships of a fourth response scalar variable, with respect to the operational configuration, can then be studied by assigning it's value to a colour map scale.
4. Subsequently, where appropriate, interpolation methods are used to build a modelled 'response field' to facilitate exploration of trends.
5. Lastly, slice extraction is used to to extract surface responses for two control variables with fixed the third control variable.

An example (without interpolation) has been provided in Fig. 5.3 with the run number as the fourth dimension scalar variable, this is provided for demonstration purposes of steps 1 to 3.

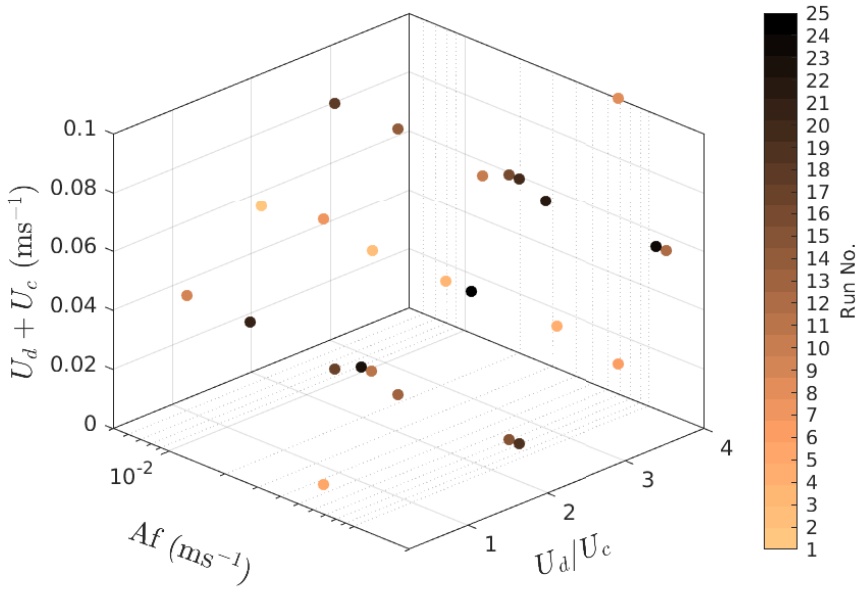

Figure 5.3: Four-dimensional plot demonstrating the position of each run within the three-dimensional operational range investigated. The fourth-dimension scalar information (Run no.) has been visualised via a colour value on a colour map scale.

For this investigation, a *Nearest-Neighbour method* and *Linear Interpolation* was used (for step 4). Nearest-neighbour performs a search on all unassigned grid points and assigns a value that is equal to the nearest triangulated point that contains a specified value. It can be considered a zeroth-order discontinuous interpolation method. Linear interpolation uses *Delaunay triangulation* to assign values to unassigned points based on the linear scaling of the value between three adjacent points with specified values. This method can be considered a first-order continuous interpolation method.

Both the methods used are robust forms of spatial data interpolation, and are typical techniques used in statistical analysis to transform scattered data. They provide a rich set of modelled data fields which facilitate comprehensive analysis of qualitative and quantitative trends and relationships (James *et al.*, 2017).

5.4.2 Regression Techniques

As mentioned, one unique and novel goal of the analysis is to provide means of determining significance and influence of certain variables in key hydrodynamic phenomena, namely flooding. *Logistic Regression* is a form of regression analysis, borrowed from statistical analysis, that provides a probability outcome of a binary classification response. In the context of this work, the binary response studied is whether the PSEC simulated shows flooding behaviour or not, initially identified using the method in Section 5.3.1. The Logistic function allows one to form a statistical model based on the direct effects of one more continuous variables in producing a negative or positive flooding response.

The framework provides a method to develop a linearised model of the 'predictor variables' (x_i) that calculate the log-odds in the event of a positive flooding response occurring James *et al.* (2017):

$$ln\frac{Probability_{Flooding}}{1 - Probability_{Flooding}} = \beta_0 + \beta_1 x_1 ... + \beta_n x_n \tag{5.7}$$

This model can then be transformed to provide the probability (P) that a positive flooding response occurs:

$$Probability_{Flooding} = \frac{e^{\beta_0+\beta_1 x_1 ...+\beta_n x_n}}{e^{\beta_0+\beta_1 x_1 ...+\beta_n x_n} + 1} = \frac{1}{e^{-(\beta_0+\beta_1 x_1 ...+\beta_n x_n)}} \tag{5.8}$$

and the statistical p-values, of each variable included, can be recovered to the determine their significance.

5.4.3 Data Preparation

A number of linear regression models using *'least-squares'* method, were examined between all available variables (control and observed). This allows one to perform a simple cross-check for any obvious relationships before deeper analysis was performed and give an indication to any potential non-linearity to in models going forward (James *et al.*, 2017).

Where noted, the data was normalised to mitigate the effects of differences in unit scale length between variables in any models produced or to provide a directly comparison of model coefficients. This is done using the following scaling factor:

$$x_{Scaled} = \frac{x - x_{Min}}{x_{max} - x_{min}} \tag{5.9}$$

Additionally, data was also filtered, using the 'quartiles method', to remove erroneous data points that lie more than 1.5 quartile ranges above the upper quartile or below the lower quartile. Both operations are common methods to realise accurate and reliable statistical analysis (James *et al.*, 2017).

5.5 Results and Discussion

5.5.1 Flooding Observations in Comparison with Flooding Correlations

Out of the 25 designed simulations, 8 cases produced a positive flooding response. A summary of the observed flooding response for each case, and their conditions, are included in Table 5.2. Note that Table 5.2 also includes additional information which is used in the assessment of Section 5.5.2.

The flooding results have been plotted on a traditional two-dimension flooding curve, see Fig. 5.4. In this study, the flooding correlation from Smoot *et al.* (1959), Eq. (2.7), has been used to construct the curve. This correlation proposes an upper throughput ($U_d + U_c$) limit for a given pulse velocity (Af). Not all cases can be visualised by this graph at once given the two-dimensional nature of the original correlation. Therefore, a three-dimensional version of this curve has been produced also, Fig. 5.5. It is noted that the correlation from Smoot *et al.* (1959) does provide a variable term for solvent-flow-ratio. However, it is weakly correlated and does not provide substantial change to the output. Consequently, the flooding surface is a near-constant projection of the curve when solvent-flow-ratio (U_d/U_c) is added as a third dimension.

As seen on Figs. 5.4 and 5.5, the majority of cases which did show a positive flooding response existed above the flooding curve. This supports the assumption that a large throughput and/or high pulse velocity can produce conditions leading to flooding (Yadav & Patwardhan, 2008). Fig. 5.5 shows two flooded cases which exist under the flooding curve (circled) in the middle pulse velocity ranges (at Af = 0.06875 and 0.0275 ms^{-1}) both at the same throughput ($U_d + U_c$ = 0.01 ms^{-1}). Taking only the data points showing a positive flooding response into consideration, it could be concluded that the Smoot *et al.* (1959) correlation is functional but optimistic in evaluating the upper stable pulse velocity limit (before flooding occurs).

Although somewhat successful for predicting positive flooding responses, the cases with negative flooding responses show a complete disagreement with the predictions of the Smoot *et al.* (1959) correlation. On Fig. 5.5, 12 of the 17 cases giving a negative flooding response can be seen above the flooding curve. Only 5 of 17 cases giving a negative flooding response were positioned under the flooding curve and showed agreement with the Smoot *et al.* (1959) correlation. Furthermore, 3 of those cases existed under the curve (at Af = 0.06875, 0.11 and 0.125 ms^{-1}; $U_d + U_c$ = 0.01 ms^{-1}) at pulse velocities higher than two flooded cases mentioned previously (at Af = 0.06875 and 0.0275 ms^{-1}; $U_d + U_c$ = 0.01 ms^{-1}). This behaviour is unexpected and shows a return to stability at higher pulse velocities. The flooding curve/surface produced by Smoot *et al.* (1959), as well as

others, produces power-law style decay curve. This information may suggest the relationship should take a parabolic formulation with respect to Af vs. $U_d + U_c$.

The effect of solvent-flow-ratio was investigated on three discrete levels ($U_d/U_c =$ 0.25, 2.125 and 4). At the lower limit where $U_d/U_c = 0.25$, 3 out of 6 cases (50 %) produced a positive flooding response at higher pulse velocities ($Af = 0.065$, 0.11 and 0.125 ms^{-1}). At $U_d/U_c = 2.125$, the 3 out of 13 cases (23.1%) produced a positive flooding repose at the lower-middle pulse velocities ($Af = 0.0275$ and 0.11 ms^{-1}). At the upper limit where $U_d/U_c = 4$, 2 out of cases 6 (33.3%) produced a positive flooding response at the lower-mid and upper-mid pulse velocities ($Af = 0.0275$ and 0.11 ms^{-1}). The effect of solvent flow ratio also points towards parabolic (clearly non-linear) behaviour in producing positive flooding responses with increases in the ratio of dispersed phase to continuous phase feed.

Similarly, the effect of throughput was investigated on three discrete levels ($U_d + U_c = 0.01$, 0.055 and 0.1 ms^{-1}). At the lower limit where $U_d + U_c = 0.01$ ms^{-1}, 2 out of 6 cases (33.3%) produced a positive flooding response at middle pulse velocity range ($Af = 0.06875$ and 0.0275 ms^{-1}). At $U_d + U_c = 0.055$ ms^{-1}, 5 out of 13 cases (38.5%) produced a positive flooding response at two discrete regions of pulse velocities ($Af = 0.02$ and 0.0275 ms^{-1}, and $Af = 0.11$ and 0.125 ms^{-1}). This is a compelling observation as it points towards an 'island of stability' with regards of operation, something that has not been reported in literature before. Lastly, at the upper limit where $U_d + U_c = 0.1$ ms^{-1}, only 1 out 6 cases (16.7%) showed a positive flooding response at a lower-middle pulse velocity ($Af = 0.0275$ ms^{-1}). Again, the results highlight some non-linearity in the flooding response with increases in throughput.

To summarise, the cases investigated produced flooding responses which could not be predicted from the Smoot *et al.* (1959) correlation taken from literature. Particularly, in cases which produced a negative flooding response and were operationally stable. This is shown on Fig. 5.4, wherein, stable cases existed above the flooding curve and vice versa. Some of these observations could be have been consequential of the variation of an additional variable, solvent-flow-ratio, alongside pulse velocity and total throughput. The curve was transformed into a three-dimensional flooding surface factoring all three control variables. This highlighted further the inadequacies of the Smoot *et al.* (1959) correlation, and correlations like it that are formulated from one variable at a time experimentation. When assessing each control variable individually, and with respect to their discrete levels, it became apparent that the behaviour was highly non-linear and potentially parabolic in their mathematical relation. Observations from analysis of the total throughput suggested an island of stability wherein stable operation could exist between regions of flooding at medium throughput.

It is important to note that the above points are only describing what can be

observed from the data set of a limited number of simulation cases. A designed method of varying the controlled operational variables has been used to remove bias and produce a statistically effective spread of variable ranges, see Section 5.2.1. Later in this chapter, interpolation techniques are used to model the scattered data into continuous data sets. The observations above serve as a screening method in order to inform the direction of subsequent analysis.

Table 5.2: Summary of the flooding response and calculated quantities from the volume fraction field.

	Control Variable			**Measured Variable**				
Run	(Af)	$U_d + U_c$	U_d/U_c	Flooding	Stage-Wise ϕ^{*b}	SD	C_V	Plate-Wise ϕ^{*b}
No.	(ms^{-1})	(ms^{-1})	-	Response^{*a}	(%)	(%)	-	(%)
1	0.005	0.055	2.125	0	4.927	10.410	2.113	42.279
2	0.02	0.055	2.125	1	NaN	NaN	NaN	NaN
3	0.05	0.055	2.125	0	5.182	10.587	2.043	33.069
4	0.2	0.055	2.125	0	4.936	10.350	2.097	36.843
5	0.06875	0.01	0.250	1	NaN	NaN	NaN	NaN
6	0.06875	0.01	4.000	0	4.907	10.294	2.098	36.726
7	0.06875	0.1	0.250	0	4.993	10.339	2.071	39.485
8	0.06875	0.1	4	0	5.047	10.381	2.057	40.185
9	0.0125	0.055	0.250	0	5.012	10.377	2.070	38.687
10	0.0125	0.055	4	0	5.082	10.432	2.053	42.171
11	0.125	0.055	0.250	1	NaN	NaN	NaN	NaN
12	0.125	0.055	4	0	5.032	10.565	2.100	37.986
13	0.0275	0.01	2.125	1	NaN	NaN	NaN	NaN
14	0.0275	0.1	2.125	1	NaN	NaN	NaN	NaN
15	0.11	0.01	2.125	0	5.024	10.326	2.055	32.988
16	0.11	0.1	2.125	0	4.998	10.402	2.081	39.664
17	0.0125	0.01	2.125	0	5.021	10.454	2.082	39.078
18	0.0125	0.1	2.125	0	4.982	10.337	2.075	34.327
19	0.125	0.01	2.125	0	4.944	10.118	2.047	43.005
20	0.125	0.1	2.125	0	5.346	10.578	1.978	29.138
21	0.0275	0.055	0.250	0	5.086	10.551	2.074	25.55
22	0.0275	0.055	4	1	NaN	NaN	NaN	NaN
23	0.11	0.055	0.250	1	NaN	NaN	NaN	NaN
24	0.11	0.055	4	1	NaN	NaN	NaN	NaN
25	0.06875	0.055	2.125	0	5.286	10.943	2.070	37.468

[a] A value of 1 reports a positive flooding response where flooding was diagnosed.

[b] Steady-state hold-up is calculated from the instantaneous data field. Flooded runs, by definition, do not exhibit steady-state convergence of hold-up and so are omitted.

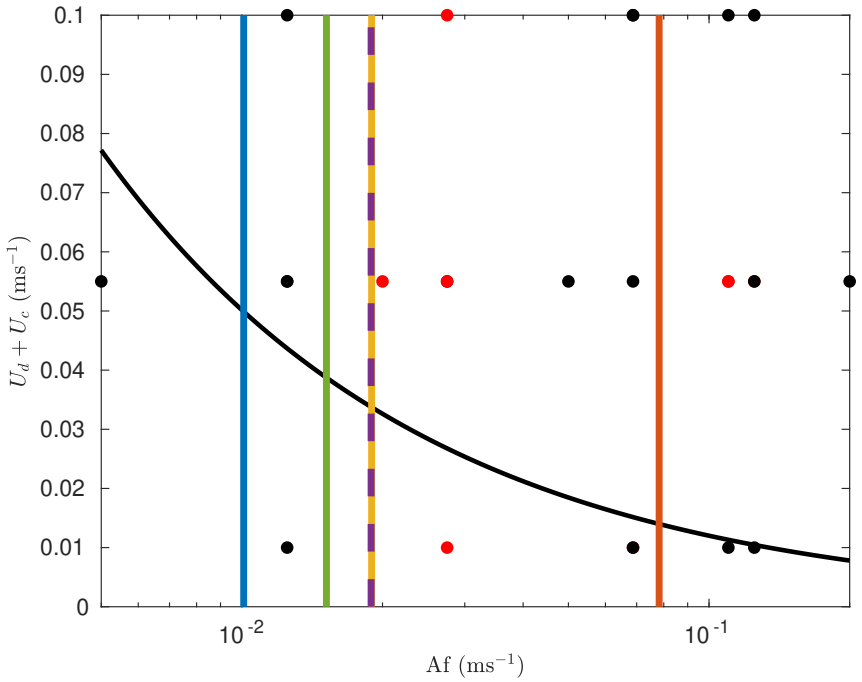

Figure 5.4: Calculated 2-dimensional PSEC flooding curve from Smoot *et al.* (1959) (—) were the simulations showing a negative flooding response (•) and positive flooding response (•) plotted as scattered points. Mixer-settler to dispersion regime transition boundary from Kumar & Hartland (1994) (—), dispersion to emulsion regime transition boundary from Kumar & Hartland (1983)(—), dispersion to emulsion regime transition boundary from Miyauchi & Oya (1965) (—), dispersion to emulsion regime transition boundary from Boyadzhiev & Spassov (1982) (—), dispersion to emulsion regime transition boundary Tung & Luecke (1986) (—).

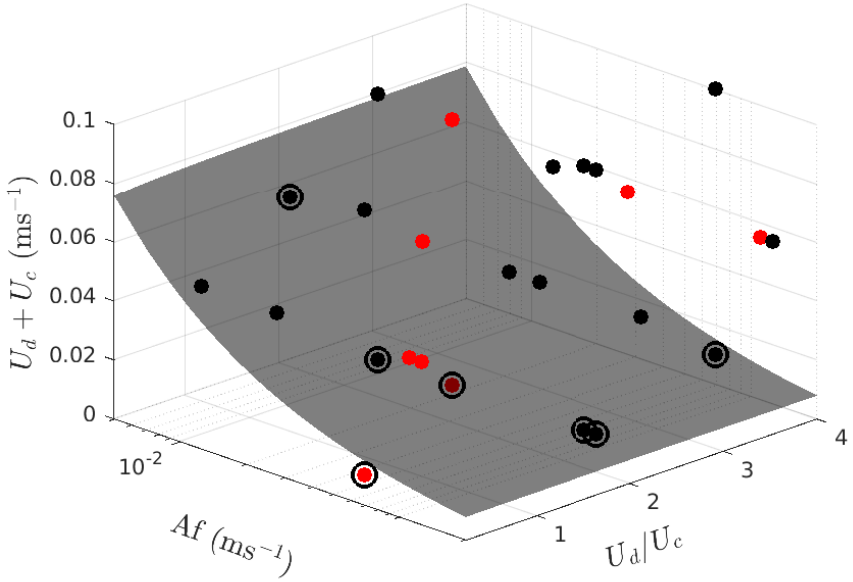

Figure 5.5: Calculated 3-dimensional PSEC flooding surface from Smoot *et al.* (1959) (—) were the simulations showing a negative flooding response (•) and positive flooding response (•) plotted as scattered points. Points that lie underneath the calculated flooding surface have been (○) have been marked for visualisation purposes.

5.5.2 Assessment of the Volume Fraction Fields

An example of the dispersed phase volume fraction (α_d) field for a case producing a positive flooding response (Run 2) as well as cases which produced negative flooding responses (Run 8 and Run 21) have been presented in Fig. 5.6. The latter two cases are included to compare example cases operating at either extreme of the operational range.

Run 2 (positive flooding response) has very similar α_d field characteristics to Run 8 and Run 21 (negative flooding responses). One might expect Run 2 to show high levels of accumulated oil under the plate(s), described in literature as flooding due to insufficient pulsation. However, this characteristic is not observed. Furthermore, in a case producing a positive flooding response, the global hold-up exhibits large fluctuations of gains and losses as the global α_d decreases, see Fig. 5.2. This supports the notion that flooding due to insufficient pulsation is being observed despite low accumulation. The balancing of forces driving the dispersed phase flow are not reaching equilibrium near the plates (Yadav & Patwardhan, 2008). These observations are important because it shows that flooding due to insufficient pulsation can be subtle and occur in instances of low hold-up. Traditionally, this mode of flooding is associated with high hold-up and interpreted as unstable mixer-settler operation. Emulsion flooding is possible where droplets are prevented from rising due to entrainment in the free-stream continuous phase flow. Aspects of emulsion flooding are not observed and so flooding due to insufficient pulsation is identified as the phenomena investigated.

When comparing the two volume fraction fields of Run 8 and Run 21, there are little qualitative differences despite operating at opposite extremes of the control variable ranges. Therefore, examination of the volume fraction field requires a more quantitative approach. For the 17 cases that did not show flooding behaviour, the hold-up, and standard deviation and coefficient of variation of the dispersed phase volume fraction field was calculated for each case individually using the inter-stage volume, see Section 5.3.3. This information has been summarised in Table 5.2.

Fig. 5.7 compares the hold-up and standard deviation of the volume fraction field. The most striking observation is that there is very little quantitative differences in hold-up between all the cases investigated. The lowest hold-up was observed in Run 6 ($\phi = 4.907\%$) and the highest in Run 20 ($\phi = 5.356\%$). This shows only a difference of 0.449% in hold-up when using VOF to model the multiphase behaviour of the PSEC under a wide range of conditions.

Fig. 5.8 compares the relative standard deviations, coefficient of variation (C_V), of each case to provide a comparison of dispersion in each system. A value of $C_V << 1$ would indicate a homogeneously dispersed system. A value of $C_V \geqslant 1$ would indicate a heterogeneous dispersed system where the stage-wise volume hosts a range of α_d values away from the mean. First of all, the C_V is useful in preventing

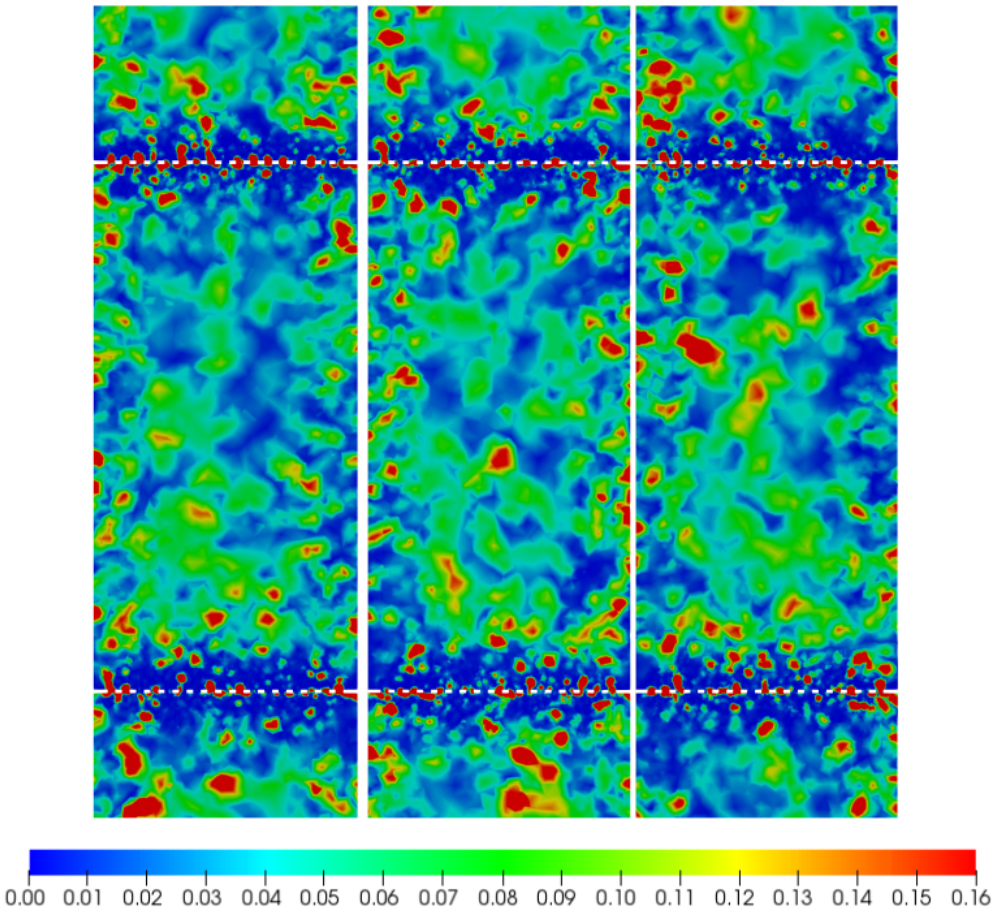

Figure 5.6: Plots of the instantaneous dispersed phase volume fraction field, α_d. Comparison between a case showing a positive flooding response, Run 2 (right), and two runs showing a negative flooding response at either extremes of the operational range investigated, Run 8 (centre) and Run 21 (left). The colour map has been scaled to 0 - 0.16, within the range of one standard deviation, for the purpose of visualising the extent of dispersion.

misinterpretation of observations taken from a plot of the hold-up and standard deviation, Fig. 5.7. For example Run 1 and Run 4 appear to have a smaller absolute range of α_d values to Run 3. The C_V shows, in fact, the opposite is true. The C_V of Run 3 is lower than that of Run 1 and 4. Therefore, Run 3 has a smaller range of α_d values from the mean value (the stage-wise hold-up) and thus indicates closer to mono-dispersion in the system, over Runs 1 and 4. Again, only minor differences in the extent of dispersion are seen in Fig. 5.8. The lowest C_V was observed in Run 20 (1.978) and the highest in Run 1 (2.113). This shows only a 0.135 difference in C_V. For reference, this is minor increase 6.83% in the C_V from Run 1 to Run 20. It is difficult to asses the significance of a particular C_V value when taken out context. Moreover, this detail of statistical analysis is seldom seen in VOF post-processing. What is known is that in every case the majority (1 standard deviation) of α_d values between the plates occupy values of 0 - 16%, $\frac{4}{25}$ of the theoretical range.

This indicates that the system is not well dispersed. However, this is not to be confused with diffusiveness. All cases show a mean of $\alpha_{d,cell} = 5\%$ which indicates all system are very diffuse in nature and there is little occupied volume wherein pure organic phase exists (where $\alpha_d = 1$).

The above observations can be used to provide a quantitatively informed assessment of the mode of operation observed in each case. As well as serving as a comparison against literature for flooding observations, Fig. 5.4 also includes various regime transition correlations for different modes of operation. The equations used to construct these boundaries, Table 2.1, have been previously reviewed in Section 2.2.2. In all 17 stable simulation cases investigated, only dispersion regime operation was observed. This is characterised by 'low' stage-wise hold-up and a largely diffuse field of dispersed phase fluid, with little-to-no dispersed phase collecting under each plate (Yadav & Patwardhan, 2008).

In summary, for stable runs little difference was observed in the calculated metrics for hold-up and extent of dispersion. For both the stable and flooded runs, little differences could be observed qualitatively between the plots of the dispersed phase volume fraction field. This is a particularly informative observation with regards to discussions of flooding within PSECs. The method used here to identify flooding at these time scales is quantitative and analytical in nature, (see Section 5.3.1). However, the literature clearly shows that many previous investigators rely on observation of the flow to determine flooding using visual cues that are only emergent well past the point of stable operation, (see Section 2.2.3.1).

All stable systems showed dispersion mode operation characterised by low stage-wise hold-up ($\sim$ 5%) and a diffuse dispersed phase volume fraction field. This evidence may indicate that the VOF model fails to provide variability in prediction of modes of operation. However, the VOF model has been useful in providing predictions of flooding due to insufficient pulsation, i.e. surface tension dominated flow behaviour near the plates. For regions of heavily diffuse flow it is likely the wrong approach. Droplet size, slip, and drag are not considered in regions of unresolved VOF. Therefore, all diffuse regions have very similar terminal rise velocities dictated purely by the density difference. Consequently, the residence time, and therefore hold-up, of the dispersed phase fluid is likely to be consistent despite variation to the PSEC operational conditions. This clearly highlights a need for the exploration of other multiphase approaches for the study of stage-wise hold-up, potentially requiring the development of new ones. This will be chiefly addressed and form the basis of Chapter 6.

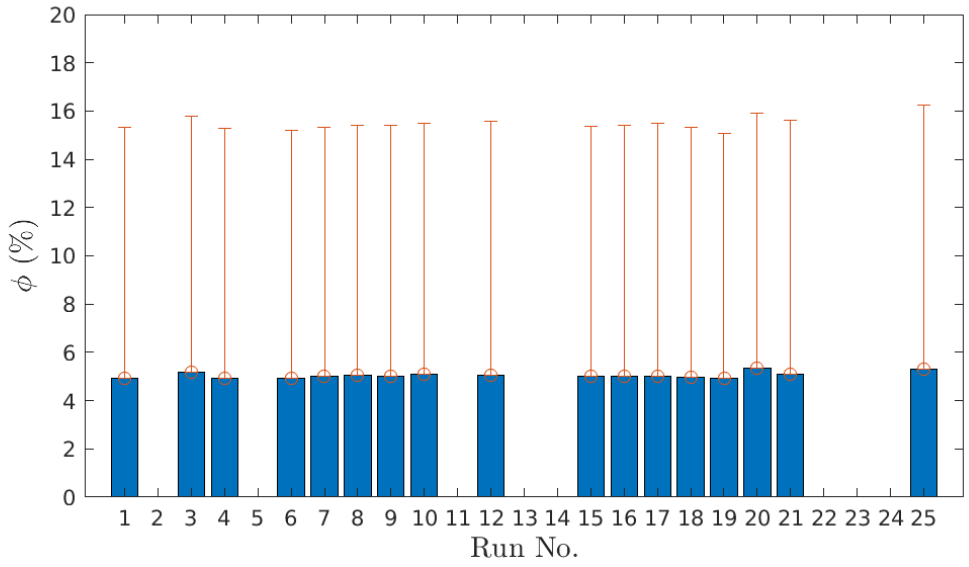

Figure 5.7: Bar plots to visualise the variation in hold-up between runs. The calculated standard deviations have been included as range bars. Simulations were positive flooding response was identified have been excluded.

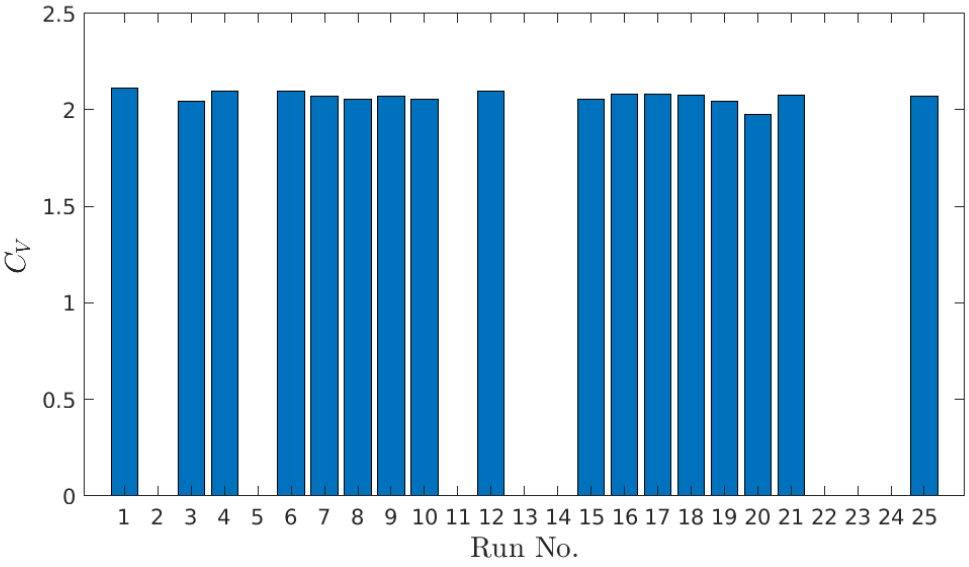

Figure 5.8: Bar plots to visualise how the coefficient of variation between runs. Simulations were positive flooding response was identified have been excluded.

5.5.3 Plate Study and True Flooding Surface

It was concluded from an assessment of the volume fraction field, Section 5.5.2, that the VOF method was capable of providing predictions of flooding. This is due to explicitly resolving the dispersed phase interface(s) around the sieve-plate(s), consequently, capturing their physics. This observation was explored further with the concept of resolving a 'true flooding surface' using the plate-wise hold-up in Table 5.2.

The objective is to use interpolation to map the region of instability within the investigated three-dimensional operational range. The result will be a three-dimensional operational 'volume', with respect to conditions of Af, $U_d + U_c$ and U_d/U_c, where flooding is thought to occur. The extents of the region of instability is then marked via an isosurface. This produces an explicit three-dimensional flooding curve, i.e. a true flooding surface, for the system studied. The novelty of this method is not use dimensional analysis to curve fit a two-dimensional operational boundary, as in done in literature. Here, one seeks to quantitatively resolve the operational region of instability. This can provide insight into the physical relationships of the controlled operational variables and the hydrodynamic phenomena of flooding. Although simple in concept, an example of this is yet to be seen in published literature for PSECs or similar.

For the the interpolation, the dispersed phase hold-up within the sieve-plate holes was taken as a single averaged value. This was calculated using the method outlined in Section 5.3.3 and is described as the plate-wise hold-up. The philosophy is that the predictions of flooding could be related to the balance of both phases occupying a share of the fractional free area of the sieve-plate(s).

For this study, the flooded points are considered as NaN values. Physically, the global hold-up does not converge under flooding conditions. The nearest-neighbours method was first used as a screening method to observe how the plate-wise hold-up develops towards flooding. The method is explained in Section 5.4.1. The modelled data is mapped on the three-dimensional grid in Fig. 5.9. The nearest-neighbours method was successful in providing a zeroth-order approximation of the plate-wise hold-up near observed points of flooding. In certain planer regions, only one point is used to model the data for the surrounding points. In some cases this extends through a whole range. This is seen prominently on the first slice (Row 1, Plot 1) and results in the values surrounding the flooding region, NaN grid-points, is not consistent around its parameter. Moreover, although this method is not used to map to true flooding surface, it produces clear over-approximation of interpolating the extents of the flooding grid-points. However, it can be seen that the method suggests the plate-wise hold-up decreases towards points of flooding. This observation is most clear in the centre slice plots (Row 1, Plot 2; Row 2 Plot 2; Row 3 Plot 3). The centre region of the grid is where the flooded points are most dense. Here the majority of

the boundaries with flooded grid-points show the lowest predicted plate-wise hold-up. This relationship can now be used to inform the method of interpolation for a first-order continuous method.

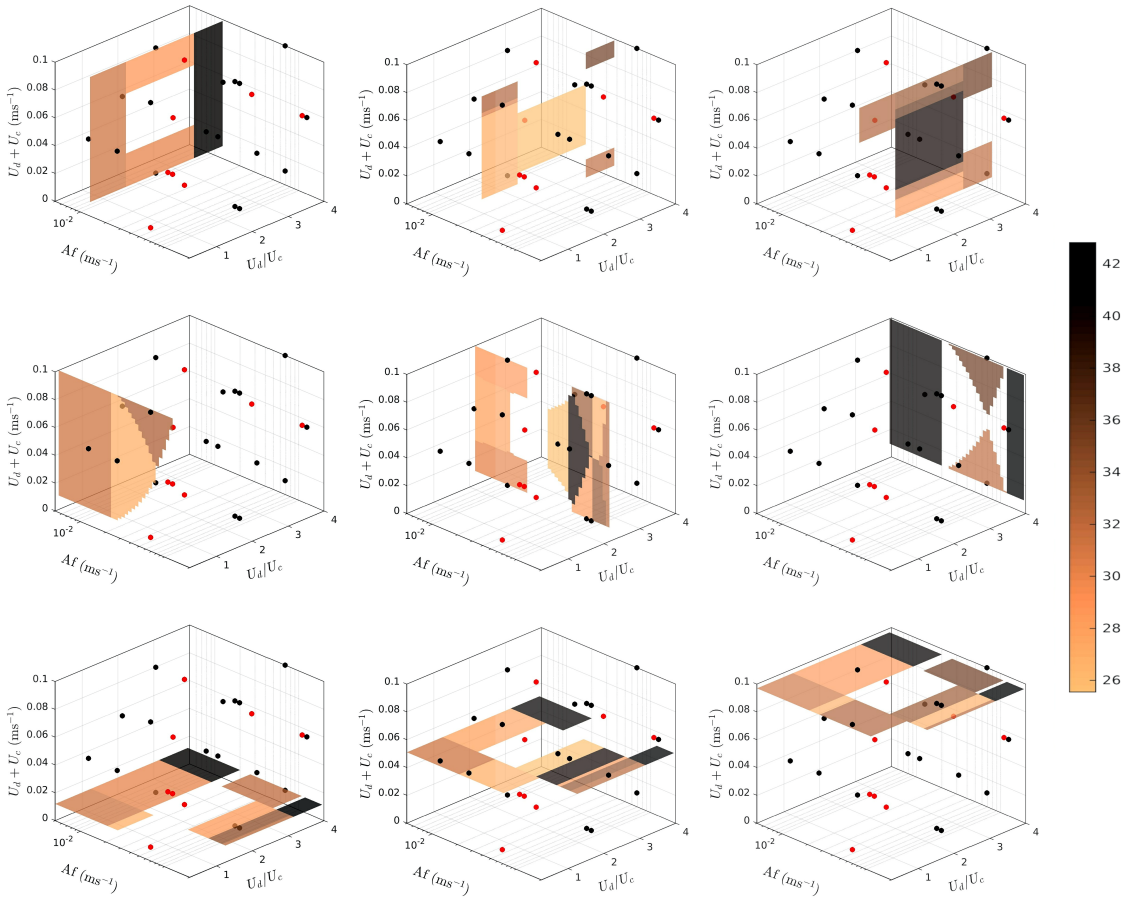

Figure 5.9: Nearest-Neighbours interpolation of the plate-wise hold-up data for stable cases into three-Dimensional modelled gridded data. Points are included to represent negative flooding responses (●) and positive flooding responses (●).
Colour map shows the plate-wise hold-up in %.
Rows represent slices moving through one planar dimension.
Row 1: $U_d + U_c$ vs. U_d/U_c for changes in Af.
Row 2: $U_d + U_c$ vs. Af for changes in U_d/U_c.
Row 3: Af vs. U_d/U_c for changes in $U_d + U_c$.

Next, linear interpolation was used to provide unique values for each point of the modelled grid-point data. In this method the flooded points are assigned a value below the minimum observed plate-wise hold-up, i.e. $min(\phi) - min(\phi)0.1$. Now values exist at each scattered point. Grid-point values between each scattered point can be calculated to produce linear gradients using Delaunay triangulation. Subsequently, an isosurface is plotted at $min(\phi) - min(\phi)0.05$ and all values below $min(\phi)$ are reassigned back to NaN values. This results in a conservative plot of the isosurface surrounding the flooded grid-points. The results of the interpolation are plotted in Fig. 5.10 in the same fashion as in Fig. 5.9. The full isosurface has been isolated and plotted from different viewing angles in Fig. 5.11.

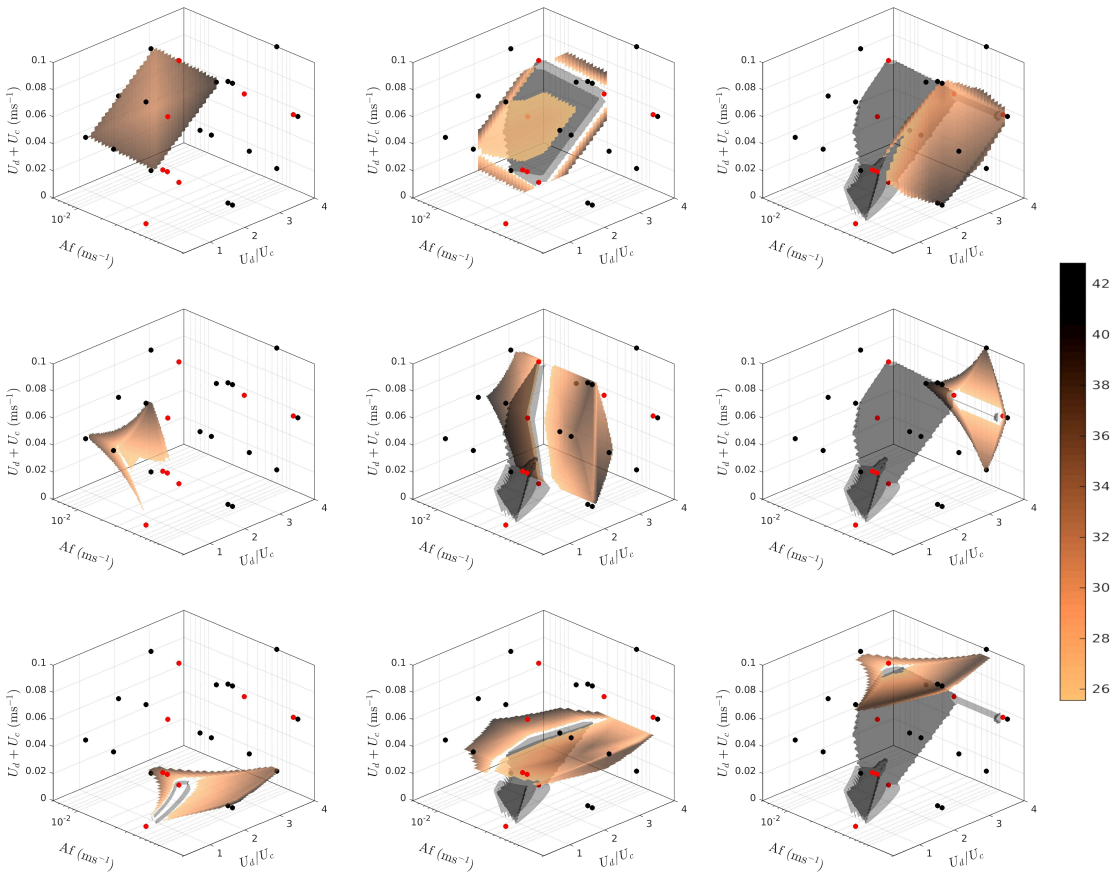

Figure 5.10: Linear interpolation of the plate-wise hold-up data for stable cases into three-Dimensional modelled gridded data. Points are included to represent negative flooding responses (•) and positive flooding responses (•).
Colour map shows the plate-wise hold-up in %.
Rows represent slices moving through one planer dimension.
Row 1: $U_d + U_c$ vs. U_d/U_c for changes in Af.
Row 2: $U_d + U_c$ vs. Af for changes in U_d/U_c.
Row 3: Af vs. U_d/U_c for changes in $U_d + U_c$.
Black isosurface represents unstable region where flooding is predicted to occur based on the modelled data.

The linear interpolation was successful in incorporating the observations of the nearest-neighbours analysis, and providing reasonable predictions in the modelled data. Namely, by producing consistent behaviour towards the flooding boundary. It is worth noting that linear interpolation is a point-point method and so will not provide values for grid-points outside of the explicit operational limit investigates. This is unlike nearest-neighbours method and is why there is a particular structure in the slices shown in Fig. 5.10. The relationships with plate-wise hold-up are seen to be highly non-linear, with respect to one control variable, and can differ depending on particular combinations of the control variables. However, some generalised observations can be made. The plate-wise hold-up is seen to be highest at high and low values of Af. It also tends to be higher at mid to high values of U_d/U_c.

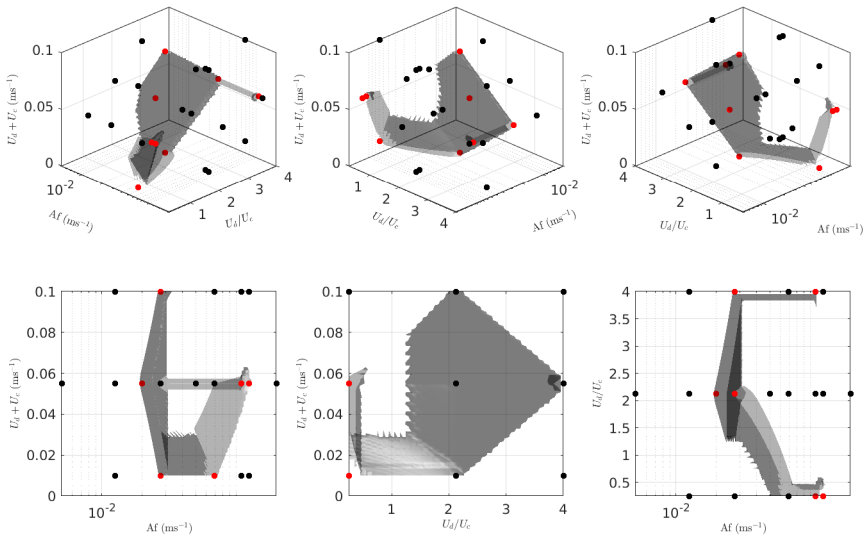

Figure 5.11: Isosurface of the unstable region calculated via linear interpolation of the plate-wise hold-up data. Multiple viewing angles have been provided.

With regards to the flooding surface, Figs. 5.10 and 5.11 show that a distinct region of instability exists within the centre of the plot and extends to certain extents of the operational range. Quantitatively, flooding is observed most at: $0.05 < Af < 0.1$, $1 < U_d/U_c < 2.25$, and $0.04 < U_d + U_c < 0.07$. The region of instability is thin within the Af range investigated. At low Af flooding appears to be easily avoidable. Similarly, high U_d/U_c at high and low $U_d + U_c$ produce stable systems. Flooding seems to be more influenced by Af and U_d/U_c rather than $U_d + U_c$. This is the most noticeable on the Row 2 views of Fig. 5.11. Here, regions can be seen where flooding is unavoidable regardless of the $U_d + U_c$. The isosurface does not show any form of symmetry and is unique. This quality proves that it is unfeasible to provide a prediction of flooding using only simple functions which are heavily depended on in published literature (Yadav & Patwardhan, 2008). Moreover, for flooding to occur, required are a particular combination of the control variables that lead to instability.

In summary, interpolation methods were successful in providing a conservative mapping of the regions of instability. This analysis was based on the plate-wise hold-up data collected from a simulation campaign of 17 stable cases. The nearest-neighbours analysis could highlight the main behaviours of the plate-wise hold-up towards flooding. Subsequently, linear interpolation could then provide a resolved flooding surface. It highlighted the complexity and non-linearity of the control variables effecting the stability of the system, but showed that some clear relationships could be extracted. Most notability, that flooding was observed is unavoidable in the the mid pulse velocity ranges. The analysis uncovered the complexity of flooding phenomena that literature sources can not capture using two-dimensional flooding limit functions, namely, those reviewed in Section 2.2.3.

5.5.4 Pressure Field Flooding Diagnostics

One objective of this chapter was to use statistical methods to provide diagnostics of the stability of the PSEC under certain conditions. Analysis in Section 5.5.3 has shown that it is impracticable to use the three control variables (Af, $U_d + U_c$, U_d/U_c) to form predictive tools for flooding. Therefore, analysis of the pressure field was explored. This serves as a means of reducing the degrees of freedom to a variable commonly measured already in industrial systems. The observations of the instantaneous pressure field, summarised Table 5.3, was used from all 25 cases in building the logistic models. Specifically, the mean pressure between the sieve-plates ($P-\rho gh_{Mean}$), the maximum pressure found at each sieve-plate ($P-\rho gh_{Max,TP}$, $P-\rho gh_{Max,BP}$), and the pressure drop with respect to each phase ($\Delta P_d, \Delta P_c$) taken as the difference of the inlet and outlet pressures. More details on how these variables were calculated in post-processing are mentioned in Section 5.3.2.

The method of logistic regression is discussed in Section 5.4.2. A log odds model is created using the logistic function and transformed to output the probabilty of flooding given certain predictor variables. In this case, variables of the pressure field

Table 5.3: Summary of the flooding response and calculated quantities from the pressure field.

Run No.	Flooding Response[a]	$P-\rho gh_{Mean}$ (Pa)	$P-\rho gh_{TP,Max}$ (Pa)	$P-\rho gh_{BP,Max}$ (Pa)	ΔP_d (Pa)	ΔP_c (Pa)
1	0	126	1866	1087	111	3667
2	1	115	1833	1147	101	3558
3	0	131	1851	1019	113	3672
4	0	128	1869	1065	106	3671
5	1	133	1857	1153	110	3665
6	0	128	1853	1149	108	3670
7	0	129	1858	1056	109	3667
8	0	128	1873	1092	113	3670
9	0	110	1837	1119	91	3556
10	0	131	1868	1087	113	3669
11	1	138	1867	1170	115	3665
12	0	130	1881	1143	107	3668
13	1	131	1877	1138	117	3672
14	1	125	1868	1020	106	3664
15	0	129	1871	1115	112	3669
16	0	130	1879	1046	109	3670
17	0	129	1857	1157	108	3673
18	0	128	1873	1166	112	3673
19	0	128	1857	1133	115	3672
20	0	138	1865	1079	109	3680
21	0	133	1854	1080	108	3667
22	1	135	1897	1127	117	3672
23	1	133	1899	1183	114	3665
24	1	133	1899	1183	114	3665
25	0	131	1850	1103	111	3665

characteristics are used. All pressure variables were normalised and outliers were removed using the techniques mentioned in Section 5.4.3. The logistic model takes the form of:

$$Probability_{Flooding} = \frac{1}{1 - e^{-f}} \tag{5.10}$$

where the function (f) is a linear model derived from non-interacting variables. Since the pressure characteristics themselves are resultant qualities of the system, it is unlikely they are interacting, and so a linear model assumption is valid. However, for completeness, linear regression was performed on a number of variables, including with themselves, to screen for correlation and dependence. This screening is provided as supplementary evidence in Appendix A.

A number of logistic models were produced for this analysis and are listed below. The model the coefficient (β_i) and their cosponsoring p-values are included in Table 5.4.

Single variate models:

$$\text{I} \quad f = \beta_0 + \beta_1(P - \rho g h_{Max,BP})$$

$$\text{II} \quad f = \beta_0 + \beta_1(P - \rho g h_{Mean})$$

$$\text{III} \quad f = \beta_0 + \beta_1(P - \rho g h_{Max,TP})$$

$$\text{IV} \quad f = \beta_0 + \beta_1 \Delta P_d$$

$$\text{V} \quad f = \beta_0 + \beta_1 \Delta P_c$$

Multivariate models:

$$\text{VI} \quad \begin{aligned} f = &\beta_0 + \beta_1(P - \rho g h_{Max,BP}) + \beta_2(P - \rho g h_{Mean}) + \beta_3(P - \rho g h_{Max,TP}) \\ &+ \beta_4 \Delta P_d + \beta_5 \Delta P_c \end{aligned}$$

$$\text{VII} \quad f = \beta_0 + \beta_1(P - \rho g h_{Max,BP}) + \beta_2(P - \rho g h_{Max,TP})$$

$$\text{VIII} \quad f = \beta_0 + \beta_1(P - \rho g h_{Max,BP}) + \beta_3(P - \rho g h_{Mean}) + \beta_3(P - \rho g h_{Max,TP})$$

$$\text{IX} \quad f = \beta_0 + \beta_1(P - \rho g h_{Max,BP}) + \beta_3(P - \rho g h_{Mean})$$

$$\text{X} \quad f = \beta_0 + \beta_1 \Delta P_d + \beta_2 \Delta P_c$$

Table 5.4: Summary of the logistic model coefficients and their statistical p-values.

Model	β_i	**p-value**$_i$
I	[4.416; -0.062]	[0.014; 0.033]
II	[2.464; -0.037]	[0.023; 0.075]
III	[2.927; -0.034]	[0.038; 0.086]
IV	[-0.657; 0.051]	[0.452; 0.073]
V	[2.824; -0.039]	[0.025; 0.062]
VI	[439.205; -8.594; -1.085; -0.339; 12.015; -4.464]	[5.612×10^{-321}; 7.148×10^{-298}; 5.346×10^{-38}; 2.1556×10^{-10}; 0; 1.45 $\times10^{-315}$]
VII	[5.241; -0.054; -0.022]	[0.013; 0.079; 0.302]
VIII	[5.879; -0.051; -0.025; -0.017]	[2.534; -1.535; -1.181; -0.738]
IX	[5.397; -0.058; -0.028]	[0.011; 0.070; 0.168]
X	[1.820; 0.117; -0.082]	[0.231; 0.044; 0.038]

The univariate logistic models I-V were built and assessed first. It is understood that single variable models are likely to be weakly correlated and not particularly robust. Therefore, this stage of modelling was used as a screening process for each variable and to assess the feasibility of the technique before looking into more complex models. Each of the resultant models are plotted in Fig. 5.12 as static sigmoid curves for assessing the probability relationship with flooding. The positive and negative flooding responses, for each case, have been included as binary values 1 and 0 respectively. The p-values, listed in Table 5.4, show that all variables are close to the standard 5% significance level. Notably, All models except IV show a negative relationship with probability of flooding. This is denoted by negative coefficient values in front of their variable terms and seen clearly in Fig. 5.12. Moreover, all models to do not produce steep sigmoid slopes. This suggests flooding is uncertain within the range of operation investigated. For each model, the binary response is unique and, in some cases, difficult to model leading to a weak relationships and uncertainty. Model I is the only model shown to have statistical significance with respect to flooding. Here, p-value$_{P-\rho gh_{Max,BP}}$ = 3.33%. However, flooding can only be predicted with certainty if the maximum pressure drop at the bottom plate is below that of the minimum range tested, or vice versa. This is not particularly useful or robust for flooding diagnostics in a practical scenario. Nevertheless, this first stage of analysis was successful in identifying significance.

Next, a series of multivariate models, VI-X were built and analysed. Initially, a full five variate model was built incorporating all the characteristic pressure variables. The p-values and coefficients for model VI, listed in Table 5.4, indicate

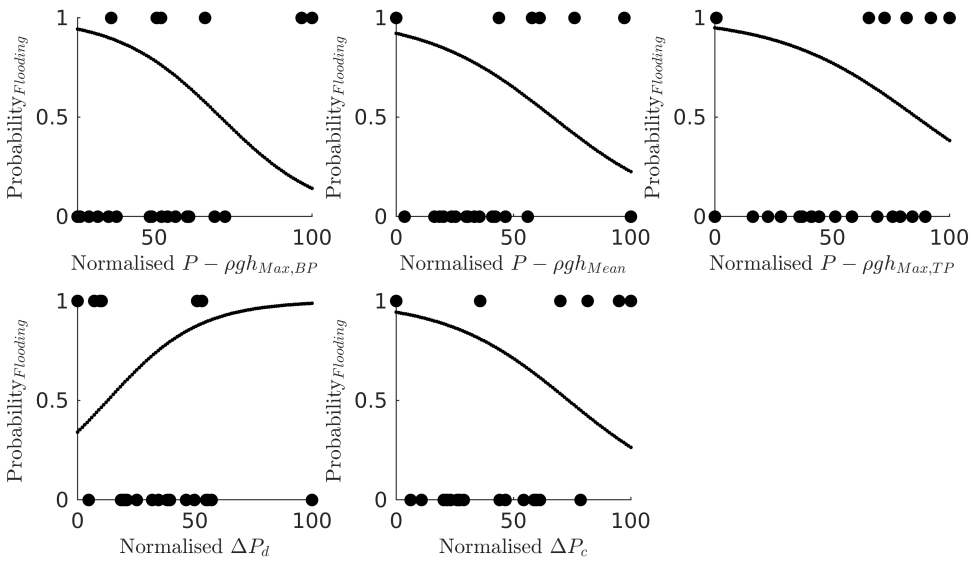

Figure 5.12: Sigmoid plots for univariate logistic models I - V. The sigmoid curve is static and used to predict the probability of flooding for a given value of the single predictor variable.

that the method was unsuccessful in providing a sensical model to predict the probability of flooding. The intercept coefficient term is much larger than those created in the univariate models ($\beta_0 = 439.205$). Moreover, the p-values for each term are very close to 0%. The p-values could be misinterpreted as indication of high significance. However, when assessed in conjunction with the large intercept coefficient, it is clear the model was unsuccessful in forming a usable model.

An alternative approach was then taken to group variables into logical combinations. Models VII, VIII and IX are models combining characteristics of the internal pressure field ($P - \rho g h_{Max,BP}$, $P - \rho g h_{Max,TP}$ and/or $P - \rho g h_{Mean}$). Model X is a grouping of the boundary pressure field characteristics, the pressure drops calculated from the inlet and outlet pressures (ΔP_d and ΔP_c).

The logistic regression was successful in creating models VII, VIII and IX with reasonable coefficients. However, their p-values reveal that none of these three models showed statical significance (p-value $< 5\%$) for all the variables included. Most notability, model VIII performed the worse when all three variables are included, and is arguably a failed regression due to non-physical p-values > 1. Limiting the system to a two variable model showed greater success. Model IX performed much better VII when $P - \rho g h_{Mean}$ is included instead of $P - \rho g h_{Max,TP}$. However, even in model IX, p-value$_{P-\rho g h_{Mean}} = 16.8\%$ and is above the acceptable statistical significance level. Finally, model X was the most successful and provides reasonable model coefficients and all p-values $< 5\%$.

Fig. 5.13 is a plot of the dynamic sigmoid curve for model X. The plot can be used to predicted probability of flooding is for values of ΔP_d, but has been recalculated for a range of ΔP_c values. Instances of the recalculated curve are provided and show

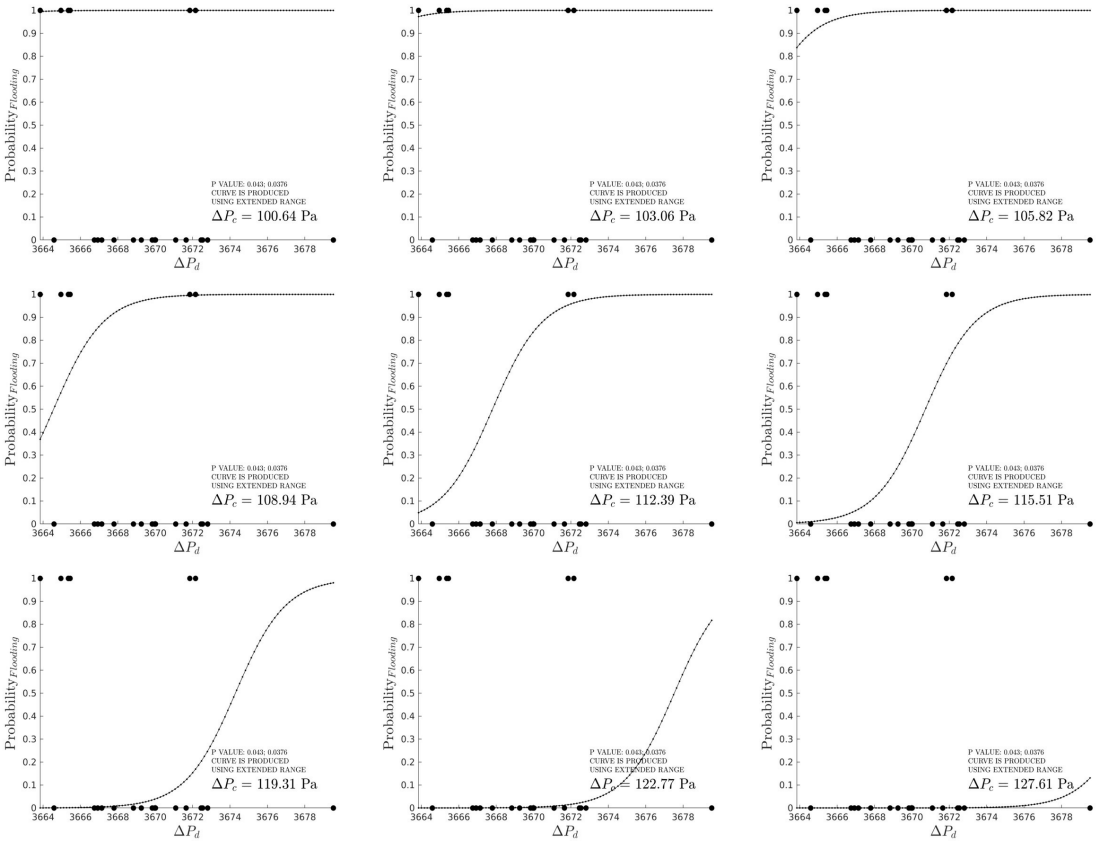

Figure 5.13: Sigmoid plot for multivariate logistic model X. The sigmoid curve is dynamic used to predict the probability of flooding for a given ΔP_d. The curve must be recalculated for the full range of ΔP_c, instances are given for visualisation. Normalised values have been used to build model X but the original data-set values have been included for context.

the curve collapsing as ΔP_c increases. Moreover, the range has been extended to provide a predication through to full collapse of the sigmoid function (Row 3 Plots 2 and 3). Firstly, the term coefficients, in Table 5.4, show that ΔP_d has the greatest influence on the probability of flooding, having a larger coefficient term. Also, the sign of the coefficient terms indicates that as ΔP_d increases the probability of flooding increases, whilst ΔP_c has the opposite effect. It can be seen from Fig. 5.13 that the system is extremely likely to flood until a critical lower ΔP_c limit is reached (for the ΔP_d operational Ranges investigated). Conversely, at a higher critical limit of ΔP_c flooding is extremely unlikely to occur. Lastly, model X produced a sigmoid curves with steep slopes. This shows a strong and robust relationship. This feature is best represented in Fig. 5.13 (Row 2 Plot 3; Row 3 Plot 1).

An attempt was made to see if there are any direct correlations between the pressure characteristics and the operational variables Af, U_d+U_c and U_d/U_c. Linear regression models, included in Appendix A, did not indicate anything noteworthy in this regard. The analysis here has highlighted, for the first time, the importance of the pressure field characteristics in understanding and predicting PSEC behaviour. Therefore, future PSEC research should incorporate a focus on these variables.

In a practical scenario, the conclusions from this analysis have brought to light new implications of PSEC control and optimisation. What has been demonstrated is that low-cost logistic models can be built from a limited data set, in this case of 17 stable and 8 flooded systems. A logistic model can then be used to diagnose and/or predict the stability of the PSEC systems. All that is required is information of their boundary stream pressure drops, information that is typically monitored anyway. The analysis shows that the potential for flooding decreases with increases in the continuous phase pressure drop or with decreases in the dispersed phase pressure drop. In the context of this study, the pressure drops are regarded as dependent variables. In reality these variables can be manipulated via alterations to the downstream or upstream process conditions. Some examples may include flow constriction at the inlet or outlet streams, feed stream pressurisation or alternate sieve-plate design. Most importantly, pressure characteristics have seldom seen any recognition in discussions of PSEC flooding. This study has explicitly investigated the statistical significance of pressure variables on the state of operation of PSECs. Namely that of the first sieve-plate peak (maximum) pressure and the compound relationship of continuous and dispersed phase pressure drops.

5.6 Conclusions

A simulation campaign of 25 CFD runs was undertaken to asses the behaviour of PSECs with unique combinations of operational conditions. The VOF multiphase model was used in combination with the highly accurate, but expensive, LES turbulence resolving method, the merits of which have been justified in Chapter 4. To date, a CFD analysis of PSECs has never been undertaken on a scale of this magnitude.

The work presented within this chapter has yielded a wealth of information regarding the nature of PSECs and their operation. The analytical methods used have demonstrated value and a feasible framework of analysis for complex industrial systems with limited resource. The methods have been successful in uncovering trends and relationships between PSEC hydrodynamic phenomena and their operational variables, which have not been discussed in this level of detail previously.

Most notably, a method of providing a clear distinction of flooding within PSECs was defined and tested. As mentioned in Section 5.3.1, the global hold-up was tracked during the simulation for a significant amount of operational time. Flooding was identified when the hold-up became consistently non-convergent. It was clear that for certain combinations of operational conditions the system was unstable and this criteria was clearly apparent showing that there is likely a tipping point wherein flooding suddenly occurs. This contrasts to definitions of flooding from observation of the flow, such as when the phenomena of carry over is observed in the process (see Section 2.2.3.1). This tipping point is thought to be driven by the physics of the flow occurring at the sieve-plates. Namely, the balance of interfacial forces between accumulations of dispersed phase under the plates and the momentum of the continuous phase attempting to cross the plates. However, more fundamental research is required in order to pin-point the root causes of flooding. Nevertheless, a numerical definition of flooding can now be used to identify flooding explicitly and will be fundamental to the development of control systems used to mitigate flooding. Specifically, if an on-going average of the hold-up (ϕ) during operation is nonconvergent ($d\phi_{ave}/dt \neq 0$) then flooding is occurring.

This research has also highlighted the importance of droplet modelling, or lack thereof, in the appropriateness of VOF style multiphase models. The evidence provided by this computationally expensive simulation campaign now provides unquestionable justification for the development of more complex multiphase models. This is basis of motivation for the next chapter of this thesis Chapter 6.

The conclusions produced from a limited simulation campaign for heavily dispersed phase flows in PSECs using a VOF LES model are as follows:

1. Flooding could be successfully identified by diagnosing the convergence and

behaviour of the transient global dispersed phase hold-up.

2. The observed flooding events showed non-linear behaviour that could not be described or predicted by traditional means proposed in literature. Namely, when plotted against the empirical flooding curve correlation proposed by Smoot *et al.* (1959).
3. It was observed that the VOF method produces consistent hold-up behaviour as a consequence of unresolved (or modelled) droplet dynamics in regions of diffuse interfaces. Hold-up is, therefore, thought to be consequential of the residence time which is dictated by the force balances between the droplet and continuous fluid interface(s) which are missing in unresolved VOF.
4. The VOF method was unable to model regime transitions due to the limited range of stage-wise hold-up predictions.
5. A combination of zeroth and first order interpolation methods could be used in the development of a resolved 'true flooding surface' that maps out the operational envelope of instability.
    - Instability was heavily dependent on combinations of variables.
    - Pulse velocity and solvent flow ratio were thought to influence instability more so than throughput.
    - At low pulse velocities, instability was not observed. Similarly, at low and high solvent-flow-ratios instability was not less apparent.
    - There where regions were a combination of pulse velocity and solvent-flow-ratio made instability unavoidable regardless of the throughput.
6. Linear regression analysis of the pressure field variables allowed for an initial screening of potential interaction effects. The measured pressure variables showed no interactions effects, therefore limiting flooding analysis to linear regression methods.
7. Univariate and multivariate linear logistic regression was performed for all measured pressure variables against observations of flooding which could identify useful variables for prediction of flooding phenomena.
    - The peak pressures at the bottom plate showed statistical significance for prediction of the probability of flooding but the resulting model was weakly correlated. No multivariate model for peak and or mean operating pressures, could show statistical significance for all variables included.
    - A multivariate model included the grouped pressure drop variables showed statistical significance for all variables included. The model was as able to provide definitive predictions at the extremes of the models when examined dynamically.
    - The dispersed phase pressure drop was found to have the greatest potential for predicting the likelihood of flooding when measured in conjunction with the continuous phase pressure drop.

- A high continuous phase pressure drop is likely to indicate stable operation.
- A high dispersed phase pressure drop is also likely to increase the probability of flooding.
- However, the pressure drop found to have no direct correlation to operational variables.

6

Multiphase Modelling of Dispersed Multiscale Flows in PSECs

6.1 Introduction

Thus far, a single-fluid multiphase model has been used to describe the flow development of immiscible liquid phases in an industrial PSEC geometry. Investigations in Chapter 5 successfully identified the range of applicability of the volume of fluid (VOF) approach. Two notable observations were: that the dispersed phase flow around the sieve-plates could be resolved and led to useful predictions towards flooding phenomena, and that there was little variability of hold-up predictions despite simulating an excessive range of conditions. The latter is thought to be a result of the absence of drag corrections for the momentum of the dispersed phase where the interface cannot be fully resolved. This restricts variability of the slip velocity, residence time and, therefore, hold-up of droplets within dispersed regions of the column. Clearly, this emphasises the need to explore other liquid-liquid modelling methods within the context of this study.

A review of previous PSEC modelling efforts, in Section 2.3, have highlighted that there has been no specific investigations to determine a suitable multiphase approach in CFD simulations of PSECs. Examples using the VOF method have been published by Mehra & Chaturvedi (2016) and Khatir *et al.* (2016). Others, notability Yadav & Patwardhan (2009) and Alzyod *et al.* (2018), and have chosen to use Eulerian-Eulerian (E-E) two-fluid methods with 3/2-dimensional RANS techniques to predict the transient PSEC flow field description. The latter were useful in showcasing the alternative multiphase approaches. Particularly with inclusion of a population balance and comparisons of the residence time distributions with experimental results (Alzyod *et al.*, 2018). However, as the review (Section 2.3) highlights, there are number of concerns with these implementations. Moreover, the conclusions of Chapter 4 state the requirement of large eddy simulation (LES) techniques in predictions of the flow.

As mentioned, there are concerns of the applicability of VOF in predictions in

coarse-mesh regions. However, resolving the interface is still necessary close to the sieve-plates for the simulation of flooding phenomena. Conversely, the E-E examples in literature have shown their usefulness in simulating dispersions in PSECs, but could struggle to perform well in the sieve-plate regions where the phases become segregated and surface tension dominates. Outside of PSEC research, there are number of novel examples in literature attempting to merge both approaches into a hybrid E-E/VOF *'multiscale'* implementations. This is typically done by building on a two-fluid E-E framework with the addition of resolved interface treatments and/or flow regime dependent interface momentum exchange models along with blending functions.

An early example of multiscale dispersion modelling is that by Tomiyama & Shimada (2001). This is an E-E model which uses a number of additional phases to characterise intermediate dispersed phase regimes. Each additional phase can be defined with unique interface momentum exchange descriptions. Although this is not a coupled E-E/VOF example, it describes one of the first attempts to locally account for variability of the dispersed phase regime.

Elsewhere, Cerne *et al.* (2001) sought to directly couple the VOF and E-E approaches via the mutually similar volume fraction field description. Here, a simple switching function is used to determine weather a given mesh-cell should operate within a VOF or E-E model based on defined thresholds of the volume fraction. Although not explicitly explained, this method by definition involves switching between the different formulations of the momentum equations (single or two-fluid) which could ultimately lead to numerical instability and inconsistencies. Moreover, there are self-reported issues within the VOF mode when chunks of dispersed phase, that are larger than 6 cell-lengths, approach each other. Subsequently, the switching criterion from Cerne *et al.* (2001) was adopted in a hybrid E-E/level-set model by Štrubelj & Tiselj (2011). Here, the level set is used to sharpen the interface of the E-E method in stratified regions.

Most recently, Wardle & Shonibare (2015) used descriptions of these methods to implement an E-E/VOF hybrid using the interface sharpening method of Weller (2008) within the two-fluid framework developed by Rusche (2002) under the OpenFOAM® general public licence, see Section 3.2. This was then further developed at the University of Leeds by De Santis *et al.* (2020) for use in the R&D of solvent extraction processes. It has been named generalised multiphase modelling approach (GEMMA). A comprehensive description of the GEMMA model is provided in Section 3.2.3.

The objective of this chapter is to provide considerable improvements to the multiphase modelling approach of PSECs. Namely, in faithfully representing the duality of the coexisting large-interface and dispersed-interface multiphase behaviours. The concept of a multiscale approach will be applied with the novel

hybrid VOF/E-E GEMMA model. Furthermore, the reduced one primary one secondary particle method (OPOSPM) population balance, coupled within the GEMMA implementation, will be included. This was introduced, with respect to PSEC modelling, by Alzyod *et al.* (2018). However, here it is coupled with the appropriate LES methods which is necessary for predicting the 3-dimensional turbulence properties which drive the breakage and coalescence kernels. Moreover, this chapter will serve as the first instance of a dedicated study for the further development of multiphase modelling in PSECs.

A comparison against the previous single-fluid VOF benchmark, analysed in Section 4.2, will be used to ensure large-interface flow characteristics are accurately represented by the two-fluid GEMMA model. Particularly in regions where the VOF simulation was observed to resolve interfaces sufficiently. Moreover, comparisons are also made against a typical two-fluid E-E style implementation. This example will be used to explore the shortfalls of E-E approach in the absence interface sharpening or population balance.

Additionally, a review of the GEMMA simulation results is performed to scrutinise the in-built modelling mechanisms. Namely, in the performance of the switching mechanism, quality of the interface sharpening and characteristics of the population balance. The latter is of particular interest for further development of GEMMA for use in solvent extraction research.

6.2 Boundary/Initial Conditions and Initialisation

The boundary conditions for both two-fluid simulations are listed in Table 6.1 for the E-E and GEMMA simulations respectively. In each case, the boundary conditions for both fluid velocities (U_c and U_d), pressure (P_{local}) and both fluid volume fractions (α_c and α_d) were specified to mimic those of the VOF simulation previously run in Chapter 4. This is in order to provide a direct operational comparison. Note that the pressure field is shared by both fluids. In both the two-fluid implementations the pressure field also requires referencing (absolute), as so was referenced to standard atmospheric pressure. The additional fields required for the initialisation of the GEMMA simulation are given and labelled in Table 6.1. The E-E simulation was initialised in the same way as the VOF with respect to the custom outlet pressure boundary condition and volume fraction field(s) interface height, see Section 4.2.2. The GEMMA model was initialised using the converged solution from the E-E simulation. The fluidic properties of the two fluids were kept the same across all simulations, see Section 4.2.1 for details.

In all cases, LES is used to resolve the flow field. For the E-E implementation, the dynamic Lagrangian sub grid scale model is used in conjunction with the LES. For GEMMA, this option was is not available, and has been noted by the developers. Due to extremely high turbulence resolution, concluded from the VOF LES simulation analysed in Chapter 4, the choice of sub grid scale model is of little consequence in this comparative analysis. Therefore, the available Smagorinsky model was used in conjunction with LES for the GEMMA simulation. Information on the sub grid scale models and their implementation is given in Chapter 3.

Table 6.1: Summary of boundary conditions used in E-E and GEMMA simulation.

	α_c	U_c (ms^{-1})	$\mathscr{F}_{LM,c}$ ($\mathrm{m}^4\mathrm{s}^{-4}$)	$\mathscr{F}_{MM,c}$ ($\mathrm{m}^4\mathrm{s}^{-4}$)	$\nu_{t,c}$ (ms^{-2})
Heavy Phase Inlet	Fixed value 1	Fixed value (0 0 0.015)	Fixed gradient 0	Fixed gradient 0	Fixed gradient 0
Light Phase Inlet	Fixed value 0	Fixed value (0 0 0)	Fixed gradient 0	Fixed gradient 0	Fixed gradient 0
Heavy Phase Outlet	Outflow: Fixed gradient 0 Return flow: Fixed Value 1	Outflow: Fixed normal gradient 0 Return flow: Calculated from flux	Fixed gradient 0	Fixed gradient 0	Fixed gradient 0
Light Phase Outlet	Outflow: Fixed gradient 0 Return flow: Fixed Value 0	Outflow: Fixed normal gradient 0 Return flow: Calculated from flux	Fixed gradient 0	Fixed gradient 0	Fixed gradient 0
Wall	Fixed gradient 0	No slip	Fixed gradient 0	Fixed gradient 0	Fixed gradient 0
Initialised Internal Field	Non-uniform value	Uniform value (0 0 0)	Uniform value 1×10^{-3}	Uniform value 1×10^{-3}	Uniform value 0
	α_d	U_d (ms^{-1})	$\mathscr{F}_{LM,d}$ ($\mathrm{m}^4\mathrm{s}^{-4}$)	$\mathscr{F}_{MM,d}$ ($\mathrm{m}^4\mathrm{s}^{-4}$)	$\nu_{t,d}$ (ms^{-2})
Heavy Phase Inlet	Fixed value 0	Fixed value (0 0 0)	Fixed gradient 0	Fixed gradient 0	Fixed gradient 0
Light Phase Inlet	Fixed value 1	Time-varying sinesoidal $A = 0.0125$ $f = 1$ $U_{offset} = 0.015$	Fixed gradient 0	Fixed gradient 0	Fixed gradient 0
Heavy Phase Outlet	Outflow: Fixed gradient 0 Return flow: Fixed Value 1	Outflow: Fixed normal gradient 0 Return flow: Calculated from flux	Fixed gradient 0	Fixed gradient 0	Fixed gradient 0
Light Phase Outlet	Outflow: Fixed gradient 0 Return flow: Fixed Value 0	Outflow: Fixed normal gradient 0 Return flow: Calculated from flux	Fixed gradient 0	Fixed gradient 0	Fixed gradient 0
Wall	Fixed gradient 0	No slip	Fixed gradient 0	Fixed gradient 0	Fixed gradient 0
Initialised Internal Field	Non-uniform value	Uniform value (0 0 0)	Uniform value 1×10^{-3}	Uniform value 1×10^{-3}	Uniform value 0
	P_{local} (Pa)	N_d [GEMMA]	C_α [GEMMA]		
Heavy Phase Inlet	Fixed gradient corrected for velocity boundary	Fixed gradient 0	Fixed gradient 0		
Light Phase Inlet	Fixed gradient corrected for velocity boundary	Fixed gradient 0	Fixed gradient 0		
Heavy Phase Outlet	0 Customised condition Eq. (4.2)	Fixed gradient 0	Fixed gradient 0		
Light Phase Outlet	0 Customised condition Eq. (4.2)	Fixed gradient 0	Fixed gradient 0		
Wall	Fixed gradient 0	Fixed gradient 0	Fixed gradient 0		
Initialised Internal Field	Uniform value 0	Uniform value 2×10^7	Uniform value 1		

6.2.1 Additional User Input settings

A number of additional user input settings are required for the E-E and GEMMA simulations. These settings are used as closures to the multiphase models. For the E-E simulation, a fixed droplet size needs to be defined. In this case, the three most recent major droplet size correlations given in Section 2.2.4.2 were assessed and compared, see Table 6.2. A fixed droplet size ($d_{[3,2]}$) of 2.2 mm was chosen from the correlation of Sreenivasulu *et al.* (1997).

Table 6.2: Comparison of the three major correlations given in Section 2.2.4.2.

Author	$d_{[3,2]}$ **Correlation**	**(mm)**
Míšek (1964)	Eq. (2.21)	1.30
Kumar & Hartland (1996)	Eq. (2.23)	1.97
Sreenivasulu *et al.* (1997)	Eq. (2.24)	2.20

For the GEMMA simulations, the switching algorithm requires limits on each of the three criteria. A detailed explanation of the switching mechanism is given in Section 3.2.3.1. For the critical interface resolution quality cut-off: $IRQ_{crit} = 4$. For the minimum and maximum volume fractions: $\alpha_{min} = 0.111$ and $\alpha_{max} = 0.999$ respectively. For the droplet size local mesh size factor: $\Gamma = 2$. Additionally, the minimum and maximum limits of the OPOSPM population balance are required and were defined to provide a balance between solution stability and preventing restriction of the solution. A lower limit of $d_{[3,2]} = 0.1$ mm and upper limit of $d_{[3,2]} = 5$ mm was used in this case.

6.3 Solution Method

In each case, a transient Euler time-derivative scheme was used along with a multi-dimensional cell limited least-squares gradient scheme for all equations solved. Additionally, the velocity and volume fraction transport equations were solved using second-order divergence schemes. The SGS model transport equations (for E-E) were solved using a bounded first-order upwind divergence scheme. Convergence for the transient cases was reached when the final residual fell below 1×10^{-6} for each transport equation at each time step. The transient PIMPLE algorithm was used, see Section 3.3.2, solving within 2 outer-loop iterations at each time step. Within each outer-loop, 3 inner-loop iterations are preformed. Here, the pressure equation is solved and repeated an additional 2 times via 'corrector loops'. No under-relaxation is used in order to maintain transient accuracy. A fixed maximum Courant number of 0.8 was applied using adjustable time-stepping. Final solutions were taken when time step convergence was observed, and the volume fractions and outlet velocities showed cyclic steady-state behaviour.

The GEMMA simulations ran across 192 processors (28,650 cells per processor) using the university of Leeds' ARC3 HPC facilities (University of Leeds, 2019). The time step was in the order of 5×10^{-5} once fully developed cyclic steady-state flow had been achieved. On average, a wall-clock time of 20.88 hrs produced 1 s of simulated transient flow. The E-E simulation ran across 560 processors (28,650 cells per processor) using the university of Leeds' ARC2 HPC facilities (University of Leeds, 2019). The time step was in the order of 1.6×10^{-4} one fully cyclic steady-state flow had been achieved. On average, a wall-clock time of 2.05 hrs produced 1 s of simulated transient flow.

6.4 Post-Processing Operations and Analysis Methods

6.4.1 Calculating the actual size distribution

The GEMMA model uses a the OPOSPM population balance to predict the droplet size ($d_{[3.2]}$) field present based on breakage and coalescence rates. The resulting field only provides a prediction on the droplet size if a volume of dispersed phase is present locally. The consequence of this method is that is the physical droplets are not tracked explicitly.

To produce droplet count histograms and probability density functions of the $d_{[3,2]}$ distribution, one must use the information of the discretised mesh cell volumes (V_{cell}), local cell droplet number density ($N_{d,cell}$), cell volume fraction (α_{cell}), and predicted local (cell) droplet size ($d_{[3,2],cell}$). In this instance, a novel means of post-processing workflow was used to combine this information to output the desired droplet count histograms. This method assesses the region between both sieve-plates (stage-wise region). Moreover, only cells which are consistently using dispersed-interface modelling were evaluated, for consistency, using the ensemble averaged C_α data. The specific workflow data operations are represented as a flow diagram in Fig. 6.1. This workflow was repeated for both instantaneous and ensemble averaged data for each cycle time: peak of the pulse ($\frac{1}{2}\pi$), median (middle) of the pulse (π), minimum of the pulse ($\frac{3}{2}\pi$), and median (start) of the pulse (2π). Once the data had been converted into droplet count histograms, each distribution could be converted in to probability density functions through a standard normalisation technique,

$$ProbabilityDensity = \frac{BinCount_i}{\sum BinCount_i} \tag{6.1}$$

The mean of the (normal) distributions was calculated using:

$$Mean = \sum ProbabilityDensity(Bin_i) \tag{6.2}$$

and the standard deviation was calculated using:

$$StandardDeviation = \sqrt{\sum ProbabilityDensity(Bin_i - Mean)^2} \qquad (6.3)$$

here, Bin_i refers to the discretised *'set'* for which a particular droplet belongs to and $BinCount_i$ is the total of number of droplets belong to a set. The bin sizes are discretised ranges of droplet sizes. 100 linearly spaced bin ranges were generated within the maximum and minimum *'edges'* (E) of the distribution, 0.5 mm and 2 mm, evaluated *a posteriori*.

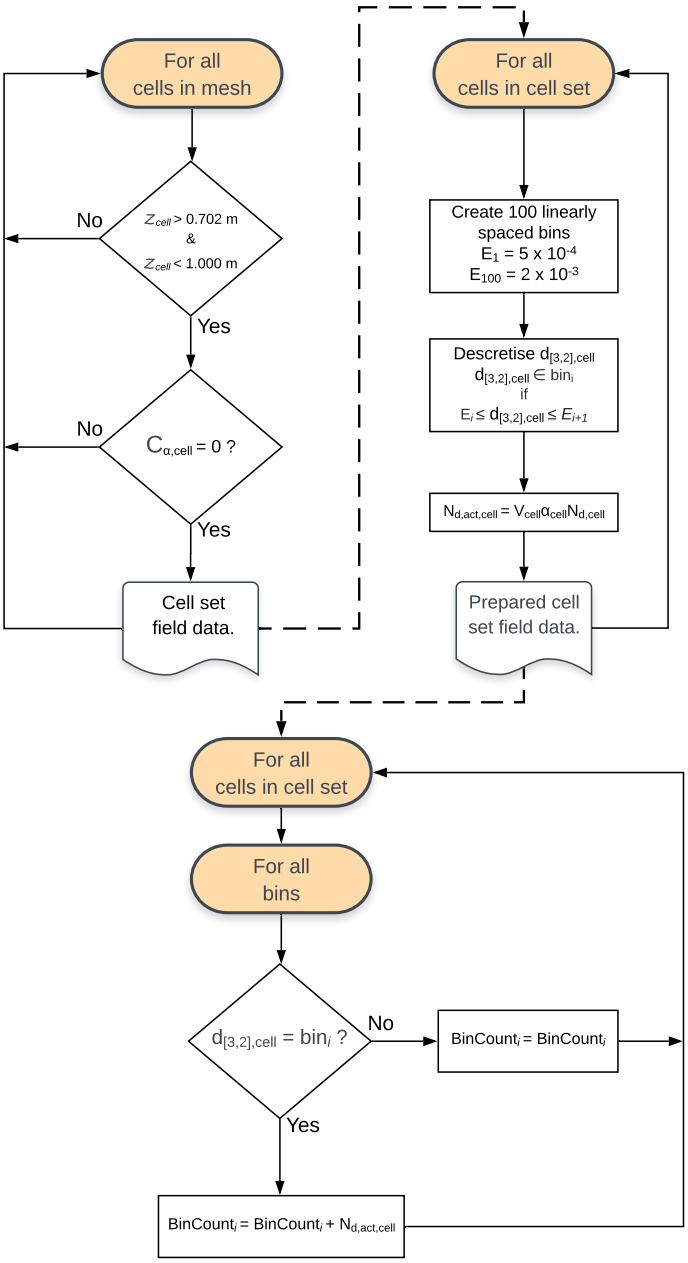

Figure 6.1: Flow diagram representing the workflow used to calculate the number of droplets of a category $d_{[3,2]}$ size for the analysis of the analysis of the OPOSPM population balance.

6.5 Results and Discussion

6.5.1 Comparison of the Transient Flow Fields

For comparison of the transient flow behaviour, the instantaneous velocity fields from the GEMMA, VOF and E-E approaches are given in Fig. 6.2. Additionally, the volume fraction fields are presented in Fig. 6.3. Here, the velocity magnitude ($|U|$) and z-component of the velocity field (U_z) are compared in conjunction with the volume fraction fields. Velocity results have been discretised using colour contour plots of 20 levels. The volume fraction field has been presented using a continuous contour plot from 0 - 16% to improve visualisation of the dispersed phase fluid. This comparison will serve as an indication of how differences in coupling with the volume fraction field lead to different predictions in the flow behaviour (velocities).

At the bottom inlet, the predictions of VOF and E-E are very different. The VOF, predicts that the dispersed phase fluid enters the column as slugged/churned high velocity turbulent flow. Without interface resolving methods, the E-E assumes a fixed droplet size as dispersed phase fluid enters the column. Consequently, the velocities are substantially lower overall and smoother in characteristic, although still turbulent. In this region, effective resolution of the interface(s) is seen with GEMMA. This leads to similar slugged/churned flow and a characteristic velocity field much closer to that of VOF. With GEMMA, it is clear when comparing the contour plots of U_z that the velocities are much closer to that of that of VOF than to E-E. Moreover, in both GEMMA and VOF U_z contour plots, segregation of the flow emerges from the buoyancy of the dispersed phase. This feature is not observed in E-E where the U_z field is more diffuse.

At the exit of the inlet pipe, where a clear plume emerges, the U_z flow profiles of both the VOF and GEMMA are similar. The plume is much weaker with E-E which forms a low velocity flow path up the (left) side of the column towards the first sieve-plate. Interestingly, the volume fraction contours show that VOF is able to maintain the interface morphology of the dispersed flow despite the mesh resolution being much lower in this region, see Section 3.4 Fig. 3.4. With GEMMA, the interface sharpening is clearly switched off in this region, but the dispersed-interface modelling is still able to predict similar velocity magnitudes to VOF.

Before the first sieve-plate, where the flow disperses, the predictions of the three approaches are quite different. VOF shows the dispersed phase (numerically) diffusing rapidly forming many droplets. Here, the interface sharpening should not be in effect with GEMMA and, instead, a population balance method is used to calculate the droplet size which drives the buoyant flow and phase momentum exchange. Note that the E-E uses a fixed droplet size throughout. In both two-fluid approaches, GEMMA and E-E, the dispersed phase maintains a tight grouping with GEMMA showing more dispersion than E-E. A low mesh resolution

in this region would cause VOF to disperse prematurely. The result is numerical diffusion of the velocity field. This concern is not present with GEMMA as the dispersed-interface modelling takes effect which is not hindered in the same way by numerical diffusion. The structures arising in the U_z are still qualitatively comparable between GEMMA and VOF despite their differences. As for E-E, poor predictions of the flow development within the inlet pipe will carry forward to produce questionable flow definition in the region before the first plate.

Comparison of the volume fraction fields at/above the first sieve-plate reveals that GEMMA provides a mixed prediction between that of VOF and E-E. The VOF shows resolution of the droplet formation arising from the sieve-plate. E-E predicts a stream of droplets forming from the left side of the plate only. GEMMA does provide resolution of some of the larger droplets but fails to capture the formation of droplets from all of the dispersed phase that passes through this region. This is likely to be a result of the definition of the interface sharpening limits and definitions used in the switching algorithm, see Section 3.2.3.1 Fig. 3.1. However, these variables can be modified to produce modelling behaviour closer to that seen by the VOF in this region. This concept is explored deeper in Section 6.5.4 where suggestions are provided. That said, even without full resolution, the distribution of the dispersed phase across the plate in GEMMA is comparable to VOF. Moreover, both GEMMA and VOF predict lower velocity (magnitudes) close the plate, with some sieve-hole jetting behaviour, whereas E-E does not.

In the centre compartment (between the sieve-plates), the dispersed phase distribution is similar in both the VOF and GEMMA but not with E-E. This seems to a consequence of the how the flow is initially distributed at the first plate. In the U_z contour plots, it can be seen that GEMMA and VOF both predict higher velocities in the upper half of the compartment closer to the top sieve-plate. The E-E U_z contour plots show the velocities to be highest in the centre region of the compartment. The developing velocity fields in centre compartment are going to be highly dependent on the predictions of the droplet sizes. As this region is of particular interest for hold-up predictions, it is discussed in more detail in Section 6.5.3 in conjunction with the results of the population balance from GEMMA.

Lastly, the improvements in predictions in the velocity and volume fraction fields continue with GEMMA beyond the top sieve-plate. At the top-sieve plate, similar observations are made between all three cases as with the bottom plate. However, it is important to note that E-E shows a redistribution of the dispersed phase under the plate leading to more uniform dispersion thereafter. The $|U|$ contours show the velocity is heavily under-predicted in the E-E. GEMMA and VOF are much more similar qualitatively in the amount of momentum present in the region and in how the continuous phase fluid is introduced into the column. The equilibrium primary

interface level (height) in all three systems are different. Comparing the velocity and volume fraction contours once more, VOF and GEMMA show that the primary interface height is physically affected by the dispersed phase breaking at this phase boundary and the momentum (velocities) present in that (continuous phase) region. In the E-E the flow is almost quiescent in proximity of the primary interface resulting in no height difference (from the set-point).

In summary, all three approaches are defined to simulate the same system. Moreover, all are coupled with high-fidelity LES to resolve the velocity and, therefore, turbulence fields. Any differences in the flow behaviour are a consequence of the approach to modelling the two fluid interactions. Broadly speaking, all three methods produce different predictions in the volume fraction fields which lead to differences in the resulting velocity fields. The GEMMA model clearly provides improvements in the velocity and volume fraction field predictions over E-E in regions expected to be well resolved by VOF. Namely, in the development of the flow in the dispersed phase inlet pipe, near the plates, and at the primary interface where the dispersion brakes before leaving the column. The addition of interface resolving methods in GEMMA were clearly active in these regions when compared against the E-E. This resulted in clear improvements to how the dispersed phase is introduced/distributed into the column initially, as well as the droplet evolution from the sieve-plates. Moreover, the equilibrium level of the primary interface appears to show some dependency on the momentum of the droplets upon breaking at the interface.

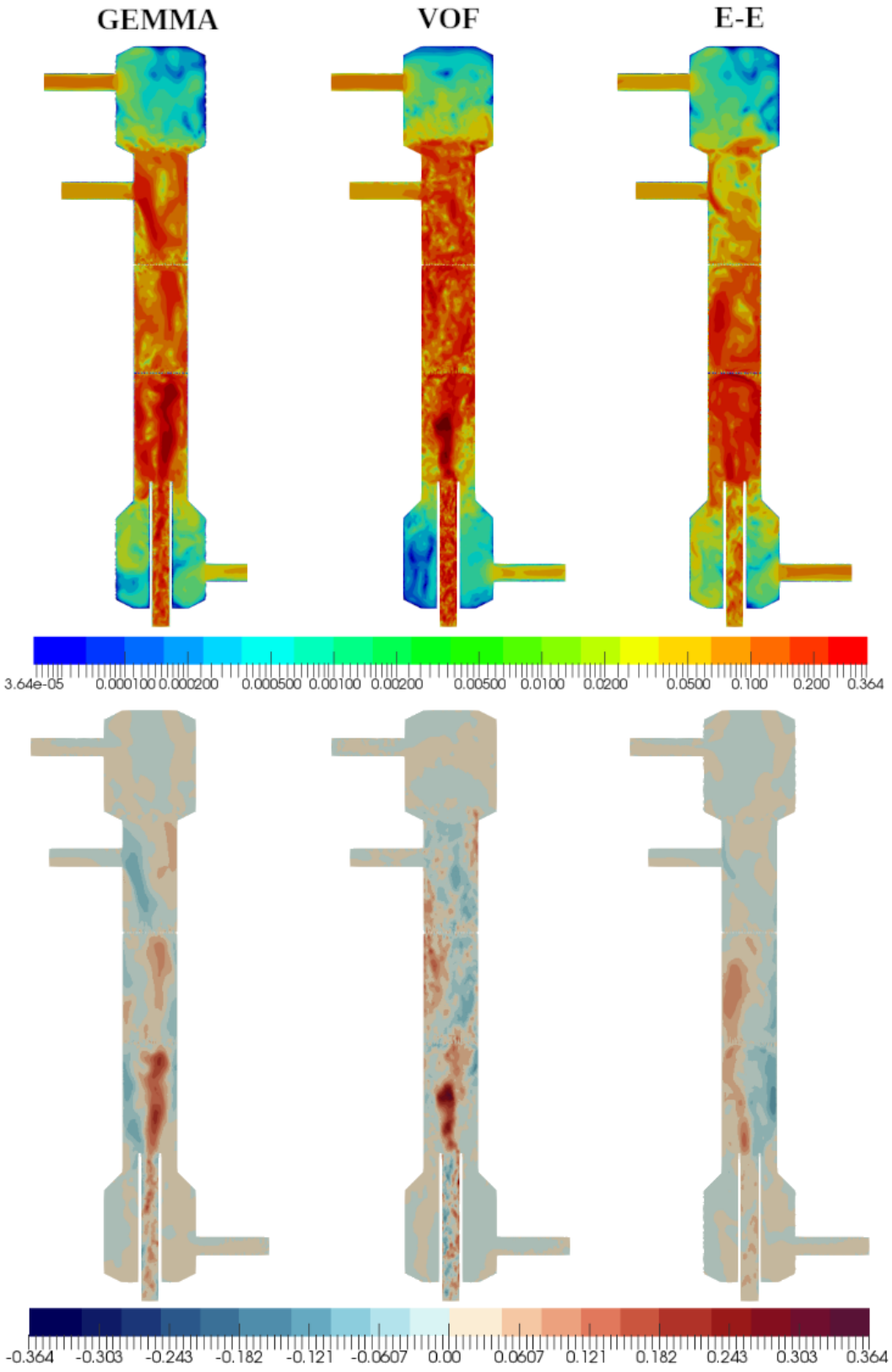

Figure 6.2: Magnitude of the magnitude of the instantaneous velocity field ($|U|$) (top) and the instantaneous z-component velocity (U_z) (bottom) for GEMMA, VOF and E-E simulations at 2π. Velocities in ms^{-1}.

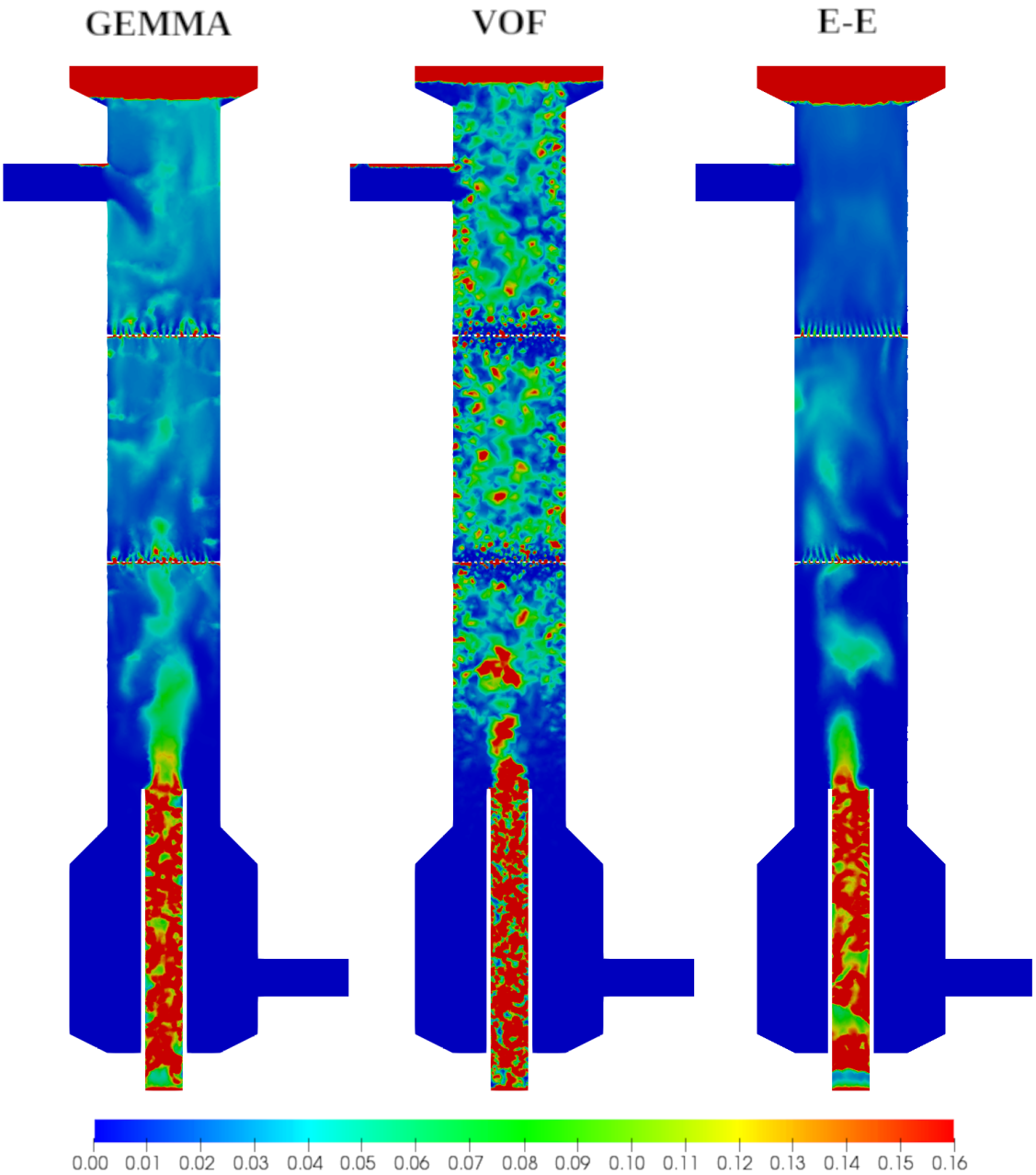

Figure 6.3: The volume fraction field α_d for GEMMA, VOF and E-E simulations at 2π. For visualisation purposes, the colour map has been scaled to 0 - 16 %, within the range of one standard deviation of the VOF predictions, see Section 5.5.2.

6.5.2 Comparison of the Ensemble Averaged Field Properties

The ensemble averaged field properties of velocity, pressure ($P_{static} - \rho gh$), turbulence kinetic energy, turbulence kinetic dissipation rate and mixing index from the GEMMA approach predictions are compared against the VOF and E-E multiphase predictions. In each case the results were ensemble averaged until converged data resulted; 20, 40, and 200 pulse cycles were used for averaging for the GEMMA, E-E, and VOF approaches respectively.

Figs. 6.4, 4.6 and 6.5 contain line plots of the ensemble averaged velocities for the GEMMA, VOF and E-E approaches respectively. In each case, velocities are taken across the columns (x-axis at $y = 0$) at heights corresponding to the centre of the bottom plate ($z = 0.701$ m), the centre of the middle compartment ($z = 0.850$ m), and the centre of the top plate ($z = 1.001$ m) for each velocity component. This is repeated for each time in the sinusoidal pulse: peak of the pulse ($\frac{1}{2}\pi$), median (middle) of the pulse (π), minimum of the pulse ($\frac{3}{2}\pi$), and median (start) of the pulse (2π).

As a generalised comment, each multiphase model shows good corroboration in some major features of the flow. In each case, all velocity components show little variance with respect to times in the pulse cycle, especially for flow in the middle compartment. Furthermore, the flow is dominant in the U_z component direction, and there is clear evidence of counter-current flow and rotation along this direction. However, there are notable differences in the prediction between E-E predictions and evidence of improvement with GEMMA.

Firstly, the velocity profiles are compared at the sieve-plates using the VOF predictions as the benchmark. Here the mesh resolution is high enough for the VOF model to resolve the fluid interactions and, therefore, provide faithful predictions of the fluid velocities in those regions. At the bottom sieve-plate, VOF shows a concentrated flow path of the dispersed phase in the centre of the plate in the U_z component. This characteristic is present in the GEMMA results, particularly at peak flow ($\frac{1}{2}\pi$), but less so in the E-E model. E-E shows the flow to be more diffuse across the plate and concentrated more to the negative x-direction (left) and not the centre. Here, the peak velocities are in closer agreement between VOF (at $U_z = 0.55$) and GEMMA (at $U_z = 4.5$) than with E-E (at $U_z = 0.30$). Similar is also observed for the $|U|$. Moreover, both VOF and GEMMA predict decreases in the U_z component in the radial (outer) direction of the bottom sieve-plate at all other times. The negative U_z flow across the bottom plate is more consistent in time with E-E.

At the top plate, VOF shows segregation of the flow with the dispersed phase flowing up the the side of the column at $x = -0.03$ to -0.07 m. GEMMA also shows evidence of segregated flow paths of the phases across the top sieve-plate

where $x = 0.02$ to 0.06 m. Whereas, E-E predicts mostly positive U_z flow across the centre of the top sieve-plate as in the bottom sieve-plate velocity profile. Again the peak velocities are greater in the VOF and GEMMA than with E-E, particularity in the negative U_z component. The above observations are expected, the E-E model assumes two interpenetrating fluids which are coupled via momentum exchange interfacial models; this does not resolve the interactions. In highly dispersed regions this model assumption is valid. In regions where flow obstructions and surface tension effects dominate, this model application becomes invalid. Therefore, when proper interface treatments are applied, in GEMMA or VOF, the flows develops the necessary features.

In the middle compartment, It is apparent that the VOF model results are substantially different to that from the E-E. Also, the flow is much more dispersed and the mesh resolution is less dense. Therefore, the dispersed-interface modelling should take effect and be observable in the GEMMA flow predictions. This is evident when comparing the likeness of the velocity profiles of GEMMA to E-E. However, there are some differences. GEMMA predicts a greater negative U_z flow where $x = 0.035$ to 0.07 m. Additionally, the U_x and U_y velocity components are greater in magnitude. This suggests that some large scale rotational flow, that was observed with VOF, still develops between the sieve-plates with GEMMA but less so with E-E. Also, where $x = -0.015$ to -0.04 m the GEMMA U_z profile flattens, note that this is where large negative U_z flow is observed from the top sieve-plate. Lastly, the magnitude of the peak U_z velocities in VOF are greater than that in GEMMA or E-E. The final point is to be expected. In the low mesh resolutions areas, the interface cannot be fully resolved by the VOF method leading to over-predictions of the velocities which are not corrected by the drag force. The U_z in the high velocity regions are of interest here due speculation of accurate residence time predictions of VOF in low resolution regions where drag cannot be fully accounted for.

In summary, GEMMA was able to provide velocity predictions near the plates that were similar to the resolved velocity profiles from the VOF method. Moreover, GEMMA was successful in providing velocity predictions between in the sieve-plates (in the centre compartments) that closely resembled that of the E-E method. More to the latter point, there was an observed effect on the top sieve-plate influencing the flow within the centre-compartment below. This leads to two important conclusions of multiphase modelling in PSECs. Firstly, it is important to resolve the interactions between both phases at the sieve-plates to provide accurate predictions of the flow therein. In turn, this leads to alterations in flow regions nearby that would not be fully captured via a standard E-E implementation. Secondly, that the drag interfacial forces, when accounted for, result in the necessary smaller U_z predictions.

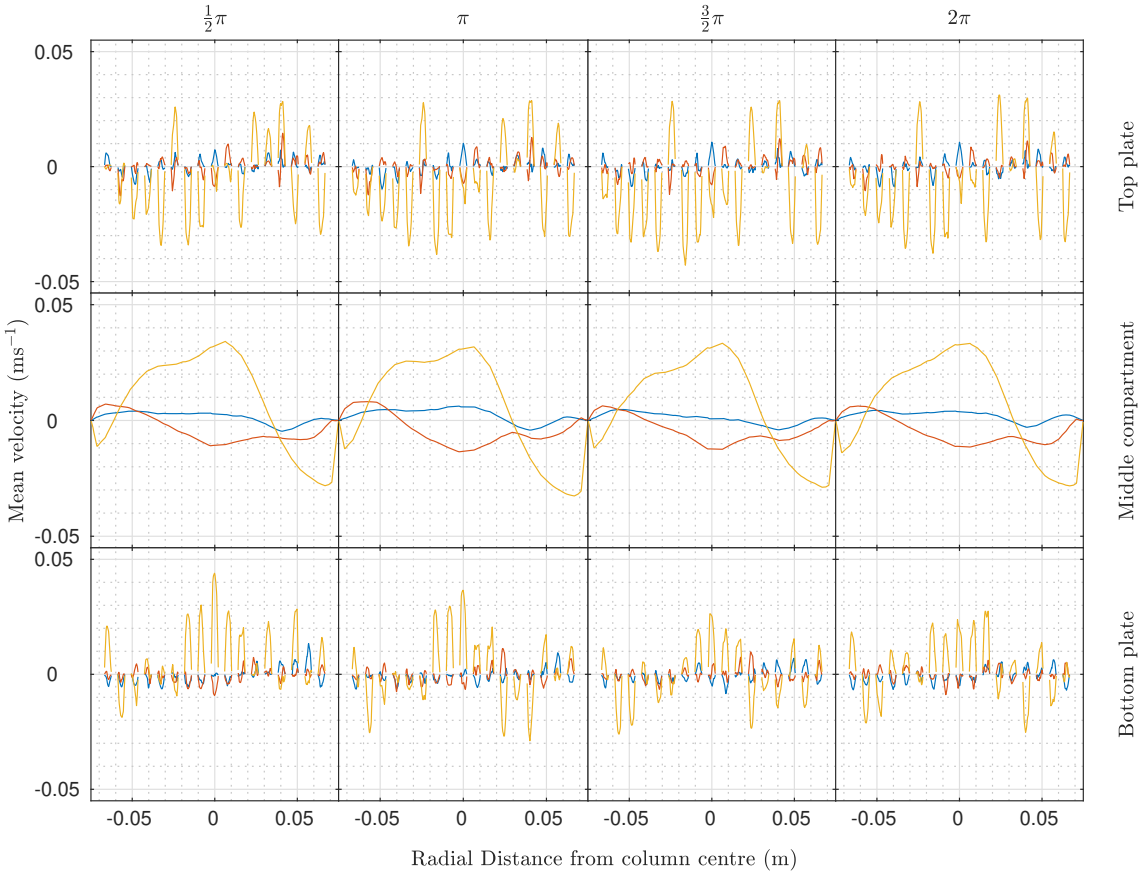

Figure 6.4: GEMMA ensemble averaged mean velocity components plotted along the x-axis ($y = 0$ m) at $z = 0.701$ m (centre bottom sieve-plate), $z = 0.850$ m (middle of the compartment), $z = 1.001$ m (centre of top sieve-plate) at $\frac{1}{2}\pi$, π, $\frac{3}{2}\pi$ and 2π;
$\langle U_x \rangle$ (—), $\langle U_y \rangle$ (—), $\langle U_z \rangle$ (—).

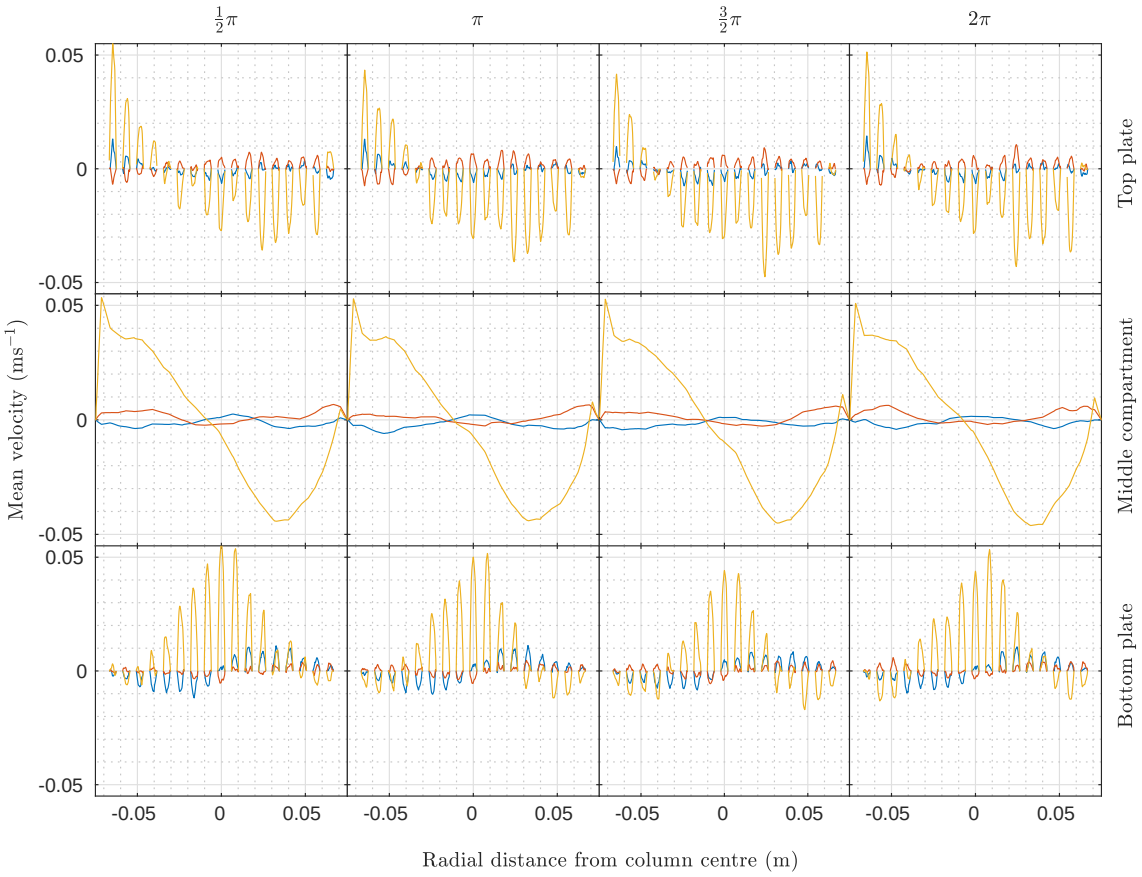

Figure 4.6: VOF ensemble averaged mean velocity components plotted along the x-axis ($y = 0$ m) at $z = 0.701$ m (centre bottom sieve-plate), $z = 0.850$ m (middle of the compartment), $z = 1.001$ m (centre of top sieve-plate) at $\frac{1}{2}\pi$, π, $\frac{3}{2}\pi$ and 2π; $\langle U_x \rangle$ (—), $\langle U_y \rangle$ (—), $\langle U_z \rangle$ (—).

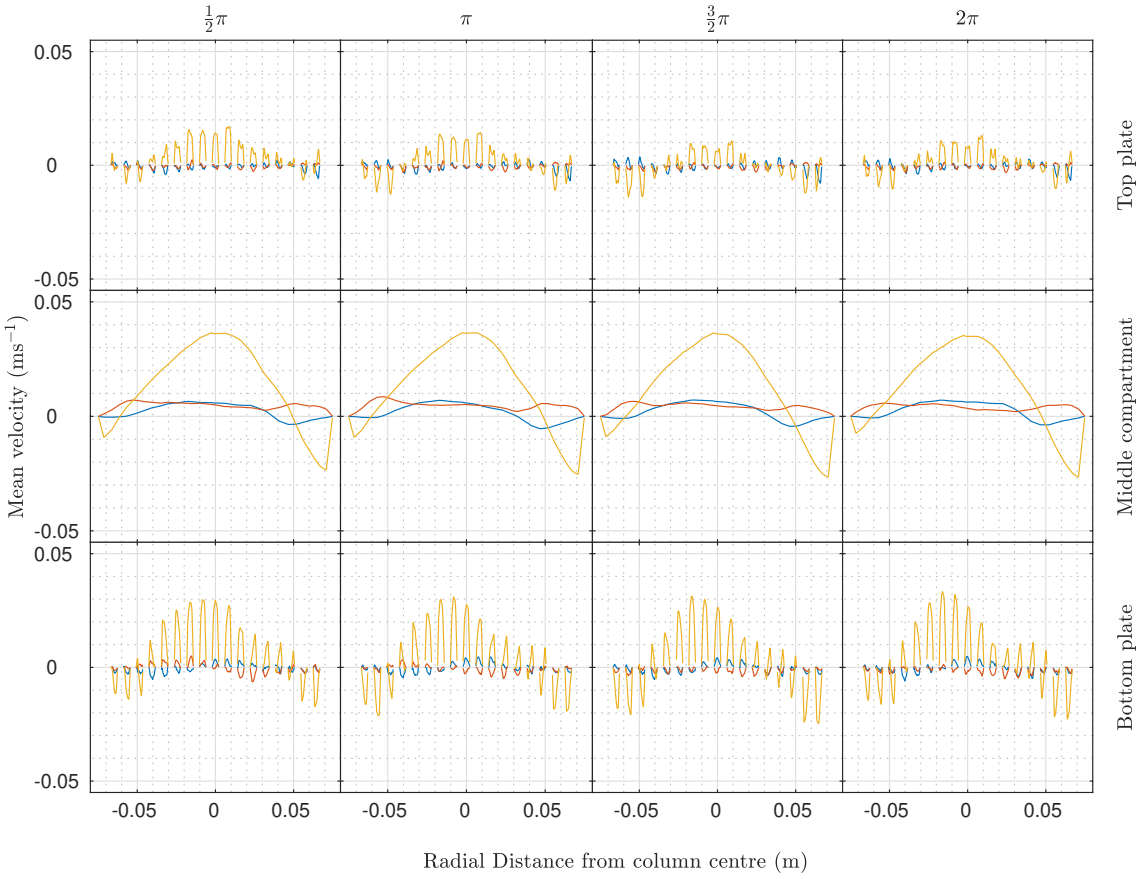

Figure 6.5: E-E ensemble averaged mean velocity components plotted along the x-axis ($y = 0$ m) at $z = 0.701$ m (centre bottom sieve-plate), $z = 0.850$ m (middle of the compartment), $z = 1.001$ m (centre of top sieve-plate) at $\frac{1}{2}\pi$, π, $\frac{3}{2}\pi$ and 2π; $\langle U_x \rangle$ (—), $\langle U_y \rangle$ (—), $\langle U_z \rangle$ (—).

Figs. 6.6, 4.7 and 6.7 are axial centreline plots of pressure ($P_{stastic} - \rho gh$), turbulence kinetic energy, turbulence kinetic energy dissipation rate and mixing index parameter for the GEMMA, VOF and E-E approaches respectively. A quantitative summary of the observations taken for each field inspected is available in Tables 6.4 and 6.5. A discussion of the observations follows.

The pressure field predictions from all three approaches are similar in their characteristic profiles. However, the GEMMA results are much closer, numerically, to that of the E-E predictions. The VOF model tends to produce larger predictions overall. The characteristic drop in pressure before the sieve-plates is less pronounced in both GEMMA and E-E. Moreover, they predict larger pressure peaks at the bottom plate than for the top sieve-plate, whereas, VOF predicts similar pressure spikes at each sieve-plate based on the observations in Figs. 6.6, 6.7 and 4.7 respectively. However, these line-plots may not be fully representative of a fair comparison of the pressure field predictions.

The findings in Chapter 5 stressed the significance of predictions of the pressure field for development of predictive/diagnostic tools for flooding. Therefore, additional information has been provided in Table 6.3 regarding pressure predictions at the sieve-plates and the pressure drops (ΔP_d and ΔP_c) with respect to each phase stream across the column. Here, planar averages of the ensemble averaged $P_{static} - \rho gh$ field are taken at the $z = 0.701$ m and $z = 1.001$ m at time $\frac{1}{2}\pi$ for comparison. Additionally, ΔP_d and ΔP_c are calculating from the ensemble averaged $P_{static} - \rho gh$ field using the method in Section 5.3.2. Comparison of the planar averages across each plate show that GEMMA does in-fact provide very close to predictions to that of VOF whereas E-E does not. This is most clear at the bottom plate where the GEMMA and VOF results are in close agreement and where E-E produces much lower predictions. In all three approaches, the predicted ΔP_d are very similar. However, the ΔP_c predictions in all three cases are quite

Table 6.3: Summary of the planer-mean ensemble averaged results at cycle time $\frac{1}{2}\pi$.

	$P_{static} - \rho gh_{mean}$ (Pa)		
	GEMMA	VOF	E-E
Inlet$_d$	3726.610	3616.770	3669.200
Outlet$_d$	-0.113	-0.008	-0.113
Inlet$_c$	194.759	105.830	38.000
Outlet$_c$	0	0.1044	0
Bottom Plate	539.621	655.471	427.619
Top Plate	429.900	408.301	137.587
ΔP_d	3726.723	3616.778	3669.313
ΔP_c	194.759	105.726	39.000

different, GEMMA still providing closer agreement with VOF than with E-E.

Overall VOF does provide higher pressure predictions. The dampening /diffusion of the velocities (momentum) within the two-fluid approaches, where dispersed-interface drag is included, results in corrections within the pressure field when compared against the VOF. This means the lower pressure predictions from the GEMMA approach are expected. However, the E-E approach tends to greatly under predict the pressure in characteristic regions of the system due the lack interface resolving methods.

Comparisons of the turbulence kinetic energy field are very different between E-E and VOF. In each case, the most turbulence kinetic energy is found below the first-plate, but develops into different profiles. The predictions in the dispersed phase inlet pipe are much greater in VOF. Moreover, the VOF predicts the turbulence kinetic energy to stabilise after the first sieve-plate, whereas E-E shows a consistent decay of energy up the height of the column. When interface resolving methods are introduced with GEMMA, the turbulence kinetic energy profiles become much closer to that of VOF. Particularly, in the inlet pipe and development of the profile to the first sieve-plate. However, GEMMA does still produce lower predictions and a decaying profile of the turbulence kinetic energy up the height of the column.

Comparisons of the dissipation rate of turbulence kinetic energy reveal much closer agreement in all three approaches with how the profile develops after the first sieve-plate. Qualitatively, all three are quite similar from the first sieve-plate to the top of the column, although VOF shows more fluctuations. Quantitatively, both two-fluid approaches show much lower predictions in the magnitude of dissipation rate due to the lower predictions in the turbulence kinetic energy in the system. Below the first sieve-plate the E-E profile is different to that of VOF due the predictions of the turbulence behaviour in the inlet pipe. These characteristics are corrected to provide agreement with VOF when using GEMMA.

A summary of the observations in both the turbulence kinetic energy and the dissipation rate of turbulence kinetic energy reveal two clear conclusions. Firstly, without interface resolving methods, the turbulence characteristics can be misrepresented especially at the inlet pipe and development of turbulence towards the sieve-plates. Secondly, with dispersed-interface modelling (in GEMMA and E-E), there appears to be a missing source-term that results in decay of the turbulence kinetic energy up the column. The latter is likely a result of the implementation. The two-fluid approaches will neglect the buoyant flux term in the production of turbulence which is dependent on the local density fluctuations. Also, when interface modelling with phase momentum exchange, the velocity gradients across the interface are likely neglected. Conversely, the VOF (attempts) to resolve these features which produce better predictions of the velocity and density fluctuations resulting in better predictions for the mechanical production

and buoyant flux terms respectively, see Section 4.2.4 Eq. (4.9). In all three cases, LES is used to predict the flow field and so no turbulence transport equations exist, strictly speaking. Rather, turbulence is an emergent statistical property of the resolved velocity field, lower energy scales are accounted for in the sub grid scale model. Therefore the missing source-term(s) cannot simply be added to a budget equation. This makes it difficult to provide direct suggestions for improvements in GEMMA without a deep discussion of the how the code libraries handle each of the phase momentum equations. However, there is clear evidence that these concerns must be addressed within later developments and is likely due to how the unique solution of both phases disregards the gradients otherwise resolved at the interface(s) which contribute heavily to the production of turbulence kinetic energy. Moreover, there is evidence to conclude that, because of this, turbulence predictions with LES E-E implementations are going to be misrepresentative in this regard also.

Lastly, comparisons of the mixing index criterion provides information on the large-scale flow characteristics which, in this system, is dominated by the continuous phase flow. For reference, the mixing index is the ratio of the rotational to irrotation flow components, see Section 4.2.4 Eq. (4.10). All three approaches produce corroborating predictions that have very similar profiles and magnitudes. Therefore, all three produce very similar conclusions of the large scale dispersive mixing properties of the system. These are observations are discussed in analysis of the VOF in Section 4.2.5.3. However, the results of the both GEMMA and E-E show much more fluctuations. If these simulations could be run for much longer, the ensemble averaging would reduce the fluctuations to levels seen in the VOF results. To conclude, the results here show evidence that the LES is able to produce consistent predictions for the mixing criterion regardless of the multiphase approach used.

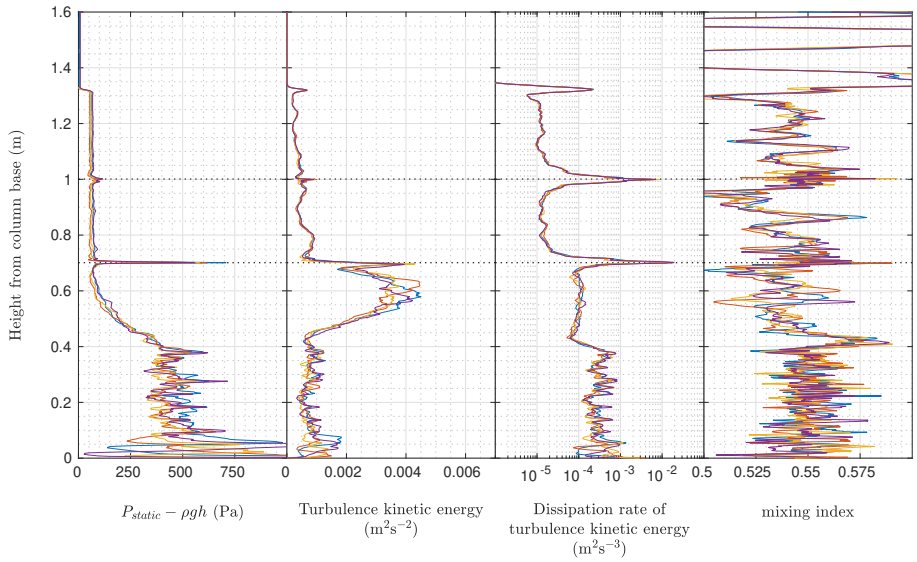

Figure 6.6: GEMMA field properties plotted along the height of the column at $x = 0.05$ m, $y = 0$ m; $\frac{1}{2}\pi$ (—), π (—), $\frac{3}{2}\pi$ (—), 2π (—).

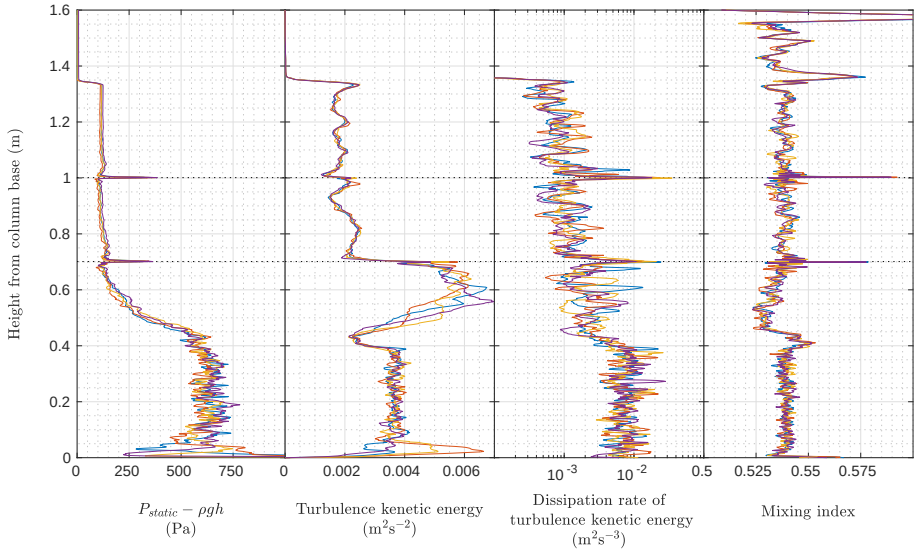

Figure 4.7: VOF properties plotted along the height of the column at $x = 0$ m, $y = 0$ m; $\frac{1}{2}\pi$ (—), π (—), $\frac{3}{2}\pi$ (—), 2π (—).

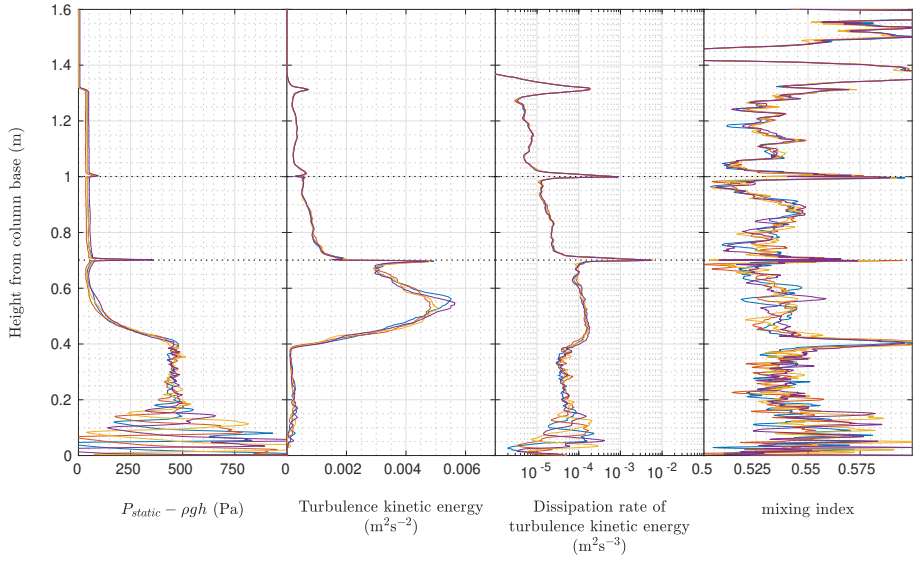

Figure 6.7: E-E field properties plotted along the height of the column at $x = -0.05$ m, $y = 0$ m; $\frac{1}{2}\pi$ (—), π (—), $\frac{3}{2}\pi$ (—), 2π (—).

Table 6.4: Summary of observations of pressure and turbulence kinetic energy for Figs. 6.6, 4.7, and 6.7

Observation	GEMMA	VOF	E-E
Pressure ($P_{static} - \rho gh$)			
Dispersed phase inlet pipe ($z = 0 - 0.4$ m)	Small local fluctuations. Average of 490 Pa. Stabilises immediately. Exit pressure of 420 Pa	Small local fluctuations. Average of 625 Pa. Stabilises immediately. Exit pressure of 600 Pa.	Large fluctuations from the inlet. Oscillations converge with increase in height. Stabilises to 450 Pa.
Bottom compartment ($z = 0.4 - 0.7$ m)	Smooth decrease in pressure with height to 70 Pa.	Steady decrease in pressure with height to 125 Pa.	Very Smooth decrease to 50 Pa
Bottom plate	Drop, spike and recovery, Peak of 700 Pa.	Drop, spike and recovery. Peak of 372 Pa.	Smooth increase to 70 Pa towards bottom plate then spike and recovery. Peak of 360 Pa.
Centre compartment ($z = 0.7 - 1$ m)	Drop from 70 to 50 Pa.	Drop from 125 to 90 Pa.	Drop from 60 to 50 Pa.
Top plate	Drop, spike and recovery. Peak of 115 Pa.	Drop, spike and recovery. Peak of 385 Pa.	Spike and recovery to 50 Pa. Peak of 95 Pa.
Upper compartment ($z = 1 - 1.3$ m)	Steady pressure at 68 Pa.	Steady pressure at 116 Pa.	Steady pressure at 50 Pa.
Disengagement section ($z = 1.3 - 1.6$ m)	Drop to 9 Pa across primary interface.	Drop to 0 Pa across primary interface.	Drop to 7 Pa across Primary interface.
Turbulence kinetic energy			
Dispersed phase inlet pipe ($z = 0 - 0.4$ m)	Small local fluctuations. Average of 0.00075 m^2s^{-2}.	Small local fluctuations. Average of 0.00375 m^2s^{-2}.	Very low at inlet ~ 0 m^2s^{-2} increases slightly to average of 0.0002 m^2s^{-2}.
Bottom compartment ($z = 0.4 - 0.7$ m)	Increase to 0.0045 m^2s^{-2} towards bottom plate. Decrease to 0.0018 m^2s^{-2} before bottom plate.	Sudden drop to 0.002 m^2s^{-2} then increase to 0.007 m^2s^{-2} towards bottom plate.	Increases rapidly to 0.0055 m^2s^{-2} towards bottom plate early on. Decreases to 0.003 m^2s^{-2} before bottom plate.
Bottom plate	Spike and drop again to 0.00044 m^2s^{-2}. Peak at 0.004 m^2s^{-2}	Drop to 0.002 m^2s^{-2}.	Spike and drop to 0.0015 m^2s^{-2}. Peak at 0.0049 m^2s^{-2}.
Centre compartment ($z = 0.7 - 1$ m)	Slow drop to 0.0003 m^2s^{-2} then increase to 0.00063 m^2s^{-2} towards top plate.	Slow drop to 0.0015 m^2s^{-2} then increase to 0.0021 m^2s^{-2} towards top plate.	Slow drop to 0.0057 m^2s^{-2}.
Top plate	Drop to 0.0004 m^2s^{-2}, spike at 0.001 m^2s^{-2} and drop again to 0.0003 m^2s^{-2}.	Drop to 0.0014m^2s^{-2}.	Drop to 0.00026m^2s^{-2} and recovery to 0.0006m^2s^{-2}.
Upper compartment ($z = 1 - 1.3$ m)	Slow drop to 0.0002 m^2s^{-2}.	Recovery to 0.002 m^2s^{-2}.	Drop to 0.0002 m^2s^{-2}, slow increase to 0.00036 m^2s^{-2} and decrease to 0.00018 m^2s^{-2}.
Disengagement section ($z = 1.3 - 1.6$ m)	Drop to 0 m^2s^{-2} across primary interface. Peak before interface to 0.00066 m^2s^{-2}.	Drop to m^2s^{-2} across primary interface. Peak before interface to 0.0024 m^2s^{-2}.	Drop to 0 m^2s^{-2} across primary interface. Peak before interface to 0.0007 m^2s^{-2}.

Table 6.5: Summary of observations of turbulence dissipation rate and mixing index for Figs. 6.6, 4.7, and 6.7

Observation	GEMMA	VOF	E-E
Dissipation of turbulence kinetic energy			
Dispersed phase inlet pipe ($z = 0 - 0.4$ m)	Small fluctuations. Average of 0.00026 m^2s^{-3}.	Large local fluctuations spanning an order of magnitude. Average value of 0.005 m^2s^{-3} increasing to 0.009 m^2s^{-3}.	Large fluctuations from inlet. Oscillations converge with increase in height. Stabilises at 3×10^{-5} m^2s^{-3}.
Bottom compartment ($z = 0.4 - 0.7$ m)	Drop to 6×10^{-5} m^2s^{-3}. Small recovery to 0.0001 m^2s^{-3}. Second drop to 8×10^{-5} m^2s^{-3}. Smooth exponential increase towards bottom plate.	Drop to 0.002 m^2s^{-3}.	Initial increase to 0.00017 m^2s^{-3}. Smooth drop to 8×10^{-5} m^2s^{-3}. Smooth exponential increase towards bottom plate.
Bottom plate	Spike of 0.01 m^2s^{-3}.	Spike of 0.025 m^2s^{-3}.	Peak of 0.0 m^2s^{-3}.
Centre compartment ($z = 0.7 - 1$ m)	Fast exponential decrease away from plate to 1×10^{-5} m^2s^{-3}. Slow exponential increase towards to top plate.	Steady decrease from 0.0013 - 0.0009 m^2s^{-3}.	Fast exponential decrease away from plate to 2.5×10^{-5}. Decrease to 1.1×10^{-5} m^2s^{-3} and exponential increase towards top plate.
Top plate	Peak at 0.007 m^2s^{-3}.	Spike of 0.035 m^2s^{-3}.	Peak of 0.0008 m^2s^{-3}.
Upper compartment ($z = 1 - 1.3$ m)	Smooth exponential decrease to 1.1×10^{-5}.	Steady decrease from 0.001 - 0.0005 m^2s^{-3}.	Smooth exponential decrease to 4×10^{-6} m^2s^{-3}.
Disengagement section ($z = 1.3 - 1.6$ m)	Drop to 0 m^2s^{-3} across primary interface. Peak before interface to 0.0002 m^2s^{-3}.	Drop to 0 m^2s^{-3} across primary interface. Peak before interface to 0.0013 m^2s^{-3}.	Drop to 0 m^2s^{-3} across primary interface. Peak before interface to 0.00015 m^2s^{-3}.
Mixing index			
Dispersed phase inlet pipe ($z = 0 - 0.4$ m)	Local fluctuations from 0.525 to 0.575. Average value of 0.55.	Minor local fluctuations. Average value of 0.51.	Large fluctuations at inlet stabilising to smaller local fluctuations. Average value of 0.53.
Bottom compartment ($z = 0.4 - 0.7$ m)	Peak initially to 0.58 and smooth decrease to average of 0.53.	Small drop to 0.49 and recovery towards bottom plate to 0.51.	Peak initially to 0.6 and smooth decrease to average of 0.53.
Bottom plate	Spike at 0.59.	Spike of 0.55.	Spike of 0.59
Centre compartment ($z = 0.7 - 1$ m)	Fluctuations from 0.51 to 0.57. Drop to 0.49 before plate.	Average value of 0.51.	Increase to 0.55 then decrease to 0.51 before top plate.
Top plate	Spike of 0.59.	Spike of 0.59.	Spike of 0.595.
Upper compartment ($z = 1 - 1.3$ m)	Fluctuations from 0.51 - 0.56.	Average value of 0.51.	Fluctuations from 0.51 - 0.54.
Disengagement section ($z = 1.3 - 1.6$ m)	Drop to 0.5 and increase to 0.6 after interface.	Spike before interface of 0.54.	Drop to 0.48 and increase to 0.72 after interface.

6.5.3 The OPOSPM Population Balance and Hold-up Predictions

This subsection will discuss the results of the population balance included within the GEMMA implementation. Also discussed is the relative stage-wise hold-up predictions between all three multiphase approaches. Previously, it was postulated that the stage-wise hold-up would be a resultant property of the droplet sizes within the system.

Here, the OPOSPM population balance calculates the zeroth and third moment of the droplet size distribution. In other words, it includes transport equations for the number density (N_d) and volume fraction (α_d) of the dispersed phase. As explained in Section 3.2.3.4, this means the $d_{[3,0]}$ can be calculated and converted to $d_{[3,2]}$ using a coefficient multiplier (conversion factor) of 0.76. Although not strictly a direct method for calculating $d_{[3,2]}$, it avoids the issue of requiring higher order quadrature moment methods to return the second moment of the droplet size distribution, and is the method used by De Santis *et al.* (2020) for this reason.

Figure 6.8 are discretised contour plots, at 20 levels, used to qualitatively describe the droplet size distribution predicted by the OPOSPM for instances in the four chosen cycle times. In regions where pure dispersed phase fluid exists and/or the large-interface modelling is activated the $d_{[3,2]}$ is represented at 5 mm. It should be noted that this is an artefact of the population balance modelling. This is not physical, but indicates the upper limit defined by the user input parameters. The same is true for the lower limit of 0.1 mm where pure continuous phase fluid exists. From Fig. 6.8, it can be seen that in the pulsing inlet condition and sieve-plates are shown to facilitate the turbulence production and dissipation (ε) which drives the breakage kernel, see Section 3.2.3.4 Eq. (3.50). Moreover, the coalescence kernel becomes dominant in the middle compartment's mid/upper regions where (ε) is seen to be low, see Fig. 6.6. Both previous observations serve as an indication that the population balance is functioning as intended.

Figure 6.9 and Fig. 6.10 show the droplet count and probability density function (PDF) at each cycle time, both instantaneous and after ensemble-averaging, for all cells where $C_\alpha = 0$ between both sieve-plates. A summary of the mean and standard deviation of the PDF is included in Table 6.6. Information on how the PDF was produced is found in Section 6.4.1. Firstly, it can seen from Fig. 6.9 that the number of cells included in the droplet count differs depending on the cycle time analysed. This implies that the switch is the least active at peak flow ($\frac{1}{2}\pi$). This could be due to coalesced dispersed phase fluid under the first sieve-plate being released. In this scenario, this observation will not be consequential to the results of the PDF. It is still an interesting quality to note and may be an important flow characteristic in high hold-up systems. In each case the instantaneous droplet count histograms show a tight grouping around a stable mean value within normal distributions. By

normalising these results into PDFs (Fig. 6.10) comparisons can more easily be made. Almost no difference is observed between the cycle times in the instantaneous or ensemble averaged PDFs. Additionally, all PDFs show clearly a normal distribution in the predicted $d_{[3,2]}$. The mean of the instantaneous $d_{[3,2]}$ sits at 1.312 - 1.337 mm and the mean of the ensemble averaged PDFs at 1.231-1.275 mm. Also, in both cases the standard deviation is an order of magnitude smaller in comparison to the mean. Quantitatively, this shows that in this case, the PSEC produces a strongly homogenous stage-wise droplet size distribution. Experimental data from PSEC systems analysed by Sreenivasulu *et al.* (1997) and in similar systems (disk and doughnut pulsed columns) by Amokrane *et al.* (2016) report similar droplet size ranges as normal distributions as homogenous systems.

The OPOSPM population balance was successful in producing corroborating predictions, when compared against those from the literature correlations (Table 6.2) for this system, namely against that from Míšek (1964). However, the predicted size is still smaller than the preferred correlation from Sreenivasulu *et al.* (1997) which could be down to two factors. The droplet size predicted in the correlation could be incorrect and/or the way in which OPOSPM is implemented requires adjustment. It is impossible to draw a conclusion on this observation without like-for-like experimental data to compare against. However, it has been noted that the OPOSPM requires a significant amount of knowledge *a priori* in its implementation. Moreover, the investigation in Section 6.5.2 highlights how this implementation of GEMMA produces low predictions for the turbulence characteristics which will affect the function of both the breakage and coalescence kernels.

With regards to the hold-up predictions in all three cases, the stage-wise hold up was compared using the method described in Section 5.3.3. VOF, GEMMA and E-E each predict a stage wise hold-up of 5.1%, 3.01% and 1.67% respectively under the same operational conditions. As mentioned, the VOF will not (in this case) predict a droplet size. The simulation campaign in Chapter 5 has highlighted the lack of variation in hold-up emergent as a result of the unaccounted droplet physics. Therefore, it is difficult to compare the two-fluid approaches against because of this, but it is known that VOF struggles in this regard. For the E-E implementation where a fixed droplet size of 2.2 mm was used, the droplet stage-wise hold-up is predicted to be very low. When the population balance is included in GEMMA, and consequently the average droplet size is reduced to 1.2 mm, the stage-wise hold-up increases (to almost double). This observation is inline with what is expected from classical hydrodynamic theory, namely derivations of *Stokes' law*, wherein the velocity of a dispersed particle increases with an increase in the particle radius, see Section 2.2.5.1 Eq. (2.26b). To test this directly, the volume-weighted mean of the z-component relative velocity ($U_{r,z}$) are also calculated for comparison in the same

way the stage-wise hold-up was calculated. Physically, this is average slip velocity between the dispersed and continuous phase calculated for the region between the two sieve-plates. For GEMMA and E-E the average slip velocity was calculated as 0.0602 ms^{-1} and 0.0994 ms^{-1} respectively. Indeed, a reduction in the droplet size prediction of GEMMA OPOSPM results in a lower slip compared to the E-E which coincides with an increase stage-wise hold-up despite the same operational conditions and dispersed-interface momentum transfer models.

The above observations and discussion lead to number of interesting conclusions on PSECs dispersion behaviour, as well as in GEMMA being a strong candidate for PSEC simulation. The droplet count histograms and PDFs showed little variance in the distribution of $d_{[3,2]}$ and the mean values reported were inline with those predicted from literature. Moreover, the observations on the homogeneity in the dispersion behaviour seen in the PDFs are close in nature to those reported for PSECs and similar extraction columns in literature. The inclusion of the OPOSPM population balance in the two-fluid approach (with GEMMA) lead to a reduction in the droplet size prediction and slip velocity resulting in an increase in the stage-wise hold-up (compared to E-E). This final point explicitly emphasises the need for dispersed-interface modelling in regions where the VOF fails to resolve the interface morphology. The population balance was successful in producing sensical results and is numerically stable, despite the range being rather large (relaxed). Inclusion of the $d_{[3,2]}$ is of particular interest for solvent extraction research and has brought with it novel methods of column performance analysis. Nevertheless, there was speculation over the performance due to the underlying dependence on the turbulence prediction which drive the breakage and coalescence kernels.

Table 6.6: Summary of the details of probability density normal distributions in Fig. 6.10

		Pulse Cycle Time			
		$\frac{1}{2}\pi$	π	$\frac{3}{2}$	2π
No. of Cells Evaluated		181,186	90,109	121,795	131,063
Instantaneous Predictions	**Mean**	1.337×10^{-3}	1.335×10^{-3}	1.312×10^{-3}	1.313×10^{-3}
	Standard Deviation	1.733×10^{-4}	1.819×10^{-4}	1.819×10^{-4}	1.777×10^{-4}
Ensemble Averaged Predictions	**Mean**	1.275×10^{-3}	1.231×10^{-3}	1.244×10^{-3}	1.249×10^{-3}
	Standard Deviation	0.859×10^{-4}	0.825×10^{-4}	0.811×10^{-4}	0.813×10^{-4}

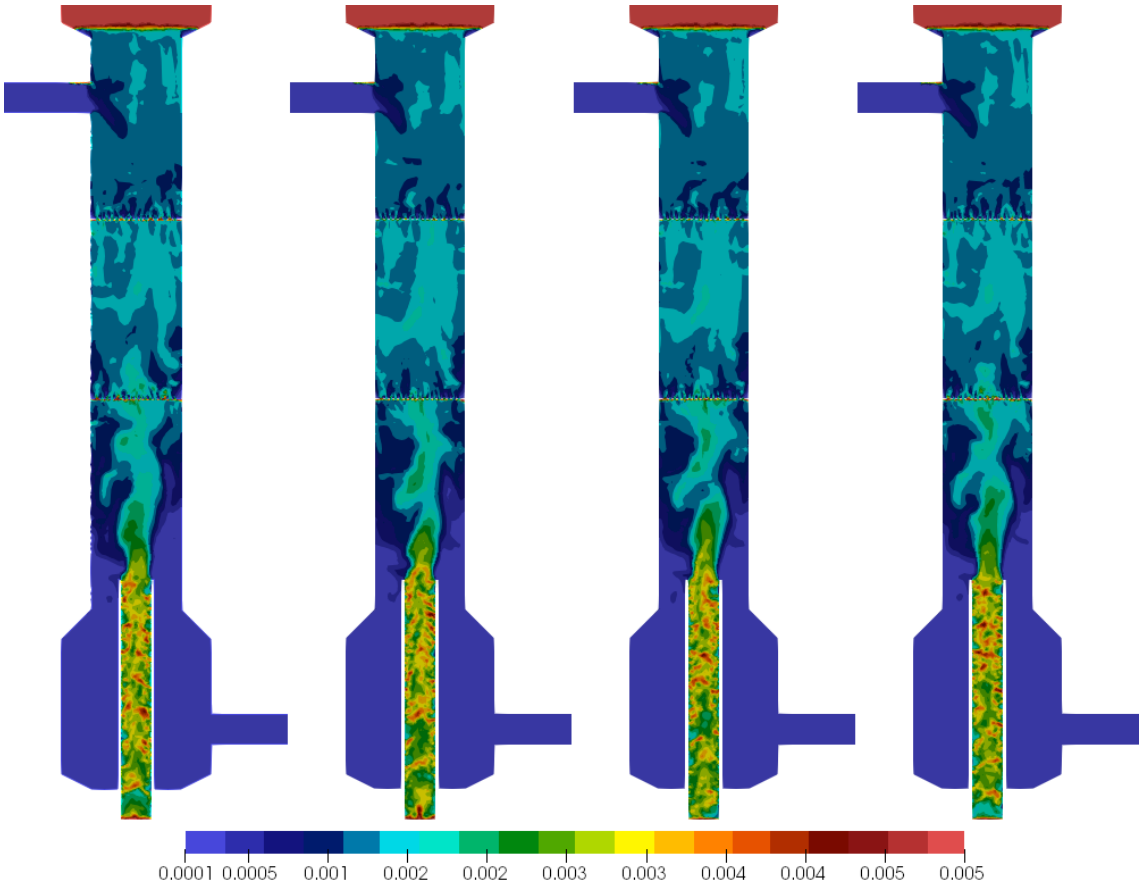

Figure 6.8: Contour plot of the $d_{[3,2]}$ distribution calculated using the OPOSPM population balance at $\frac{1}{2}\pi$, π, $\frac{3}{2}\pi$ and 2π.
(Note: results do not represent the actual droplet distribution, only the predicted $d_{[3,2]}$ for any dispersed phase fluid that would be in that cell.)

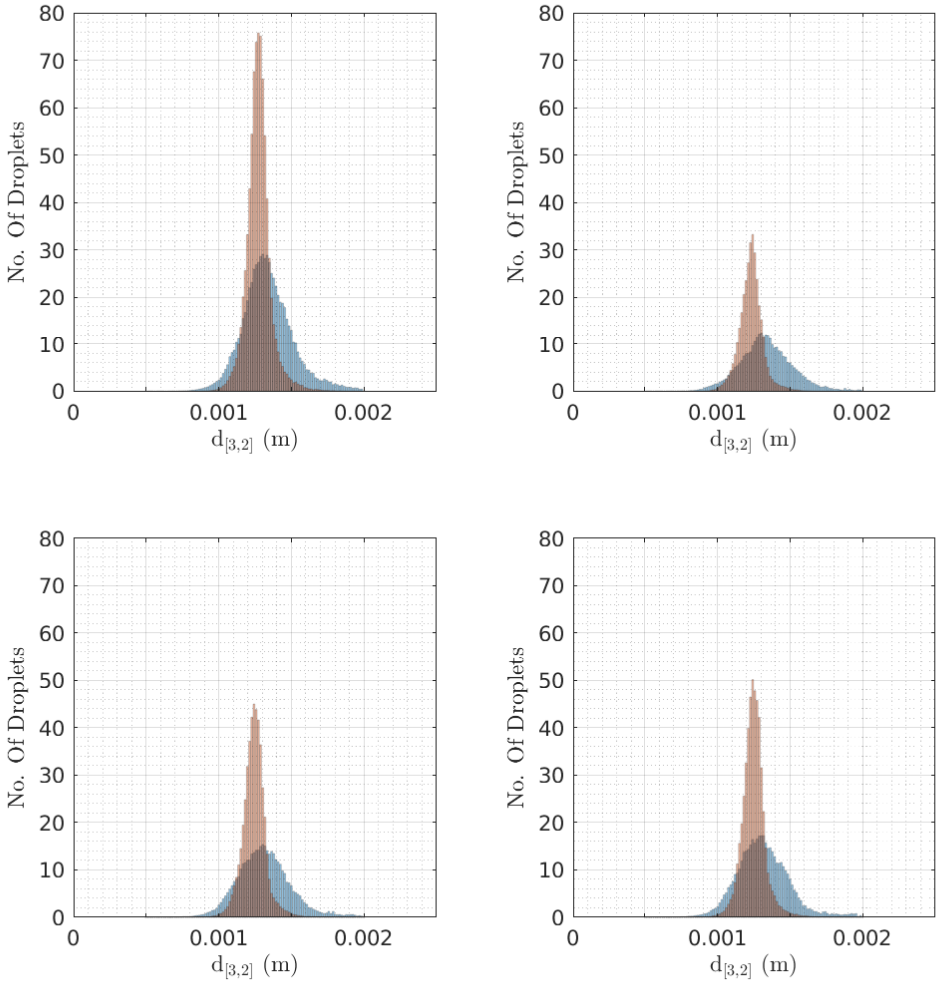

Figure 6.9: Droplet count distribution of the instantaneous results (—), and of the ensemble-averaged results (—) from the OPOSPM predictions calculated using the algorithm shown in Fig. 6.1 at cycle times $\frac{1}{2}\pi$ (top-left), π (top-right), $\frac{3}{2}\pi$ (bottom-left), 2π (bottom-right).

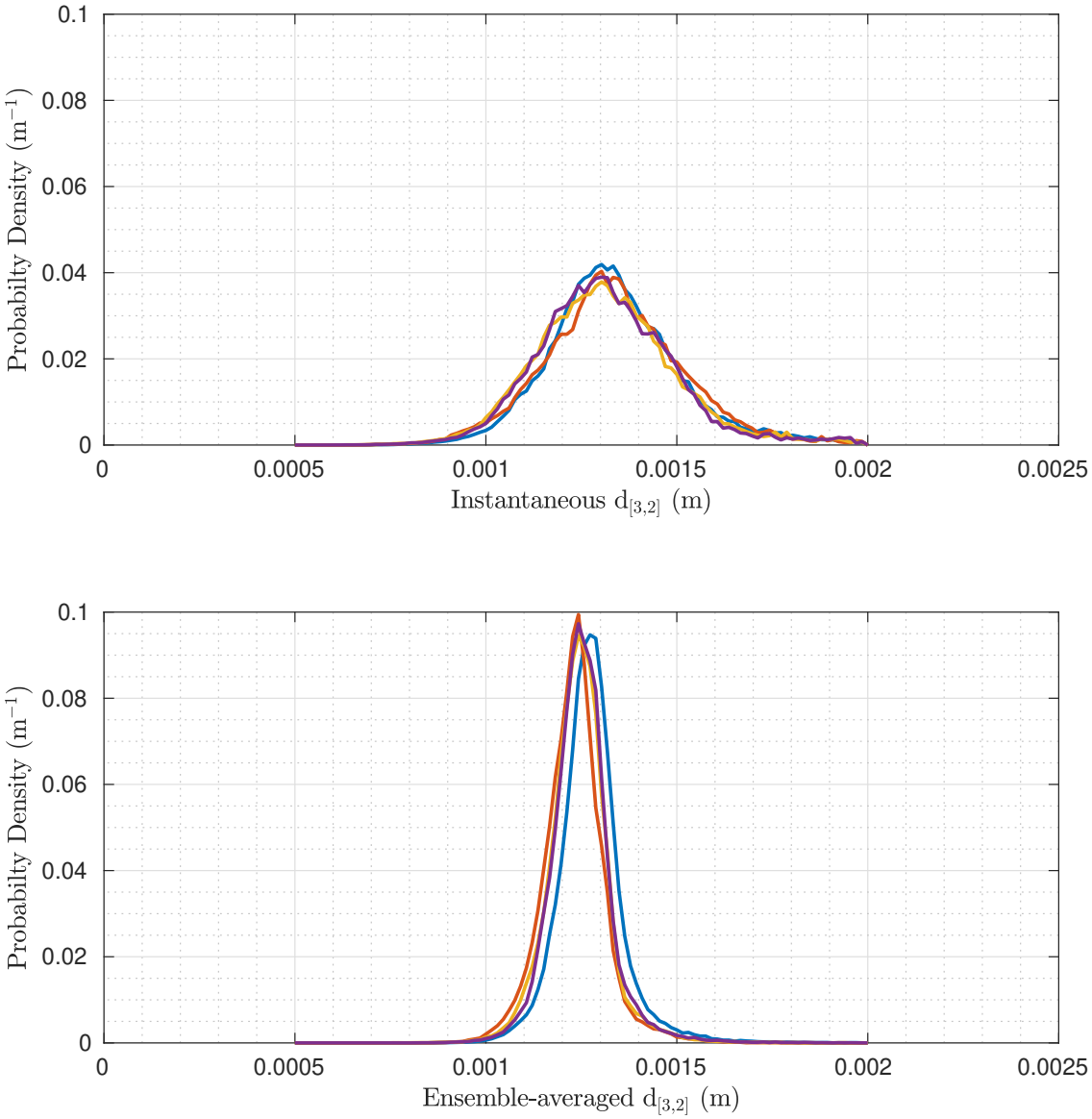

Figure 6.10: Instantaneous predicted PDF of the $d_{[3,2]}$ size distribution, calculated from OPOSPM, and the PDF of the $d_{[3,2]}$ size distribution after ensemble averaging; $\frac{1}{2}\pi$ (—), π (—), $\frac{3}{2}\pi$ (—), 2π (—).

6.5.4 The GEMMA Interface Model Switch

This final section will review the interface model switch implemented within GEMMA. It is understood that a switching mechanism is required to dynamically assign regions where VOF style resolved large-interface modelling is active and where two-fluid style dispersed-interface momentum transfer models are more appropriate. In this case, a novel algorithm is used which passes each mesh-cell through three criteria to determine if interface compression (VOF) is active via the binary velocity compression coefficient (C_α). As mentioned in detail in Section 3.2.3.1, if $C_\alpha = 0$ the standard dispersed-interface momentum transfer models are used to asses droplet drag, lift and virtual mass forces. When $C_\alpha = 1$ the momentum transfer models are no longer contributing, instead a specific large-interface drag model is assigned, the interface velocities are compressed and surface tension forces are included.

Figure 3.1 includes plots to compare the three criteria used to assign values of C_α to cells against the actual instantaneous C_α field where $C_\alpha = 1$. Here, cells are rendered where $C_\alpha = 0$ for the criteria $IRQ < 4$, $C_\alpha = 0$ for the criteria $\alpha_d < 0.111$ or $\alpha_d > 0.999$, and $C_\alpha = 1$ for the criteria $d_{3,2} > 2\Delta$ (double the cell length). Note that the criteria assessments are sequential in nature and that is taken into account, i.e. if a cell is switch off by its IRQ value, it will not be considered by the subsequent $\alpha_{min/max}$ or droplet size criteria.

Firstly, the IRQ criteria is in place to identify cells with resolvable interface morphologies based on the local curvature. This criteria has been successful in identifying the cells which are clearly dispersed in nature and, therefore, assigning $C_\alpha = 0$. Namely, the cells in the main bulk flow regions between the two decanters are captured and the cells under each sieve-plate are ignored and passed onto the next assessment.

The $\alpha_{min/max}$ criteria provides mixed results. Its intended purpose is to switch off interface compression in regions where pure phase exists only. Physically it does not make sense to provide interface compression when an interface is not in close proximity. In the top and bottom decanters there are a large number of cells that are assigned $C_\alpha = 0$ as expected. At the sieve-plates and primary interface (top decanter), a number of cells are assigned $C_\alpha = 0$. Similarly, a number of cells in the dispersed phase inlet pipe are assigned $C_\alpha = 0$ from heavy dispersion or, potentially, from numerical diffusion of the interface. Within this inlet region, it is known that the VOF is not able to completely resolve the interfaces and so this behaviour happens to be desirable. However, it would be more appropriate for these regions to be assessed by the droplet size criteria.

The droplet size criteria was effective in identifying cells that require large-interface modelling and, therefore, being assigned $C_\alpha = 1$. Namely, those comprising the slugging behaviour at the inlet pipe, coalescence at the plates and

around the primary interface (top decanter). However, at the primary interface the cells are not assessed in the centre. This is either because the maximum droplet size included in the population balance was fixed at 5 mm or the cells were assessed by the previous steps (IRQ or $\alpha_{min/max}$) and so were not considered by the droplet size criteria. The latter scenario is less likely, when comparing the final plot vs. the actual C_α field one can see the cells missing in the droplet assessment still retain a value of $C_\alpha = 1$ suggesting that those cells still retain this value from a previous time step (or from the original initialised field).

Overall, the switching criteria produced a desirable assessment of the interface modelling requirements on a dynamic and local basis. Specifically, in providing interface resolving at the large primary interface at the top decanter, across the sieve-plates where the droplet evolution is known to be easily resolved by VOF, and in capturing the mixed slugging and dispersion flow characteristics in the dispersed phase inlet pipe.

Nevertheless, a number of of useful statements can be derived from the observations and discussion of each criteria. The summary that follows can be used to inform users in their case definitions or as grounds for suggestions to improve the code by the developers. In this case $IRQ_{crit} = 4$, experimenting with lower values may reduce the number of cells that are filtered at the first stage so that they can be more appropriately assessed at the droplet size criteria stage. It is known the developers have included an option to remove this stage all together and is worth considering for this flow scenario. It was observed that the switching algorithm was highly sensitive to the choice of $\alpha_{min/max}$, this criteria is only in place to remove cells that are well within pure phase regions. As the system is particularly diffuse in the VOF cases (i.e. very low volume fraction regions where abundant) a conservative α_{min} value of 0.111 was used. In retrospect, it can be appropriate to use a stricter (lower) α_{min} value which will allow more cells to be passed on to the droplet size switching criteria which works excellently. As for the droplet size criteria, one obvious improvement was apparent with regards to its user implementation. The maximum droplet size set within the population balance will limit the effective range of this criteria. Therefore, careful consideration should be made, comparing the cell sizes in regions where large-interfaces are expected and the maximum droplet size set. Lastly, it is known in this version of GEMMA, the developers have not included a final assignment if cells are filtered by any of the criteria, and therefore retain the value set from the previous time step(s) or from initialisation. The developers have already considered this in the lasted version of GEMMA, (De Santis *et al.*, 2020). The above suggestions and recommendations are made with this in mind.

Figure 6.11: Distribution of cells switched on/off by steps in the GEMMA interfacial model switching algorithm, see Section 3.2.3.1 Fig. 3.1, at cycle time $\frac{1}{2}\pi$.
Row 1: Three-dimensional cell-view rendering.
Row 2: Two-dimensional slice along the the centre y-plane of cell-view renderings.

6.6 Conclusions

The work presented in this chapter has sought to provide a definitive assessment of available multiphase modelling approaches for faithful simulations of PSECs. A common E-E two-fluid approach was compared in conjunction with the previous single-fluid VOF run (Chapter 4) against a novel hybrid multi-scale approach. The hybrid VOF/EE model GEMMA is used to capture both the large-interface scales of flow apparent near the sieve-plates, dispersed phase inlet pipe and primary interface (top decanter), as well as the fine (unresolvable) dispersions apparent elsewhere. Moreover, a reduced population balance is included to avoid the need for assignment of a fixed droplet-size which is known to be a difficult closure parameter to justify for two-fluid frameworks *a priori*.

All three approaches were defined to simulate the same system using LES to resolve the velocity and turbulence. The differences observed between the three methods were ultimately consequential of the approach to the modelling the two fluid interactions. Through this study a number of unique conclusions were drawn with regards to both the modelling requirements of PSECS as well as in their hydrodynamic behaviour:

1. All three methods produced different predictions in the volume fraction fields which lead to differences in the resulting velocity fields. Without any form of interface resolving methods (E-E) the droplet evolution at the sieve plates was not correctly represented. Similarly, the distribution of the dispersed phase into the system, via the inlet slugging behaviour, could not be properly captured with pure dispersed-interface modelling. GEMMA was successful in addressing these issues leading to clear improvements to the two-fluid framework via successful interface resolution in those regions.
2. Comparisons of the ensemble-averaged velocity fields revealed that all three methods show, qualitatively, corroborating characteristics overall. However, quantitatively the GEMMA model was able to provide better predictions (over E-E) of the velocities across the sieve-plates against the benchmark VOF methods (considered resolved predictions for those regions). Moreover, it was apparent that the position of the primary interface (top decanter) is reliant on the momentum of the dispersed phase on approach. In the dispersed-interface regions, GEMMA was also able to provide the desired corrections within the z-directional velocity in the dispersed-interface regions, thought to be disregarded within the VOF implementation. Moreover, highlighted was the necessity to resolve the fluid interactions at the sieve-plates as this lead to considerable alterations to the flow regions nearby.
3. Predictions in the characteristics of the pressure field were found be in close agreement between the VOF and GEMMA approaches. Namely, in the

pressure drops of each phase stream across the column and in the pressure at each plate. The E-E method tended to produce lower predictions in the pressure field.

4. Comparisons in the predictions of the turbulence properties lead to some notable conclusions with regards to the two-fluid implementation. Firstly, without interface resolving methods, the turbulence characteristics can be misrepresented especially at the inlet pipe and development of turbulence towards the sieve-plates. Secondly, with dispersed-interface modelling, there appears to be a missing source-term that results in decay of the turbulence kinetic energy up the column.
5. The predictions of the mixing index criterion showed that all three approaches were able to produce results in close agreement. This provided evidence to show the LES was able to consistently provide predictions of the large scale dispersive mixing performance.
6. A specific review of the OPOSPM reduced population balance provided some interesting conclusions of the droplet dynamics of the system.
    - The droplet size ($d_{[3,2]}$) probability density functions showed normal distributions with stable mean values and small variance. Additionally, the distributions did not change with respect to the characteristic time in the pulse cycle.
    - The characteristics observed were inline with what was available for comparison against the literature.
    - The predicted droplet size was found to be smaller that that set for E-E taken from solution of the correlation by Sreenivasulu *et al.* (1997), but was in agreement with that predicted by Míšek (1964) correlation.
    - Some speculation of over the performance of the turbulence prediction raised concern over the resulting accuracy of the breakage and coalescence kernels.
7. Comparisons of the predicted stage-wise hold-up, slip velocity and droplet size between the E-E and GEMMA results confirmed speculations over why the VOF was unable to provide variations in the stage-wise hold up in the simulation campaign in Chapter 5. With dispersed interface modelling, the inclusion of drag forces produced the expected increase in the stage-wise hold-up when the droplet size predicted decreased. This was confirmed with comparisons of the slip velocities from the E-E and GEMMA predictions.
8. A review of the interface model switching, present in the GEMMA, provided a number of suggestions for users in their implementation of the model and/or for future development of the model. Nevertheless, the switching criteria was successful in producing a desirable assessment of the interface modelling requirements on a dynamic and local basis.

7

Conclusions & Recommendations for Further work

7.1 Conclusions

Since the conception of the first PSEC design by Van Dijck (1935), the underlying hydrodynamic complexities have never been fundamentally understood. There is undoubtedly a paucity of robust design methods which has been bred out of decades of repetitive empirical analysis. Such investigations have seldom contributed any novel advancements in the functional understanding of PSEC operation and design. There are a network of multivariate parameters: column geometry, sieve-plate design, throughput, solvent-flow-ratio, pulse leg design...the list goes on. After a comprehensive review of the history of PSEC R&D (Chapter 2) it is evident that a reductionist approach founded on empirical observation, although still useful, is not appropriate for engineering PSEC systems. This thesis has sought to leverage modern advancements in computing and computer aided engineering for novel research and system analysis.

High fidelity three-dimensional transient flow calculations were performed using large eddy simulation (LES), coupled with the volume of fluid method in Chapter 4. The objective here was to produce a CFD model capable of defining the turbulence characteristics of industrial PSECs for an explicit detailed analysis of the key hydrodynamic descriptions. This study finds that LES is effective at capturing the different scales of turbulence present within PSECs, and their operational influence. Explicit analysis of the hydrodynamics established that the sieve-plates drive dispersive mixing through their influence on the resulting turbulent flow and flow structures, and not in viscous stresses induced at the sieve-plates. This milestone discovery represents the first explicit example of understanding PSEC functionality during operation and provides the designer with an optimisation parameter. Namely, turbulence production. Consequently, the standard round-hole sieve-plate design is found to perform poorly at producing and distributing the types of flow and turbulence beneficial to droplet size reduction required for efficient mass transfer.

The LES approach is one that can be computationally expensive and has been

out of reach for many designers in previous years. With this in mind, the suitability of typical URANS methods was evaluated against the benchmark LES predictions. These methods have been heavily relied on in previous examples of PSEC turbulence modelling available in literature, see Section 2.3. Therefore, it is of paramount importance to provide an unbiased evaluation of the applicability of such methods. Specifically, with using the $k-\varepsilon$ and SSG RSM turbulence closures (Launder & Spalding, 1974; Speziale *et al.*, 1991). Both URANS methods could not provide agreeable solutions with the inherently more accurate LES predictions. The distinct and contradictory multiphase behaviour between all three solutions is thought to be due to the differences in the solutions of the velocity fields. This is due to deficiencies in the k$-\varepsilon$ model (not being able to handle rotational, impinging and buoyancy driven flows) and from the SSG RSM model as result of the turbulence boundary/initial conditions used that are derived from the solution of the k-ε model. Moreover, the resulting turbulence predictions from both URANS approaches either vastly overpresdict ($k-\varepsilon$) or under predict (SSG RSM) solutions. As mentioned previously, this quantisation of the turbulence parameters is essential for PSEC simulation. The benefit of using URANS to provide a fast solutions is voided by the accuracy of the provided solution. It is therefore clear that URANS methods are not suitable for prediction of complex multiphase flows in counter-current PSECs. Therefore, LES has been identified as the necessary method for turbulence characterisation and sets the standard for PSEC CFD simulation.

The coupled LES VOF PSEC model was then carried forward for a campaign of 25 unique simulations in Chapter 5. The aim was to develop a means of predicting and/or identifying flooding, as well as to investigate the appropriateness of VOF in predicting inter-stage hold-up and modes of operation. Statistical methods for design of the simulation matrix, and subsequent analysis, allowed for an efficient and rich data set to provide a comprehensive operational analysis. Statically distinct combinations of the operational variables, pulse velocity (Af), total throughput ($U_d + U_c$) and solvent-flow-ratio (U_d/U_c), were used to investigate an extensive operational range.

Tracking the convergence behaviour of the transient global dispersed phase hold-up allowed for a positive or negative flooding response to be identified for each run. This is a novel means of flooding diagnosis, in PSEC CFD analysis, that has been extended from the philosophy presented by Thornton (1957) and used at the ORNL in physical PSEC trails. The flooding behaviour observed was found to be highly non-linear in nature and dependent on all three operational variables tested. Comparisons against accepted empirical correlations, Smoot *et al.* (1959), highlight the deficiencies in these reductionist approaches. Instead, first-order data modelling methods were employed to resolve a true flooding surface which maps out, explicitly,

the operational envelope of instability. Additionally, logistic regression analysis of the resulting pressure field characteristics of each case resulted in the development of a diagnostic tool to predict the likelihood of flooding, with quantifiable confidence, based on the observed dispersed and continuous phase pressure drops across the column. Both of the aforementioned analytical methods are extremely valuable contributions to PSEC R&D. They prove that with a limited number of runs, the designer can produce rich diagnostic models that can be directly integrated into PSEC control systems or used to inform operational design.

Statistical descriptions were used to analyse the variability of the stage-wise hold-up data taken from the simulation campaign. The consistency of the predicted hold-up, across the all cases, lead to suspicions in the ability of VOF to capture the complete multiphase behaviour in PSECs. As a consequence, no other modes of operation, other than dispersed regime and flooding, were observed despite the wide operational range investigated. It was then postulated that this artefact is likely a result of missing force balances between the dispersed and continuous phase in regions of high dispersion and low interface resolution. This was then used as justification for the subsequent development of the multiphase model in Chapter 6.

The work presented in Chapter 6 provides, a clear definitive assessment of available multiphase modelling approaches. It is understood, from the examples published in literature, that no specific assessment of the two main approaches (single-fluid VOF and two-fluid E-E) has been discussed and both methods are used without justification. When in fact, the previous investigations have highlighted the necessity for interface resolving methods (VOF) but also admit its shortfalls. This final study has sought to continue progression in the advancement of PSEC simulation through implementation of state-of-art multiphase modelling. The hybrid VOF/E-E GEMMA multiscale model with population balance, developed in-house at the University of Leeds, has been used to bridge the gap between both standard approaches (De Santis *et al.*, 2020). The aim being to identify a model that can resolve the phase interactions and droplet evolution at the sieve-plates and incorporate appropriate force balances (momentum exchange models) across dispersed interfaces in high dispersion and low resolution regions. The addition of a reduced population balance, previously used by (Alzyod *et al.*, 2018), also allows for modelled predictions of the $d_{[3,2]}$ distributions which, typically, has to be defined for E-E implementations *a priori* and is a known closure issue.

The hybrid multiphase GEMMA model was found to be successful in many areas for providing faithful predictions of the multiphase behaviour. In the sieve-plate and dispersed phase inlet regions, the resulting fluid interactions were successfully resolved. This meant the GEMMA model was able to resolve the flow development in these regions leading to predictions of the velocity and,

importantly, pressure field characteristics (pressure drops) that are in agreement with the VOF method. The latter point means that the tools developed in Chapter 5 will be reproducible under the GEMMA model framework. In the bulk flow regions, were the interface becomes exceedingly difficult to explicitly resolve, the underlying population balance and dispersed-interface modelling provided the desired improvements in the dispersed phase velocity predictions. This was made most evident when comparing the slip velocity predictions between the E-E and GEMMA results. Each model ran under the assumption of different $d_{[3,2]}$ closures, as a consequence of the population balance implemented in GEMMA. As a result, the expected variability in the hold-up emerged due to inclusion of the slip velocity mechanics (absent in VOF). This makes GEMMA an ideal candidate for exploring the alternate modes of PSEC operation to compliment and/or refine the findings presented Chapter 5.

With regards to the population balance modelling, the resulting PDF normal distributions and droplet size ranges were qualitatively inline with those reported for similar equipment (Amokrane *et al.* (2016)) and previous published PSEC PDF data (Sreenivasulu *et al.* (1997)). The PDF mean $d_{[3,2]}$ sizes also provide some corroboration against those calculated from empirical correlations, namely by Míšek (1964). This reveals exciting opportunities for coupled mass transfer models now that the $d_{[3,2]}$ can be confidently defined and modelled. The result being a complete computational model that encapsulates all the required physics necessary for industrial design and optimisation of PSECs for nuclear solvent-extraction processes.

7.2 Proposal for Further Work

The work presented in this thesis has provided leaps and bounds in available knowledge gained from the assessment of CFD PSEC modelling. Moreover, it has set standards for PSEC simulations through interrogation of turbulence and multiphase modelling approaches. Furthermore, the work presented has provided a number of analytical frameworks and diagnostic tools for further PSEC investigations. As such, this work has set the stage for numerous potential advancements the field in PSECs R&D.

The findings from comparisons against the $k - \varepsilon$ and SSG RSM URANS closures in Chapter 4 has shown, undoubtedly, the need for transient eddy resolving techniques for turbulence characterisation in PSECs. However, the LES methods employed are, admittedly, very computationally expensive. Alternative hybrid LES/URANS methods can help to reduce the mesh size dependency in order cut on computational times, such as detached eddy simulation (DES) and delayed detached eddy simulation (DDES). Moreover, modern advancements on discretisation of the filtered LES equations using the Lattice-Boltzmann method can allow for computation on highly parallelised computational architecture, specifically on GPUs. Similarly, work is underway to parallelise LES FVM code onto GPUs. Advancements in GPU technology, and architecture, does provide exciting opportunity for eddy resolving methods to be efficient and accessible, potentially replacing RANS techniques entirely in the coming decades (Sim-scale, 2020).

The conclusions from Chapter 5 has yielded a number of potential work packages. It has also provided evidence for the value of this work and necessity for using novel methods of analysis/data modelling techniques in order interrogate engineered systems in greater detail. The data modelling interpolation methods used demonstrated the feasibility and value in multivariable investigation. To repeat this simulation campaign with the revised multiphase model GEMMA would provide insight into the development of hold-up within PSECs and their operational conditions. Moreover, this method could be efficiently applied to research of physical columns wherein hold-up can be measured via loading cell monitoring the global changes in the column mass. Analysis of the logistic regression modelling has uncovered new possibilities into engineered approaches to PSEC control and optimisation. Mentioned was the potential to manipulate the operational envelope via modification of the upstream and downstream pressure conditions. It would be recommended that this concept is explored seriously as it has potential to mitigate flooding and increase the operable range of PSECs. From an initial screening against the control variables, no direct correlations were apparent between pressure drop of the continuous or dispersed phase fluids and

operational variables. Therefore, as a first-step there is a clear need to evaluate factors effecting pressure drops within PSECs.

The novel multiphase investigation undertaken in Chapter 6 has drawn attention to the need for a multiscale framework as necessary to faithfully simulate PSECs. Work, is still required to provide better quantification of the turbulence properties emergent from the statistics of the velocity predictions. The two-fluid framework, from which GEMMA is founded, naturally leads to absence of consideration of the velocity and density gradients crossing the interface(s) between the two fluids. As a result, the buoyant flux term in the production of turbulence kinetic energy is not accounted for. Modifications to how the density and velocity is scaled at interfaces can help in this regard. This is a recommendation that the developers, De Santis *et al.* (2020), should consider in detail. In turn, these improvements will provide better confidence in the predictions of the turbulence quantities and the dependent terms in the population balance (in the breakage and coalescence kernels).

Also noted was potential improvements to the OPOSPM population balance. It is not certain if the developers will continue to champion this method of droplet size quantification in favour richer alternatives. Namely, in those that calculate the $d_{[3,2]}$ directly and provide cell-wise droplet size multi-level groupings. Nevertheless, the method has proven successful in this instance. Some fine-tuning of the breakage and coalescence kernels will help to improve and build confidence in the $d_{[3,2]}$ predictions. Moreover, the conversion factor of 0.76 used for $d_{[3,0]} \rightarrow d_{[3,2]}$ is taken from Wardle & Weller (2013). It is a constant evaluated from the data taken from the droplet size distributions out of centrifugal contactors. It performs well for the log-normal distributions apparent in centrifugal contactors but may not be appropriate for PSECs. The applicability of this constant for PSEC droplet size distributions will need to be tested. There is, therefore, a clear need for physical PSEC experimental data which would be used to validate the droplet size predictions, as well as other hydrodynamic predictions.

There is potential to couple mass transfer models with predicted $d_{[3,2]}$ distributions from the population balance. These models could be empirical or, ideally, mechanistic in their implementation. It is understood that new recruits at the University of Leeds are already underway in providing these developments. The coupled stage-wise mass transfer models are to be cross validated against a recently erected PSEC within the Nuclear Engineering Research department aimed at providing necessary experimental data.

Discussions of the switching mechanism of the GEMMA model has produced a number of clear suggestions for user operation of the code. Apparent was the need to properly quantify the critical IRQ cut-off value and the maximum droplet size limit (in OPOSPM). One clear improvement to the 'switching algorithm' would be to include a final assignment of the C_α cell value at the end of the algorithm loop

if no criteria are met. However, it is understood that this issue has already been addressed by the developers.

The investigations into the hold-up predictions between both two-fluid methods confirmed the suspicions in the concerns the VOF model. Specifically, that the VOF model failed to provide variability in the predicted stage-wise hold-up. It is recommanded that a reduced simulation campaign is again undertaken with the GEMMA approach. This would be used to supplement the knowledge gained from the campaign undertaken with VOF in Chapter 5 and allow for analysis of the stage-wise hold-up and its relationships with other variables. Specifically, the pressure drop of the two fluid phases, operational variables, and approach to the flooding limit. In doing so, one could also produce a more logical 'true flooding surface' that resolves the flooding regions (unstable operation) from the development of the stage-wise hold-up.

References

Alzyod, S., Attarakih, M. & Bart, H.J. (2018). CFD modelling of pulsed sieve plate liquid extraction columns using OPOSPM as a reduced population balance model: hydrodynamics and mass transfer. *Computer Aided Chemical Engineering*, **43**, 451–456.

Amani, P., Safdari, J., Abolghasemi, H., Mallah, M.H. & Davari, A. (2016). Two-phase pressure drop and flooding characteristics in a horizontal-vertical pulsed sieve-plate column. *International Journal of Heat and Fluid Flow*, **65**, 266–276.

Amokrane, A., Maass, S., Lamadie, F., Puel, F. & Charton, S. (2016). On droplets size distribution in a pulsed column. Part I: In-situ measurements and corresponding CFD-PBE simulations. *Chemical Engineering Journal*, **296**, 366–376.

Ansys (2009). *ANSYS FLUENT 12.0 User's guid*. ANSYS Inc.

Asadollahzadeh, M., Haghighi-Asl, A., Safdari, J. & Torab-Mostaedi, M. (2011). Flooding characteristics in pulsed packed extraction columns. *Brazilian Journal of Chemical Engineering*, **28**, 639–648.

Bahmanyar, H., Chang-Kakoti, D.K., Garro, L., Liang, T.B. & Slater, M.J. (1990). Mass transfer from single drops in rotating disc, pulsed sieve plate and packed liquid-liquid extraction columns. *Chemical engineering research & design*, **68**, 74–83.

Berger, R. & Walter, K. (1985). Flooding in pulsed sieve plate extractors. *Chemical Engineering Science*, **40**, 2175–2184.

Box, G.E.P. & Behnken, D.W. (1960). Some New Three Level Designs for the Study of Quantitative Variables. *Technometrics*, **2**, 455–475.

Boyadzhiev, L. & Spassov, M. (1982). On the size of drops in pulsed and vibrating plate extraction columns. *Chemical Engineering Science*, **37**, 337–340.

Brackbill, J.U., Kothe, D.B. & Zemach, C. (1992). A continuum method for modeling surface tension. *Journal of Computational Physics*, **100**, 335–354.

Bril, K.J. & Costa, E.C. (1964). Technology of Pulsed Sieve-Plate Extraction Columns. Tech. rep., IEA, San Paulo.

Burkhart, L.E. & Fahien, R.W. (1958). Pulse Column Design. Tech. Rep. November, Ames laboratory, Iowa state college, Ames.

Burns, W. & Johnson, W. (1953). Plate design for pulse columns.

Burns, W.A., Groot, C. & Slansky, C.M. (1949). HW-14728: The Design and Operation of the Pulse Column. Tech. rep., Hanford Site Works, Hanford.

Cerne, G., Petelin, S. & Tiselj, I. (2001). Coupling of the Interface Tracking and the Two-Fluid Models for the Simulation of Incompressible Two-Phase Flow. *Journal of Computational Physics*, **171**, 776–804.

Chhabra, R. (1993). *Bubbles, drops, and particles in non-Newtonian fluids*. CRC Press, Boca Raton.

Cohen, R. & Beyer, G. (1952). Performance of a Pulse Extraction Column - ISC294. Tech. rep., United States Atomic Energy Comission, Oak Ridge.

Coleman, G.N. & Sandberg, R.D. (2010). A primer on direct numerical simulation of turbulence-methods, procedures and guidelines. Tech. rep., Areodynamics & Flight Mechanics Research Group, Southamption.

Cullen, P.J. (2009). *Food Mixing: Principles and Applications*. Wiley.

Daly, B.J. & Harlow, F.H. (1970). Transport Equations in Turbulence. *The Physics of Fluids*, **13**, 2634–2649.

De Santis, A., Colombo, M., Hanson, B.C. & Fairweather, M. (2020). A generalized multiphase modelling approach for multiscale flows. *Journal of Computational Physics (In Review)*.

Deshpande, S.S., Anumolu, L. & Trujillo, M.F. (2012). Evaluating the performance of the two-phase flow solver interFoam. *Computational Science and Discovery*, **5**.

Din, G.U., Chughtai, I.R., Inayat, M.H., Khan, I.H. & Qazi, N.K. (2010). Modeling of a Two-Phase Countercurrent Pulsed Sieve Plate Extraction Column - A Hybrid CFD and Radiotracer RTD Analysis Approach. *Separation and Purification Technology*, **73**, 302–309.

Drumm, C., Attarakih, M., Hlawitschka, M.W. & Bart, H.J. (2010). One-group reduced population balance model for CFD simulation of a pilot-plant extraction column. *Industrial and Engineering Chemistry Research*, **49**, 3442–3452.

Duan, W., Zhao, M., Wang, C. & Cao, S. (2014). Recent Advances in the Development and Application of Annular Centrifugal Contactors in the Nuclear Industry. *Solvent Extraction and Ion Exchange*, **32**, 1–26.

Edwards, C.R. & Oliver, A.J. (2000). Uranium processing: A review of current methods and technology. *JOM*, **52**, 12–20.

Ellison, C.V. (1951). Study of a half-inch pulse column with a TBP system. Tech. rep., Oak Ridge National Laboratory, Oak Ridge, Tennessee.

Feick, G. & Anderson, H.M. (1952). Performance of a Packed Liquid-Liquid Extraction Column. *Industrial & Engineering Chemistry*, **44**, 404–409.

Gambill, W.R. (1959). How to estimate mixtures viscosities. *Chemical Engineering*, **66**, 151–152.

Gameiro, M.L.F., Machado, R.M., Ismael, M.R.C., Reis, M.T.A. & Carvalho, J.M.R. (2010). Copper extraction from ammoniacal medium in a pulsed sieve-plate column with LIX 84-I. *Journal of Hazardous Materials*, **183**, 165–175.

Garthe, D. (2006). *Fluid dynamics and mass transfer of single particles and swarms of particles in extraction columns*. Ph.D. thesis, Technische Universitat Munchen.

Gayen, B. & Sarkar, S. (2011). Negative turbulent production during flow reversal in a stratified oscillating boundary layer on a sloping bottom. *Physics of Fluids*, **23**.

Gayler, R.L., Roberts, N.W. & Pratt, H.R.C. (1953). Liquid-liquid extraction. Part 4. A further study of hold-up in packed columns. Tech. rep., Atomic Energy Research Establishment, Harwell.

Germano, M. (1992). Turbulence: the filtering approach. *Journal of Fluid Mechanics*, **238**, 325.

Green, D.W. & Perry, R.H. (2008). *Perry's Chemical Engineers' Handbook, Eighth Edition*. McGraw-Hill Education, New York, 8th edn.

Hafez, M.M. & Baird, M.H.I. (1978). Power consumption in a reciprocating plate extraction column. *Trans. Inst. Chem. Eng*, **56**, 229–238.

Han Li, W. (1952). *Liquid-Liquid Extraction in a Pulsed Perforated-Plate Column*. Ph.D. thesis, Georgia Instute of Technology.

He, C.H., Gao, Y.H., Yang, S.H. & Edwards, D.W. (2004). Optimization of the process for recovering caprolactam from wastewater in a pulsed-sieve-plate column using green design methodologies. *Journal of Loss Prevention in the Process Industries*, **17**, 195–204.

Hecht, N. (2015). Towards general purpose LES model of injection and atomization.

Hinze, J. (1955). Fundementals of the hydrodynamic mechanism of splitting in dispersion processes. *AIChE Journal*, **1**, 289.

Hu, S. & Kintner, R.C. (1955). The Fall of Single Liquid Drops Through Water. *AIChE Journal*, **1**, 42–48.

IEA (2020). Innovation needs in the Sustainable Development Scenario. *Energy Technology Perspectives 2020*, 61–89.

Ingham, J., Slater, M.J. & Retamales, J. (1995). Single phase axial mixing studies in pulsed sieve plate liquid-liquid extraction columns. *Chemical engineering research & design*, **73**, 492–496.

IPCC (2018). Global Warming of 1.5 deg C and IPCC special report on the impacts. Tech. rep., IPCC, Geneva.

Irvine, A..R. (1957). Pulse Pumping: A Means for Transfer. Tech. rep., ORNL, Oak Ridge, Tennessee.

James, G., Witten, D., Hastie, T. & Tibshirani, R. (2017). *An Introduction to Stastical Learning*, vol. 11. Springer, New York.

Jaradat, M., Attarakih, M. & Bart, H.J. (2011). Population Balance Modeling of Pulsed (Packed and Sieve-Plate) Extraction Columns: Coupled Hydrodynamic and Mass Transfer. *Industrial and Engineering Chemistry Research*, **50**, 14121–14135.

Jealous, A. & Johnson, H. (1955). Power Requirements for Pulse Generation in Pulse Columns. *Industrial & Engineering Chemistry*, **47**, 1159–1166.

Jiao, C., Ma, S. & Song, Q. (2013). Mass transfer characteristics in a standard pulsed sieve-plate extraction column. *Energy Procedia*, **39**, 348–357.

Johnson, A. & Hamielec, A.E. (1960). Mass transfer inside drops. *AIChE Journal*, **6**, 145–149.

Jones, S. (1962). *On the Behaviour of a Pulsed Extraction Column*. Ph.D. thesis, Universtiy of Michigan.

Kagan, S.Z., Aerov, M.E., Lonik, V. & Volkova, T.S. (1965). Some hydrodynamic and mass-transfer problems in pulsed sieve-plate extractors. *International Chemical Engineering*, **5**, 656.

Khatir, Z., Hanson, B.C., Fairweather, M. & Heggs, P.J. (2016). High-fidelity CFD simulations of pulsed sieve-plate extraction columns. In *ETMM11*, White Rose Uniersity Consortium, Palermo.

Kim, K.Y., Samad, A. & Benini, E. (2019). *Design Optimization of Fluid Machinery: Applying Computational Fluid Dynamics and Numerical Optimization*. Wiley.

Kishbaugh, A.A. (2000). Development and Performance of Centrifugal Mixer-Settlers in the Reprocessing of Nuclear Fuel. Tech. rep., Savannah River Site, Savannah.

Kolhe, N.S., Mirage, Y.H., Patwardhan, A.V., Rathod, V.K., Pandey, N.K., Mudali, U.K. & Natarajan, R. (2011). CFD and Experimental Studies of Single Phase Axial Dispersion Coefficient in Pulsed Sieve Plate Column. *Chemical Engineering Research and Design*, **89**, 1909–1918.

Kolmogoroff, A. (1941a). Dissipation of energy in the locally isotropic turbulance. *C.R. Acad. Sci. URSS*, **32**, 19.

Kolmogoroff, A. (1941b). The local structure of turbulence in incompressible viscous fluid for very large Reynold's numbers. *C.R. Acad. Sci. URSS*, **30**, 301.

Kowalczuk, P. & Drzymala, J. (2016). Physical meaning of the Sauter mean diameter of spherical particulate matter. *Particulate Science and Technology*, **34**, 645–647.

Kumar, A. & Hartland, S. (1983). Correlations for dispersed phase hold-up in pulsed sieve-plate liquid-liquid extraction columns. *Chemical Engineering Research and Design*, **61**, 248–252.

Kumar, A. & Hartland, S. (1986). Prediction of Drop Size in Pulsed Perforated-Plate Extraction Columns. *Chemical Engineering Communications*, **44**, 163–182.

Kumar, A. & Hartland, S. (1988). Prediction of dispersed phase hold-up in pulsed perforated-plate extraction columns. *Chemical Engineering and Processing*, **23**, 41–59.

Kumar, A. & Hartland, S. (1989). Prediction of continuous-phase axial mixing coefficients in pulsed perforated-plate extraction columns. *Industrial & Engineering Chemistry Research*, **28**, 1507–1513.

Kumar, A. & Hartland, S. (1994). Empirical prediction of operating variables. In J.C. Godfrey & M. Slater, eds., *Liquid-Liquid Extraction Equipment*, 141–226, John Wiley & Sons Ltd, chichester.

Kumar, A. & Hartland, S. (1996). Unified Correlations for the Prediction of Drop Size in Liquid-Liquid Extraction Columns. *Industrial & Engineering Chemistry Research*, **35**, 2682–2695.

Kumar, A. & Hartland, S. (1999). Correlations for Prediction of Mass Transfer Coefficients in Single Drop Systems and Liquid–Liquid Extraction Columns. *Chemical Engineering Research and Design*, **77**, 372–384.

Laddah, G.S. & Degaleesan, T.E. (1976). *Transport Phenomena in Liquid Extraction*. McGraw-Hill, New York.

Lade, V.G., Rathod, V.K., Bhattacharyya, S., Manohar, S. & Wattal, P.K. (2013). Comparison of normal phase operation and phase reversal studies in a pulsed sieve plate extraction column. *Chemical Engineering Research and Design*, **91**, 1133–1144.

Launder, B. & Spalding, D. (1974). The numerical computation of turbulent flows. *Computer Methods in Applied Mechanics and Engineering*, **3**, 269–289.

Legendre, D. & Magnaudet, J. (1998). The lift force on a spherical bubble in a viscous linear shear flow. *Journal of Fluid Mechanics*, **368**, 81–126.

Leonard, A. (1975). Energy Cascade in Large-Eddy Simulations of Turbulent Fluid Flows. *Advances in Geophysics*, **18**, 237–248.

Lochiel, A.C. & Calderbank, P.H. (1964). Mass transfer in the continuous phase around axisymmetric bodies of revolution. *Chemical Engineering Science*, **19**, 471–484.

Logsdail, D. & Slater, M. (1983). Pulsed Perforated-Plate Columns. In T. Lo, M. Baird & C. Hanson, eds., *Handbook of Solvent Extraction*, 355–372, Wiley, New York.

Logsdail, D. & Slater, M. (1991). Pulsed Perforated-Plate Columns. In T.C. Lo, M.H.I. Baird & C. Hanson, eds., *Handbook of Solvent Extraction*, 355–457, Krieger Publishing Company, Florida.

Lorenz, M., Haverland, H. & Vogelphol, A. (1990). Fluid dynamics of pulsed sieve plate extraction columns. *Chemical Engineering & Technology*, **13**, 411–422.

Lovasic, Z. (2008). Spent Fuel Reprocessing Options. Tech. Rep. August, IAEA, Vienna.

Luo, G., Li, H., Fei, W. & Wang, J. (1998). A simplified correlation of mass transfer in a pulsed sieve plate extraction column. *Chemical Engineering and Technology*, **21**, 823–827.

Marschall, H. (2011). Towards the Numerical Simulation of Multi-Scale Two-Phase Flows. 322.

Martínez-Bazán, C., Lasheras, J.C. & Montañés, J.L. (1999). On the breakup of an air bubble injected into a fully developed turbulent flow. Part I: Breakup frequency. *30th Fluid Dynamics Conference*, **401**, 157–182.

Matar, O. (2015). No more empirical correlations. *TCE The Chemical Engineer*, 42–45.

Mcallister, R.A., Groenier, W.S. & Ryon, A.D. (1967). Correlation of flooding in pulsed, perforated-plate extraction columns. *Chemical Engineering Science*, **22**, 931–944.

McKetta, J.J. (1992). *Petroleum Processing Handbook*. Taylor & Francis.

McKetta, J.J. (1998). *Encyclopedia of Chemical Processing and Design: Volume 65 – Waste: Nuclear Reprocessing and Treatment Technologies to Wastewater Treatment: Multilateral Approach*. Chemical Processing and Design Encyclopedia, Taylor & Francis, Boca Raton.

Mehra, V. & Chaturvedi, S. (2016). Determination of the flooding curve of a pulsed sieve-plate extraction column through open FOAM CFD simulations. In *Proceedings of SESTEC-2016*, 1 –11.

Meneveau, C., Lund, T.S. & Cabot, W.H. (1996). A Lagrangian dynamic subgrid-scale model of turbulence. *Journal of Fluid Mechanics*, **319**, 353–385.

Milot, J., Duhamet, J., Gourdon, C. & Casamatta, G. (1990). Simulation of a pneumatically pulsed liquid-liquid extraction column. *The Chemical Engineering Journal*, **45**, 111–122.

Míšek, T. (1964). The hydrodynamic behaviour of pulsed liquid-liquid extractors. *Collection of Czechoslovak Chemical Communications*, **29**, 1755–1766.

Misra, V.N., Das, S.C. & Rao, K.S. (2002). *Proceedings of the International Symposium on Solvent Extraction (ISSE)*. Allied Publ.

Miyauchi, T. & Oya, H. (1965). Longitudinal dispersion in pulsed perforated-plate columns. *AIChE Journal*, **11**, 395–402.

Nash, K.L. & Lumetta, G.J. (2011). *Advanced Separation Techniques for Nuclear Fuel Reprocessing and Radioactive Waste Treatment*. Woodhead Publishing Series in Energy, Elsevier Science, Cambridge.

Newman, A.B. (1931). Th e dr ying of porous solids: Diffusions and surface emission equations, Tr ans. *Am. Inst. Chem. Eng*, **27**, 203–220.

OpenCFD Ltd (2016). OpenFOAM User Guide. Tech. rep., Bracknell.

OpenFOAM (2011). OneEqEddy.C and OneEqEddy.H.

Pacek, A.W., Man, C.C. & Nienow, A.W. (1998). On the Sauter mean diameter and size distributions in turbulent liquid/liquid dispersions in a stirred vessel. *Chemical Engineering Science*, **53**, 2005–2011.

Phillips, C. (1992). Uranium-Plutonium Partitioning by Pulsed Column in the First Cycle of the Thermal Oxide Reprocessing Plant. *WM Symposia Journal*, 1041–1047.

Pietzsch, W. & Blass, E. (1987). A new method for the prediction of liquid pulsed sieve-tray extractors. *Chemical engineering & technology*, **10**, 73–86.

Pietzsch, W. & Pilhofer, T.H. (1984). Calculation of the drop size in pulsed sieve-plate extraction columns. *Chemical Engineering Science*, **39**, 961–965.

Pinzow, L. (1957). *Characteristics of a pulsed packed, liquid-liquid extraction column.*. Ph.D. thesis, US Naval Postgraduate School.

Pope, S.B. (2000). *Turbulent Flows*. Cambridge University Press, Cambridge.

Pope, S.B. (2004). Ten questions concerning the large-eddy simulation of turbulent flows. *New Journal of Physics*, **6**.

Pratt, H.R.C. (1991). Interphase Mass Transfer. In T.C. Lo, M. Baird & C. Hanson, eds., *Handbook of Solvent Extraction*, chap. 3, 91–125, John Wiley & Sons Ltd, New York.

Prince, M.J. & Blanch, H.W. (1990). Bubble coalescence and break-up in air-sparged bubble columns. *AIChE Journal*, **36**, 1485–1499.

Rauwendaal, C. (1999). New dispersive mixers based on elongational flow. *Plastics, Additives and Compounding*, **1**, 21–23.

Rincón-Rubio, L.M., Kumar, A. & Hartland, S. (1993). Characterization of flooding in a wirz extraction column. *The Canadian Journal of Chemical Engineering*, **71**, 844–851.

Rousseau, R.W. (1987). *Handbook of Separation Process Technology*. A Wiley-Interscience publication, John Wiley & Sons, New York.

Rusche, H. (2002). *Computational fluid dyanmics of dispersed two-phase flows at high phase fractions*. Ph.D. thesis, Imperial college of science, technology and medicine.

Sagaut, P. (2010). *Large Eddy Simulation for Incompressible Flows: An Introduction*. Scientific Computation, Springer Berlin Heidelberg, Berlin, 2nd edn.

Schiller, L. & Naumann, A. (1933). Ub¨ er die grundlegenden Berechnungen bei der Schwerkraftaufbereitung. *Z. Vereins deutscher Ing.*, **77**, 318–320.

Schlichting, H. & Gersten, K. (2016). *Boundary-Layer Theory*. Springer Berlin Heidelberg, Berlin, 9th edn.

Schramm, L.L. (2005). *Emulsions, Foams, and Suspensions: Fundamentals and Applications*. Wiley, Weinheim.

Sehmel, G.A. & Babb, A.L. (1963). Holdup studies in a pulsed sieve plate solvent extraction column. *Industrial & Engineering Chemistry process design and development*, **2**, 38–42.

Sen, N., Singh, K.K., Patwardhan, A.W., Mukhopadhyay, S. & Shenoy, K.T. (2015). CFD Simulations of Pulsed Sieve Plate Column: Axial Dispersion in Single-Phase Flow. *Separation Science and Technology (Philadelphia)*, **50**, 2485–2495.

Sen, N., Singh, K.K., Patwardhan, A.W., Mukhopadhyay, S. & Shenoy, K.T. (2016). CFD simulation of two-phase flow in pulsed sieve-plate column – Identification of a suitable drag model to predict dispersed phase hold up. *Separation Science and Technology (Philadelphia)*, **51**, 2790–2803.

Sen, N., Singh, K.K., Patwardhan, A.W., Mukhopadhyay, S. & Shenoy, K.T. (2018). CFD simulations to predict dispersed phase holdup in a pulsed sieve plate column. *Separation Science and Technology (Philadelphia)*, **00**, 1–14.

Shinnar, R. & Church, J. (1960). Statistical theories of turbulence in predicting particle size in agitated disperions. *Industrial and Engineering Chemistrery*, **52**, 253.

Sim-scale (2020). Rapid CFD, OpenFOAM running on GPU.

Singh Brar, L. (2018). Application of response surface methodology to optimize the performance of cyclone separator using mathematical models and CFD simulations. In *Materials Today: Proceedings*.

Smagorinksy, J. (1963). General circulation experiments with the primative equations. *Monthly Weather Review*, **91**, 99–164.

Smoot, L.D., Mar, B.W. & Babb, A.L. (1959). Flooding characteristics and separation efficiencies of pulsed sieve plate extraction columns. *Industrial and Engineering Chemistry*, **51**, 1005–1010.

Smoot, L.D.a.D.B. & Babb, a.L.a.L. (1962). Mass transfer studies in a pulsed extraction column Longitudinal Concentration Profiles. *Industrial Engineering Chemistry Fundamentals*, **1**, 93–103.

Speziale, C.G., Sarkar, S. & Gatski, T.B. (1991). Modelling the pressure-strain correlation of turbulence:an invariant dynamical systems approach. *J. of Fluid Mech.*, **227**, 245–272.

Sreenivasulu, K., Venkatanarasaiah, D. & Varma, Y.B.G. (1997). Drop size distributions in liquid pulsed columns. *Bioprocess Engineering*, **17**, 189–195.

Stamenković, O.S., Kostić, M.D., Radosavljević, D.B. & Veljković, V.B. (2018). Comparison of box-behnken, face central composite and full factorial designs in optimization of hempseed oil extraction by n-hexane: A case study. *Periodica Polytechnica Chemical Engineering*, **62**, 359–367.

Stoll, R. & Porté-Agel, F. (2006). Dynamic Subgrid-Scale Models for Momentum and Scalar Fluxes in Large-Eddy Simulations of Neutrally Stratified Atmospheric Boundary Layers Over Heterogeneous Terrain. *Water Resources Research*, **42**, 1–18.

Štrubelj, L. & Tiselj, I. (2011). Two-fluid model with interface sharpening. *International Journal for Numerical Methods in Engineering*, **85**, 575–590.

Takahashi, K. & Nii, S. (1999). Behavior of multistage mixer-settler extraction column. *Memoirs-School of Engineering*, 1–51.

Taylor, R. (2015). *Reprocessing and Recycling of Spent Nuclear Fuel*. Elsevier, Oxford.

Tennekes, H. & Lumley, J.L. (1972). *A First Course in Turbulence*. The MIT PRess, Massachusetts.

The OpenFOAM Foundation (2017). OpenFOAM.

Thornton, J.D. (1957). Liquid-Liquid Extraction Part Xiii: The Effect of Pulse Wave-Form and Plate Geometry in the Performance and Throughput of a Pulsed Column. *Transations of the Institution of Chemical Engineers*, **35**, 316–330.

Todd, T.A., Law, J.D., Herbst, R.S. & Lumetta GJ andMoyer, B.A. (2000). Treatment of Radioactive Wastes Using Liquid-Liquid Extraction Technologies-Fears, Facts, and Issues. In *Proc. Waste Management 00*, 1, Tucson.

Tomiyama, A. & Shimada, N. (2001). A Numerical Method for Bubbly Flow Simulation Based on a Multi-Fluid Model . *Journal of Pressure Vessel Technology*, **123**, 510–516.

Torab-Mostaedi, M., Safdari, J., Moosavian, M.A. & Ghannadi-Maragheh, M. (2009). Flooding characteristics in a Hanson mixer-settler extraction column. *Chemical Engineering and Processing: Process Intensification*, **48**, 1249–1254.

Torab-Mostaedi, M., Ghaemi, A. & Asadollahzadeh, M. (2011). Flooding and drop size in a pulsed disc and doughnut extraction column. *Chemical Engineering Research and Design*, **89**, 2742–2751.

Tretola, G., Vogiatzaki, K. & Navarro-Martinez, S. (2017). Detailed simulation of air-assisted spray atomization: effect of numerical scheme at intermediate Weber number. In *28th conference on liquid atomization and spray systems*, September, 6–8.

Treybal, R.E. (1968). *Mass-transfer Operations*. Chemical Engineering Series, McGraw-Hill kogakusha, Tokyo, 2nd edn.

Tribess, A. & Brunello, G. (1998). Flooding in pulsed sieve plate extraction columns with mass transfer effects. *Brazilian Journal of Chemical Engineering*, **15**.

Tung, L.S. & Luecke, R.H. (1986). Mass transfer and drop sizes in pulsed-plate extraction columns. *Industrial & Engineering Chemistry Process Design and Development*, **25**, 664–673.

University of Leeds (2019). Advanced research and computing, ARC3.

UxC (2020). Global Nuclear Market Assessment Based on IPCC Global Warming of 1 . 5 ° C Report IPCC Report Implications for Nuclear Energy Importance of Maintaining Existing Reactor Fleet. **50**, 1–12.

Van Dijck, W.J.D. (1935). Process and apparatus for intimately contacting fluids. *U.S. Official Gazette (2.011.186)*, **457**, 380.

Vankova, N., Tcholakova, S., Denkov, N.D., Ivanov, I.B., Vulchev, V.D. & Danner, T. (2007). Emulsification in turbulent flow: 1. Mean and maximum drop diameters in inertial and viscous regimes. *Journal of Colloid and Interface Science*, **312**, 363–380.

Vedaiyan, S. (1969). Hydrodynamics of two phase flow in spray columns.

Venkatanarasaiah, D. & Varma, Y.B.G. (1998). Dispersed phase holdup and mass transfer in liquid pulsed column. *Bioprocess and Biosystems Engineering*, **18**, 119–126.

Verma, A. & Mahesh, K. (2012). A Lagrangian subgrid-scale model with dynamic estimation of Lagrangian time scale for large eddy simulation of complex flows. *Physics of Fluids*, **24**, 85101.

Versteeg, H.K. & Malalasekera, W. (2007). *An Introduction to Computational Fluid Dynamics: The Finite Volume Method*. Pearson Education Limited, Malaysia, 2nd edn.

von Karman, T. (1930). Mechanical Similitude and Turbulence. Tech. rep., National Advisory Comitte for Aeronautics.

Wardle, K.E. (2013). Hybrid multiphase CFD simulation for liquid-liquid interfacial area prediction in annular centrifugal contactors. *International Nuclear Fuel Cycle Conference, GLOBAL 2013: Nuclear Energy at a Crossroads*, **2**, 1217–1226.

Wardle, K.E. & Shonibare, O.Y. (2015). Numerical Investigation of Vertical Plunging Jet Using a Hybrid Multifluid – VOF Multiphase CFD Solver. *International Journal of Chemical Engineering*, **2015**.

Wardle, K.E. & Weller, H.G. (2013). Hybrid Multiphase CFD Solver for Coupled Dispersed / Segregated Flows in Liquid-Liquid Extraction. *International Journal of Chemical Engineering*, **2013**.

Wardle, K.E., Allen, T.R. & Swaney, R. (2006). Computational Fluid Dynamics (CFD) Study of the Flow in an Annular Centrifugal Contactor. *Separation Science and Technology*, **41**, 2225–2244.

Weech, M.E. & Knight, B.E. (1967). Design of Air Pulsers for Pulse Column Application. *Industrial and Engineering Chemistry Process Design and Development*, **6**, 480–486.

Weech, M.E., MacQueen, D.K., P'Pool, R.S., Plant., I.C.P., Company., P.P. & National Reactor Testing Station, I.U. (1961). Interim report on the development of an air pulser for pulse column application.

Weech, W.E. & Knight. B. E. (1977). Design of Air Pulsars for Pulse Column Application. *Industrial and Engineering Chemistry Process Design and Development*, **6**, 480–486.

Weller, H. (2008). A new approach to vof-based interface capturing methods for incompressible and compressible flow. Tech. rep., OpenCFD Ltd.

Welty, J.R., Wicks, C.E., Wilson, R.E. & Rorrer, G.L. (2007). *Fundementals of Heat and Mas Transfer*. John Wiley & Sons Ltd, New York, 5th edn.

Wilke, C.R. & Chang, P. (1955). Correlation of diffusion coefficients in dilute solutions. *AIChE Journal*, **1**, 264–270.

Yadav, R.L. & Patwardhan, A.W. (2008). Design Aspects of Pulsed Sieve Plate Columns. *Chemical Engineering Journal*, **138**, 389–415.

Yadav, R.L. & Patwardhan, A.W. (2009). CFD Modeling of Sieve and Pulsed-Sieve Plate Extraction Columns. *Chemical Engineering Research and Design*, **87**, 25–35.

Yi, H. (2018). *Studies on Modeling and Scale-up of Ceramic Hybrid Pulsed Column*. Ph.D. thesis, Tsinghua University and the University of Melbourne.

Yi, H., Wang, Y., Smith, K.H., Fei, W.Y. & Stevens, G.W. (2017). Hydrodynamic Performance of a Pulsed Solvent Extraction Column with Novel Ceramic Internals: Holdup and Drop Size. *Industrial & Engineering Chemistry Research*, **56**, 999–1007.

Yi, H., Smith, K.H., Fei, W. & Stevens, G.W. (2020). CFD Simulation of Two-Phase Flow in a Hybrid Pulsed Sieve-Plate Solvent Extraction Column: Prediction of Holdup and Axial-dispersion Coefficients. *Solvent Extraction and Ion Exchange*, **38**, 88–102.

A

Appendix 1

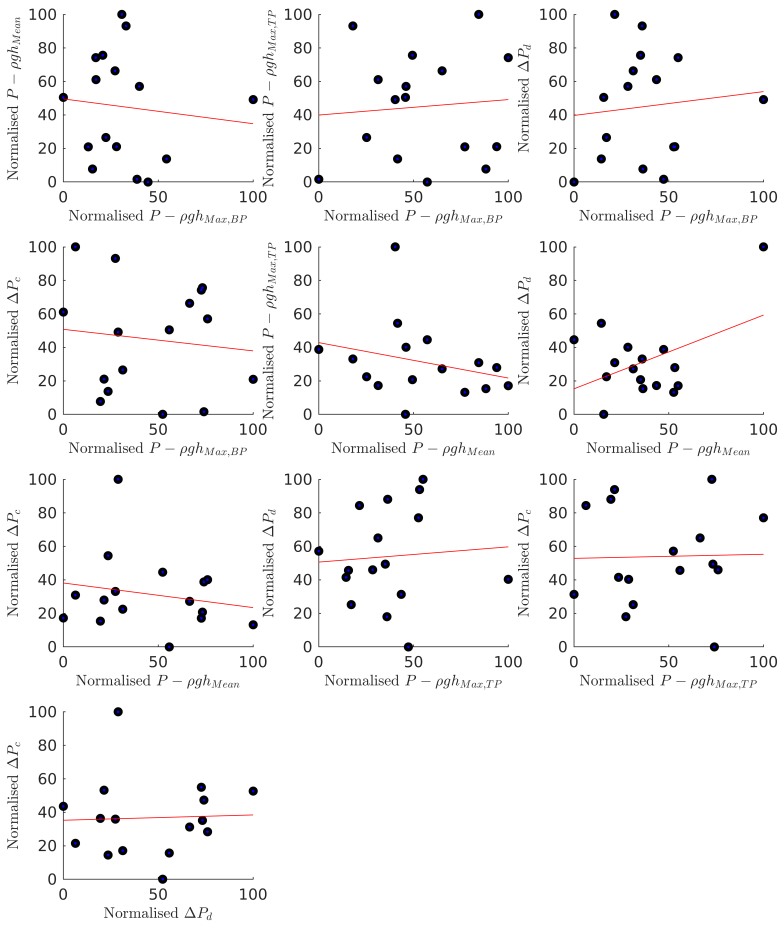

Figure A.1: Linear regression models of the characteristic pressure variables used to screen for correlation or interaction.

Table A.1: Details of the Linear regression models in Fig. A.1

	Graph No.									
	1	2	3	4	5	6	7	8	9	10
Gradient	-0.15	0.09	0.14	-0.13	-0.21	0.44	-0.15	0.09	0.02	0.03
Intercept	49.59	39.95	39.70	50.80	42.86	15.27	38.15	50.62	52.85	35.28
R sqrd	0.01	0.01	0.01	0.01	0.07	0.20	0.04	0.01	0.00	0.00

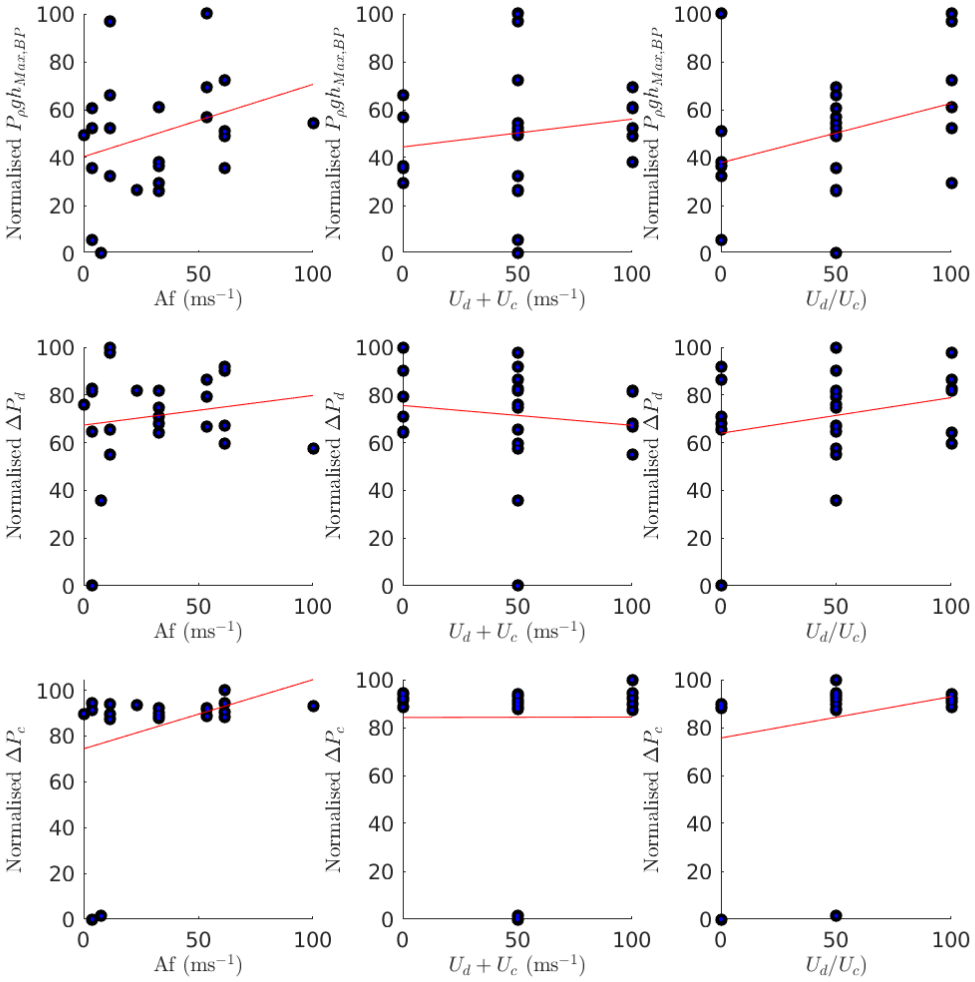

Figure A.2: Linear regression models of the characteristic pressure variables used to screen for correlation or interaction.

Table A.2: Details of the Linear regression models in Fig. A.2

	Graph No.								
	1	2	3	4	5	6	7	8	9
Gradient	0.3	0.12	0.25	0.12	-0.08	0.15	0.3	0	0.17
Intercept	40.38	44.44	37.85	67.36	75.58	63.95	74.43	84.21	75.65
R sqrd	0.1	0.03	0.12	0.02	0.02	0.06	0.1	6.5x10-6	0.06